

ABSTRACT

SAARE, HOLGER. Investigations of Atomic Layer Deposition and Thermal Atomic Layer Etching: Nucleation Trends, Area-Selectivity, and Phase Change Memory Materials. (Under the direction of Dr. Gregory Parsons).

Atomic layer deposition (ALD) is a rapidly evolving self-limiting vapor-phase deposition method, which enables angstrom-level control over the resulting thin film thickness. The precise control along with high uniformity and conformality have made ALD a vital nanofabrication technology, especially in the semiconductor industry. Along with ALD, a self-limiting etching method, atomic layer etching (ALE), has been actively studied for its ability to remove material at a highly controllable etch rate in both isotropic and anisotropic manner. A comprehensive understanding of the mechanisms present during both techniques is necessary as the semiconductor industry advances towards more complex 3D device architectures and beyond 5 nm technology nodes.

This dissertation studies various fundamental mechanisms and principles present in ALD and ALE processes. First, we demonstrate the impact precursor structure has on thin film growth trends during Al_2O_3 ALD. We compare trimethylaluminum $[(\text{CH}_3)_3\text{Al}]$, triethylaluminum $[(\text{C}_2\text{H}_5)_3\text{Al}]$, and dimethylaluminum chloride $[(\text{CH}_3)_2\text{AlCl}]$ as Al precursors for deposition on hydroxyl terminated Si-OH and hydrogen terminated Si-H surfaces. We show that while all precursors studied lead to imminent growth on the Si-OH substrate and a growth delay on the Si-H, the resulting growth trends greatly differ, providing vital insight into the importance of precursor selection during ALD on different substrates.

In a similar manner, the importance of the chemical structure of a co-reactant during ALE of metal oxides when coupled with WF_6 for a fluorination/ligand-exchange process is presented. Boron trichloride (BCl_3), thionyl chloride (SOCl_2), and titanium tetrachloride (TiCl_4) are studied

as co-etchants and the resulting etching pathways are compared for titania and zirconia substrates. The experimental measurements and thermodynamic simulations indicate that both the etchants and the substrate studied affect the etch rate, the temperature window, and the purity of the resulting sample. In addition to ALE, it was shown that TiO_2 can be chemical vapor etched individually by WF_6 or SOCl_2 at temperatures above the ALE temperature window (≥ 200 °C).

ALD and ALE can be combined to achieve area-selective deposition, during which the desired material is deposited onto one substrate, but not the other. We combined TiO_2 ALD with TiO_2 ALE to achieve deposition on the Si-OH substrate, with no growth on the Si-H substrate. We demonstrate that the selectivity between the substrates during ALD/ALE super-cycles can be significantly enhanced by limiting the precursor exposure. In particular, we show that the H_2O exposure plays an important role in the selectivity-loss mechanism on the Si-H substrate.

Finally we study and characterize an ALD process for GeTe and Sb_2Te_3 thin films for phase change memory (PCM) applications. While PCM cells have been primarily deposited by physical vapor deposition methods, the conformality of ALD deposited films enable more advanced 3D architectures, leading to higher memory densities.

© Copyright 2021 by Holger Saare

All Rights Reserved

Investigations of Atomic Layer Deposition and Thermal Atomic Layer Etching: Nucleation
Trends, Area-Selectivity, and Phase Change Memory Materials

by
Holger Saare

A dissertation submitted to the Graduate Faculty of
North Carolina State University
in partial fulfillment of the
requirements for the degree of
Doctor of Philosophy

Physics

Raleigh, North Carolina
2021

APPROVED BY:

Gregory Parsons
Committee Chair

David Aspnes

Divine Kumah

Michael Dickey

BIOGRAPHY

Holger Saare was born and grew up in Kohila, Estonia. After graduating from the local high school with honors in 2012 he attended the University of Tartu, where he graduated *cum laude* with BSc in Physics. During his studies he was a member of an innovative startup company ReLaDe, which aims to design and commercialize a reusable laundry detergent based on superparamagnetic nanoparticles. He continued his studies as a master's student in Materials Science, however it was cut short as he received the prestigious Fulbright Scholarship to spend a year studying and performing research in the United States. As North Carolina State University kindly offered him a spot in the Ph.D. program in Physics, he joined the Wolfpack as a master's student in 2016 and started to pursue his doctorate a year later, in 2017. Fascinated by the vast world of atomic layer deposition, Holger joined the Parsons research group in August 2017. In addition to atomic layer deposition, he learned about reactor building and maintenance, selective deposition, atomic layer etching, *in-situ* characterization techniques and countless other skills. After the graduation he will be working at ASM America in Phoenix, AZ, as a senior process engineer, continuing his journey in the world of atomic layer deposition.

ACKNOWLEDGMENTS

First and foremost, I am grateful to my advisor for the opportunity to join and perform research in his group. I appreciate him encouraging me to find answers to questions I did not know existed and enabling me to become a better researcher and a better person.

Special thanks to all the previous and current Parsons group members with whom I've had the pleasure to interact and discuss ideas with. I am very grateful to be a member of such a supporting group. In particular, I would like to extend my thanks to Michael Fusco, Mike Mantini, and Bruce Ash for helping me keep my reactor running even when everything was broken.

Finally, I would like to thank my family for their continuous support throughout my education path, despite it leading me to the other side of the world. A special thanks to my girlfriend, for tolerating my long working hours with me never being home and helping me get through the pandemic with a sane mind.

TABLE OF CONTENTS

LIST OF TABLES	viii
LIST OF FIGURES	ix
Chapter 1: Introduction and Background	1
1.1 Atomic Layer Deposition (ALD)	1
1.2 Atomic Layer Etching (ALE).....	7
1.3 Area-Selective Atomic Layer Deposition (AS-ALD)	10
1.4 Phase Change Memories	16
1.5 Scope and Organization.....	20
1.6 References	21
Chapter 2: Experimental Instrumentation	48
2.1 Thin Film Processing and Characterization System.....	48
2.2 Spectroscopic Ellipsometry	50
2.3 Auger Electron Spectroscopy	53
2.4 X-ray Photoelectron Spectroscopy	56
2.5 Fourier Transform Infrared Spectroscopy	57
2.6 Scanning Electron Microscopy	58
2.7 Transmission Electron Microscopy	58
2.8 Atomic Force Microscopy	59
2.9 X-ray Diffraction	59
2.10 References	59

Chapter 3: Comparative *In-situ* Study of the Initial Growth Trends of Atomic Layer

Deposited Al₂O₃ films	87
3.1 Preface	87
3.2 Introduction	88
3.3 Methodology	91
3.4 Results and Discussion	93
3.4.1 Film Thickness Evolution	93
3.4.2 Process Selectivity	95
3.4.3 Elemental Analysis by <i>In-situ</i> Auger Electron Spectroscopy	97
3.4.4 Ellipsometry Trends During Initial Half-Cycles	100
3.4.5 <i>In-situ</i> Fourier Transform Infrared Spectroscopy Analysis	101
3.5 Discussion	105
3.6 Conclusion	107
3.7 Acknowledgments	108
3.8 Supplemental Material	109
3.9 References	114

Chapter 4: Comparison of Chlorinating Agents for Thermal Atomic Layer Etching of

Titania and Zirconia using Tungsten Hexafluoride	126
4.1 Preface	126
4.2 Introduction	127
4.3 Experimental Details	131
4.3.1 Reactor Design	131
4.3.2 Substrate Preparation and Etching	132

4.3.3 Process Characterization	132
4.4 Results and Discussion.....	133
4.4.1 Thermodynamic Modeling of Reactions on TiO ₂ and ZrO ₂	133
4.4.2 <i>In-situ</i> Ellipsometry Study of Reactions on TiO ₂ and ZrO ₂	136
4.4.3 Thermodynamic Modeling of Reactions During ALE	139
4.4.4 <i>In-situ</i> Ellipsometry Measurements of TiO ₂ and ZrO ₂ ALE	141
4.4.5 Elemental Characterization of TiO ₂ and ZrO ₂ ALE	144
4.4.6 Surface Morphology of Metal Oxides Etched by ALE	147
4.5 Conclusion.....	148
4.6 Acknowledgments	150
4.7 Supplemental Material	150
4.8 References	154
 Chapter 5: Effect of Reactant Dosing on Selectivity During Area-Selective Deposition	
of TiO₂ Via Integrated Atomic Layer Deposition and Atomic Layer Etching.....	
5.1 Preface	161
5.2 Introduction	162
5.3 Experimental Details	165
5.3.1 Reactor Design.....	165
5.3.2 Substrate Preparation	167
5.3.3 Deposition and Etching Process.....	167
5.3.4 Process Characterization.....	168
5.3.5 Material Characterization.....	172
5.4 Results And Discussion.....	172

5.4.1 Effect of Dosing Time on ALD Growth	172
5.4.2 Combined ALD/ALE Super-cycles	175
5.4.3 Effect of Dosing Time on Patterned Substrates	182
5.5 Conclusion.....	184
5.6 Supplemental Material	186
5.7 References	186
Chapter 6: Atomic Layer Deposition of GeTe-Sb₂Te₃ Phase Change Memories	195
6.1 Preface	195
6.2 Introduction	195
6.3 Experimental Details	197
6.4 Results and Discussion.....	198
6.5 Conclusion.....	210
6.6 Acknowledgments	211
6.7 References	213
Appendix.....	218
A.1 Integrated Isothermal Atomic Layer Deposition/Atomic Layer Etching Supercycles for Area-Selective Deposition of TiO ₂	219

LIST OF TABLES

Table S3.1	Atomic percentages of elements measured by <i>in-vacuo</i> Auger Electron Spectroscopy as a function of ALD cycles at 200 °C. The measurements were performed on Si-H and Si-OH substrates using MTA, TEA, or DMAC as Al precursors and H ₂ O as an oxygen source.....	112
Table 5.1	Elemental composition of hydrogen-terminated (100) Si wafers exposed to different TiCl ₄ /H ₂ O dosing times as measured by X-ray photoelectron spectroscopy (XPS). One super-cycle consists of 30 ALD and 5 ALE cycles.....	180

LIST OF FIGURES

Figure 1.1	Schematic representation of one cycle of atomic layer deposition. Each cycle ideally results in a monolayer of deposited material and can be repeated to achieve the desired thin film thickness	2
Figure 1.2	Schematic of ALD process growth rate dependence of deposition temperature illustrating a temperature window	4
Figure 1.3	Schematic representation of primary ALD growth modes: (a) Frank–van der Merwe (layer-by-layer growth) mode; (b) Volmer–Weber (island growth) mode; (c) Stranski-Krastnov(layer-plus-island) mode.....	6
Figure 1.4	Growth rate of the ALD film for various initial growth regimes: (a) steady-state; (b) substrate-enhanced, (c) type 1 substrate-inhibited growth, and (d) type 2 substrate-inhibited growth. The figure is reproduced from ³⁷	6
Figure 1.5	Schematic diagram of a single cycle of plasma atomic layer etching (top) and thermal atomic layer etching (bottom). While the surface activation step is similar in the two processes, the plasma ALE uses ion bombardment to remove the surface layer, while thermal ALE converts the layer into volatile etching products.....	8
Figure 1.6	Overview of two conventional approaches to achieve area-selective atomic layer deposition: area-deactivation (left) and area-activation (right).....	12

Figure 1.7 Total Gibbs free energy as a function of nucleus radius for two different surfaces as predicted by classical nucleation theory. Redrawn from ⁶⁰ 15

Figure 1.8 Illustration of a combined atomic layer deposition and atomic layer etching supercycle. As nuclei start to grow on the preferred non-growth surface during ALD, intermittent ALE cycles can be performed to remove these nuclei before proceeding. By selecting proper process conditions, selectivity can be greatly enhanced compared to an ALD-only case. 16

Figure 1.9 Diagram illustrating the operation principle of a phase change memory. A low long pulse is used to revert the material into crystalline phase with low resistance. A short high pulse brings the PCM to an amorphous state with high resistance. Figure reproduced.⁹⁰ 18

Figure 1.10 Ternary phase diagram of a Ge-Sb-Te phase change memory materials system. The color map indicates the crystallization temperature of the specific composition. The black lines represent the Sb_2Te_3 -GeTe tie line on which GST225 is located and the Sb_2Te_3 - Ge_2Te_3 line, which represents the lowest crystallization temperatures. Figure reproduced.⁹⁵ 19

Figure 2.1 Diagram and a photo of the multi-chamber cluster tool used in this work. The chamber is capable of both thermal and plasma-enhanced atomic layer deposition and atomic layer etching. It is equipped with Auger electron spectroscopy, multi-wavelength ellipsometry for *in-situ* process characterization 49

Figure 2.2	Simplified configuration of an ellipsometer with a rotating analyzer. The polarizer produces linearly polarized light at 45° angle. The elliptically polarized light, resulting from interaction with the sample, is transmitted through an analyzer. The detector records a sinusoidal signal with periodicity of 2α . Figure reproduced. ¹¹¹	51
Figure 2.3	Schematic of the modelling and data analysis procedure for spectroscopic ellipsometry. Figure reproduced. ¹¹²	52
Figure 2.4	Diagram of the Auger effect illustrating an emission process for $KL_{2,3}L_{2,3}$ Auger electron. Figure reproduced. ¹²⁰	55
Figure 2.5	Auger spectrum of Cu (a) as measured and (b) in a differentiated mode. The derivative mode is used to remove the noisy background and emphasize Auger peaks. Figure reproduced. ¹²¹	56
Figure 2.6	Illustration of the ALD reactor equipped with in-situ FTIR capability used in this work. Figure reproduced. ¹²²	58
Figure 3.1	Simplified schematic of the chamber system used in this work, including the reaction chamber equipped with <i>in-situ</i> spectroscopic ellipsometry and analysis chamber with Auger electron spectroscopy	93
Figure 3.2	The thickness of Al_2O_3 thin film on Si-OH and Si-H surfaces deposited by ALD using TMA/ H_2O , TEA/ H_2O , and DMAC/ H_2O at 200 °C as measured by <i>in-situ</i> ellipsometry.	94
Figure 3.3	Calculated selectivity fraction S as a function of Al_2O_3 film thickness on Si-OH. Data were collected for TMA, TEA, and DMAC ALD processes at 200 °C	96

Figure 3.4	Auger electron spectroscopy spectra of Al ₂ O ₃ thin films deposited at 200 °C on Si-H and Si-OH using TMA (top row), TEA (middle row), or DMAC (bottom row) as Al precursors. The data are presented in derivative mode.....	99
Figure 3.5	Al to Si+Al atomic percentage ratios of Al ₂ O ₃ deposited Si-H and Si-OH starting substrates at 200 °C as measured by <i>in-situ</i> Auger electron spectroscopy.....	100
Figure 3.6	Ellipsometric delta parameter changes at 465 nm wavelength during half-cycles of Al ₂ O ₃ ALD using TMA, TEA, or DMAC as Al precursor on (a) Si-OH, (b) native Si oxide, and (c) Si-H surfaces. All data were collected <i>in-situ</i> at 200 °C deposition temperature.....	101
Figure 3.7	Difference FTIR spectra of the half-reactions of the 1 st and 2 nd ALD cycles of TMA/H ₂ O (a,b) and TEA/H ₂ O (c,d) on porous Si-OH and Si-H substrates.....	103
Figure 3.8	Integrated area under -OH peak between 3350-2780 cm ⁻¹ for (a) TMA/H ₂ O and (c) TEA/H ₂ O and under C-H peak between 2850-2295 cm ⁻¹ for (b) TMA/H ₂ O and (d) TEA/H ₂ O on porous silicon	105
Figure S3.1	The thickness of Al ₂ O ₃ film on Si-OH and Si-H surfaces for ALD by TMA/H ₂ O, TEA/H ₂ O, and DMAC/H ₂ O in temperature range 150-250 °C as measured by <i>in-situ</i> ellipsometry.....	109
Figure S3.2	Calculated selectivity between Si-OH and Si-H surfaces as a function of Al ₂ O ₃ thickness on Si-OH substrate for ALD by TMA/H ₂ O, TEA/H ₂ O, and DMAC/H ₂ O in temperature range 150-250 °C.....	110

Figure S3.3 Calculated selectivity between Si-OH and Si-H surfaces as a function of Al₂O₃ ALD cycle number for ALD by TMA/H₂O, TEA/H₂O, and DMAC/H₂O in temperature range 150-250 °C..... 111

Figure S3.4 Delta parameter change at 465 nm wavelength during half-cycles of Al₂O₃ ALD using TMA/H₂O, TEA/H₂O, or DMAC/H₂O on Si-OH (top row), native Si oxide (middle row), and Si-H (bottom row) surfaces at 150 °C, 200°C, and 250 °C. Δ parameter characterizes the phase change upon polarized light reflection and is correlated with the thin film optical thickness change – in the current regime, the film thickness increases as Δ decreases and vice versa 113

Figure 4.1 Schematic view of warm-walled chamber system. The system consists of a processing chamber, equipped with in-situ ellipsometer, and of an analysis chamber with in-situ Auger electron spectroscopy 130

Figure 4.2 Expected equilibrium species determined by thermodynamic modeling in the temperature range from 25 °C to 400 °C for (a/e) 1 mol TiO₂/ZrO₂ & 1 mol WF₆, (b/f) 0.75 mol TiO₂/ZrO₂ & 1 mol BCl₃, (c/g) 0.5 mol TiO₂/ZrO₂ & 1 mol SOCl₂, and (d/h) 1 mol TiO₂/ZrO₂ & 1 mol TiCl₄..... 134

Figure 4.3 Thickness change of TiO₂ and ZrO₂ thin films when exposed to WF₆ (a,e), BCl₃ (b,f), SOCl₂ (c,g), or TiCl₄ (d,h) doses at various temperatures as measured by *in-situ* ellipsometry..... 137

Figure 4.4 Expected equilibrium species determined by thermodynamic modeling in the temperature range from 25 °C to 400 °C for 1 mol WO₃ reacting with

(a) 4/3 mol BCl₃, (b) 1 mol TiCl₄, (c) 1 mol SOCl₂, and for 1 mol ZrF₄ reacting with (d) 4/3 mol BCl₃, (e) 1 mol TiCl₄, (f) 2.4 mol SOCl₂ 140

Figure 4.5 Saturation curves of etch rate dependence on WF₆ and co-reactant dose times for TiO₂ (a,b) and for ZrO₂ (c,d). All TiO₂ etching processes were performed at 170 °C and ZrO₂ etching at 325°C. The etch rate per cycle was determined by *in-situ* ellipsometry over 10 ALE cycles 142

Figure 4.6 Influence of substrate temperature on the etch rates during atomic layer etching of (a) TiO₂ and (b) ZrO₂ thin films..... 142

Figure 4.7 *In-situ* ellipsometry (top) and Auger electron spectroscopy (bottom) measurements of TiO₂ thermal ALE using WF₆ and BCl₃, TiCl₄, or SOCl₂ at 170 °C. The ellipsometry data were collected after every ALE cycle, while AES measurements were done before etching and after 5 and 25 ALE cycles 144

Figure 4.8 *In-situ* ellipsometry (top) and Auger electron spectroscopy (bottom) measurements of TiO₂ thermal ALE using WF₆ and BCl₃, TiCl₄, or SOCl₂ at 170 °C. The ellipsometry data were collected after every ALE cycle, while AES measurements were done before etching and after 5 and 25 ALE cycles 146

Figure 4.9 RMS surface roughness evolution as a function of ALE cycles as measured by atomic force microscopy. The ALE of TiO₂ films was performed at 170 °C and the ZrO₂ films at 325°C 147

Figure S4.1 Expected equilibrium species determined by thermodynamic modeling in the temperature range from 25 °C to 400 °C for (a) 1 mol B₂O₃, 1 mol WF₆, and (b) 1 mol Zr(SO₄)₂, 2 mol WF₆..... 149

Figure S4.2 Thickness values of TiO₂/ZrO₂ thin films when etched by WF₆ and BCl₃ (a/d), SOCl₂ (b/e), or TiCl₄ (d/f). The TiO₂ was etched at 170 °C and ZrO₂ at 325 °C. Data measured by *in-situ* ellipsometry..... 150

Figure S4.3 Auger electron spectroscopy (AES) spectra of atomic layer etched TiO₂ and ZrO₂ thin films. Spectra are shown before etching, and after 5 and 25 cycles of atomic layer deposition. The TiO₂ films are deposited on chemical Si oxide and etched at 170 °C, while the ZrO₂ are deposited on Al₂O₃ and etched at 325 °C 151

Figure S4.4 Atomic force microscopy images of TiO₂ and ZrO₂ as-deposited, and after 5 and 25 ALE cycles using WF₆ and BCl₃, TiCl₄ or SOCl₂..... 152

Figure 5.1 Simplified schematic representation of deposition chamber used in this work, including the gas delivery lines setup, pumping system and attached spectroscopic ellipsometer 166

Figure 5.2 In-situ ellipsometry data collected during deposition and etching steps on Si-OH surface. (a) and (b) show the raw delta (Δ) and psi (Ψ) parameters, respectively, which are fitted by a Cauchy model to (c) measure TiO₂ layer thickness..... 169

Figure 5.3 Growth per cycle (GPC) of TiO₂ on TiO₂ thin films deposited on Si-OH surface measured by in-situ ellipsometry. One of the precursor dosing times

is held constant at 300 ms, while dosing time of (a) TiCl_4 and (b) H_2O is varied 174

Figure 5.4 The thickness of TiO_2 layer on Si-OH and Si-H surfaces for 90 ms, 180 ms, and 270 ms $\text{TiCl}_4/\text{H}_2\text{O}$ dosing times as measured by in-situ ellipsometry 175

Figure 5.5 The thickness of TiO_2 layer on Si-H as a function of number of super-cycles using $\text{TiCl}_4/\text{H}_2\text{O}$ dosing times of 90, 180, and 270 ms as measured by in-situ ellipsometry. Data is collected after each 5 ALD cycles and after each individual ALE cycle. The data for 180 and 270 ms is offset on the y-axis by 1 nm and 2 nm, respectively, to improve visualization.... 177

Figure 5.6 XPS data of the Ti 2p signal for deposition carried out using: (a) 90; (b) 180; and (c) 270 ms H_2O and TiCl_4 dosing times for varying number of deposition/etch super-cycles (N) on Si-H 178

Figure 5.7 The thickness of TiO_2 layer on Si-H for $\text{TiCl}_4/\text{H}_2\text{O}$ 90/270 ms and 270/90 ms dosing times as measured by in-situ ellipsometry. Data is shown for 15 super-cycles, consisting of 30 ALD and 5 ALE cycles each, with data points taken every 5 cycles for ALD and every cycle for ALE. The data for 90/270 ms is offset on the y-axis by 1 nm to improve visualization 180

Figure 5.8 TiO_2 film thickness on Si-H and Si-OH surfaces during ALE/ALE super-cycles with 90 ms dosing conditions for $\text{TiCl}_4/\text{H}_2\text{O}$. The measurement was done by in-situ ellipsometry, with data point taken after every 5 cycles for ALD and every cycle for ALE 181

Figure 5.9	SEM images of TiO ₂ ALD/ALE on patterned Si/SiO ₂ substrates using (a) 270 ms dosing conditions for 10 super-cycles and (b) 90 ms dosing conditions for 30 super-cycles	183
Figure 5.10	(a) Cross-sectional TEM and (b) TEM-EDS mapping of 10 ALD/ALE super-cycles at 270 ms dosing conditions on Si/SiO ₂ pattern. (c) Cross-sectional TEM and (d) TEM-EDS mapping of 30 ALD/ALE super-cycles at 90 ms dosing conditions on Si/SiO ₂ pattern.....	184
Figure S5.1	XPS spectra of the B 1s/Si 2s plasmon (a,b,c) and W 4d (d,e,f) signal for deposition carried out using: (a,d) 90; (b,e) 180; and (c,f) 270 ms H ₂ O and TiCl ₄ dosing times for varying number of deposition/etch super-cycles (N) on Si-H. One super-cycle consists of 30 ALD and 5 ALE cycles. The B 1s peak is located at 191 eV, overlapped by a Si 2s plasmon loss signal.....	186
Figure 6.1	Film thickness of GeTe films as a function of the number of ALD cycles at 70 °C for varying (a) HGeCl ₃ and (b) BTMSTe dosing times. Resulting first cycle and steady-state growth rates as a function of (c) HGeCl ₃ and (d) BTMSTe dosing times	199
Figure 6.2	Effect of (a) process temperature and (b,c) precursor purge times on the initial and steady-state growth rates of GeTe thin films	201
Figure 6.3	Measured ellipsometric delta parameter as a function of GeTe ALD cycles on (a) Si-OH, (b) Si-H, (c) W, and (d) TiN surfaces. Decrease in the delta parameter indicates an increase in the films optical thickness in the current growth regime	203

Figure 6.4	Atomic force microscopy images of GeTe ALD on W, Si-H and TiN surfaces for varying number of ALD cycles. The calculated RMS roughness as a function of the cycle number is plotted	204
Figure 6.5	XPS spectra of GeTe ALD for 40 cycles on Si-OH (left column), 100 cycles on Si-H (middle column), and 100 cycles on W (right column)	206
Figure 6.6	Grazing-incidence X-ray diffraction (GIXRD) measurements of GeTe after 100 ALD cycles on Si-H (left column) and W (right column) as-deposited at 70 °C and after annealing at 170 °C for 15 minutes under argon flow	207
Figure 6.7	Ellipsometric delta parameter at 465 nm wavelength as a function of number of ALD cycles for (a) Sb ₂ Te ₃ ALD on Si-OH and (b) consecutive deposition of GeTe on Si-OH, Sb ₂ Te ₃ on GeTe, and GeTe on Sb ₂ Te ₃ at 70 °C. (c,d) XPS spectra of Sb 3d and Te 3d peaks after 50 cycles	209

CHAPTER 1

Introduction and Background

1.1 Atomic Layer Deposition (ALD)

Atomic layer deposition (ALD) is a vapor-phase thin film deposition method that allows growth of various materials with monolayer precision. The process follows a cyclical scheme with each step, also referred to as half-cycles, consisting of self-limiting reactions, which are enabled by the fact that chemical precursors react only with the sample surface and not with the same molecules.¹ Moreover, the exposure of each reactant is separated by an inert gas purge, preventing them from reacting in the gas phase. As such, a well-designed ALD experiment results in a uniform and conformal film with a desired thickness on both planar substrates and on more complex 3D structures.²

An example of a general ALD cycle, commonly consisting of two half-cycles, is displayed in figure 1.1. First the substrate is exposed to a pulse of the first precursor, which chemisorbs onto the surface, enabling self-limiting growth as further exposure is inhibited from reacting with the sample. This pulse is followed by a purge step, where an inert gas, commonly nitrogen or argon, is flown through the reactor to remove the resulting reaction byproducts and the unreacted precursor molecules. The co-reactant is then introduced, reacting with the surface, and ideally resulting in a monolayer of the desired thin film material. Once again, the excess molecules and byproducts are purged, and the cycle can be repeated from the first step until the desired thickness is achieved. A frequent example and one of the most commonly used processes is deposition of alumina on a silicon oxide surface using trimethylaluminum (TMA) and water as precursors.³⁻⁵

The reaction can be described as follows:



As a first step, the pulsed TMA reacts with surface functional groups, in this case hydroxyls, resulting in precursor ligands left on the surface and CH_4 that is purged from the chamber using an inert gas. These ligands subsequently react with a pulsed H_2O dose, forming a layer of the Al_2O_3 film and restoring the -OH surface determination, enabling the cycle to be repeated.^{6,7}

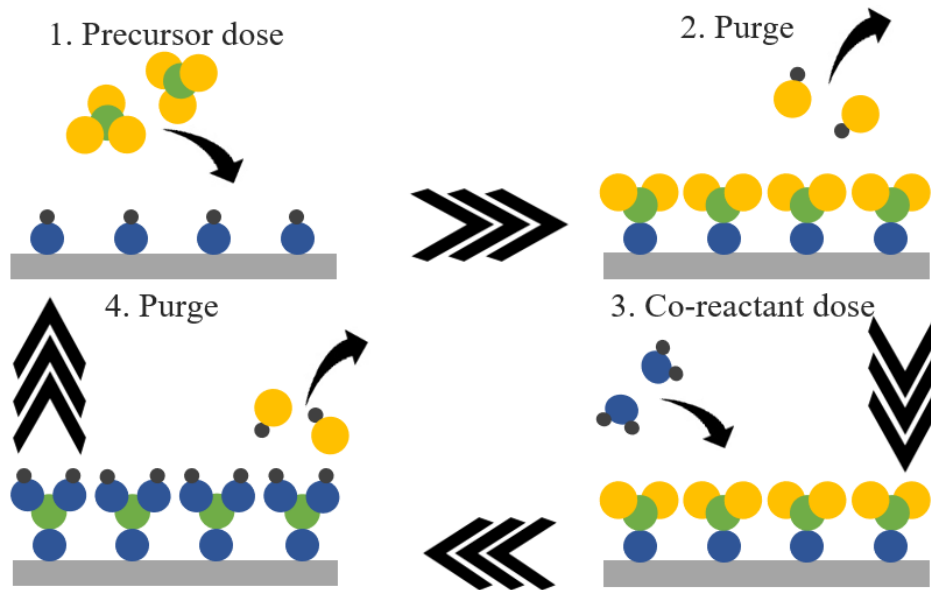


Figure 1.1. Schematic representation of one cycle of atomic layer deposition. Each cycle ideally results in a monolayer of deposited material and can be repeated to achieve the desired thin film thickness.

While an ideal ALD model predicts a monolayer-by-monolayer growth of the film, the experimental data reveals that the typical growth rates (known as growth per cycle, GPC) are less than a monolayer per cycle.^{8,9} Despite the self-limiting nature, the growth rate is limited by steric hindrance of the molecules, incomplete removal, and desorption of the precursor ligands.¹⁰⁻¹² In addition to precursor structure, the saturated growth rate is affected by the process temperature. A

typical ALD process is characterized by an “ALD temperature window”, which is a temperature range within which the GPC is affected mildly or not at all by fluctuations in the process temperature.¹³⁻¹⁵ Outside that range various phenomena can affect the growth as indicated in figure 1.2. At temperatures below the defined ALD window the reactants can condensate onto the substrate, leading to enhanced growth rates. In other cases, the growth rate can drop at low temperatures, as the low reactivity leads to slow reaction kinetics. At processing temperatures above the ALD window the reactants can thermally decompose, leading to chemical vapor deposition. Alternatively, the GPC might drop due to re-evaporation of the precursors from the surface. In addition to affecting the deposition rates, these effects may lead to undesirable film properties, such as increased porosity, impurities and nonuniform growth. As such it is always beneficial to determine and operate within the ALD temperature window to achieve the benefits of an ALD process.¹⁶

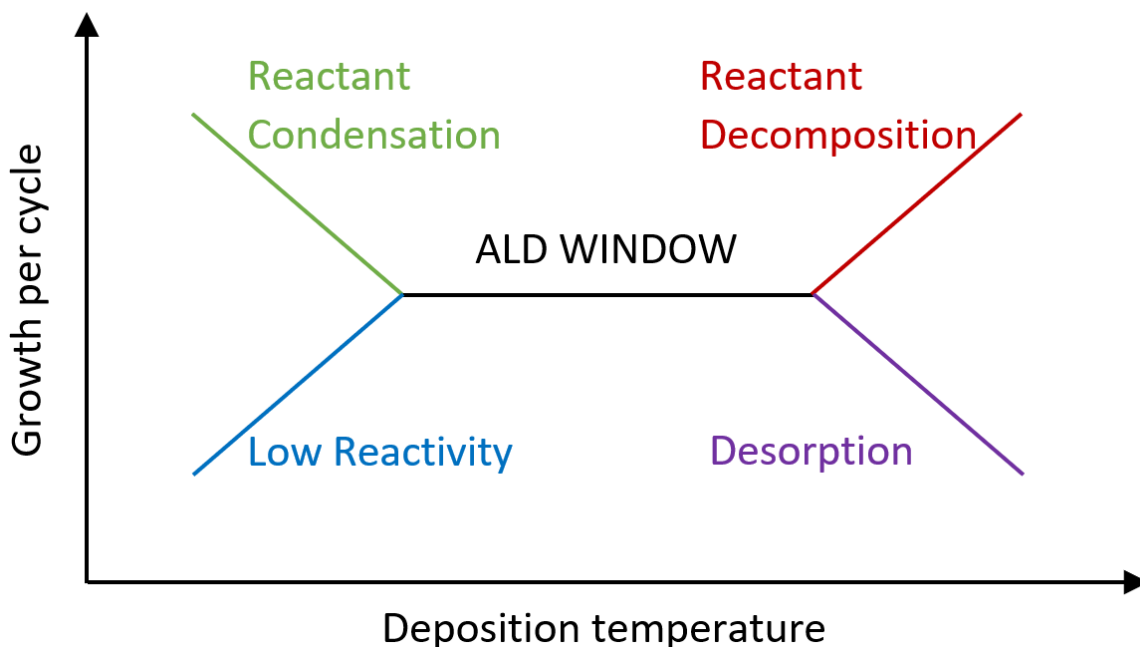


Figure 1.2. Schematic of ALD process growth rate dependence of deposition temperature illustrating a temperature window.

Substrate characteristics, precursor design, and process conditions affect the thin film growth trends during atomic layer deposition.¹⁷ Three primary growth trends of an ALD process are illustrated in figure 1.3. In Frank-van der Merwe mode, also referred to as layer-by-layer growth mode, the material is deposited as smooth uniform layers.¹⁸ Such trend is assumed to be the ideal ALD growth mode and occurs when the deposited species are more strongly attracted to the surface than to each other. For example, Frank-van der Merwe mode is often observed during metal oxide or nitride deposition on oxide substrates.^{19–21} During Volmer-Weber growth mode, also known as island growth, the thin film deposits as small islands onto the substrate, resulting in non-conformal film.²² As more ALD cycles are performed, the islands grow and eventually coalesce into a thin film layer after which the growth proceeds at a steady state.²³ The Volmer-Weber growth mode occurs when the reactants are more strongly attracted to each other than to the sample surface. This growth mode is of great interest as initial non-uniform nucleation can cause issues in applications, where ultrathin layer of material is desired, for example, in dielectric gate oxides in MOSFETs.^{24–27} This growth mode can occur during metal oxide ALD on hydrogen-terminated Si surface or during metal ALD on a silicon oxide substrate.^{28–32} The third growth mode, Stranski-Krastnov mode (layer-plus-island growth mode) is the combination of the previous two and is less commonly reported during ALD processes.³³ In this mode the growth begins as uniform layers, just as Frank-van der Merwe growth mode. However, as the strain of the film increases and a critical thickness is reached, the material starts depositing as islands to reduce the strain.³⁴ The layer-plus-island growth mode have been observed for TiN deposition on SiO₂ substrates or during alumina growth on W nanoparticles.^{35,36}

Different growth regimes can be deduced by plotting the film thickness growth as a function of deposition cycles as illustrated in figure 1.4.³⁷ If the growth rate is constant throughout

the deposition process the growth is linear and proceeds at the same rate on the initial surface as it does on the deposited film. The GPC can also be higher during the initial cycles after which it slows to a steady-state growth rate. Such regime is referred to as substrate-enhanced growth, as it occurs when the initial substrate has more available reaction sites compared to the deposited film layer. In contrast, during substrate-inhibited growth, the GPC is lower during the initial cycles followed by an acceleration to the steady-state GPC. Two types of substrate-inhibited growth modes exist, in Type 1 the GPC steadily accelerates to the constant value, in Type 2 the GPC goes through a maximum before settling at the constant value.¹¹ Substrate-inhibited growth takes place when there are less reactive sites on the initial starting surface compared to the deposited material.

(a) Frank – van der Merwe

(b) Volmer - Weber

(c) Stranski-Krastanov

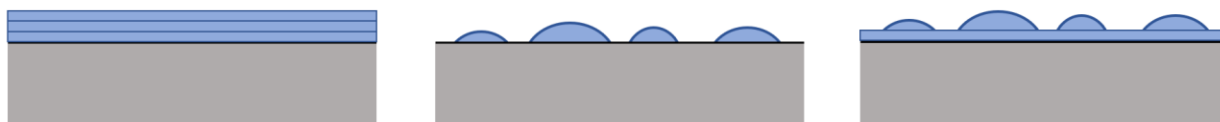


Figure 1.3. Schematic representation of primary ALD growth modes: (a) Frank–van der Merwe (layer-by-layer growth) mode; (b) Volmer–Weber (island growth) mode; (c) Stranski-Krastanov (layer-plus-island) mode.

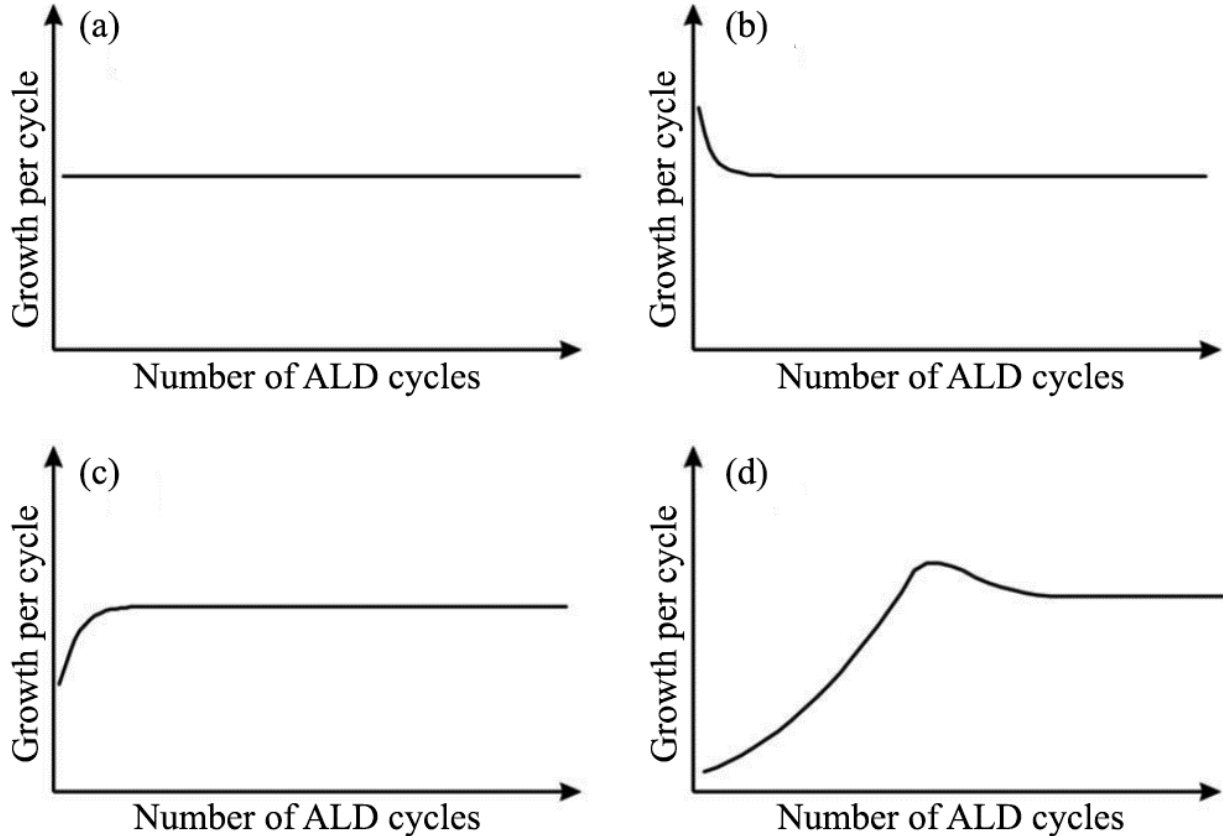


Figure 1.4. Growth rate of the ALD film for various initial growth regimes: (a) steady-state; (b) substrate-enhanced, (c) type 1 substrate-inhibited growth, and (d) type 2 substrate-inhibited growth. The figure is reproduced from ³⁷.

1.2 Atomic Layer Etching (ALE)

Atomic layer etching (ALE) is an emerging process, which enables to remove the top monolayers of a material at a controlled rate. The process is self-limiting and uses sequential reactions, which is why it is sometimes referred to as “reverse-ALD”.³⁸ ALE is commonly a two-step process, with the first step modifying the surface and the second step converting the modified layer to volatile species, effectively removing the layer. In general, as illustrated in figure 1.5, ALE processes can be divided into two categories: plasma ALE and thermal ALE. Compared to more commonly used continuous etching methods, such as reactive ion etching (RIE), atomic layer

etching processes have the benefit of less process variability, improved uniformity, and more control over the etch rate with the drawback of slower etching.³⁹

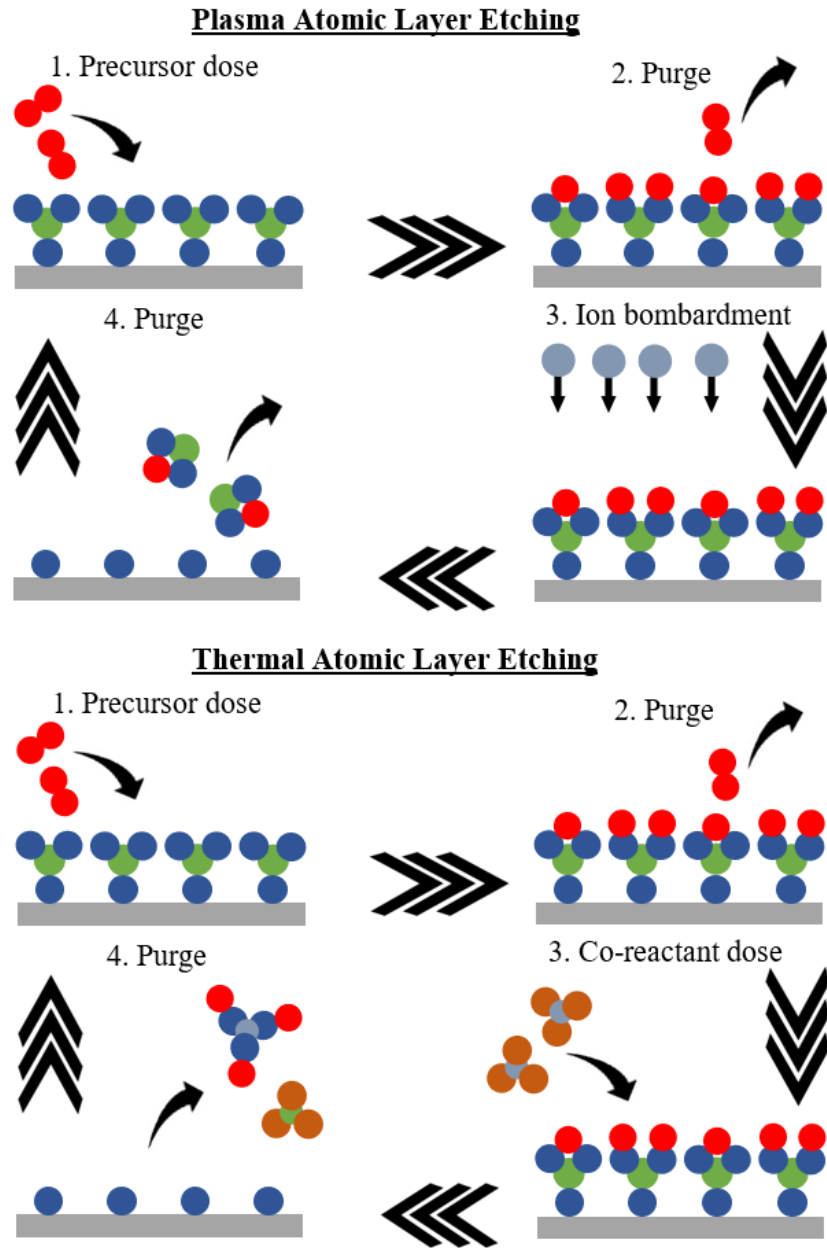


Figure 1.5. Schematic diagram of a single cycle of plasma atomic layer etching (top) and thermal atomic layer etching (bottom). While the surface activation step is similar in the two processes, the plasma ALE uses ion bombardment to remove the surface layer, while thermal ALE converts the layer into volatile etching products.

The processes present in plasma-based ALE have been actively studied since 1989 when articles on controlled etching of synthetic diamond films and GaAs were published.⁴⁰ Since then many more materials have been etched, primarily the ones of interest to the semiconductor industry, including various metals, insulators, and semiconductors.^{38,39,41-44} During the first step of plasma ALE the top surface layer is modified to make it more readily removable compared to the original material. The second step includes bombarding the surface with low energy inert ions to remove the modified layer. In ideal conditions both steps are separated in time and are self-limiting. This means that the modification must passivate the surface, limiting further reactions, and that the removal step must not sputter the material below the modified layer.⁴⁵

In a thermal ALE process the modified surface layer is removed due to a thermally-driven reaction resulting in volatile products. The advantages of the thermal ALE process are conformal, isotropic etching, improved selectivity, and no plasma damage, enabling to uniformly etch more complex 3D structures.^{38,43}

Depending on the chemistry used and the material being etched, several atomic layer etching mechanisms have been identified: “fluorination & ligand-exchange,” “oxidation & fluorination,” “conversion-etch,” and more.³⁸ During the “fluorination & ligand-exchange” mechanism the surface is modified through fluorination after which the modified layer is volatilized through a ligand-exchange. This process is commonly used for ALE of metal oxides, which do not result in volatile metal fluorides, for example Al_2O_3 , HfO_2 , and TiO_2 .⁴⁶⁻⁵² It has been shown that Al_2O_3 layer can be converted to AlF_3 using HF, after which the fluorinated layer can be volatilized using $\text{Al}(\text{CH}_3)_3$, $\text{Al}(\text{CH}_3)_2\text{Cl}$, or $\text{Sn}(\text{acac})_2$.^{46,53,54} Likewise, it has been shown that titania can be etched using WF_6/BCl_3 during which the WF_6 converts the TiO_2 into solid TiO_yF_z and WO_xF_y species.⁵² The layer is subsequently volatilized by BCl_3 exposure, creating volatile

WOCl₄, TiCl₄ and BF₃ species, however, leaving a solid B₂O₃ layer on the surface, which can be removed by the following WF₆ exposure. It has been shown that at temperatures below 350 °C the process selectively etches TiO₂ over Al₂O₃ due to lower volatility of AlF₃ and AlCl₃ species. During the “oxidation & fluorination” ALE mechanism the material is first oxidized and then the layer is volatilized using fluorinating reactants.⁴³ This can be used to etch metals or nitrides by converting them to metal oxide, which enables subsequent fluorination. This mechanism has been demonstrated on W using O₂/WF₆ as reactants and on TiN using O₃/HF.^{55,56} The “conversion-etch” mechanism can be used to achieve ALE of materials that cannot be etched using previous methods. During the process, a material can be converted to another, that is susceptible to a different method, for example fluorination.⁴³ For example, ZnO and SiO₂ have been etched by exposing the sample to alternating HF and TMA pulses.^{57,58} The TMA converts the top layer into Al₂O₃, which then can be etched through fluorination and ligand exchange.

1.3 Area-Selective Atomic Layer Deposition (AS-ALD)

Area-selective deposition is a method during which a thin film is grown in one region of the sample while preventing growth on the other. While nanopatterning is commonly done using lithography and employing masks, AS-ALD makes use of the chemical information present on the surface. As such the great benefit of selective deposition is the self-aligning nature of the process. During a common lithographic patterning process an error in alignment can occur, also referred to as edge placement error (EPE). However, AS-ALD can be employed to reduce the number of steps required and to prevent the alignment error – enabling further downscaling of critical device dimensions.⁵⁹

To compare the selectivity between different substrates, conditions and experiments, a selectivity parameter, S, must be defined.^{23,60} For area-selective deposition, it is beneficial to define

selectivity through more easily measurable parameters, such as surface coverage θ or film thickness t . Surface coverage describes the fraction of surface that is covered by the deposited material on the preferred growth surface θ_1 and on the preferred non-growth surface θ_2 . It can be quantified using methods such as scanning electron microscopy, atomic force microscopy or others.⁶¹ Alternatively, film thicknesses, t_1 and t_2 , for thickness on growth and non-growth surfaces, respectively, can be used to estimate the selectivity S . There are various methods to quantify the film thickness including spectroscopic ellipsometry, X-ray reflectometry, X-ray photoelectron spectroscopy, Auger electron spectroscopy, and many more.⁶² In both cases S can be estimated as

$$S = \frac{\theta_1 - \theta_2}{\theta_1 + \theta_2} \approx \frac{t_1 - t_2}{t_1 + t_2} \quad (1.3)$$

The value of S can vary from 0 to 1. In an ideal case, where the growth occurs only on the preferred surface ($t_1 \neq 0$, $t_2 = 0$) S equals 1. When there is no selectivity between the two surfaces and $t_1 = t_2$, then S equals 0. It is important to note that the value of S depends on the number of ALD cycles performed and generally decreases as more cycles are performed in an ALD-only process.

In general, AS-ALD processes can be divided into 2 categories based on the nature of the substrate: area passivation and area activation.⁶³ The difference between the two is illustrated in figure 1.6. During the passivation step a blocking layer of material, such as self-assembled monolayers (SAMs), is used to functionalize a specific area to deactivate further growth on that material. SAMs have been used to achieve area-selective deposition of numerous metals and metal oxides on wide variety of substrates.⁶⁴ For example, alkanethiol SAMs have been shown to inhibit Al_2O_3 , ZnO and MnO ALD on modified vs non-modified Au surfaces for 20 deposition cycles or more.⁶⁵ Similarly, it has been shown that deposition of Pt and Pd can be inhibited by using plasma-polymerized fluorocarbon CF_x layer.⁶⁶ Up to ~ 15 nm and ~ 20 nm thicknesses with selectivity

values of ~ 0.99 were achieved for Pd and Pt, respectively, showing promising results for future CMOS device fabrication applications. However, there are several factors that limit achieving higher selectivity using SAMs. First, SAMs in general have low thermal stability, for example, alkanethiols can desorb at temperatures as low as 100 °C, exposing the substrate underneath.^{67–69} Moreover, most SAMs used are not compatible with plasma-assisted or ozone-based processes.⁶³ In addition to SAMs-related damage, the selectivity is limited by reactant physisorption on a SAM and by precursors diffusion through SAM to the underlying surface.^{64,70}

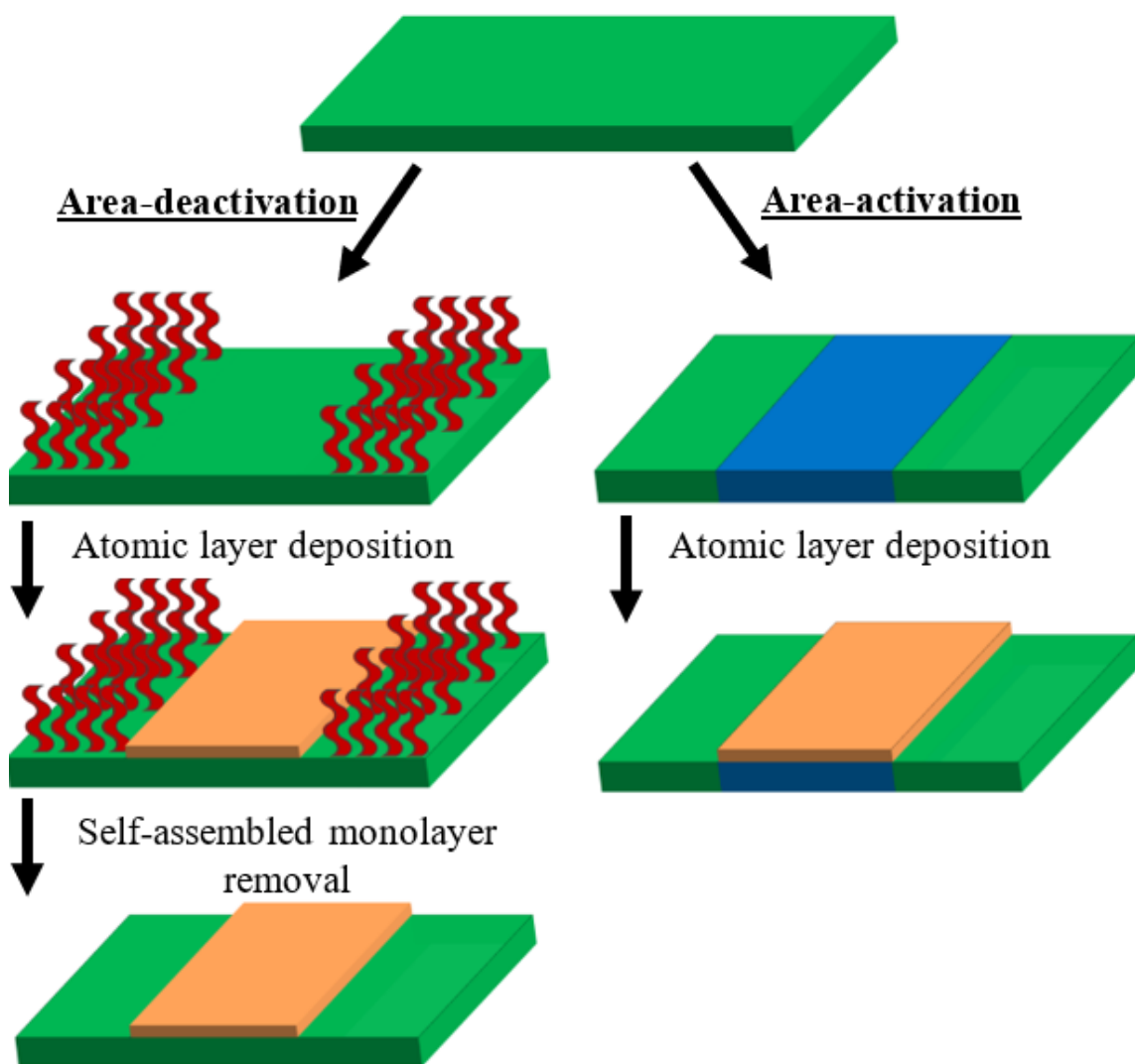


Figure 1.6. Overview of two conventional approaches to achieve area-selective atomic layer deposition: area-deactivation (left) and area-activation (right).

Alternatively, area-selective ALD can be achieved through area activation or by exploiting inherent chemical information present on the substrates. During area activation a sample can be locally patterned to enable deposition in certain areas while keeping the rest of the surface inert. AS-ALD has been achieved using various methods for activation, such as electron beams, vacuum ultraviolet light, flash lamp annealing and patterns by electron-beam induced deposition patterning.⁷¹⁻⁷⁴ Meanwhile inherent AS-ALD utilizes the fact that deposition can occur on different surfaces at different rates. On ideal “growth” surfaces the deposition is uniform and instant, while on “nongrowth” surfaces there is a delay before growth is achieved due to precursor adsorption inhibition. A common example includes metal oxide, such as Al₂O₃, deposition which proceeds readily on SiO₂, however exhibits a delay on a Si-H surface.⁷⁵⁻⁷⁷ Conversely, many metals, like W, exhibit uninhibited deposition on Si-H surface, but experience a delay when deposited on SiO₂.^{78,79}

Whether the deposition is inhibited or proceeds readily on a specific surface can be estimated by classical nucleation theory as illustrated in figure 1.7. The theory predicts the probability of nucleation based on surface-energy minimization. The total Gibbs free energy can be estimated as:

$$\Delta G(r) = \frac{2}{3}\pi r^3 \Delta G_V + 2\pi r^2 \sigma_s + \pi r^2 \sigma_i \quad (1.4)$$

where r is the radius of the nuclei, ΔG_V the volume free energy of the material being deposited, σ_s the surface tension of the material being deposited, and σ_i the surface tension of the interface between the material and underlying substrate. The first term presumes deposition of hemispherical nuclei and is always negative since $\Delta G_V < 0$, which dominates at higher r values due to the r^3 term. The second and third terms dominate at lower r values, resulting in positive ΔG as $\sigma_s > 0$. As apparent in figure 1.7, this results in a trend where a nucleus radius needs to reach a

critical size to form a stable nucleus. Beyond the critical size, further growth reduces the free energy of the nuclei and enables deposition. As different surfaces have distinct interfacial energies, the critical size varies between surfaces, creating a window of selective growth. Inside the window, the nuclei on the “non-growth surface” are unstable and will spontaneously decompose, however, the nuclei on the “growth surface” exceed the critical size, are stable, and will lead to growth.

As the selectivity achieved by inherent AS-ALD processes is usually limited by the substrates, experimental conditions, and the precursors used, various processes can be integrated within the ALD cycles to improve the selective deposition. For example, ALD cycles can be combined with intermittent ALE cycles into so called “supercycles”, where etching is performed after certain number of deposition cycles, as illustrated in figure 1.8. The etching step removes the material deposited on the non-preferred growth surface, leaving ideally a clean surface, which inhibits growth in subsequent ALD cycles.⁸⁰⁻⁸² While the ALE also etches some of the material grown on the preferred growth substrate, the relative amount is much smaller in comparison, due to the thicker film. By choosing the right cycle combinations and processing conditions, significant improvements in selectivity can be achieved compared to an “ALD-only” case without ALE steps.⁸³

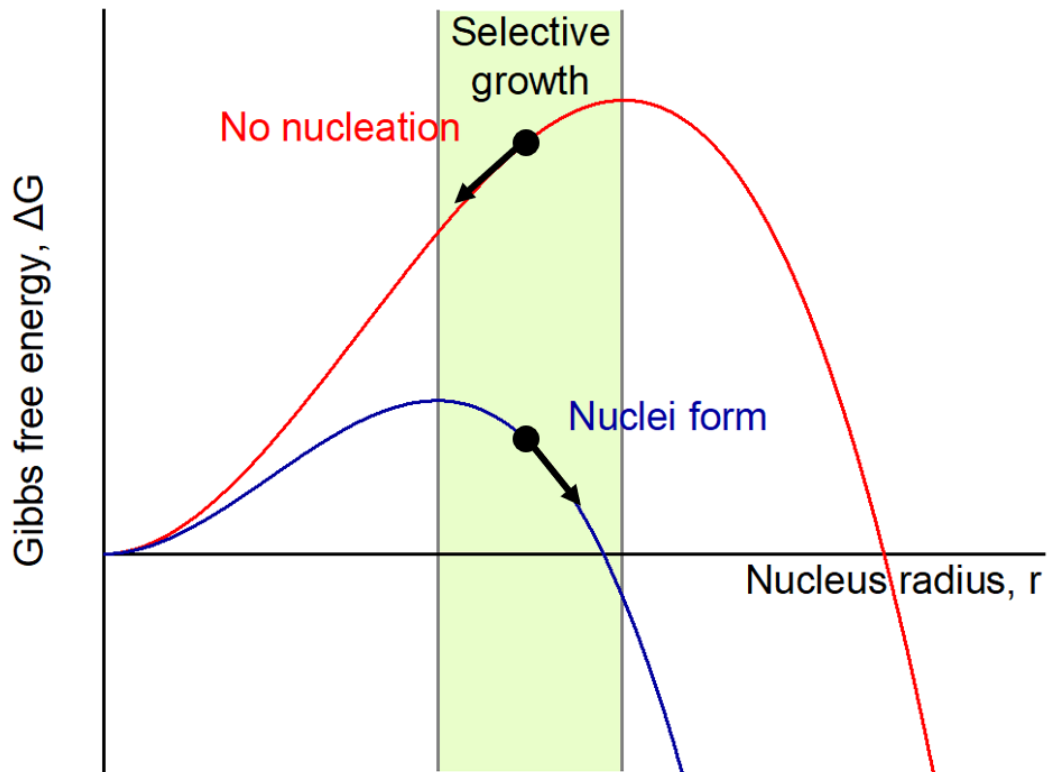


Figure 1.7. Total Gibbs free energy as a function of nucleus radius for two different surfaces as predicted by classical nucleation theory. Redrawn from ⁶⁰.

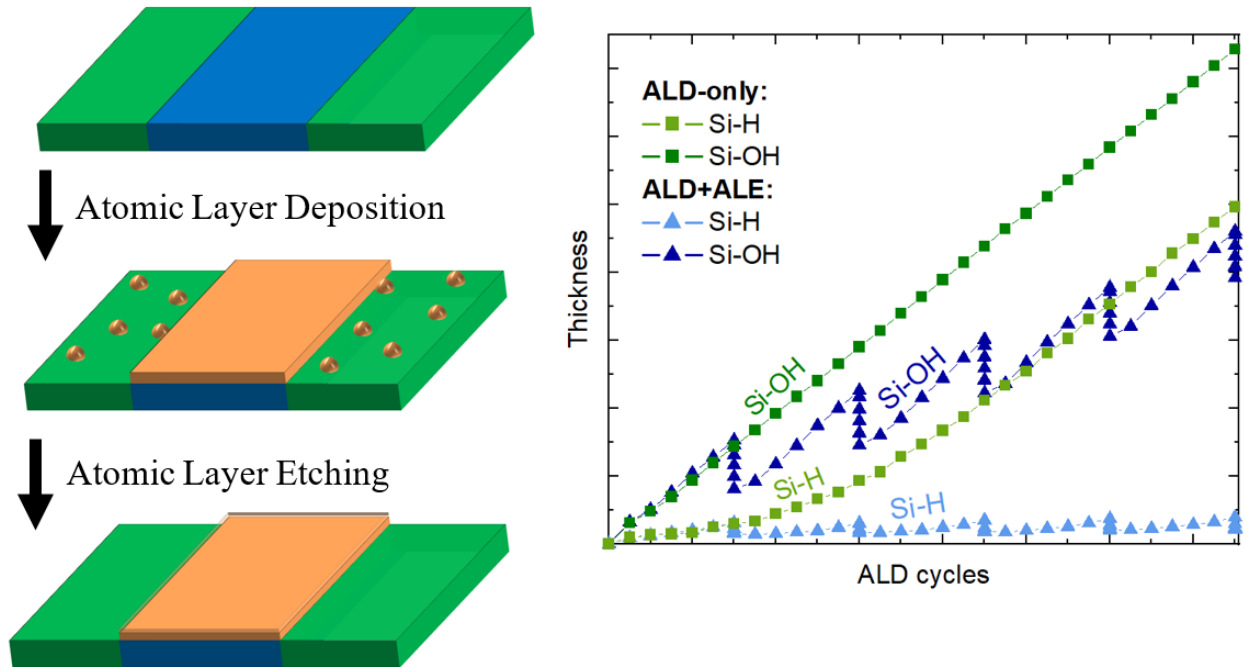


Figure 1.8. Illustration of a combined atomic layer deposition and atomic layer etching supercycle. As nuclei start to grow on the preferred non-growth surface during ALD, intermittent ALE cycles can be performed to remove these nuclei before proceeding. By selecting proper process conditions, selectivity can be greatly enhanced compared to an ALD-only case.

1.4 Phase Change Memories

Phase change memories (PCM) are promising candidates in overcoming data storage and processing challenges present in artificial intelligence machines. Phase change memories, usually made of chalcogenides materials, are based on reversible transitions of crystalline and amorphous phases and function as non-volatile memories. While in current common use computers there are separate systems for data transfer (SRAMs and DRAMs) and storage (HDDs and SSDs), PCMs have the capability to both store and process data at the same physical location.⁸⁴ This removes the need to transfer data back-and-forth in the computers architecture, reducing power consumption and reducing latency.⁸⁵

The basic operating principle of a PCM was proposed back in 1960s⁸⁶ and later commercialized in CDs, DVDs, and Blu-ray disks.⁸⁷ However, it is only in the recent years when research interest in PCMs increased as a potential improvement for current state-of-the-art DRAM and NAND flash memory. In 2020, Intel launched a Optane™ Persistent Memory 200 Series, a PCM-based technology, promoting accelerated large-data computing and reduced power consumption.⁸⁸ However, despite advancement of commercially launched products, there are challenges in memory cell integration, material selection and in fundamental understanding.^{84,89}

As illustrated in figure 1.9, the phase of a PCM can be changed through temperature control.⁹⁰ The amorphous chalcogenide material can be crystallized by applying a long weak electrical current pulse (SET pulse) through the cell, annealing it to a temperature between the crystallization and the melting temperature due to Joule heating. The PCM is turned back to amorphous phase (RESET) by rapidly melting and quenching in a short period of time. The low-resistance crystalline phase is equivalent to logical '1', while the high-resistance amorphous phase is equivalent to state '0', and they can be read by passing a weak current through the cell.⁹¹ In the optical memory devices, such as CDs, the contrast of reflectivity, not resistivity, is used as an information source and laser is used for heating in lieu of current.⁸⁹ Although the crystallization process of the PCM material has been widely studied and even utilized in commercial products, the exact mechanism of the threshold switching is still in a debate. Several models, that can widely be categorized as either as thermal or electronic, have been proposed.⁹²⁻⁹⁴

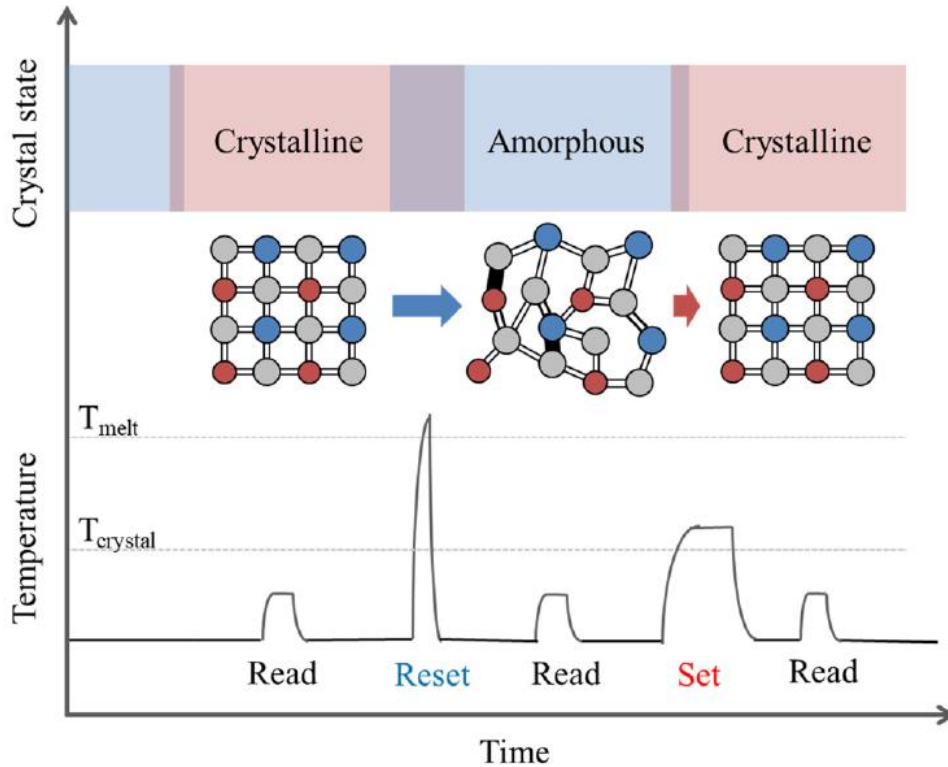


Figure 1.9. Diagram illustrating the operation principle of a phase change memory. A low long pulse is used to revert the material into crystalline phase with low resistance. A short high pulse brings the PCM to an amorphous state with high resistance. Figure reproduced.⁹⁰

The most researched materials for PCM applications are germanium-antimony-tellurium (GST) alloys with several compositional variations as shown in figure 1.10.⁹⁵ It has been demonstrated that a higher GeTe to Sb_2Te_3 ratio in a GST-based PCM results in improved data retention time but decreases the switching speed and vice versa.⁹⁶ As such, $Ge_2Sb_2Te_5$ (GST225) is commonly used as a compromise between the two properties. However, the applications of GST225 are limited due to its low crystallization temperature and thermal stability. The properties of the GST material can be improved by introducing dopants. It has been shown that introducing N, C, O, Bi, or Sb as dopants can increase the crystallization temperature of the material.^{97–103} Typically the GST cells are deposited using physical vapor deposition (PVD) due to fast deposition

rates and high control over the resulting stoichiometry.¹⁰⁴ However, PVD does not result in a uniform, conformal film in high aspect ratio structures and in more complex 3D architectures.¹⁰⁵ As such, ALD of chalcogenide materials has gained significant interest due to the self-limiting nature and high conformality of the process. Compared to the 2D crossbar structure present in the current PCM cells, ALD enables deposition of 3D architectures that have been shown to lower the required operation power and fabrication costs.^{106–109}

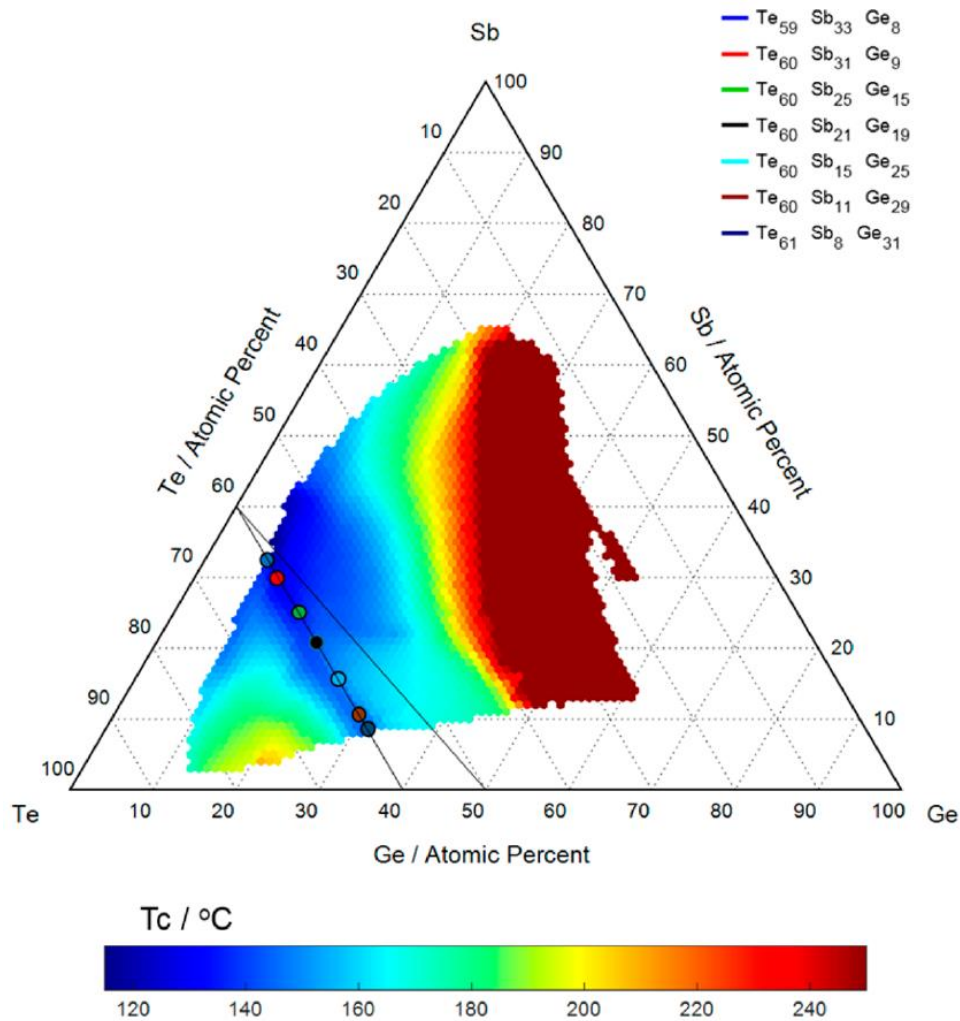


Figure 1.10. Ternary phase diagram of a Ge-Sb-Te phase change memory materials system. The color map indicates the crystallization temperature of the specific composition. The black lines represent the Sb_2Te_3 -GeTe tie line on which GST225 is located and the Sb_2Te_3 - Ge_2Te_3 line, which represents the lowest crystallization temperatures. Figure reproduced.⁹⁵

1.5 Scope and Organization

The primary objective of this dissertation is to investigate various aspects of atomic layer deposition and thermal atomic layer etching processes. The main focus is on the fundamentals of film nucleation, area-selectivity, impact of deposition and etching precursor designs, and on ALD of phase change memory materials.

While the first chapter provided a summary of the processes used in this work, the following chapter describes the experimental tools used for thin film processing and characterization, while also providing the reader with a cursory background of the physical phenomenon enabling the measurements. Each of the following chapters discusses a specific project along with novel contributions that were achieved.

In chapter 3, the effect of precursor structure on the initial growth trends on Si-OH and Si-H is studied using trimethylaluminum $[\text{Al}(\text{CH}_3)_3]$, triethylaluminum $[\text{Al}(\text{C}_2\text{H}_5)_3]$, and dimethylaluminum chloride $[\text{Al}(\text{CH}_3)_2\text{Cl}]$ as Al precursors. Using various *in-situ* methods, the measurements indicate that the precursor choice has a significant impact on the growth trends on the two different substrates and an appropriate precursor should be used depending on the preferred application.

In chapter 4 the impact of the co-etchant selection in a metal oxide ALE process with WF_6 is demonstrated. Boron trichloride (BCl_3), thionyl chloride (SOCl_2), and titanium tetrachloride (TiCl_4) were used as co-etchants for ALE of titania and zirconia. Above 200 °C WF_6 and SOCl_2 were shown to lead to chemical vapor etching of TiO_2 , while none of the chemicals etched ZrO_2 individually. For atomic layer etching, each of the chlorinating reactants, when pulsed after the WF_6 exposure etched both TiO_2 and ZrO_2 at different temperatures, resulting in different etch

behaviors. The study illustrates the importance of choosing an appropriate ALE co-etchants depending on the material being etched.

In chapter 5 isothermal area-selective deposition of TiO_2 is being studied by using super-cycles of TiO_2 ALD using $\text{TiCl}_4/\text{H}_2\text{O}$ and TiO_2 ALE using WF_6/BCl_3 at 170°C . Using Si-OH and Si-H as growth and non-growth surfaces, respectively, it is shown that significant selectivity can be achieved by limiting reactant exposure during the TiO_2 ALD cycles. In particular, by limiting the H_2O exposure, 32.7 nm thick TiO_2 layer was deposited on SiO_2 with no significant deposition on Si on a Si/ SiO_2 patterned wafer.

In chapter 6 ALD of phase change memory materials GeTe and Sb_2Te_3 is studied using trichlorogermane (HGeCl_3), bis(trimethylsilyl)telluride ($(\text{Me}_3\text{Si})_2\text{Te}$), and antimony(III)ethoxide ($\text{Sb}(\text{OEt})_3$) as precursors. The growth characteristic and the ALD growth regime are analyzed using *in-situ* ellipsometry, atomic force microscopy (AFM), X-ray photoelectron spectroscopy (XPS), and X-ray diffractometry (XRD). While the study confirms the feasibility of the ALD of GeTe and Sb_2Te_3 using precursors tried, it also raises several challenges, creating opportunities for future research.

1.6 References

1. Dhanaraj, G., Byrappa, K., Prasad, V. & Dudley, M. *Springer Handbook of Crystal Growth*. Springer Handbook of Crystal Growth (Springer, 2010). doi:10.1007/978-3-540-74761-1.
2. Kääriäinen, T., Cameron, D., Kääriäinen, M.-L. & Sherman, A. *Atomic Layer Deposition: Principles, Characteristics, and Nanotechnology Applications*. (Wiley-Scrivener, 2013).
3. Delabie, A. *et al.* Reaction mechanisms for atomic layer deposition of aluminum oxide on semiconductor substrates. *Journal of Vacuum Science & Technology A: Vacuum, Surfaces, and Films* **30**, 01A127 (2012).
4. Puurunen, R. L. Surface chemistry of atomic layer deposition: A case study for the trimethylaluminum/ water process. *J. Appl. Phys* **97**, 121301 (2005).
5. Higashi, G. S. & Fleming, C. G. Sequential surface chemical reaction limited growth of high quality Al₂O₃ dielectrics. *Applied Physics Letters* **55**, 1963–1965 (1989).
6. Stempel, V. E., Knemeyer, K., D'Alnoncourt, R. N., Driess, M. & Rosowski, F. Investigating the trimethylaluminium/water ALD process on mesoporous silica by in situ gravimetric monitoring. *Nanomaterials* **8**, (2018).
7. Pan, D., Ma, L., Xie, Y., Jen, T. C. & Yuan, C. On the physical and chemical details of alumina atomic layer deposition: A combined experimental and numerical approach. *Journal of Vacuum Science & Technology A: Vacuum, Surfaces, and Films* **33**, 021511 (2015).
8. Puurunen, R. L. Growth per cycle in atomic layer deposition: A theoretical model. *Chemical Vapor Deposition* **9**, 249–257 (2003).

9. Ylilammi, M. Monolayer thickness in atomic layer deposition. *Thin Solid Films* **279**, 124–130 (1996).
10. Richey, N. E., de Paula, C. & Bent, S. F. Understanding chemical and physical mechanisms in atomic layer deposition. *Journal of Chemical Physics* vol. 152 40902 (2020).
11. Puurunen, R. L. Surface chemistry of atomic layer deposition: A case study for the trimethylaluminum/water process. *Journal of Applied Physics* vol. 97 121301 (2005).
12. Mackus, A. J. M., Macisaac, C., Kim, W. H. & Bent, S. F. Incomplete elimination of precursor ligands during atomic layer deposition of zinc-oxide, tin-oxide, and zinc-tin-oxide. *Journal of Chemical Physics* **146**, 052802 (2017).
13. Dillon, A. C., Ott, A. W., Way, J. D. & George, S. M. Surface chemistry of Al₂O₃ deposition using Al(CH₃)₃ and H₂O in a binary reaction sequence. *Surface Science* **322**, 230–242 (1995).
14. Pinna, N. & Knez, M. *Atomic Layer Deposition of Nanostructured Materials. Atomic Layer Deposition of Nanostructured Materials* (Wiley-VCH, 2012). doi:10.1002/9783527639915.
15. Suntola, T. Surface chemistry of materials deposition at atomic layer level. *Applied Surface Science* **100–101**, 391–398 (1996).
16. Johnson, R. W., Hultqvist, A. & Bent, S. F. A brief review of atomic layer deposition: From fundamentals to applications. *Materials Today* vol. 17 236–246 (2014).
17. Hwang, C. S. *Atomic layer deposition for semiconductors. Atomic Layer Deposition for Semiconductors* vol. 9781461480549 (Springer US, 2014).

18. Burgers, J. M., Dehlinger, U., Frenkel, J., Kontorowa, T. & Garber, R. One-dimensional dislocations. II. Misfitting monolayers and oriented overgrowth. *Proceedings of the Royal Society of London. Series A. Mathematical and Physical Sciences* **198**, 216–225 (1949).
19. George, S. M. Atomic layer deposition: An overview. *Chemical Reviews* **110**, 111–131 (2010).
20. Ritala, M. *et al.* Perfectly Conformal TiN and Al₂O₃ Films Deposited by Atomic Layer Deposition. *Chemical Vapor Deposition* **5**, 7–9 (1999).
21. Marichy, C., Bechelany, M. & Pinna, N. Atomic layer deposition of nanostructured materials for energy and environmental applications. *Advanced Materials* **24**, 1017–1032 (2012).
22. Volmer, M. & Weber, A. Keimbildung in übersättigten Gebilden. *Zeitschrift für Physikalische Chemie* **119U**, 277–301 (1925).
23. Parsons, G. N. Functional model for analysis of ALD nucleation and quantification of area-selective deposition. *Journal of Vacuum Science & Technology A* **37**, 020911 (2019).
24. Copel, M., Gribelyuk, M. & Gusev, E. Structure and stability of ultrathin zirconium oxide layers on Si(001). *Applied Physics Letters* **76**, 436–438 (2000).
25. Besling, W. F. A. *et al.* Characterisation of ALCVD Al₂O₃-ZrO₂ nanolaminates, link between electrical and structural properties. *Journal of Non-Crystalline Solids* **303**, 123–133 (2002).

26. Gusev, E. P., Cabral, C., Copel, M., D'Emic, C. & Gribelyuk, M. Ultrathin HfO₂ films grown on silicon by atomic layer deposition for advanced gate dielectrics applications. in *Microelectronic Engineering* vol. 69 145–151 (Elsevier, 2003).
27. Frank, M. M., Chabal, Y. J. & Wilk, G. D. Nucleation and interface formation mechanisms in atomic layer deposition of gate oxides. *Applied Physics Letters* **82**, 4758–4760 (2003).
28. Nie, X., Ma, F., Ma, D. & Xu, K. Growth mode evolution of hafnium oxide by atomic layer deposition. *Journal of Vacuum Science & Technology A: Vacuum, Surfaces, and Films* **32**, 01A109 (2014).
29. Baker, L. *et al.* Nucleation and growth of Pt atomic layer deposition on Al₂O₃ substrates using (methylcyclopentadienyl)-trimethyl platinum and O₂ plasma. *Journal of Applied Physics* **109**, 084333 (2011).
30. Elam, J. W., Nelson, C. E., Grubbs, R. K. & George, S. M. Nucleation and growth during tungsten atomic layer deposition on SiO₂ surfaces. *Thin Solid Films* **386**, 41–52 (2001).
31. George, S. M., Elam, J. W., Grubbs, R. K. & Nelson, C. E. Nucleation and growth during tungsten atomic layer deposition on oxide surfaces. in *Materials Research Society Symposium - Proceedings* vol. 672 1–7 (Materials Research Society, 2001).
32. Halls, M. D., Raghavachari, K., Frank, M. M. & Chabal, Y. J. Atomic layer deposition of Al₂O₃ on H-passivated Si: Al(CH₃)₂OH surface reactions with H/Si(100)–2×1. *Physical Review B - Condensed Matter and Materials Physics* **68**, 161302 (2003).
33. Stranski, I. N. & Krastanow, L. Zur Theorie der orientierten Ausscheidung von Ionenkristallen aufeinander. *Monatshefte für Chemie* **71**, 351–364 (1937).

34. Argile, C. & Rhead, G. E. Adsorbed layer and thin film growth modes monitored by Auger electron spectroscopy. *Surface Science Reports* **10**, 277–356 (1989).
35. Manandhar, K., Wollmershauser, J. A. & Feigelson, B. N. Growth mode of alumina atomic layer deposition on nanopowders. *Journal of Vacuum Science & Technology A: Vacuum, Surfaces, and Films* **35**, 041503 (2017).
36. Xie, S., Cai, J., Wang, Q., Wang, L. & Liu, Z. Properties and morphology of TiN films deposited by atomic layer deposition. *Tsinghua Science and Technology* **19**, 144–149 (2014).
37. Puurunen, R. L. & Vandervorst, W. Island growth as a growth mode in atomic layer deposition: A phenomenological model. *Journal of Applied Physics* **96**, 7686–7695 (2004).
38. Fang, C., Cao, Y., Wu, D. & Li, A. Thermal atomic layer etching: Mechanism, materials and prospects. *Progress in Natural Science: Materials International* vol. 28 667–675 (2018).
39. Kanarik, K. J. *et al.* Overview of atomic layer etching in the semiconductor industry. *J. Vac. Sci. Technol. A* **33**, 20802 (2015).
40. Maki, P. A. & Ehrlich, D. J. Laser bilayer etching of GaAs surfaces. *Applied Physics Letters* **55**, 91–93 (1989).
41. T. Carver, C. *et al.* Atomic Layer Etching: An Industry Perspective. *ECS Journal of Solid State Science and Technology* **4**, N5005–N5009 (2015).
42. Kanarik, K. J., Tan, S. & Gottscho, R. A. Atomic Layer Etching: Rethinking the Art of Etch. *J. Phys. Chem. Lett* **9**, 37 (2018).

43. George, S. M. Mechanisms of Thermal Atomic Layer Etching. *Accounts of Chemical Research* **53**, 1151–1160 (2020).
44. Yuan, G., Wang, N., Huang, S. & Liu, J. A brief overview of atomic layer deposition and etching in the semiconductor processing. in *2016 17th International Conference on Electronic Packaging Technology, ICEPT 2016* 1365–1368 (Institute of Electrical and Electronics Engineers Inc., 2016). doi:10.1109/ICEPT.2016.7583377.
45. Agarwal, A. & Kushner, M. J. Plasma atomic layer etching using conventional plasma equipment. *Journal of Vacuum Science & Technology A: Vacuum, Surfaces, and Films* **27**, 37–50 (2009).
46. Lee, Y., Huffman, C. & George, S. M. Selectivity in Thermal Atomic Layer Etching Using Sequential, Self-Limiting Fluorination and Ligand-Exchange Reactions. *Chemistry of Materials* **28**, 7657–7665 (2016).
47. Fischer, A., Routzahn, A., Lee, Y., Lill, T. & George, S. M. Thermal etching of AlF_3 and thermal atomic layer etching of Al_2O_3 . *Journal of Vacuum Science & Technology A* **38**, 022603 (2020).
48. Lee, Y., Dumont, J. W. & George, S. M. Mechanism of thermal Al_2O_3 atomic layer etching using sequential reactions with $\text{Sn}(\text{acac})_2$ and HF. *Chemistry of Materials* **27**, 3648–3657 (2015).
49. Gertsch, J. C., Cano, A. M., Bright, V. M. & George, S. M. SF_4 as the Fluorination Reactant for Al_2O_3 and VO_2 Thermal Atomic Layer Etching. *Chemistry of Materials* (2019) doi:10.1021/acs.chemmater.8b05294.

50. Murdzek, J. A. & George, S. M. Effect of crystallinity on thermal atomic layer etching of hafnium oxide, zirconium oxide, and hafnium zirconium oxide. *Journal of Vacuum Science & Technology A* **38**, 022608 (2020).
51. Lee, Y., DuMont, J. W. & George, S. M. Atomic Layer Etching of HfO₂ Using Sequential, Self-Limiting Thermal Reactions with Sn(acac)₂ and HF. *ECS Journal of Solid State Science and Technology* **4**, N5013–N5022 (2015).
52. Lemaire, P. C. & Parsons, G. N. Thermal Selective Vapor Etching of TiO₂: Chemical Vapor Etching via WF₆ and Self-Limiting Atomic Layer Etching Using WF₆ and BCl₃. *Chemistry of Materials* **29**, 6653–6665 (2017).
53. Lee, Y. & George, S. M. Atomic layer etching of Al₂O₃ using sequential, self-limiting thermal reactions with Sn(acac)₂ and hydrogen fluoride. *ACS Nano* **9**, 2061–2070 (2015).
54. Lee, Y., Dumont, J. W. & George, S. M. Trimethylaluminum as the Metal Precursor for the Atomic Layer Etching of Al₂O₃ Using Sequential, Self-Limiting Thermal Reactions. *Chemistry of Materials* **28**, 2994–3003 (2016).
55. Lee, Y. & George, S. M. Thermal atomic layer etching of titanium nitride using sequential, self-limiting reactions: Oxidation to TiO₂ and fluorination to volatile TiF₄. *Chemistry of Materials* **29**, 8202–8210 (2017).
56. Xie, W., Lemaire, P. C. & Parsons, G. N. Thermally Driven Self-Limiting Atomic Layer Etching of Metallic Tungsten Using WF₆ and O₂. *ACS Applied Materials and Interfaces* **10**, 9147–9154 (2018).

57. Zywojtko, D. R. & George, S. M. Thermal Atomic Layer Etching of ZnO by a “Conversion-Etch” Mechanism Using Sequential Exposures of Hydrogen Fluoride and Trimethylaluminum. *Chemistry of Materials* **29**, 1183–1191 (2017).
58. DuMont, J. W., Marquardt, A. E., Cano, A. M. & George, S. M. Thermal Atomic Layer Etching of SiO₂ by a “Conversion-Etch” Mechanism Using Sequential Reactions of Trimethylaluminum and Hydrogen Fluoride. *ACS Applied Materials and Interfaces* **9**, 10296–10307 (2017).
59. Mackus, A. J. M., Merckx, M. J. M. & Kessels, W. M. M. From the Bottom-Up: Toward Area-Selective Atomic Layer Deposition with High Selectivity. *Chemistry of Materials* **31**, 2–12 (2019).
60. Parsons, G. N. & Clark, R. D. Area-Selective Deposition: Fundamentals, Applications, and Future Outlook. *Chemistry of Materials* vol. 32 4920–4953 (2020).
61. Schmitt, P. *et al.* Influence of Substrate Materials on Nucleation and Properties of Iridium Thin Films Grown by ALD. *Coatings* **11**, (2021).
62. Whiteside, P. J. D., Chininis, J. A. & Hunt, H. K. Techniques and challenges for characterizing metal thin films with applications in photonics. *Coatings* vol. 6 35 (2016).
63. Mackus, A. J. M. Approaches and opportunities for area-selective atomic layer deposition. in *2018 International Symposium on VLSI Technology, Systems and Application, VLSI-TSA 2018* 1–2 (Institute of Electrical and Electronics Engineers Inc., 2018). doi:10.1109/VLSI-TSA.2018.8403864.

64. Lee, H. B. R. & Bent, S. F. Nanopatterning by Area-Selective Atomic Layer Deposition. in *Atomic Layer Deposition of Nanostructured Materials* 193–225 (Wiley-VCH, 2012). doi:10.1002/9783527639915.ch9.
65. Sampson, M. D., Emery, J. D., Pellin, M. J. & Martinson, A. B. F. Inhibiting metal oxide atomic layer deposition: Beyond zinc oxide. *ACS Applied Materials and Interfaces* vol. 9 33429–33436 (2017).
66. Deminskyi, P., Haider, A., Eren, H., Khan, T. M. & Biyikli, N. Area-selective atomic layer deposition of noble metals: Polymerized fluorocarbon layers as effective growth inhibitors. *Journal of Vacuum Science & Technology A* **39**, 022402 (2021).
67. Kulkarni, S. A., Mirji, S. A., Mandale, A. B. & Vijayamohan, K. P. Thermal stability of self-assembled octadecyltrichlorosilane monolayers on planar and curved silica surfaces. *Thin Solid Films* **496**, 420–425 (2006).
68. Lee, H.-B.-R. *et al.* High Quality Area-Selective Atomic Layer Deposition Co Using Ammonia Gas as a Reactant. *Journal of The Electrochemical Society* **157**, D10 (2010).
69. Prathima, N. *et al.* Thermal study of accumulation of conformational disorders in the self-assembled monolayers of C8 and C18 alkanethiols on the Au(111) surface. *Langmuir* **21**, 2364–2374 (2005).
70. Seo, S. *et al.* Reaction Mechanism of Area-Selective Atomic Layer Deposition for Al₂O₃ Nanopatterns. (2017) doi:10.1021/acsami.7b13365.
71. Henke, T. *et al.* Flash-Enhanced Atomic Layer Deposition: Basics, Opportunities, Review, and Principal Studies on the Flash-Enhanced Growth of Thin Films. *ECS Journal of Solid State Science and Technology* **4**, P277–P287 (2015).

72. Chalker, P. R. *et al.* Vacuum ultraviolet photochemical selective area atomic layer deposition of Al₂O₃ dielectrics. *AIP Advances* **5**, 17115 (2015).
73. Mameli, A. *et al.* Area-Selective Atomic Layer Deposition of ZnO by Area Activation Using Electron Beam-Induced Deposition. *Chemistry of Materials* **31**, 1250–1257 (2019).
74. Mackus, A. J. M., Dielissen, S. A. F., Mulders, J. J. L. & Kessels, W. M. M. Nanopatterning by direct-write atomic layer deposition. *Nanoscale* **4**, 4477–4480 (2012).
75. Longo, R. C. *et al.* Selectivity of metal oxide atomic layer deposition on hydrogen terminated and oxidized Si(001)-(2×1) surface. *Journal of Vacuum Science & Technology B, Nanotechnology and Microelectronics: Materials, Processing, Measurement, and Phenomena* **32**, 03D112 (2014).
76. Halls, M. D. & Raghavachari, K. Atomic Layer Deposition Growth Reactions of Al₂O₃ on Si(100)-2×1. *Journal of Physical Chemistry B* **108**, 4058–4062 (2004).
77. Vandalon, V. & Erwin Kessels, W. M. M. Initial Growth Study of Atomic-Layer Deposition of Al₂O₃ by Vibrational Sum-Frequency Generation. *Langmuir* **35**, 10374–10382 (2019).
78. Lemaire, P. C., King, M. & Parsons, G. N. Understanding inherent substrate selectivity during atomic layer deposition: Effect of surface preparation, hydroxyl density, and metal oxide composition on nucleation mechanisms during tungsten ALD. *Journal of Chemical Physics* **146**, 052811 (2017).

79. Kalanyan, B., Lemaire, P. C., Atanasov, S. E., Ritz, M. J. & Parsons, G. N. Using Hydrogen to Expand the Inherent Substrate Selectivity Window during Tungsten Atomic Layer Deposition. *Chemistry of Materials* **28**, 117–126 (2016).
80. Song, S. K., Saare, H. & Parsons, G. N. Integrated Isothermal Atomic Layer Deposition/Atomic Layer Etching Supercycles for Area-Selective Deposition of TiO₂. *Chemistry of Materials* **31**, (2019).
81. Vallat, R., Gassilloud, R., Eychenne, B. & Vallée, C. Selective deposition of Ta₂O₅ by adding plasma etching super-cycles in plasma enhanced atomic layer deposition steps. *Journal of Vacuum Science & Technology A: Vacuum, Surfaces, and Films* **35**, 01B104 (2017).
82. Vos, M. F. J. *et al.* Area-Selective Deposition of Ruthenium by Combining Atomic Layer Deposition and Selective Etching. *Chemistry of Materials* **31**, 3878–3882 (2019).
83. Saare, H., Song, S. K., Kim, J.-S. & Parsons, G. N. Effect of reactant dosing on selectivity during area-selective deposition of TiO₂ via integrated atomic layer deposition and atomic layer etching. *Journal of Applied Physics* **128**, (2020).
84. Cheng, H. Y., Carta, F., Chien, W. C., Lung, H. L. & Brightsky, M. J. 3D cross-point phase-change memory for storage-class memory. *Journal of Physics D: Applied Physics* vol. 52 473002 (2019).
85. Burr, G. W. *et al.* Phase change memory technology. *Journal of Vacuum Science & Technology B, Nanotechnology and Microelectronics: Materials, Processing, Measurement, and Phenomena* **28**, 223–262 (2010).

86. Ovshinsky, S. R. Reversible electrical switching phenomena in disordered structures. *Physical Review Letters* **21**, 1450–1453 (1968).
87. Wuttig, M. & Yamada, N. Phase-change materials for rewriteable data storage. *Nature Materials* **6**, 824–832 (2007).
88. Intel® Optane™ Persistent Memory 200 Series Brief. <https://www.intel.com/content/www/us/en/products/docs/memory-storage/optane-persistent-memory/optane-persistent-memory-200-series-brief.html>.
89. le Gallo, M. & Sebastian, A. An overview of phase-change memory device physics. *Journal of Physics D: Applied Physics* vol. 53 213002 (2020).
90. Shen, M. *et al.* Review on recent progress in patterning phase change materials. *Journal of Vacuum Science & Technology A* **38**, 060802 (2020).
91. Wong, H. S. P. *et al.* Phase change memory. in *Proceedings of the IEEE* vol. 98 2201–2227 (Institute of Electrical and Electronics Engineers Inc., 2010).
92. Bogoslovskiy, N. A. & Tsandin, K. D. Physics of switching and memory effects in chalcogenide glassy semiconductors. *Semiconductors* vol. 46 559–590 (2012).
93. Adler, D., Shur, M. S., Silver, M. & Ovshinsky, S. R. Threshold switching in chalcogenide-glass thin films. *Journal of Applied Physics* **51**, 3289–3309 (1980).
94. Ielmini, D. & Zhang, Y. Analytical model for subthreshold conduction and threshold switching in chalcogenide-based memory devices. *Journal of Applied Physics* **102**, 054517 (2007).
95. Guerin, S., Hayden, B., Hewak, D. W. & Vian, C. Synthesis and Screening of Phase Change Chalcogenide Thin Film Materials for Data Storage. *ACS Combinatorial Science* **19**, 478–491 (2017).

96. Zhang, W., Mazzarello, R., Wuttig, M. & Ma, E. Designing crystallization in phase-change materials for universal memory and neuro-inspired computing. *Nature Reviews Materials* vol. 4 150–168 (2019).
97. Fang, L. W. W. *et al.* Dependence of the properties of phase change random access memory on nitrogen doping concentration in Ge₂Sb₂Te₅. *Journal of Applied Physics* **107**, 104506 (2010).
98. Wang, K., Wamwangi, D., Ziegler, S., Steimer, C. & Wuttig, M. Influence of Bi doping upon the phase change characteristics of Ge₂Sb₂Te₅. *Journal of Applied Physics* **96**, 5557–5562 (2004).
99. Jeong, T. H., Kim, M. R., Seo, H., Park, J. W. & Yeon, C. Crystal structure and microstructure of nitrogen-doped Ge₂Sb₂Te₅ thin film. *Japanese Journal of Applied Physics, Part 1: Regular Papers and Short Notes and Review Papers* **39**, 2775–2779 (2000).
100. Privitera, S., Rimini, E. & Zonca, R. Amorphous-to-crystal transition of nitrogen- and oxygen-doped Ge₂Sb₂Te₅ films studied by in situ resistance measurements. *Applied Physics Letters* **85**, 3044–3046 (2004).
101. Zhou, X. *et al.* Understanding phase-change behaviors of carbon-doped Ge₂Sb₂Te₅ for phase-change memory application. *ACS Applied Materials and Interfaces* **6**, 14207–14214 (2014).
102. Navarro, G. *et al.* N-Doping Impact in Optimized Ge-Rich Materials Based Phase-Change Memory. in *2016 IEEE 8th International Memory Workshop, IMW 2016* (Institute of Electrical and Electronics Engineers Inc., 2016). doi:10.1109/IMW.2016.7495284.

103. Kim, K. H., Chung, J. G., Kyoung, Y. K., Park, J. C. & Choi, S. J. Phase-change characteristics of nitrogen-doped Ge₂Sb₂Te₅ films during annealing process. *Journal of Materials Science: Materials in Electronics* **22**, 52–55 (2011).
104. Burr, G. W. *et al.* Recent Progress in Phase-Change Memory Technology. *IEEE Journal on Emerging and Selected Topics in Circuits and Systems* **6**, 146–162 (2016).
105. Ahn, S. J. *et al.* Reliability perspectives for high density PRAM manufacturing. in *Technical Digest - International Electron Devices Meeting, IEDM* (2011). doi:10.1109/IEDM.2011.6131542.
106. Yoon, K. J., Kim, Y. & Hwang, C. S. What Will Come After V-NAND—Vertical Resistive Switching Memory? *Advanced Electronic Materials* vol. 5 1800914 (2019).
107. Qin, S. *et al.* Next-Generation Ultrahigh-Density 3-D Vertical Resistive Switching Memory (VRSM)-Part I: Accurate and Computationally Efficient Modeling. *IEEE Transactions on Electron Devices* **66**, 5139–5146 (2019).
108. Jiang, Z. *et al.* Next-Generation Ultrahigh-Density 3-D Vertical Resistive Switching Memory (VRSM)-Part II: Design Guidelines for Device, Array, and Architecture. *IEEE Transactions on Electron Devices* **66**, 5147–5154 (2019).
109. Lee, Y. K., Yoo, C., Kim, W., Jeon, J. W. & Hwang, C. S. Atomic layer deposition of chalcogenides for next-generation phase change memory. *Journal of Materials Chemistry C* vol. 9 3708–3725 (2021).
110. Tompkins, H. & Irene, E. A. *Handbook of Ellipsometry*. (William Andrew, 2005).
111. Hinrichs, K. & Eichhorn, K.-J. *Ellipsometry of Functional Organic Surfaces and Films*. vol. 52 (Springer International Publishing, 2018).
112. Fujiwara, H. *Spectroscopic Ellipsometry: Principles and Applications*. (Wiley, 2007).

113. Press, W. H., Flannery, B. P., Teukolsky, S. A. & Vetterling, W. T. *Numerical Recipes in C: The Art of Scientific Computing*. (Cambridge university press, 1992).
114. Jellison, G. E. & Modine, F. A. Parameterization of the optical functions of amorphous materials in the interband region. *Applied Physics Letters* **69**, 371–373 (1996).
115. Jellison, G. E. & Modine, F. A. Erratum: Parameterization of the optical functions of amorphous materials in the interband region. *Applied Physics Letters* vol. 69 2137 (1996).
116. Likhachev, D. v., Malkova, N. & Poslavsky, L. Modified Tauc-Lorentz dispersion model leading to a more accurate representation of absorption features below the bandgap. *Thin Solid Films* **589**, 844–851 (2015).
117. Rodríguez-de Marcos, L. v. & Larruquert, J. I. Analytic optical-constant model derived from Tauc-Lorentz and Urbach tail. *Optics Express* **24**, 28561 (2016).
118. Franta, D., Čermák, M., Vohánka, J. & Ohlídal, I. Dispersion models describing interband electronic transitions combining Tauc's law and Lorentz model. *Thin Solid Films* **631**, 12–22 (2017).
119. Briggs, D. & Seah, M. P. *Practical surface analysis by Auger and X-ray photoelectron spectroscopy*. *Surface and Interface Analysis* (John Wiley and Sons Ltd, 1984). doi:10.1002/sia.740060611.
120. Watts, J. F. & Wolstenholme, J. *An Introduction to Surface Analysis by XPS and AES*. *An Introduction to Surface Analysis by XPS and AES* (John Wiley & Sons, Ltd, 2003). doi:10.1002/0470867930.
121. Hofmann, S. *Auger- and X-Ray Photoelectron Spectroscopy in Materials Science*. (Springer, 2013). doi:10.1007/978-3-642-27381-0.

122. Gong, B., Peng, Q. & Parsons, G. N. Conformal Organic-inorganic hybrid network polymer thin films by molecular layer deposition using trimethylaluminum and glycidol. *Journal of Physical Chemistry B* **115**, 5930–5938 (2011).
123. Biyikli, N., Haider, A., Deminskyi, P. & Yilmaz, M. Self-aligned nanoscale processing solutions via selective atomic layer deposition of oxide, nitride, and metallic films. in *Low-Dimensional Materials and Devices 2017* (eds. Kobayashi, N. P., Talin, A. A., Davydov, A. V. & Islam, M. S.) vol. 10349 20 (SPIE, 2017).
124. Mackus, A. J. M., Bol, A. A. & Kessels, W. M. M. The use of atomic layer deposition in advanced nanopatterning. *Nanoscale* **6**, 10941–10960 (2014).
125. Vallat, R., Gassilloud, R., Eychenne, B. & Vallée, C. Selective deposition of Ta₂O₅ by adding plasma etching super-cycles in plasma enhanced atomic layer deposition steps. *Citation: Journal of Vacuum Science & Technology A* **35**, 1–104 (2017).
126. Minaye Hashemi, F. S., Birchansky, B. R. & Bent, S. F. Selective Deposition of Dielectrics: Limits and Advantages of Alkanethiol Blocking Agents on Metal-Dielectric Patterns. *ACS Applied Materials and Interfaces* **8**, 33264–33272 (2016).
127. Seo, E. K., Lee, J. W., Sung-Suh, H. M. & Sung, M. M. Atomic layer deposition of titanium oxide on self-assembled-monolayer-coated gold. *Chemistry of Materials* **16**, 1878–1883 (2004).
128. Avila, J. R. *et al.* Real-time observation of atomic layer deposition inhibition: Metal oxide growth on self-assembled alkanethiols. *ACS Applied Materials and Interfaces* **6**, 11891–11898 (2014).

129. Chen, R., Kim, H., McIntyre, P. C. & Bent, S. F. Investigation of self-assembled monolayer resists for hafnium dioxide atomic layer deposition. *Chemistry of Materials* **17**, 536–544 (2005).
130. Kanarik, K. J. *et al.* Overview of atomic layer etching in the semiconductor industry. *Journal of Vacuum Science & Technology A: Vacuum, Surfaces, and Films* **33**, 020802 (2015).
131. Puurunen, R. L. Analysis of hydroxyl group controlled atomic layer deposition of hafnium dioxide from hafnium tetrachloride and water. *Journal of Applied Physics* **95**, 4777–4786 (2004).
132. Alam, M. A. & Green, M. L. Mathematical description of atomic layer deposition and its application to the nucleation and growth of HfO₂ gate dielectric layers. *Journal of Applied Physics* **94**, 3403–3413 (2003).
133. Puurunen, R. L. Growth Per Cycle in Atomic Layer Deposition: A Theoretical Model. *Chemical Vapor Deposition* **9**, 249–257 (2003).
134. Ylilammi, M. Monolayer thickness in atomic layer deposition. *Thin Solid Films* **279**, 124–130 (1996).
135. Green, M. L. *et al.* Nucleation and growth of atomic layer deposited HfO₂ gate dielectric layers on chemical oxide (Si–O–H) and thermal oxide (SiO₂ or Si–O–N) underlayers. *Journal of Applied Physics* **92**, 7168–7174 (2002).
136. Green, M. L. *et al.* Nucleation of atomic-layer-deposited HfO₂ films, and evolution of their microstructure, studied by grazing incidence small angle x-ray scattering using synchrotron radiation. *Applied Physics Letters* **88**, 32907 (2006).

137. Gusev, E. P., Cabral, C., Copel, M., D'Emic, C. & Gribelyuk, M. Ultrathin HfO₂ films grown on silicon by atomic layer deposition for advanced gate dielectrics applications. *Microelectronic Engineering* **69**, 145–151 (2003).
138. Damlencourt, J.-F. *et al.* Electrical and physico-chemical characterization of HfO₂/SiO₂ gate oxide stacks prepared by atomic layer deposition. *Solid-State Electronics* **47**, 1613–1616 (2003).
139. Hackley, J. C., Gougousi, T. & Demaree, J. D. Nucleation of HfO₂ atomic layer deposition films on chemical oxide and H-terminated Si. *Journal of Applied Physics* **102**, 34101 (2007).
140. Cho, M. *et al.* Chemical interaction between atomic-layer-deposited HfO₂ thin films and the Si substrate. *Applied Physics Letters* **81**, 334–336 (2002).
141. Gusev, E. P. *et al.* Ultrathin high-K metal oxides on silicon: processing, characterization and integration issues. *Microelectronic Engineering* **59**, 341–349 (2001).
142. Kirsch, P. D. *et al.* Nucleation and growth study of atomic layer deposited HfO₂ gate dielectrics resulting in improved scaling and electron mobility. *Journal of Applied Physics* **99**, 23508 (2006).
143. Aarik, J. *et al.* Effects of precursors on nucleation in atomic layer deposition of HfO₂. *Applied Surface Science* **230**, 292–300 (2004).
144. Copel, M., Gribelyuk, M. & Gusev, E. Structure and stability of ultrathin zirconium oxide layers on Si(001). *Applied Physics Letters* **76**, 436–438 (2000).

145. Ferrari, S., Modreanu, M., Scarel, G. & Fanciulli, M. X-Ray reflectivity and spectroscopic ellipsometry as metrology tools for the characterization of interfacial layers in high- κ materials. *Thin Solid Films* **450**, 124–127 (2004).
146. Puurunen, R. L. *et al.* Island growth in the atomic layer deposition of zirconium oxide and aluminum oxide on hydrogen-terminated silicon: Growth mode modeling and transmission electron microscopy. *Journal of Applied Physics* **96**, 4878–4889 (2004).
147. Kukli, K., Ritala, M., Aarik, J., Uustare, T. & Leskelä, M. Influence of growth temperature on properties of zirconium dioxide films grown by atomic layer deposition. *Journal of Applied Physics* **92**, 1833–1840 (2002).
148. Methapanon, R. & Bent, S. F. Comparative Study of Titanium Dioxide Atomic Layer Deposition on Silicon Dioxide and Hydrogen-Terminated Silicon. *The Journal of Physical Chemistry C* **114**, 10498–10504 (2010).
149. Mitchell, D. R. G., Attard, D. J. & Triani, G. Transmission electron microscopy studies of atomic layer deposition TiO₂ films grown on silicon. *Thin Solid Films* **441**, 85–95 (2003).
150. Song, S. K., Saare, H. & Parsons, G. N. Integrated Isothermal Atomic Layer Deposition/Atomic Layer Etching Supercycles for Area-Selective Deposition of TiO₂. *Chemistry of Materials* **31**, 4793–4804 (2019).
151. Kanarik, K. J., Tan, S. & Gottscho, R. A. Atomic Layer Etching: Rethinking the Art of Etch. *J. Phys. Chem. Lett* **9**, 4821 (2018).
152. George, S. M. & Lee, Y. Prospects for Thermal Atomic Layer Etching Using Sequential, Self-Limiting Fluorination and Ligand-Exchange Reactions. *ACS Nano* **10**, 4889–4894 (2016).

153. Fang, C., Cao, Y., Wu, D. & Li, A. Thermal atomic layer etching: Mechanism, materials and prospects. *Progress in Natural Science: Materials International* **28**, 667–675 (2018).
154. Langereis, E. *et al.* In situ spectroscopic ellipsometry as a versatile tool for studying atomic layer deposition. *Journal of Physics D: Applied Physics* **42**, 073001 (2009).
155. Kief, M. T. In-situ ellipsometry: applications to thin film research, development, and production. in vol. 10294 1029403 (International Society for Optics and Photonics, 1999).
156. Junige, M., Geidel, M., Knaut, M., Albert, M. & Bartha, J. W. Monitoring atomic layer deposition processes in situ and in real-time by spectroscopic ellipsometry. in *2011 Semiconductor Conference Dresden* 1–4 (IEEE, 2011). doi:10.1109/SCD.2011.6068739.
157. Mackus, A. J. M., Verheijen, M. A., Leick, N., Bol, A. A. & Kessels, W. M. M. Influence of Oxygen Exposure on the Nucleation of Platinum Atomic Layer Deposition: Consequences for Film Growth, Nanopatterning, and Nanoparticle Synthesis. *Chemistry of Materials* **25**, 1905–1911 (2013).
158. Muneshwar, T. & Cadien, K. Probing initial-stages of ALD growth with dynamic in situ spectroscopic ellipsometry. *Applied Surface Science* **328**, 344–348 (2015).
159. Wind, R. W., Fabreguette, F. H., Sechrist, Z. A. & George, S. M. Nucleation period, surface roughness, and oscillations in mass gain per cycle during W atomic layer deposition on Al₂O₃. *Journal of Applied Physics* **105**, 074309 (2009).
160. Lecordier, L., Herregods, S. & Armini, S. Vapor-deposited octadecanethiol masking layer on copper to enable area selective Hf₃N₄ atomic layer deposition on dielectrics

- studied by in situ spectroscopic ellipsometry. *Journal of Vacuum Science & Technology A* **36**, 031605 (2018).
161. Baker, L. *et al.* Nucleation and growth of Pt atomic layer deposition on Al₂O₃ substrates using (methylcyclopentadienyl)-trimethyl platinum and O₂ plasma. *Journal of Applied Physics* **109**, 084333 (2011).
162. Langereis, E., Heil, S. B. S., Van De Sanden, M. C. M. & Kessels, W. M. M. In situ spectroscopic ellipsometry study on the growth of ultrathin TiN films by plasma-assisted atomic layer deposition. *Journal of Applied Physics* **100**, 023534 (2006).
163. Patsalas, P. & Logothetidis, S. Interface properties and structural evolution of TiN/Si and TiN/GaN heterostructures. *Journal of Applied Physics* **93**, 989–998 (2003).
164. Jiang, X., Wang, H., Qi, J. & Willis, B. G. In-situ spectroscopic ellipsometry study of copper selective-area atomic layer deposition on palladium. *Journal of Vacuum Science & Technology A* **32**, 41513 (2014).
165. Junige, M. *et al.* Area-selective atomic layer deposition of Ru on electron-beam-written Pt(C) patterns versus SiO₂ substratum. *Nanotechnology* **28**, 395301 (2017).
166. Raza, M. A., Zandvliet, H. J. W., Poelsema, B. & Kooij, E. S. Selective metallization by seeded growth on patterned gold nanoparticle arrays. *Journal of Applied Physics* **113**, 233510 (2013).
167. Pesce, V. *et al.* Optimization by in situ ellipsometry of ALD and ALE successive steps for the selective Atomic Layer Deposition of Ta₂O₅ on TiN and Si. *AVS 65th International Symposium* (2018).

168. Mameli, A. *et al.* Area-Selective Atomic Layer Deposition of SiO₂ Using Acetylacetone as a Chemoselective Inhibitor in an ABC-Type Cycle. *ACS Nano* **11**, 9303–9311 (2017).
169. Mameli, A. *et al.* Area-Selective Atomic Layer Deposition of ZnO by Area Activation Using Electron Beam-Induced Deposition. *Chemistry of Materials* **31**, 1250–1257 (2019).
170. Niang, K. M., Bai, G. & Robertson, J. Influence of precursor dose and residence time on the growth rate and uniformity of vanadium dioxide thin films by atomic layer deposition. *Journal of Vacuum Science & Technology A* **38**, 42401 (2020).
171. Baji, Z. *et al.* Nucleation and Growth Modes of ALD ZnO. *Crystal Growth & Design* **12**, 5615–5620 (2012).
172. Kuse, R., Kundu, M., Yasuda, T., Miyata, N. & Toriumi, A. Effect of precursor concentration in atomic layer deposition of Al₂O₃. *Journal of Applied Physics* **94**, 6411–6416 (2003).
173. Murray, C. A., Elliott, S. D., Hausmann, D., Henri, J. & LaVoie, A. Effect of Reaction Mechanism on Precursor Exposure Time in Atomic Layer Deposition of Silicon Oxide and Silicon Nitride. *ACS Applied Materials & Interfaces* **6**, 10534–10541 (2014).
174. Kukli, K. *et al.* Effect of selected atomic layer deposition parameters on the structure and dielectric properties of hafnium oxide films. *Journal of Applied Physics* **96**, 5298–5307 (2004).
175. Gordon, R. G., Hausmann, D., Kim, E. & Shepard, J. A Kinetic Model for Step Coverage by Atomic Layer Deposition in Narrow Holes or Trenches. *Chemical Vapor Deposition* **9**, 73–78 (2003).

176. Lemaire, P. C. & Parsons, G. N. Thermal Selective Vapor Etching of TiO₂: Chemical Vapor Etching via WF₆ and Self-Limiting Atomic Layer Etching Using WF₆ and BCl₃. *Chemistry of Materials* **29**, 6653–6665 (2017).
177. Garcia-Caurel, E., De Martino, A., Gaston, J. P. & Yan, L. Application of spectroscopic ellipsometry and mueller ellipsometry to optical characterization. *Applied Spectroscopy* vol. 67 1–21 (2013).
178. Parsons, G. N. Functional model for analysis of ALD nucleation and quantification of area-selective deposition. *Journal of Vacuum Science & Technology A* **37**, 020911 (2019).
179. Gladfelter, W. L. Selective Metallization by Chemical Vapor Deposition. *Chemistry of Materials* **5**, 1372–1388 (1993).
180. Parsons, G. N. & Clark, R. D. Area-Selective Deposition: Fundamentals, Applications, and Future Outlook. *Chemistry of Materials* vol. 32 4920–4953 (2020).
181. Shard, A. G. Detection limits in XPS for more than 6000 binary systems using Al and Mg K α X-rays. *Surface and Interface Analysis* **46**, 175–185 (2014).
182. Wong, H. S. P. & Salahuddin, S. Memory leads the way to better computing. *Nature Nanotechnology* vol. 10 191–194 (2015).
183. Burr, G. W. *et al.* Large-scale neural networks implemented with non-volatile memory as the synaptic weight element: Comparative performance analysis (accuracy, speed, and power). in *Technical Digest - International Electron Devices Meeting, IEDM* vols. 2016-February 4.4.1-4.4.4 (Institute of Electrical and Electronics Engineers Inc., 2015).

184. Jeong, D. S. & Hwang, C. S. Nonvolatile Memory Materials for Neuromorphic Intelligent Machines. *Advanced Materials* vol. 30 (2018).
185. Burr, G. W. *et al.* Access devices for 3D crosspoint memory. *Journal of Vacuum Science & Technology B, Nanotechnology and Microelectronics: Materials, Processing, Measurement, and Phenomena* **32**, 040802 (2014).
186. Wuttig, M., Bhaskaran, H. & Taubner, T. Phase-change materials for non-volatile photonic applications. *Nature Photonics* vol. 11 465–476 (2017).
187. Burr, G. W. *et al.* Phase change memory technology. *J. Vac. Sci. Technol. B* **28**, 223 (2010).
188. Fong, S. W., Neumann, C. M. & Wong, H. S. P. Phase-Change Memory - Towards a Storage-Class Memory. *IEEE Transactions on Electron Devices* **64**, 4374–4385 (2017).
189. Pirovano, A. *et al.* Reliability study of phase-change nonvolatile memories. *IEEE Transactions on Device and Materials Reliability* **4**, 422–426 (2004).
190. Perniola, L. *et al.* Electrical behavior of phase-change memory cells based on GeTe. *IEEE Electron Device Letters* **31**, 488–490 (2010).
191. Manivannan, A., Myana, S. K., Miriyala, K., Sahu, S. & Ramadurai, R. Low power ovonic threshold switching characteristics of thin GeTe₆ films using conductive atomic force microscopy. *Applied Physics Letters* **105**, 243501 (2014).
192. Sousa, V. & Navarro, G. Material engineering for PCM device optimization. in *Phase Change Memory: Device Physics, Reliability and Applications* 181–222 (Springer International Publishing, 2017). doi:10.1007/978-3-319-69053-7_7.

193. Guo, P., Sevison, G., Agha, I., Sarangan, A. & Burrow, J. Electrical and optical properties of nickel-doped $\text{Ge}_2\text{Sb}_2\text{Te}_5$ films produced by magnetron co-sputtering. in *Nanoengineering: Fabrication, Properties, Optics, and Devices XV* (eds. Sakdinawat, A. E., Attias, A.-J., Panchapakesan, B. & Dobisz, E. A.) vol. 10730 19 (SPIE, 2018).
194. Laudato, M. *et al.* ALD GeAsSeTe Ovonic Threshold Switch for 3D Stackable Crosspoint Memory. in *2020 IEEE International Memory Workshop, IMW 2020 - Proceedings* (Institute of Electrical and Electronics Engineers Inc., 2020). doi:10.1109/IMW48823.2020.9108152.
195. Narasimhan, V. *et al.* Physical and Electrical Characterization of ALD Chalcogenide Materials for 3D Memory Applications. (2019).
196. Lai, Y. F. *et al.* Stacked chalcogenide layers used as multi-state storage medium for phase change memory. *Applied Physics A: Materials Science and Processing* **84**, 21–25 (2006).
197. Rao, F. *et al.* Multilevel data storage characteristics of phase change memory cell with doublelayer chalcogenide films ($\text{Ge}_2\text{Sb}_2\text{Te}_5$ and Sb_2Te_3). *Japanese Journal of Applied Physics, Part 2: Letters* **46**, L25 (2007).
198. Liu, B. *et al.* Nitrogen-implanted $\text{Ge}_2\text{Sb}_2\text{Te}_5$ film used as multilevel storage media for phase change random access memory. *Semiconductor Science and Technology* **19**, L61 (2004).
199. Lyeo, H. K. *et al.* Thermal conductivity of phase-change material $\text{Ge}_2\text{Sb}_2\text{Te}_5$. *Applied Physics Letters* **89**, 151904 (2006).

200. Adinolfi, V. *et al.* Composition-Controlled Atomic Layer Deposition of Phase-Change Memories and Ovonic Threshold Switches with High Performance. *ACS Nano* **13**, 10440–10447 (2019).
201. Gwon, T. *et al.* Atomic Layer Deposition of GeTe and Ge-Sb-Te Films Using HGeCl₃, Sb(OC₂H₅)₃, and {(CH₃)₃Si}₂Te and Their Reaction Mechanisms. *Chemistry of Materials* **29**, 8065–8072 (2017).
202. Song, S. *et al.* Phase-change properties of GeSbTe thin films deposited by plasma-enhanced atomic layer deposition. *Nanoscale Research Letters* **10**, (2015).
203. Matsunaga, T. *et al.* Structural characteristics of GeTe-rich GeTe-Sb₂Te₃ pseudobinary metastable crystals. *Journal of Applied Physics* **103**, 093511 (2008).
204. Matsunaga, T. & Yamada, N. Structural investigation of GeSb₂Te₄: a high-speed phase-change material. *Physical Review B - Condensed Matter and Materials Physics* **69**, 104111 (2004).
205. Lazarenko, P. I. *et al.* Investigation of transport mechanisms in Bi doped Ge₂Sb₂Te₅ thin films for phase change memory application. in *International Conference on Micro- and Nano-Electronics 2014* (ed. Orlikovsky, A. A.) vol. 9440 944006 (SPIE, 2014).
206. Bai, N. *et al.* Effect of the Sn dopant on the crystallization of amorphous Ge₂Sb₂Te₅ films induced by an excimer laser. *Optics and Laser Technology* **74**, 11–15 (2015).
207. Privitera, S., Rimini, E. & Zonca, R. Amorphous-to-crystal transition of nitrogen- and oxygen-doped Ge₂Sb₂Te₅ films studied by in situ resistance measurements. *Applied Physics Letters* **85**, 3044–3046 (2004).

208. Ryu, S. W. *et al.* Phase transformation behaviors of SiO₂ doped Ge₂Sb₂Te₅ films for application in phase change random access memory. *Applied Physics Letters* **92**, 142110 (2008).
209. Li, T. *et al.* Carbon doping induced Ge local structure change in as-deposited Ge₂Sb₂Te₅ film by EXAFS and Raman spectrum. *AIP Advances* **8**, 025201 (2018).
210. Raoux, S. *et al.* Direct observation of amorphous to crystalline phase transitions in nanoparticle arrays of phase change materials. *Journal of Applied Physics* **102**, 094305 (2007).
211. Navarro, G. *et al.* Innovative PCM+OTS device with high sub-threshold non-linearity for non-switching reading operations and higher endurance performance. in *Digest of Technical Papers - Symposium on VLSI Technology* T94–T95 (Institute of Electrical and Electronics Engineers Inc., 2017). doi:10.23919/VLSIT.2017.7998208.
212. Feng, J. *et al.* Si doping in Ge₂Sb₂Te₅ film to reduce the writing current of phase change memory. *Applied Physics A: Materials Science and Processing* **87**, 57–62 (2007).
213. Wei, S. J. *et al.* Phase change behavior in titanium-doped Ge₂Sb₂Te₅ films. *Applied Physics Letters* **98**, 231910 (2011).
214. Jellison, G. E. & Modine, F. A. Parameterization of the optical functions of amorphous materials in the interband region. *Applied Physics Letters* **69**, 371–373 (1996).
215. Nilsen, O., Mohn, C. E., Kjekshus, A. & Fjellvåg, H. Analytical model for island growth in atomic layer deposition using geometrical principles. *Journal of Applied Physics* **102**, 024906 (2007).

CHAPTER 2

Experimental Instrumentation

2.1 Thin Film Processing and Characterization System

The thin film processes and *in-situ* characterizations in the following studies were performed in a home-built warm-walled cluster tool illustrated in figure 2.1. The system consists of 3 chambers: the processing chamber, the load lock and the analytical chamber. The processing sample is equipped with a PID-controlled sample heater equipped with two halogen lamps. The reactants are introduced into the chamber through 4 separate lines using argon (Arc3 Gases, 99.999% purity) as a carrier and purge gas. Both the lines and the walls are heated to 100 °C with heat tape to prevent condensation. The gases are pumped out by a turbo pump and a rotary vane pump. The processing pressure, usually held between 400 to 600 mTorr, was achieved by regulating a butterfly valve before the turbo pump to control the pump rate and by limiting the Ar flow through the lines using mass flow controllers (MFCs). The total flow rate of Ar was kept at 95 sccm. For *in-situ* thin film characterization the processing chamber is equipped with multi-wavelength ellipsometer (Film Sense FS-1).

The samples are clamped onto a chuck, which can be transferred freely between the chambers using magnetic arms. While samples can be loaded directly into the processing chamber, the load lock is necessary to load samples to the analytical chamber and to prevent the analytical chamber from being contaminated. The load lock is pumped down to ultrahigh vacuum using a turbo pump and rotary vane pump before sample transfer. The analytical chamber is equipped with Auger electron spectroscopy (AES, Perkin Elmer PHI 10-155). For proper characterization conditions the chamber is pumped down to 10^{-10} Torr by an ion pump (Digitel 500 220 l/s) and a turbo pump (Edwards EXT501).

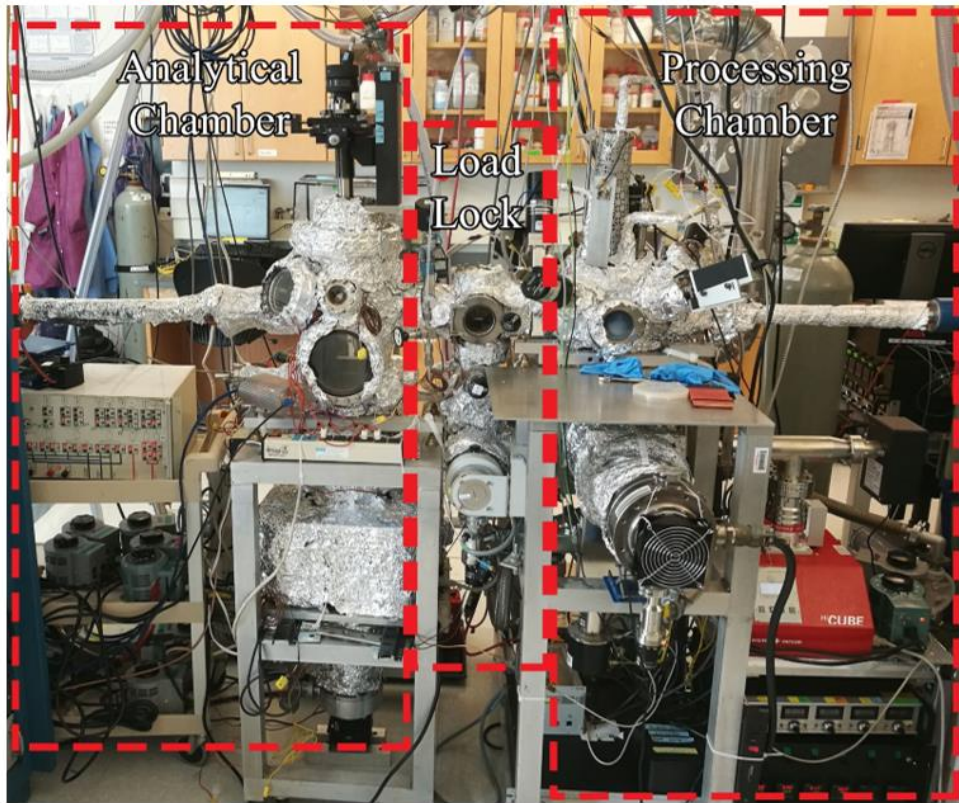
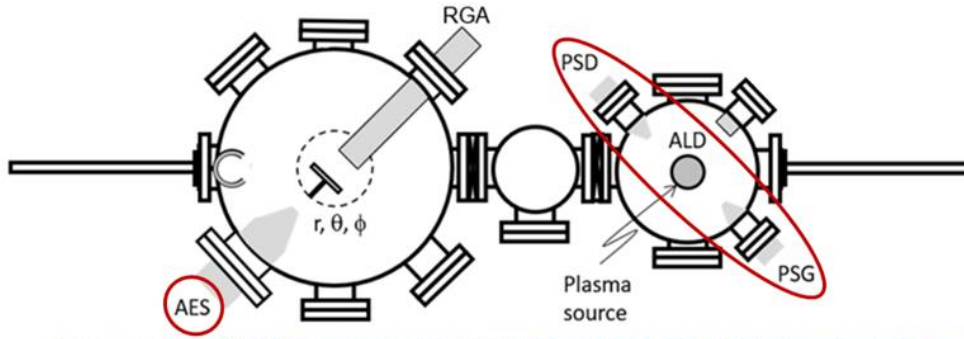


Figure 2.1. Diagram and a photo of the multi-chamber cluster tool used in this work. The chamber is capable of both thermal and plasma-enhanced atomic layer deposition and atomic layer etching. It is equipped with Auger electron spectroscopy and multi-wavelength ellipsometry for *in-situ* process characterization.

2.2 Spectroscopic Ellipsometry

The deposition rates and optical constants of thin films processed in this work were analyzed using *in-situ* ellipsometry. A FilmSense FS-1 four-wavelength ellipsometer was used *in-situ*, installed onto the processing chamber at a $65^{\circ} \pm 5^{\circ}$ angle. The instrument collects data at 465 nm, 525 nm, 595 nm, and 635 nm wavelength. A single data point for each wavelength is collected in 10 ms and the resulting output is averaged over a 10 s period, resulting in 1000 data points per single output. Software integrated into the ellipsometer was used for acquiring and modeling data.

Ellipsometry is a non-destructive surface sensitive method, which utilizes polarized light to characterize the samples.¹¹⁰ A common experimental setup for an ellipsometry measurement is illustrated in figure 2.2.¹¹¹ A light source emits an electromagnetic wave, which is converted into a linearly polarized light by a polarizer, consisting of both s-polarized and p-polarized components. Upon reflecting off surface of the sample, the polarizations have a different change in their amplitude and phase, due to interactions with electric dipoles in the sample. The resulting elliptically polarized light is passed through an analyzer to the detector, which measures the complex reflection ratio, defined as:

$$\rho = R^p / R^s = \tan \Psi e^{i\Delta} \quad (2.1)$$

The R^p and R^s are Fresnel reflection coefficient for p- and s-polarized light (light oscillating parallel and perpendicular to the plane of incidence, respectively). The measurement is performed close to the Brewster angle, to maximize the R^p/R^s ratio. The resulting ellipsometric angles, Ψ and Δ , describe the amplitude ratio and phase difference between the p- and s-polarizations, respectively and can be derived from equation 2.1:

$$\Psi = \arctan (|R^p / R^s|) \quad (2.2)$$

$$\Delta = \arg(R^p) - \arg(R^s) = \delta_p - \delta_s \quad (2.3)$$

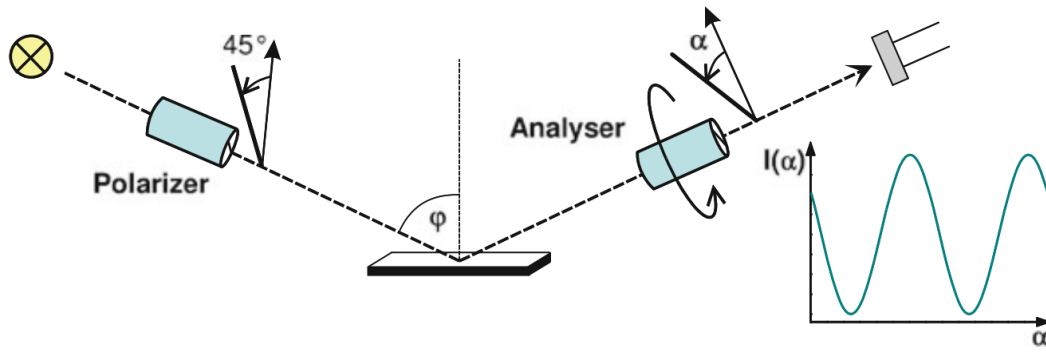


Figure 2.2. Simplified configuration of an ellipsometer with a rotating analyzer. The polarizer produces linearly polarized light at 45° angle. The elliptically polarized light, resulting from interaction with the sample, is transmitted through an analyzer. The detector records a sinusoidal signal with periodicity of 2α . Figure reproduced. ¹¹¹

To obtain thin film thickness values and optical constants a model must be constructed. The model needs to consider all individual layers and parameters that need to be extracted, such as layer thickness, optical constants, surface roughness and material mixture fractions. To extract these values, regression analysis is commonly performed as demonstrated in figure 2.3.¹¹² For this, the predicted Ψ and Δ are calculated from the model using Fresnel coefficients, Snell's law, and thin film interference equations for each wavelength.¹¹² The model output is compared to the experimentally measured values and the resulting mean square error (MSE) is calculated:

$$\text{MSE} = \sqrt{\frac{1}{2N-M} \sum_{i=1}^N \left[\left(\frac{\Psi_i^{\text{mod}} - \Psi_i^{\text{exp}}}{\sigma_{\Psi,i}^{\text{exp}}} \right)^2 + \left(\frac{\Delta_i^{\text{mod}} - \Delta_i^{\text{exp}}}{\sigma_{\Delta,i}^{\text{exp}}} \right)^2 \right]} \quad (2.4)$$

A smaller MSE value indicates that better fit was achieved. The unknown parameters in the model are then varied to improve the fit and lower the MSE value to a global minima, commonly Marquardt-Levenberg algorithm is used to efficiently reach the best fit in few iterations.¹¹³

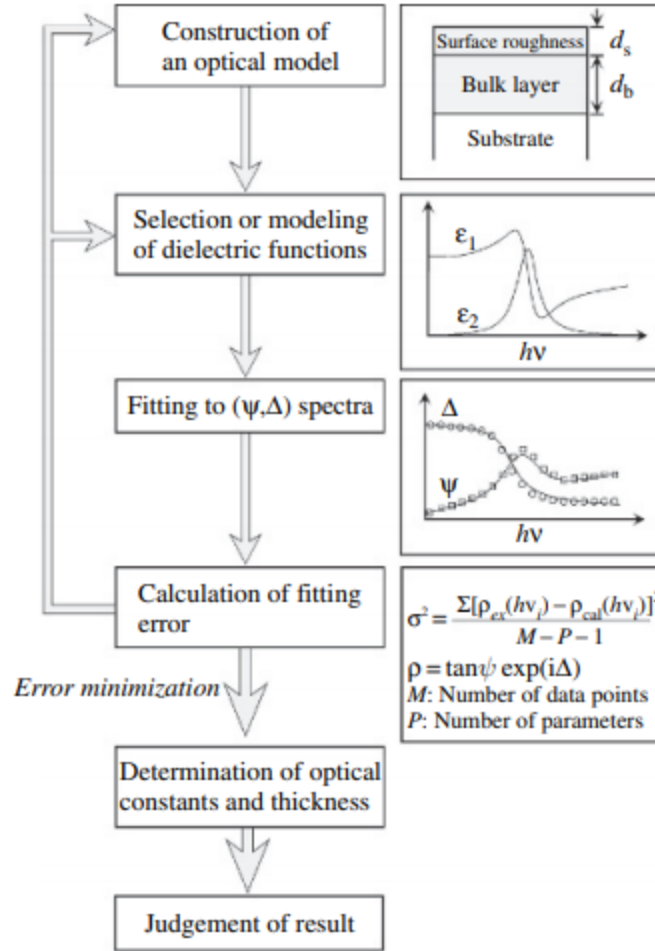


Figure 2.3. Schematic of the modelling and data analysis procedure for spectroscopic ellipsometry. Figure reproduced.¹¹²

The model applied depends on the type of material being studied. For transparent materials ($k(\lambda) \sim 0$) Cauchy relationship is typically used:

$$n(\lambda) = A + \frac{B}{\lambda^2} + \frac{C}{\lambda^4} + \dots \quad (2.5)$$

The n represents the refractive index at wavelength λ . The first two or three terms are usually considered sufficient for practical applications and the coefficients A , B , and C are obtained through fitting the model to measured results. In addition to transparent materials, the model can also be applied to a transparent wavelength region of an otherwise absorbing material.

Tauc-Lorentz dispersion formula is commonly used to describe amorphous semiconductors. The model, developed in 1996, combines Tauc's model of the density of states with the Lorentz oscillator.^{114,115} The real and imaginary parts of the dielectric function are given as

$$\varepsilon_2(E; A, E_0, E_g, C) = \Theta(E - E_g) \frac{(E - E_g)^2 A E_0 C}{(E^2 - E_0^2)^2 + C^2 E^2} \cdot \frac{1}{E} \quad (2.6)$$

$$\varepsilon_1(E; A, E_0, E_g, C, \varepsilon_1(\infty)) = \varepsilon_1(\infty) + \frac{2}{\pi} \int_{E_g}^{\infty} \frac{\varepsilon_2(E') E'}{E'^2 - E^2} dE' \quad (2.7)$$

where A is the Tauc coefficient, E_0 is the central energy of the oscillator, E_g is the bandgap energy, and C is the oscillator width. Both A and C are the fitting parameters. Θ represents the Heaviside step function, which is 1 if the photon energy E is larger than the bandgap E_g and 0 otherwise. This means that the model does not account for intra-band absorption and has resulted in several improvements being suggested to improve the model fit.¹¹⁶⁻¹¹⁸ The ε_1 is derived from ε_2 via Kramers-Kronig relation with an additional fitting parameter $\varepsilon_1(\infty)$ included to prevent ε_1 converging to zero.

2.3 Auger Electron Spectroscopy

In-vacuo Auger electron spectroscopy (AES) measurements were performed to determine the elemental composition of thin films. For this, a Physical Electronics system was used, composed of PHI 11-010 electron gun, 10-155 cylindrical mirror analyzer, 32-150 digital analyzer control, 96A V/f preamplifier, and 32-100 electron multiplier power supply. RBD Instruments software AugerScan was used to collect and analyze the spectra.

Auger electron spectroscopy was the first widely used technique used for surface analysis of thin layers.¹¹⁹ It is based on a phenomenon named Auger effect, which is illustrated in figure 2.4.¹²⁰ Electron beam is used to create a core hole by ejecting a core-level electron. To stabilize the state

an electron from a higher energy state will transition to the core level state, releasing energy equal to the energy difference between the two levels. For heavier elements this energy is more commonly released as a photon, which is a basis for X-ray fluorescence measurements. For lighter elements it is more likely that the relaxation is non-radiative, resulting in excitation of another electron in the same atom. The measurement of the kinetic energy of this tertiary electron, also referred to as Auger electron, is the basis of Auger electron spectroscopy. For historical reasons X-ray notation is used to describe the electron transitions. In the $K_1L_{2,3}L_{2,3}$ transition example shown in figure 2.4, the K_1 represents the initially ionized electron shell, the first $L_{2,3}$ the initial state of the relaxing electron, and the last $L_{2,3}$ the state of the Auger electron being emitted. The kinetic energy of the Auger electron is given by

$$E_k = E_X - E_Y - E_{Z^*} - \phi \quad (2.8)$$

The X, Y, and Z^* represent the binding energies of appropriate electron levels in XYZ^* transition, where * notates the energy change in an ion, and ϕ is the analyzer work function correction. The measured energy E_k is characteristic to atomic species present in the sample and can be used to identify both the species as well as chemical shifts. In addition, the intensity of the measured peaks can be used to determine atomic concentrations of each element present.

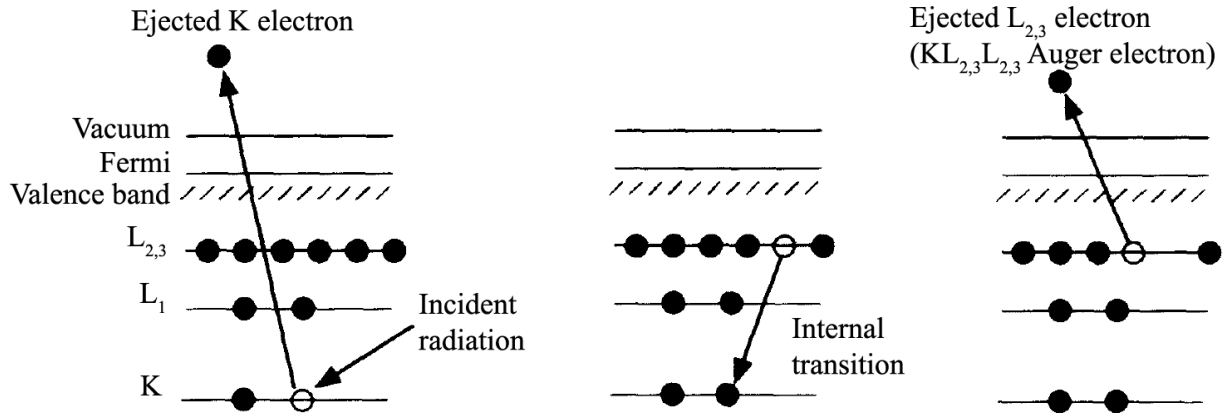


Figure 2.4. Diagram of the Auger effect illustrating an emission process for $KL_{2,3}L_{2,3}$ Auger electron. Figure reproduced.¹²⁰

An example of an acquired AES spectra is shown in figure 2.5.¹²¹ Since the measured Auger signals are weak relative to the strong background resulting from backscattered and secondary electrons, the spectra is commonly differentiated for clearer presentation. In the derivative mode the peaks are identified by their minima position and the peak shape used to characterize the oxidation state of elements.

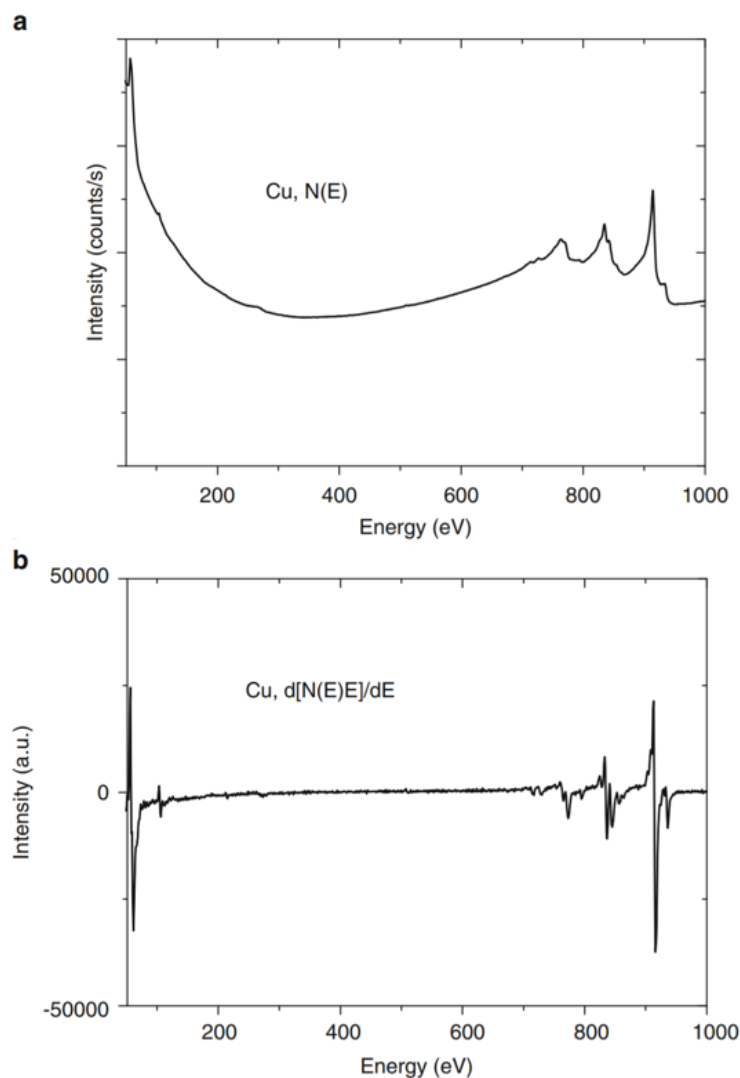


Figure 2.5. Auger spectrum of Cu (a) as measured and (b) in a differentiated mode. The derivative mode is used to remove the noisy background and emphasize Auger peaks. Figure reproduced.¹²¹

2.4 X-ray Photoelectron Spectroscopy

X-ray photoelectron spectroscopy (XPS) is a surface-sensitive chemical characterization method similar to AES. In XPS, the sample is irradiated with X-rays, which interact with core electrons, leading to the emission of photoelectrons due to the photoelectric effect. From the

incident X-ray energy and the measured kinetic energy, the binding energy of the emitted photon can be calculated. As given by equation 2.9:

$$E_b = h\nu - E_k - \phi \quad (2.9)$$

where E_b is the electron binding energy, $h\nu$ the incident X-ray energy, E_k the measured kinetic energy of the photoelectron, and ϕ the work function. An XPS spectra is generated by plotting the number of photoelectrons detected for each binding energy in the measurement range. The peaks in that spectra can be used to identify the elements and their chemical states. Compared to AES, XPS spectra is easier to interpret and is preferred for measuring non-conductive surfaces, however, AES is more surface sensitive and has a higher spatial resolution.

In the studies two different XPS system were used. Kratos Axis Ultra DLD X-ray Photoelectron Spectrometer with a monochromatic Al $K\alpha$ X-ray source and a SPECS System with PHOIBOS 150 Analyzer, equipped with Al/Mg X-ray sources. In both cases the measured spectra were calibrated based on the C 1s peak at 284.5 eV as a reference.

2.5 Fourier Transform Infrared Spectroscopy

Fourier Transform Infrared Spectroscopy (FTIR) is used to identify the chemical bonds present in a sample. The technique produces an infrared adsorption spectrum by shining a broadband light at the sample and measuring the resulting signal intensities at various wavelength throughout the measurement range. The adsorption peaks in the spectra correspond to resonant frequencies of specific chemical bonds which can be identified.

A home-built custom warm-walled reactor was used for in-situ FTIR studies as shown in figure 2.6.¹²² The FTIR was operated in transmission mode using Thermo-Fisher Nicolet 6700 spectrometer with an external MCT-A detector. The IR measurement were performed through two

CsI IR windows, which were sealed with gate valves during precursor exposure to prevent deposition on the windows.

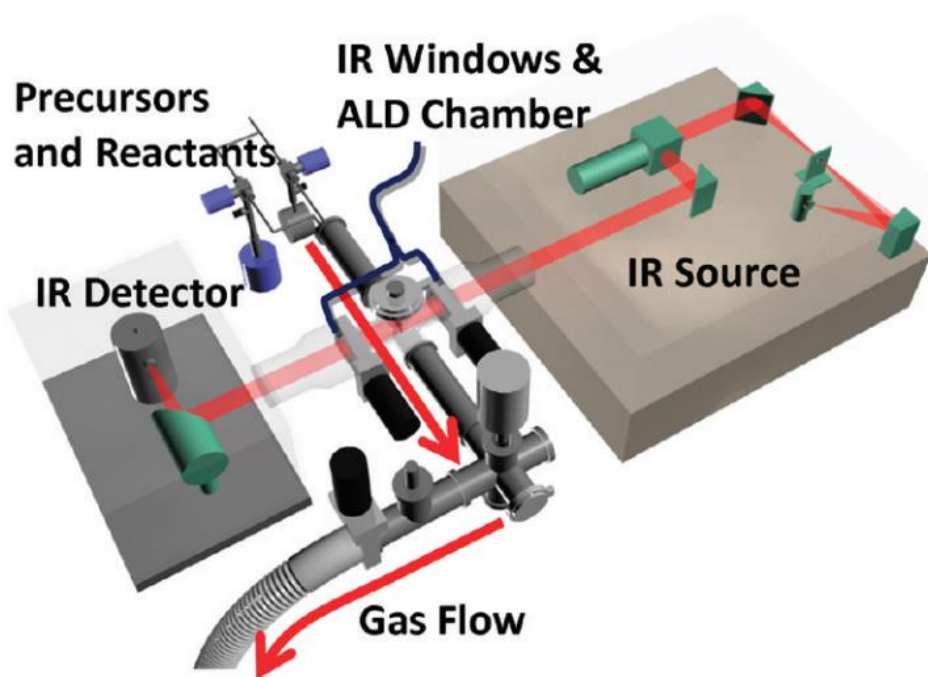


Figure 2.6. Illustration of the ALD reactor equipped with *in-situ* FTIR capability used in this work. Figure reproduced.¹²²

2.6 Scanning Electron Microscopy

Scanning electron microscopy (SEM) utilizes a focused beam of electron to produce a high-resolution image of the sample by scanning the surface. Backscattered and secondary electrons resulting from the interactions of the electron beam with the sample are detected and provide information about the composition and the surface topography, respectively. In this work field emission scanning electron microscope FEI Verios 460L was used with an Everhart-Thornley low energy electron detector in a secondary electron mode.

2.7 Transmission Electron Microscopy

In transmission electron microscopy (TEM) electrons that pass through the sample are analyzed, providing information of the structure of the sample in very high magnification (up to

50 million times). As such significant sample preparation is usually needed to create thinner samples compared to SEM measurements. In this work cross-sectional images were acquired using JEOL JEM-20000FX scanning transmission electron microscope (STEM) along with energy dispersive spectrometer (EDS) for chemical identification of the samples.

2.8 Atomic Force Microscopy

Atomic force microscopy (AFM) allows to collect information about the morphology of sample surfaces. The information is collected by scanning a cantilever tip across the sample and measuring the force between the tip and the sample surface. Depending on the approach, the cantilever can be held at a constant deflection while the force between the tip and the sample is held constant (contact mode), or the cantilever can be oscillated at its resonant frequency and the amplitude of the oscillation is measured (tapping mode). In both methods, the deflection of the cantilever is measured by a laser beam reflecting off its surface, enabling resolution up to atomic-level. In the studies, Asylum MFP-3D classic AFM was used in tapping mode in air using silicon probes with cantilever length of 125 μm and force constant of 40 N m^{-1} .

2.9 X-ray Diffraction

X-ray diffraction (XRD) is a method used to characterize the crystal structure of a sample. The method utilizes an incident X-ray beam, which interacts with a sample of interest, resulting in diffracted beams. A spectra is acquired by measuring the intensities of the beams at various angles. The resulting peaks in the spectra give information about the crystal orientation, unit cell dimensions and sample purity. In this work Rigaku SmartLab X-ray Diffractometer was used in a grazing incidence (GIXRD) mode.

2.10 References

1. Dhanaraj, G., Byrappa, K., Prasad, V. & Dudley, M. *Springer Handbook of Crystal Growth. Springer Handbook of Crystal Growth* (Springer, 2010). doi:10.1007/978-3-540-74761-1.
2. Kääriäinen, T., Cameron, D., Kääriäinen, M.-L. & Sherman, A. *Atomic Layer Deposition: Principles, Characteristics, and Nanotechnology Applications*. (Wiley-Scrivener, 2013).
3. Delabie, A. *et al.* Reaction mechanisms for atomic layer deposition of aluminum oxide on semiconductor substrates. *Journal of Vacuum Science & Technology A: Vacuum, Surfaces, and Films* **30**, 01A127 (2012).
4. Puurunen, R. L. Surface chemistry of atomic layer deposition: A case study for the trimethylaluminum/ water process. *J. Appl. Phys* **97**, 121301 (2005).
5. Higashi, G. S. & Fleming, C. G. Sequential surface chemical reaction limited growth of high quality Al₂O₃ dielectrics. *Applied Physics Letters* **55**, 1963–1965 (1989).
6. Stempel, V. E., Knemeyer, K., D'Alnoncourt, R. N., Driess, M. & Rosowski, F. Investigating the trimethylaluminium/water ALD process on mesoporous silica by in situ gravimetric monitoring. *Nanomaterials* **8**, (2018).
7. Pan, D., Ma, L., Xie, Y., Jen, T. C. & Yuan, C. On the physical and chemical details of alumina atomic layer deposition: A combined experimental and numerical approach. *Journal of Vacuum Science & Technology A: Vacuum, Surfaces, and Films* **33**, 021511 (2015).
8. Puurunen, R. L. Growth per cycle in atomic layer deposition: A theoretical model. *Chemical Vapor Deposition* **9**, 249–257 (2003).

9. Ylilammi, M. Monolayer thickness in atomic layer deposition. *Thin Solid Films* **279**, 124–130 (1996).
10. Richey, N. E., de Paula, C. & Bent, S. F. Understanding chemical and physical mechanisms in atomic layer deposition. *Journal of Chemical Physics* vol. 152 40902 (2020).
11. Puurunen, R. L. Surface chemistry of atomic layer deposition: A case study for the trimethylaluminum/water process. *Journal of Applied Physics* vol. 97 121301 (2005).
12. Mackus, A. J. M., Macisaac, C., Kim, W. H. & Bent, S. F. Incomplete elimination of precursor ligands during atomic layer deposition of zinc-oxide, tin-oxide, and zinc-tin-oxide. *Journal of Chemical Physics* **146**, 052802 (2017).
13. Dillon, A. C., Ott, A. W., Way, J. D. & George, S. M. Surface chemistry of Al₂O₃ deposition using Al(CH₃)₃ and H₂O in a binary reaction sequence. *Surface Science* **322**, 230–242 (1995).
14. Pinna, N. & Knez, M. *Atomic Layer Deposition of Nanostructured Materials. Atomic Layer Deposition of Nanostructured Materials* (Wiley-VCH, 2012). doi:10.1002/9783527639915.
15. Suntola, T. Surface chemistry of materials deposition at atomic layer level. *Applied Surface Science* **100–101**, 391–398 (1996).
16. Johnson, R. W., Hultqvist, A. & Bent, S. F. A brief review of atomic layer deposition: From fundamentals to applications. *Materials Today* vol. 17 236–246 (2014).
17. Hwang, C. S. *Atomic layer deposition for semiconductors. Atomic Layer Deposition for Semiconductors* vol. 9781461480549 (Springer US, 2014).

18. Burgers, J. M., Dehlinger, U., Frenkel, J., Kontorowa, T. & Garber, R. One-dimensional dislocations. II. Misfitting monolayers and oriented overgrowth. *Proceedings of the Royal Society of London. Series A. Mathematical and Physical Sciences* **198**, 216–225 (1949).
19. George, S. M. Atomic layer deposition: An overview. *Chemical Reviews* **110**, 111–131 (2010).
20. Ritala, M. *et al.* Perfectly Conformal TiN and Al₂O₃ Films Deposited by Atomic Layer Deposition. *Chemical Vapor Deposition* **5**, 7–9 (1999).
21. Marichy, C., Bechelany, M. & Pinna, N. Atomic layer deposition of nanostructured materials for energy and environmental applications. *Advanced Materials* **24**, 1017–1032 (2012).
22. Volmer, M. & Weber, A. Keimbildung in übersättigten Gebilden. *Zeitschrift für Physikalische Chemie* **119U**, 277–301 (1925).
23. Parsons, G. N. Functional model for analysis of ALD nucleation and quantification of area-selective deposition. *Journal of Vacuum Science & Technology A* **37**, 020911 (2019).
24. Copel, M., Gribelyuk, M. & Gusev, E. Structure and stability of ultrathin zirconium oxide layers on Si(001). *Applied Physics Letters* **76**, 436–438 (2000).
25. Besling, W. F. A. *et al.* Characterisation of ALCVD Al₂O₃-ZrO₂ nanolaminates, link between electrical and structural properties. *Journal of Non-Crystalline Solids* **303**, 123–133 (2002).

26. Gusev, E. P., Cabral, C., Copel, M., D'Emic, C. & Gribelyuk, M. Ultrathin HfO₂ films grown on silicon by atomic layer deposition for advanced gate dielectrics applications. in *Microelectronic Engineering* vol. 69 145–151 (Elsevier, 2003).
27. Frank, M. M., Chabal, Y. J. & Wilk, G. D. Nucleation and interface formation mechanisms in atomic layer deposition of gate oxides. *Applied Physics Letters* **82**, 4758–4760 (2003).
28. Nie, X., Ma, F., Ma, D. & Xu, K. Growth mode evolution of hafnium oxide by atomic layer deposition. *Journal of Vacuum Science & Technology A: Vacuum, Surfaces, and Films* **32**, 01A109 (2014).
29. Baker, L. *et al.* Nucleation and growth of Pt atomic layer deposition on Al₂O₃ substrates using (methylcyclopentadienyl)-trimethyl platinum and O₂ plasma. *Journal of Applied Physics* **109**, 084333 (2011).
30. Elam, J. W., Nelson, C. E., Grubbs, R. K. & George, S. M. Nucleation and growth during tungsten atomic layer deposition on SiO₂ surfaces. *Thin Solid Films* **386**, 41–52 (2001).
31. George, S. M., Elam, J. W., Grubbs, R. K. & Nelson, C. E. Nucleation and growth during tungsten atomic layer deposition on oxide surfaces. in *Materials Research Society Symposium - Proceedings* vol. 672 1–7 (Materials Research Society, 2001).
32. Halls, M. D., Raghavachari, K., Frank, M. M. & Chabal, Y. J. Atomic layer deposition of Al₂O₃ on H-passivated Si: Al(CH₃)₂OH surface reactions with H/Si(100)–2×1. *Physical Review B - Condensed Matter and Materials Physics* **68**, 161302 (2003).
33. Stranski, I. N. & Krastanow, L. Zur Theorie der orientierten Ausscheidung von Ionenkristallen aufeinander. *Monatshefte für Chemie* **71**, 351–364 (1937).

34. Argile, C. & Rhead, G. E. Adsorbed layer and thin film growth modes monitored by Auger electron spectroscopy. *Surface Science Reports* **10**, 277–356 (1989).
35. Manandhar, K., Wollmershauser, J. A. & Feigelson, B. N. Growth mode of alumina atomic layer deposition on nanopowders. *Journal of Vacuum Science & Technology A: Vacuum, Surfaces, and Films* **35**, 041503 (2017).
36. Xie, S., Cai, J., Wang, Q., Wang, L. & Liu, Z. Properties and morphology of TiN films deposited by atomic layer deposition. *Tsinghua Science and Technology* **19**, 144–149 (2014).
37. Puurunen, R. L. & Vandervorst, W. Island growth as a growth mode in atomic layer deposition: A phenomenological model. *Journal of Applied Physics* **96**, 7686–7695 (2004).
38. Fang, C., Cao, Y., Wu, D. & Li, A. Thermal atomic layer etching: Mechanism, materials and prospects. *Progress in Natural Science: Materials International* vol. 28 667–675 (2018).
39. Kanarik, K. J. *et al.* Overview of atomic layer etching in the semiconductor industry. *J. Vac. Sci. Technol. A* **33**, 20802 (2015).
40. Maki, P. A. & Ehrlich, D. J. Laser bilayer etching of GaAs surfaces. *Applied Physics Letters* **55**, 91–93 (1989).
41. T. Carver, C. *et al.* Atomic Layer Etching: An Industry Perspective. *ECS Journal of Solid State Science and Technology* **4**, N5005–N5009 (2015).
42. Kanarik, K. J., Tan, S. & Gottscho, R. A. Atomic Layer Etching: Rethinking the Art of Etch. *J. Phys. Chem. Lett* **9**, 37 (2018).

43. George, S. M. Mechanisms of Thermal Atomic Layer Etching. *Accounts of Chemical Research* **53**, 1151–1160 (2020).
44. Yuan, G., Wang, N., Huang, S. & Liu, J. A brief overview of atomic layer deposition and etching in the semiconductor processing. in *2016 17th International Conference on Electronic Packaging Technology, ICEPT 2016* 1365–1368 (Institute of Electrical and Electronics Engineers Inc., 2016). doi:10.1109/ICEPT.2016.7583377.
45. Agarwal, A. & Kushner, M. J. Plasma atomic layer etching using conventional plasma equipment. *Journal of Vacuum Science & Technology A: Vacuum, Surfaces, and Films* **27**, 37–50 (2009).
46. Lee, Y., Huffman, C. & George, S. M. Selectivity in Thermal Atomic Layer Etching Using Sequential, Self-Limiting Fluorination and Ligand-Exchange Reactions. *Chemistry of Materials* **28**, 7657–7665 (2016).
47. Fischer, A., Routzahn, A., Lee, Y., Lill, T. & George, S. M. Thermal etching of AlF_3 and thermal atomic layer etching of Al_2O_3 . *Journal of Vacuum Science & Technology A* **38**, 022603 (2020).
48. Lee, Y., Dumont, J. W. & George, S. M. Mechanism of thermal Al_2O_3 atomic layer etching using sequential reactions with $\text{Sn}(\text{acac})_2$ and HF. *Chemistry of Materials* **27**, 3648–3657 (2015).
49. Gertsch, J. C., Cano, A. M., Bright, V. M. & George, S. M. SF_4 as the Fluorination Reactant for Al_2O_3 and VO_2 Thermal Atomic Layer Etching. *Chemistry of Materials* (2019) doi:10.1021/acs.chemmater.8b05294.

50. Murdzek, J. A. & George, S. M. Effect of crystallinity on thermal atomic layer etching of hafnium oxide, zirconium oxide, and hafnium zirconium oxide. *Journal of Vacuum Science & Technology A* **38**, 022608 (2020).
51. Lee, Y., DuMont, J. W. & George, S. M. Atomic Layer Etching of HfO₂ Using Sequential, Self-Limiting Thermal Reactions with Sn(acac)₂ and HF. *ECS Journal of Solid State Science and Technology* **4**, N5013–N5022 (2015).
52. Lemaire, P. C. & Parsons, G. N. Thermal Selective Vapor Etching of TiO₂: Chemical Vapor Etching via WF₆ and Self-Limiting Atomic Layer Etching Using WF₆ and BCl₃. *Chemistry of Materials* **29**, 6653–6665 (2017).
53. Lee, Y. & George, S. M. Atomic layer etching of Al₂O₃ using sequential, self-limiting thermal reactions with Sn(acac)₂ and hydrogen fluoride. *ACS Nano* **9**, 2061–2070 (2015).
54. Lee, Y., Dumont, J. W. & George, S. M. Trimethylaluminum as the Metal Precursor for the Atomic Layer Etching of Al₂O₃ Using Sequential, Self-Limiting Thermal Reactions. *Chemistry of Materials* **28**, 2994–3003 (2016).
55. Lee, Y. & George, S. M. Thermal atomic layer etching of titanium nitride using sequential, self-limiting reactions: Oxidation to TiO₂ and fluorination to volatile TiF₄. *Chemistry of Materials* **29**, 8202–8210 (2017).
56. Xie, W., Lemaire, P. C. & Parsons, G. N. Thermally Driven Self-Limiting Atomic Layer Etching of Metallic Tungsten Using WF₆ and O₂. *ACS Applied Materials and Interfaces* **10**, 9147–9154 (2018).

57. Zywojtko, D. R. & George, S. M. Thermal Atomic Layer Etching of ZnO by a “Conversion-Etch” Mechanism Using Sequential Exposures of Hydrogen Fluoride and Trimethylaluminum. *Chemistry of Materials* **29**, 1183–1191 (2017).
58. DuMont, J. W., Marquardt, A. E., Cano, A. M. & George, S. M. Thermal Atomic Layer Etching of SiO₂ by a “Conversion-Etch” Mechanism Using Sequential Reactions of Trimethylaluminum and Hydrogen Fluoride. *ACS Applied Materials and Interfaces* **9**, 10296–10307 (2017).
59. Mackus, A. J. M., Merckx, M. J. M. & Kessels, W. M. M. From the Bottom-Up: Toward Area-Selective Atomic Layer Deposition with High Selectivity. *Chemistry of Materials* **31**, 2–12 (2019).
60. Parsons, G. N. & Clark, R. D. Area-Selective Deposition: Fundamentals, Applications, and Future Outlook. *Chemistry of Materials* vol. 32 4920–4953 (2020).
61. Schmitt, P. *et al.* Influence of Substrate Materials on Nucleation and Properties of Iridium Thin Films Grown by ALD. *Coatings* **11**, (2021).
62. Whiteside, P. J. D., Chininis, J. A. & Hunt, H. K. Techniques and challenges for characterizing metal thin films with applications in photonics. *Coatings* vol. 6 35 (2016).
63. Mackus, A. J. M. Approaches and opportunities for area-selective atomic layer deposition. in *2018 International Symposium on VLSI Technology, Systems and Application, VLSI-TSA 2018* 1–2 (Institute of Electrical and Electronics Engineers Inc., 2018). doi:10.1109/VLSI-TSA.2018.8403864.

64. Lee, H. B. R. & Bent, S. F. Nanopatterning by Area-Selective Atomic Layer Deposition. in *Atomic Layer Deposition of Nanostructured Materials* 193–225 (Wiley-VCH, 2012). doi:10.1002/9783527639915.ch9.
65. Sampson, M. D., Emery, J. D., Pellin, M. J. & Martinson, A. B. F. Inhibiting metal oxide atomic layer deposition: Beyond zinc oxide. *ACS Applied Materials and Interfaces* vol. 9 33429–33436 (2017).
66. Deminskyi, P., Haider, A., Eren, H., Khan, T. M. & Biyikli, N. Area-selective atomic layer deposition of noble metals: Polymerized fluorocarbon layers as effective growth inhibitors. *Journal of Vacuum Science & Technology A* **39**, 022402 (2021).
67. Kulkarni, S. A., Mirji, S. A., Mandale, A. B. & Vijayamohanan, K. P. Thermal stability of self-assembled octadecyltrichlorosilane monolayers on planar and curved silica surfaces. *Thin Solid Films* **496**, 420–425 (2006).
68. Lee, H.-B.-R. *et al.* High Quality Area-Selective Atomic Layer Deposition Co Using Ammonia Gas as a Reactant. *Journal of The Electrochemical Society* **157**, D10 (2010).
69. Prathima, N. *et al.* Thermal study of accumulation of conformational disorders in the self-assembled monolayers of C8 and C18 alkanethiols on the Au(111) surface. *Langmuir* **21**, 2364–2374 (2005).
70. Seo, S. *et al.* Reaction Mechanism of Area-Selective Atomic Layer Deposition for Al₂O₃ Nanopatterns. (2017) doi:10.1021/acsami.7b13365.
71. Henke, T. *et al.* Flash-Enhanced Atomic Layer Deposition: Basics, Opportunities, Review, and Principal Studies on the Flash-Enhanced Growth of Thin Films. *ECS Journal of Solid State Science and Technology* **4**, P277–P287 (2015).

72. Chalker, P. R. *et al.* Vacuum ultraviolet photochemical selective area atomic layer deposition of Al₂O₃ dielectrics. *AIP Advances* **5**, 17115 (2015).
73. Mameli, A. *et al.* Area-Selective Atomic Layer Deposition of ZnO by Area Activation Using Electron Beam-Induced Deposition. *Chemistry of Materials* **31**, 1250–1257 (2019).
74. Mackus, A. J. M., Dielissen, S. A. F., Mulders, J. J. L. & Kessels, W. M. M. Nanopatterning by direct-write atomic layer deposition. *Nanoscale* **4**, 4477–4480 (2012).
75. Longo, R. C. *et al.* Selectivity of metal oxide atomic layer deposition on hydrogen terminated and oxidized Si(001)-(2×1) surface. *Journal of Vacuum Science & Technology B, Nanotechnology and Microelectronics: Materials, Processing, Measurement, and Phenomena* **32**, 03D112 (2014).
76. Halls, M. D. & Raghavachari, K. Atomic Layer Deposition Growth Reactions of Al₂O₃ on Si(100)-2×1. *Journal of Physical Chemistry B* **108**, 4058–4062 (2004).
77. Vandalon, V. & Erwin Kessels, W. M. M. Initial Growth Study of Atomic-Layer Deposition of Al₂O₃ by Vibrational Sum-Frequency Generation. *Langmuir* **35**, 10374–10382 (2019).
78. Lemaire, P. C., King, M. & Parsons, G. N. Understanding inherent substrate selectivity during atomic layer deposition: Effect of surface preparation, hydroxyl density, and metal oxide composition on nucleation mechanisms during tungsten ALD. *Journal of Chemical Physics* **146**, 052811 (2017).

79. Kalanyan, B., Lemaire, P. C., Atanasov, S. E., Ritz, M. J. & Parsons, G. N. Using Hydrogen to Expand the Inherent Substrate Selectivity Window during Tungsten Atomic Layer Deposition. *Chemistry of Materials* **28**, 117–126 (2016).
80. Song, S. K., Saare, H. & Parsons, G. N. Integrated Isothermal Atomic Layer Deposition/Atomic Layer Etching Supercycles for Area-Selective Deposition of TiO₂. *Chemistry of Materials* **31**, (2019).
81. Vallat, R., Gassilloud, R., Eychenne, B. & Vallée, C. Selective deposition of Ta₂O₅ by adding plasma etching super-cycles in plasma enhanced atomic layer deposition steps. *Journal of Vacuum Science & Technology A: Vacuum, Surfaces, and Films* **35**, 01B104 (2017).
82. Vos, M. F. J. *et al.* Area-Selective Deposition of Ruthenium by Combining Atomic Layer Deposition and Selective Etching. *Chemistry of Materials* **31**, 3878–3882 (2019).
83. Saare, H., Song, S. K., Kim, J.-S. & Parsons, G. N. Effect of reactant dosing on selectivity during area-selective deposition of TiO₂ via integrated atomic layer deposition and atomic layer etching. *Journal of Applied Physics* **128**, (2020).
84. Cheng, H. Y., Carta, F., Chien, W. C., Lung, H. L. & Brightsky, M. J. 3D cross-point phase-change memory for storage-class memory. *Journal of Physics D: Applied Physics* vol. 52 473002 (2019).
85. Burr, G. W. *et al.* Phase change memory technology. *Journal of Vacuum Science & Technology B, Nanotechnology and Microelectronics: Materials, Processing, Measurement, and Phenomena* **28**, 223–262 (2010).

86. Ovshinsky, S. R. Reversible electrical switching phenomena in disordered structures. *Physical Review Letters* **21**, 1450–1453 (1968).
87. Wuttig, M. & Yamada, N. Phase-change materials for rewriteable data storage. *Nature Materials* **6**, 824–832 (2007).
88. Intel® Optane™ Persistent Memory 200 Series Brief. <https://www.intel.com/content/www/us/en/products/docs/memory-storage/optane-persistent-memory/optane-persistent-memory-200-series-brief.html>.
89. le Gallo, M. & Sebastian, A. An overview of phase-change memory device physics. *Journal of Physics D: Applied Physics* vol. 53 213002 (2020).
90. Shen, M. *et al.* Review on recent progress in patterning phase change materials. *Journal of Vacuum Science & Technology A* **38**, 060802 (2020).
91. Wong, H. S. P. *et al.* Phase change memory. in *Proceedings of the IEEE* vol. 98 2201–2227 (Institute of Electrical and Electronics Engineers Inc., 2010).
92. Bogoslovskiy, N. A. & Tsendin, K. D. Physics of switching and memory effects in chalcogenide glassy semiconductors. *Semiconductors* vol. 46 559–590 (2012).
93. Adler, D., Shur, M. S., Silver, M. & Ovshinsky, S. R. Threshold switching in chalcogenide-glass thin films. *Journal of Applied Physics* **51**, 3289–3309 (1980).
94. Ielmini, D. & Zhang, Y. Analytical model for subthreshold conduction and threshold switching in chalcogenide-based memory devices. *Journal of Applied Physics* **102**, 054517 (2007).
95. Guerin, S., Hayden, B., Hewak, D. W. & Vian, C. Synthesis and Screening of Phase Change Chalcogenide Thin Film Materials for Data Storage. *ACS Combinatorial Science* **19**, 478–491 (2017).

96. Zhang, W., Mazzarello, R., Wuttig, M. & Ma, E. Designing crystallization in phase-change materials for universal memory and neuro-inspired computing. *Nature Reviews Materials* vol. 4 150–168 (2019).
97. Fang, L. W. W. *et al.* Dependence of the properties of phase change random access memory on nitrogen doping concentration in $\text{Ge}_2\text{Sb}_2\text{Te}_5$. *Journal of Applied Physics* **107**, 104506 (2010).
98. Wang, K., Wamwangi, D., Ziegler, S., Steimer, C. & Wuttig, M. Influence of Bi doping upon the phase change characteristics of $\text{Ge}_2\text{Sb}_2\text{Te}_5$. *Journal of Applied Physics* **96**, 5557–5562 (2004).
99. Jeong, T. H., Kim, M. R., Seo, H., Park, J. W. & Yeon, C. Crystal structure and microstructure of nitrogen-doped $\text{Ge}_2\text{Sb}_2\text{Te}_5$ thin film. *Japanese Journal of Applied Physics, Part 1: Regular Papers and Short Notes and Review Papers* **39**, 2775–2779 (2000).
100. Privitera, S., Rimini, E. & Zonca, R. Amorphous-to-crystal transition of nitrogen- and oxygen-doped $\text{Ge}_2\text{Sb}_2\text{Te}_5$ films studied by in situ resistance measurements. *Applied Physics Letters* **85**, 3044–3046 (2004).
101. Zhou, X. *et al.* Understanding phase-change behaviors of carbon-doped $\text{Ge}_2\text{Sb}_2\text{Te}_5$ for phase-change memory application. *ACS Applied Materials and Interfaces* **6**, 14207–14214 (2014).
102. Navarro, G. *et al.* N-Doping Impact in Optimized Ge-Rich Materials Based Phase-Change Memory. in *2016 IEEE 8th International Memory Workshop, IMW 2016* (Institute of Electrical and Electronics Engineers Inc., 2016). doi:10.1109/IMW.2016.7495284.

103. Kim, K. H., Chung, J. G., Kyoung, Y. K., Park, J. C. & Choi, S. J. Phase-change characteristics of nitrogen-doped Ge₂Sb₂Te₅ films during annealing process. *Journal of Materials Science: Materials in Electronics* **22**, 52–55 (2011).
104. Burr, G. W. *et al.* Recent Progress in Phase-Change Memory Technology. *IEEE Journal on Emerging and Selected Topics in Circuits and Systems* **6**, 146–162 (2016).
105. Ahn, S. J. *et al.* Reliability perspectives for high density PRAM manufacturing. in *Technical Digest - International Electron Devices Meeting, IEDM* (2011). doi:10.1109/IEDM.2011.6131542.
106. Yoon, K. J., Kim, Y. & Hwang, C. S. What Will Come After V-NAND—Vertical Resistive Switching Memory? *Advanced Electronic Materials* vol. 5 1800914 (2019).
107. Qin, S. *et al.* Next-Generation Ultrahigh-Density 3-D Vertical Resistive Switching Memory (VRSM)-Part I: Accurate and Computationally Efficient Modeling. *IEEE Transactions on Electron Devices* **66**, 5139–5146 (2019).
108. Jiang, Z. *et al.* Next-Generation Ultrahigh-Density 3-D Vertical Resistive Switching Memory (VRSM)-Part II: Design Guidelines for Device, Array, and Architecture. *IEEE Transactions on Electron Devices* **66**, 5147–5154 (2019).
109. Lee, Y. K., Yoo, C., Kim, W., Jeon, J. W. & Hwang, C. S. Atomic layer deposition of chalcogenides for next-generation phase change memory. *Journal of Materials Chemistry C* vol. 9 3708–3725 (2021).
110. Tompkins, H. & Irene, E. A. *Handbook of Ellipsometry*. (William Andrew, 2005).
111. Hinrichs, K. & Eichhorn, K.-J. *Ellipsometry of Functional Organic Surfaces and Films*. vol. 52 (Springer International Publishing, 2018).
112. Fujiwara, H. *Spectroscopic Ellipsometry: Principles and Applications*. (Wiley, 2007).

113. Press, W. H., Flannery, B. P., Teukolsky, S. A. & Vetterling, W. T. *Numerical Recipes in C: The Art of Scientific Computing*. (Cambridge university press, 1992).
114. Jellison, G. E. & Modine, F. A. Parameterization of the optical functions of amorphous materials in the interband region. *Applied Physics Letters* **69**, 371–373 (1996).
115. Jellison, G. E. & Modine, F. A. Erratum: Parameterization of the optical functions of amorphous materials in the interband region. *Applied Physics Letters* vol. 69 2137 (1996).
116. Likhachev, D. v., Malkova, N. & Poslavsky, L. Modified Tauc-Lorentz dispersion model leading to a more accurate representation of absorption features below the bandgap. *Thin Solid Films* **589**, 844–851 (2015).
117. Rodríguez-de Marcos, L. v. & Larruquert, J. I. Analytic optical-constant model derived from Tauc-Lorentz and Urbach tail. *Optics Express* **24**, 28561 (2016).
118. Franta, D., Čermák, M., Vohánka, J. & Ohlídal, I. Dispersion models describing interband electronic transitions combining Tauc's law and Lorentz model. *Thin Solid Films* **631**, 12–22 (2017).
119. Briggs, D. & Seah, M. P. *Practical surface analysis by Auger and X-ray photoelectron spectroscopy. Surface and Interface Analysis* (John Wiley and Sons Ltd, 1984). doi:10.1002/sia.740060611.
120. Watts, J. F. & Wolstenholme, J. *An Introduction to Surface Analysis by XPS and AES. An Introduction to Surface Analysis by XPS and AES* (John Wiley & Sons, Ltd, 2003). doi:10.1002/0470867930.
121. Hofmann, S. *Auger- and X-Ray Photoelectron Spectroscopy in Materials Science*. (Springer, 2013). doi:10.1007/978-3-642-27381-0.

122. Gong, B., Peng, Q. & Parsons, G. N. Conformal Organic-inorganic hybrid network polymer thin films by molecular layer deposition using trimethylaluminum and glycidol. *Journal of Physical Chemistry B* **115**, 5930–5938 (2011).
123. Biyikli, N., Haider, A., Deminskyi, P. & Yilmaz, M. Self-aligned nanoscale processing solutions via selective atomic layer deposition of oxide, nitride, and metallic films. in *Low-Dimensional Materials and Devices 2017* (eds. Kobayashi, N. P., Talin, A. A., Davydov, A. V. & Islam, M. S.) vol. 10349 20 (SPIE, 2017).
124. Mackus, A. J. M., Bol, A. A. & Kessels, W. M. M. The use of atomic layer deposition in advanced nanopatterning. *Nanoscale* **6**, 10941–10960 (2014).
125. Vallat, R., Gassilloud, R., Eychenne, B. & Vallée, C. Selective deposition of Ta₂O₅ by adding plasma etching super-cycles in plasma enhanced atomic layer deposition steps. *Citation: Journal of Vacuum Science & Technology A* **35**, 1–104 (2017).
126. Minaye Hashemi, F. S., Birchansky, B. R. & Bent, S. F. Selective Deposition of Dielectrics: Limits and Advantages of Alkanethiol Blocking Agents on Metal-Dielectric Patterns. *ACS Applied Materials and Interfaces* **8**, 33264–33272 (2016).
127. Seo, E. K., Lee, J. W., Sung-Suh, H. M. & Sung, M. M. Atomic layer deposition of titanium oxide on self-assembled-monolayer-coated gold. *Chemistry of Materials* **16**, 1878–1883 (2004).
128. Avila, J. R. *et al.* Real-time observation of atomic layer deposition inhibition: Metal oxide growth on self-assembled alkanethiols. *ACS Applied Materials and Interfaces* **6**, 11891–11898 (2014).

129. Chen, R., Kim, H., McIntyre, P. C. & Bent, S. F. Investigation of self-assembled monolayer resists for hafnium dioxide atomic layer deposition. *Chemistry of Materials* **17**, 536–544 (2005).
130. Kanarik, K. J. *et al.* Overview of atomic layer etching in the semiconductor industry. *Journal of Vacuum Science & Technology A: Vacuum, Surfaces, and Films* **33**, 020802 (2015).
131. Puurunen, R. L. Analysis of hydroxyl group controlled atomic layer deposition of hafnium dioxide from hafnium tetrachloride and water. *Journal of Applied Physics* **95**, 4777–4786 (2004).
132. Alam, M. A. & Green, M. L. Mathematical description of atomic layer deposition and its application to the nucleation and growth of HfO₂ gate dielectric layers. *Journal of Applied Physics* **94**, 3403–3413 (2003).
133. Puurunen, R. L. Growth Per Cycle in Atomic Layer Deposition: A Theoretical Model. *Chemical Vapor Deposition* **9**, 249–257 (2003).
134. Ylilammi, M. Monolayer thickness in atomic layer deposition. *Thin Solid Films* **279**, 124–130 (1996).
135. Green, M. L. *et al.* Nucleation and growth of atomic layer deposited HfO₂ gate dielectric layers on chemical oxide (Si–O–H) and thermal oxide (SiO₂ or Si–O–N) underlayers. *Journal of Applied Physics* **92**, 7168–7174 (2002).
136. Green, M. L. *et al.* Nucleation of atomic-layer-deposited HfO₂ films, and evolution of their microstructure, studied by grazing incidence small angle x-ray scattering using synchrotron radiation. *Applied Physics Letters* **88**, 32907 (2006).

137. Gusev, E. P., Cabral, C., Copel, M., D'Emic, C. & Gribelyuk, M. Ultrathin HfO₂ films grown on silicon by atomic layer deposition for advanced gate dielectrics applications. *Microelectronic Engineering* **69**, 145–151 (2003).
138. Damlencourt, J.-F. *et al.* Electrical and physico-chemical characterization of HfO₂/SiO₂ gate oxide stacks prepared by atomic layer deposition. *Solid-State Electronics* **47**, 1613–1616 (2003).
139. Hackley, J. C., Gougousi, T. & Demaree, J. D. Nucleation of HfO₂ atomic layer deposition films on chemical oxide and H-terminated Si. *Journal of Applied Physics* **102**, 34101 (2007).
140. Cho, M. *et al.* Chemical interaction between atomic-layer-deposited HfO₂ thin films and the Si substrate. *Applied Physics Letters* **81**, 334–336 (2002).
141. Gusev, E. P. *et al.* Ultrathin high-K metal oxides on silicon: processing, characterization and integration issues. *Microelectronic Engineering* **59**, 341–349 (2001).
142. Kirsch, P. D. *et al.* Nucleation and growth study of atomic layer deposited HfO₂ gate dielectrics resulting in improved scaling and electron mobility. *Journal of Applied Physics* **99**, 23508 (2006).
143. Aarik, J. *et al.* Effects of precursors on nucleation in atomic layer deposition of HfO₂. *Applied Surface Science* **230**, 292–300 (2004).
144. Copel, M., Gribelyuk, M. & Gusev, E. Structure and stability of ultrathin zirconium oxide layers on Si(001). *Applied Physics Letters* **76**, 436–438 (2000).

145. Ferrari, S., Modreanu, M., Scarel, G. & Fanciulli, M. X-Ray reflectivity and spectroscopic ellipsometry as metrology tools for the characterization of interfacial layers in high- κ materials. *Thin Solid Films* **450**, 124–127 (2004).
146. Puurunen, R. L. *et al.* Island growth in the atomic layer deposition of zirconium oxide and aluminum oxide on hydrogen-terminated silicon: Growth mode modeling and transmission electron microscopy. *Journal of Applied Physics* **96**, 4878–4889 (2004).
147. Kukli, K., Ritala, M., Aarik, J., Uustare, T. & Leskelä, M. Influence of growth temperature on properties of zirconium dioxide films grown by atomic layer deposition. *Journal of Applied Physics* **92**, 1833–1840 (2002).
148. Methapanon, R. & Bent, S. F. Comparative Study of Titanium Dioxide Atomic Layer Deposition on Silicon Dioxide and Hydrogen-Terminated Silicon. *The Journal of Physical Chemistry C* **114**, 10498–10504 (2010).
149. Mitchell, D. R. G., Attard, D. J. & Triani, G. Transmission electron microscopy studies of atomic layer deposition TiO₂ films grown on silicon. *Thin Solid Films* **441**, 85–95 (2003).
150. Song, S. K., Saare, H. & Parsons, G. N. Integrated Isothermal Atomic Layer Deposition/Atomic Layer Etching Supercycles for Area-Selective Deposition of TiO₂. *Chemistry of Materials* **31**, 4793–4804 (2019).
151. Kanarik, K. J., Tan, S. & Gottscho, R. A. Atomic Layer Etching: Rethinking the Art of Etch. *J. Phys. Chem. Lett* **9**, 4821 (2018).
152. George, S. M. & Lee, Y. Prospects for Thermal Atomic Layer Etching Using Sequential, Self-Limiting Fluorination and Ligand-Exchange Reactions. *ACS Nano* **10**, 4889–4894 (2016).

153. Fang, C., Cao, Y., Wu, D. & Li, A. Thermal atomic layer etching: Mechanism, materials and prospects. *Progress in Natural Science: Materials International* **28**, 667–675 (2018).
154. Langereis, E. *et al.* In situ spectroscopic ellipsometry as a versatile tool for studying atomic layer deposition. *Journal of Physics D: Applied Physics* **42**, 073001 (2009).
155. Kief, M. T. In-situ ellipsometry: applications to thin film research, development, and production. in vol. 10294 1029403 (International Society for Optics and Photonics, 1999).
156. Junige, M., Geidel, M., Knaut, M., Albert, M. & Bartha, J. W. Monitoring atomic layer deposition processes in situ and in real-time by spectroscopic ellipsometry. in *2011 Semiconductor Conference Dresden* 1–4 (IEEE, 2011). doi:10.1109/SCD.2011.6068739.
157. Mackus, A. J. M., Verheijen, M. A., Leick, N., Bol, A. A. & Kessels, W. M. M. Influence of Oxygen Exposure on the Nucleation of Platinum Atomic Layer Deposition: Consequences for Film Growth, Nanopatterning, and Nanoparticle Synthesis. *Chemistry of Materials* **25**, 1905–1911 (2013).
158. Muneshwar, T. & Cadien, K. Probing initial-stages of ALD growth with dynamic in situ spectroscopic ellipsometry. *Applied Surface Science* **328**, 344–348 (2015).
159. Wind, R. W., Fabreguette, F. H., Sechrist, Z. A. & George, S. M. Nucleation period, surface roughness, and oscillations in mass gain per cycle during W atomic layer deposition on Al₂O₃. *Journal of Applied Physics* **105**, 074309 (2009).
160. Lecordier, L., Herregods, S. & Armini, S. Vapor-deposited octadecanethiol masking layer on copper to enable area selective Hf₃N₄ atomic layer deposition on dielectrics

- studied by in situ spectroscopic ellipsometry. *Journal of Vacuum Science & Technology A* **36**, 031605 (2018).
161. Baker, L. *et al.* Nucleation and growth of Pt atomic layer deposition on Al₂O₃ substrates using (methylcyclopentadienyl)-trimethyl platinum and O₂ plasma. *Journal of Applied Physics* **109**, 084333 (2011).
162. Langereis, E., Heil, S. B. S., Van De Sanden, M. C. M. & Kessels, W. M. M. In situ spectroscopic ellipsometry study on the growth of ultrathin TiN films by plasma-assisted atomic layer deposition. *Journal of Applied Physics* **100**, 023534 (2006).
163. Patsalas, P. & Logothetidis, S. Interface properties and structural evolution of TiN/Si and TiN/GaN heterostructures. *Journal of Applied Physics* **93**, 989–998 (2003).
164. Jiang, X., Wang, H., Qi, J. & Willis, B. G. In-situ spectroscopic ellipsometry study of copper selective-area atomic layer deposition on palladium. *Journal of Vacuum Science & Technology A* **32**, 41513 (2014).
165. Junige, M. *et al.* Area-selective atomic layer deposition of Ru on electron-beam-written Pt(C) patterns versus SiO₂ substratum. *Nanotechnology* **28**, 395301 (2017).
166. Raza, M. A., Zandvliet, H. J. W., Poelsema, B. & Kooij, E. S. Selective metallization by seeded growth on patterned gold nanoparticle arrays. *Journal of Applied Physics* **113**, 233510 (2013).
167. Pesce, V. *et al.* Optimization by in situ ellipsometry of ALD and ALE successive steps for the selective Atomic Layer Deposition of Ta₂O₅ on TiN and Si. *AVS 65th International Symposium* (2018).

168. Mameli, A. *et al.* Area-Selective Atomic Layer Deposition of SiO₂ Using Acetylacetone as a Chemoselective Inhibitor in an ABC-Type Cycle. *ACS Nano* **11**, 9303–9311 (2017).
169. Mameli, A. *et al.* Area-Selective Atomic Layer Deposition of ZnO by Area Activation Using Electron Beam-Induced Deposition. *Chemistry of Materials* **31**, 1250–1257 (2019).
170. Niang, K. M., Bai, G. & Robertson, J. Influence of precursor dose and residence time on the growth rate and uniformity of vanadium dioxide thin films by atomic layer deposition. *Journal of Vacuum Science & Technology A* **38**, 42401 (2020).
171. Baji, Z. *et al.* Nucleation and Growth Modes of ALD ZnO. *Crystal Growth & Design* **12**, 5615–5620 (2012).
172. Kuse, R., Kundu, M., Yasuda, T., Miyata, N. & Toriumi, A. Effect of precursor concentration in atomic layer deposition of Al₂O₃. *Journal of Applied Physics* **94**, 6411–6416 (2003).
173. Murray, C. A., Elliott, S. D., Hausmann, D., Henri, J. & LaVoie, A. Effect of Reaction Mechanism on Precursor Exposure Time in Atomic Layer Deposition of Silicon Oxide and Silicon Nitride. *ACS Applied Materials & Interfaces* **6**, 10534–10541 (2014).
174. Kukli, K. *et al.* Effect of selected atomic layer deposition parameters on the structure and dielectric properties of hafnium oxide films. *Journal of Applied Physics* **96**, 5298–5307 (2004).
175. Gordon, R. G., Hausmann, D., Kim, E. & Shepard, J. A Kinetic Model for Step Coverage by Atomic Layer Deposition in Narrow Holes or Trenches. *Chemical Vapor Deposition* **9**, 73–78 (2003).

176. Lemaire, P. C. & Parsons, G. N. Thermal Selective Vapor Etching of TiO₂: Chemical Vapor Etching via WF₆ and Self-Limiting Atomic Layer Etching Using WF₆ and BCl₃. *Chemistry of Materials* **29**, 6653–6665 (2017).
177. Garcia-Caurel, E., De Martino, A., Gaston, J. P. & Yan, L. Application of spectroscopic ellipsometry and mueller ellipsometry to optical characterization. *Applied Spectroscopy* vol. 67 1–21 (2013).
178. Parsons, G. N. Functional model for analysis of ALD nucleation and quantification of area-selective deposition. *Journal of Vacuum Science & Technology A* **37**, 020911 (2019).
179. Gladfelter, W. L. Selective Metallization by Chemical Vapor Deposition. *Chemistry of Materials* **5**, 1372–1388 (1993).
180. Parsons, G. N. & Clark, R. D. Area-Selective Deposition: Fundamentals, Applications, and Future Outlook. *Chemistry of Materials* vol. 32 4920–4953 (2020).
181. Shard, A. G. Detection limits in XPS for more than 6000 binary systems using Al and Mg K α X-rays. *Surface and Interface Analysis* **46**, 175–185 (2014).
182. Wong, H. S. P. & Salahuddin, S. Memory leads the way to better computing. *Nature Nanotechnology* vol. 10 191–194 (2015).
183. Burr, G. W. *et al.* Large-scale neural networks implemented with non-volatile memory as the synaptic weight element: Comparative performance analysis (accuracy, speed, and power). in *Technical Digest - International Electron Devices Meeting, IEDM* vols. 2016-February 4.4.1-4.4.4 (Institute of Electrical and Electronics Engineers Inc., 2015).

184. Jeong, D. S. & Hwang, C. S. Nonvolatile Memory Materials for Neuromorphic Intelligent Machines. *Advanced Materials* vol. 30 (2018).
185. Burr, G. W. *et al.* Access devices for 3D crosspoint memory. *Journal of Vacuum Science & Technology B, Nanotechnology and Microelectronics: Materials, Processing, Measurement, and Phenomena* **32**, 040802 (2014).
186. Wuttig, M., Bhaskaran, H. & Taubner, T. Phase-change materials for non-volatile photonic applications. *Nature Photonics* vol. 11 465–476 (2017).
187. Burr, G. W. *et al.* Phase change memory technology. *J. Vac. Sci. Technol. B* **28**, 223 (2010).
188. Fong, S. W., Neumann, C. M. & Wong, H. S. P. Phase-Change Memory - Towards a Storage-Class Memory. *IEEE Transactions on Electron Devices* **64**, 4374–4385 (2017).
189. Pirovano, A. *et al.* Reliability study of phase-change nonvolatile memories. *IEEE Transactions on Device and Materials Reliability* **4**, 422–426 (2004).
190. Perniola, L. *et al.* Electrical behavior of phase-change memory cells based on GeTe. *IEEE Electron Device Letters* **31**, 488–490 (2010).
191. Manivannan, A., Myana, S. K., Miriyala, K., Sahu, S. & Ramadurai, R. Low power ovonic threshold switching characteristics of thin GeTe₆ films using conductive atomic force microscopy. *Applied Physics Letters* **105**, 243501 (2014).
192. Sousa, V. & Navarro, G. Material engineering for PCM device optimization. in *Phase Change Memory: Device Physics, Reliability and Applications* 181–222 (Springer International Publishing, 2017). doi:10.1007/978-3-319-69053-7_7.

193. Guo, P., Sevison, G., Agha, I., Sarangan, A. & Burrow, J. Electrical and optical properties of nickel-doped $\text{Ge}_2\text{Sb}_2\text{Te}_5$ films produced by magnetron co-sputtering. in *Nanoengineering: Fabrication, Properties, Optics, and Devices XV* (eds. Sakdinawat, A. E., Attias, A.-J., Panchapakesan, B. & Dobisz, E. A.) vol. 10730 19 (SPIE, 2018).
194. Laudato, M. *et al.* ALD GeAsSeTe Ovonic Threshold Switch for 3D Stackable Crosspoint Memory. in *2020 IEEE International Memory Workshop, IMW 2020 - Proceedings* (Institute of Electrical and Electronics Engineers Inc., 2020). doi:10.1109/IMW48823.2020.9108152.
195. Narasimhan, V. *et al.* Physical and Electrical Characterization of ALD Chalcogenide Materials for 3D Memory Applications. (2019).
196. Lai, Y. F. *et al.* Stacked chalcogenide layers used as multi-state storage medium for phase change memory. *Applied Physics A: Materials Science and Processing* **84**, 21–25 (2006).
197. Rao, F. *et al.* Multilevel data storage characteristics of phase change memory cell with doublelayer chalcogenide films ($\text{Ge}_2\text{Sb}_2\text{Te}_5$ and Sb_2Te_3). *Japanese Journal of Applied Physics, Part 2: Letters* **46**, L25 (2007).
198. Liu, B. *et al.* Nitrogen-implanted $\text{Ge}_2\text{Sb}_2\text{Te}_5$ film used as multilevel storage media for phase change random access memory. *Semiconductor Science and Technology* **19**, L61 (2004).
199. Lyeo, H. K. *et al.* Thermal conductivity of phase-change material $\text{Ge}_2\text{Sb}_2\text{Te}_5$. *Applied Physics Letters* **89**, 151904 (2006).

200. Adinolfi, V. *et al.* Composition-Controlled Atomic Layer Deposition of Phase-Change Memories and Ovonic Threshold Switches with High Performance. *ACS Nano* **13**, 10440–10447 (2019).
201. Gwon, T. *et al.* Atomic Layer Deposition of GeTe and Ge-Sb-Te Films Using HGeCl₃, Sb(OC₂H₅)₃, and {(CH₃)₃Si}₂Te and Their Reaction Mechanisms. *Chemistry of Materials* **29**, 8065–8072 (2017).
202. Song, S. *et al.* Phase-change properties of GeSbTe thin films deposited by plasma-enhanced atomic layer deposition. *Nanoscale Research Letters* **10**, (2015).
203. Matsunaga, T. *et al.* Structural characteristics of GeTe-rich GeTe-Sb₂Te₃ pseudobinary metastable crystals. *Journal of Applied Physics* **103**, 093511 (2008).
204. Matsunaga, T. & Yamada, N. Structural investigation of GeSb₂Te₄: a high-speed phase-change material. *Physical Review B - Condensed Matter and Materials Physics* **69**, 104111 (2004).
205. Lazarenko, P. I. *et al.* Investigation of transport mechanisms in Bi doped Ge₂Sb₂Te₅ thin films for phase change memory application. in *International Conference on Micro- and Nano-Electronics 2014* (ed. Orlikovsky, A. A.) vol. 9440 944006 (SPIE, 2014).
206. Bai, N. *et al.* Effect of the Sn dopant on the crystallization of amorphous Ge₂Sb₂Te₅ films induced by an excimer laser. *Optics and Laser Technology* **74**, 11–15 (2015).
207. Privitera, S., Rimini, E. & Zonca, R. Amorphous-to-crystal transition of nitrogen- and oxygen-doped Ge₂Sb₂Te₅ films studied by in situ resistance measurements. *Applied Physics Letters* **85**, 3044–3046 (2004).

208. Ryu, S. W. *et al.* Phase transformation behaviors of SiO₂ doped Ge₂Sb₂Te₅ films for application in phase change random access memory. *Applied Physics Letters* **92**, 142110 (2008).
209. Li, T. *et al.* Carbon doping induced Ge local structure change in as-deposited Ge₂Sb₂Te₅ film by EXAFS and Raman spectrum. *AIP Advances* **8**, 025201 (2018).
210. Raoux, S. *et al.* Direct observation of amorphous to crystalline phase transitions in nanoparticle arrays of phase change materials. *Journal of Applied Physics* **102**, 094305 (2007).
211. Navarro, G. *et al.* Innovative PCM+OTS device with high sub-threshold non-linearity for non-switching reading operations and higher endurance performance. in *Digest of Technical Papers - Symposium on VLSI Technology* T94–T95 (Institute of Electrical and Electronics Engineers Inc., 2017). doi:10.23919/VLSIT.2017.7998208.
212. Feng, J. *et al.* Si doping in Ge₂Sb₂Te₅ film to reduce the writing current of phase change memory. *Applied Physics A: Materials Science and Processing* **87**, 57–62 (2007).
213. Wei, S. J. *et al.* Phase change behavior in titanium-doped Ge₂Sb₂Te₅ films. *Applied Physics Letters* **98**, 231910 (2011).
214. Jellison, G. E. & Modine, F. A. Parameterization of the optical functions of amorphous materials in the interband region. *Applied Physics Letters* **69**, 371–373 (1996).
215. Nilsen, O., Mohn, C. E., Kjekshus, A. & Fjellvåg, H. Analytical model for island growth in atomic layer deposition using geometrical principles. *Journal of Applied Physics* **102**, 024906 (2007).

CHAPTER 3

Comparative *In-situ* Study of the Initial Growth Trends of Atomic Layer Deposited Al₂O₃ Films

Holger Saare, Golnaz Dianat and Gregory N. Parsons

3.1 Preface

Aluminum oxide thin films are utilized in numerous applications, such as gate oxides, heat sinks, barrier materials, and more. Atomic layer deposition (ALD) of Al₂O₃ using trimethylaluminum (TMA) as the Al precursor is one of the most extensively studied ALD processes, owing to its high vapor pressure, high reactivity, and self-terminating reactions. However, for area-selective deposition (ASD) applications, such as next-generation nanopatterning, this reactivity leads to poor selectivity as TMA rapidly reacts with most surfaces. Thus, alternative precursors for the selective deposition of Al₂O₃, which result in higher selectivity between different surfaces while maintaining film quality, need to be considered. In this work we compare initial growth trends of Al₂O₃ ALD on hydrogen-terminated Si (Si-H) vs hydroxyl-terminated Si (Si-OH) surfaces using three different Al precursors and H₂O as the oxygen source. Triethylaluminum (TEA), dimethylaluminum chloride (DMAC), and TMA are chosen as the Al precursors due to comparable variations between their structures. This enables the determination of effects that alkyl ligand length and the presence of chloride groups have on the growth. The growth trends are studied in the temperature range of 150-250 °C and characterized using *in-situ* ellipsometry, *in-situ* Auger electron spectroscopy (AES), and *in-situ* Fourier transform infrared spectroscopy (FTIR). Measured thickness evolution exhibits similar behavior for all three precursors with initially accelerated growth during the first cycle on the Si-OH starting surface due to higher precursor uptake which then proceeds in a steady manner characteristic to ALD. The

lower uptake in subsequent cycles is shown to be due to unsuccessful removal of the methyl or ethyl ligands on the surface. While at 200°C both TEA and TMA reacts with 98% of -OH ligands present on the initial Si-OH substrate, the subsequent H₂O dose reacts with 50% of the C-H groups. The resulting growth rates are 0.13, 0.11, and 0.10 nm/cycle for TMA, TEA, and DMAC, respectively. Meanwhile, the growth on the Si-H surface exhibited a delay due to the lack of hydroxyl groups, leading to formation of Si-Me or Si-Et groups. While TMA results in the highest growth rates, it leads to the lowest selectivity, while the highest selectivity is achieved using TEA due to low rate of nucleation non the Si-H. While the effect of precursor design in ASD using masking layers have been previously studied, this is the first study comparing Al precursors for ASD utilizing inherent substrate selectivity. These results provide vital insight into the importance of precursor selection for area-selective ALD applications and open the pathway to realizing selective Al₂O₃ deposition based on inherent substrate selectivity.

3.2 Introduction

Atomic Layer Deposition (ALD) is a vapor-phase deposition technique that has been an enabling technology for a wide array of nanoelectronic applications. The self-limiting nature of ALD enables precise control over thin film thickness and composition, while achieving conformal coatings even on high-aspect-ratio structures at relatively low temperatures.¹⁻⁴ Whether the deposition occurs uniformly on a substrate is largely determined by the chemistry of the precursor,⁵⁻⁷ the termination of the surface,^{8,9} and the interactions present between the two at set processing conditions.¹⁰⁻¹² When the reaction is energetically unfavorable the material can still deposit as nuclei on surface defects, either present initially or generated during the process.^{13,14} During an ALD process, this effect is called “incubation” or “nucleation” period and leads to island growth until the nuclei coalesce and uniform layer-by-layer growth is achieved.^{15,16} For example,

it has been demonstrated that various metal oxides, such as Al_2O_3 ,¹⁷ TiO_2 ,^{8,17-19} and HfO_2 ,^{5,7,17,20-23} lead to uniform deposition on silicon dioxide and island growth on hydrogen-terminated silicon surfaces. In contrast, many metal ALD processes, such as Ru ,²⁴ W ,^{25,26} and Co ,²⁷ grow uniformly on the hydrogen-terminated silicon but display a nucleation period on silicon dioxides surfaces.

To date, Al_2O_3 is one of the most extensively researched thin films deposited by ALD, owing to its high permittivity, chemical and thermal stability, good adhesion, and chemical compatibility with semiconductor processes.²⁸⁻³¹ This has led to Al_2O_3 thin films being utilized in various applications, such as barrier materials, optical coatings, high- κ dielectric for gate oxides, and more.³²⁻³⁸ ALD of Al_2O_3 was developed in 1970s by Suntola and Antson for electroluminescent flat panel displays and was performed using AlCl_3 and H_2O as precursors.³⁹ Over the years various other Al_2O_3 precursors have been developed, with trimethylaluminum (TMA) being the best-known example, owing to its high reactivity, self-terminating reactions, and high-quality films even at low deposition temperatures.^{29,40} Cost-minimization and pyrophoric nature of TMA has led researchers to investigate substitute Al_2O_3 precursors, including AlMe_2Cl ,⁴¹⁻⁴⁵ $\text{Al}(\text{NEt}_2)_3$,⁴⁶⁻⁵¹ $\text{Al}(\text{NMe}_2)_3$,⁵² $\text{Al}(\text{OEt}_3)$,⁵³ $\text{Al}(\text{O}^n\text{Pr})_3$,^{53,54} $\text{AlMe}_2\text{O}^i\text{Pr}$,⁵⁵⁻⁵⁸ and many more.^{48,59-65}

While the steady-state growth of Al_2O_3 thin films is well studied, there is limited research on the initial growth phase, where the starting substrate chemistry plays a crucial role in the growth regime and properties of the deposited film. For example, the nucleation of Al_2O_3 on Si using TMA/ H_2O has been previously studied for their potential application as gate oxides, while the research of initial nucleation using other Al precursors is minimal. There is a rising need for understanding the growth of sub-nm thick films due to emerging applications, such as area-

selective deposition (ASD), where differences between initial growth on different substrates can be exploited to achieve deposition on only one of the surfaces and not on the other.⁶⁶ However, due to the high reactivity of TMA towards most surfaces, ASD of Al₂O₃ has been largely achieved through the use of blocking layers such as PMMA,^{67,68} PVP,^{67,69–71} and PS.^{72,73} For example, there have been several reports on the effect of precursor selection on the selectivity achieved using self-assembled monolayers.^{74,75} On blanket substrates it has been demonstrated that the growth rate of Al₂O₃ exhibited a noticeably smaller degree of selectivity between H-terminated and oxidized Si(001) surfaces than TiO₂, attributing the difference to higher chemisorption probability of the TMA molecule compared to TiCl₄.¹⁷ Density functional theory (DFT) has been actively employed to investigate the energy barriers, mechanisms and reactions in ALD by TMA/H₂O on Si(001) surface with varying terminations.^{12,76–80} Recently, experimental results analyzing the initial growth regime of TMA/H₂O process on H/Si(111) and SiO₂ substrates using broadband sum-frequency generation (BB-SFG) were published.⁸¹ The results demonstrated that while Al₂O₃ grows immediately on both surfaces, the H-terminated surfaces has a reduced growth rate during the initial 20 cycles, indicating limited selectivity between the two surfaces. To expand the understanding of the initial growth regime and to achieve improved selectivity between starting substrates, needed for area selective deposition applications, different aluminum precursors need to be studied.

In this work, the initial growth behavior of Al₂O₃ ALD on OH-terminated and H-terminated Si(100) were compared using trimethylaluminum [(CH₃)₃Al, TMA], triethylaluminum [(C₂H₅)₃Al, TEA], and dimethylaluminum chloride [(CH₃)₂AlCl, DMAC] as precursors and H₂O as a coreactant. TEA and DMAC were chosen due to their similar structure to TMA, with the methyl groups replaced by ethyl groups for TEA, resulting in a larger molecule size. Compared to TMA,

DMAC has one of the methyl ligands replaced by chlorine, leading to lower reactivity. The resulting growth trends, film compositions and surface functional groups at various temperatures were characterized using *in-situ* ellipsometry, *in-situ* Auger electron spectroscopy (AES) and *in-situ* Fourier transform infrared spectroscopy (FTIR).

3.3 Methodology

Trimethylaluminum (Strem Chemicals, 97% purity), dimethylaluminum chloride (Sigma-Aldrich, 99% purity), triethylaluminum (Strem Chemicals, 93% purity) were used as Al-precursors as received. Deionized water was used as the oxygen source. TMA and DMAC were kept at room temperature, while TEA was heated to 75 °C due to its lower vapor pressure. Blanket silicon substrates used in this study were single-sided p-type boron-doped Si (100) wafers with resistivity of 5-10 Ω cm. The wafers were cut in small 1x1 cm pieces and piranha (1:1 H₂SO₄:H₂O₂) cleaned to remove the organic contamination from the substrate and form a hydrophilic hydroxyl-terminated Si-OH surface. To obtain a hydrophobic hydrogen-terminated Si-H surface, the substrates were dipped into 5% HF solution for 30 seconds. The porous silicon samples used for FTIR measurements were double-side-polished p-type (100) wafers with resistivity of 30-60 Ω cm. They were prepared by electrochemical etching in 50% aqueous HF and 99.8% ethanol 1:1 solution for 20 minutes at a current density of 14 mA/cm². To obtain hydroxyl-terminated porous Si substrates, the resulting porous wafers were held in hydrogen peroxide (H₂O₂, 30% in water) at room temperature for 60 minutes.

Two different reactor systems with *in-situ* characterization capabilities were used in this study. The Al₂O₃ films on blanket substrates were deposited in a home-built warm-walled reaction chamber equipped with an *in-situ* ellipsometer and connected with a loadlock and an ultrahigh vacuum (UHV) analysis chamber with Auger electron spectroscopy. The schematic of the reactor

system is shown in Figure 3.1. The sample stage in the reactor chamber was heated using two halogen lamps controlled by a PID and kept at a constant temperature (150-250 °C) during the process. The samples were attached to a 2-inch diameter stainless steel puck, which could be transferred *in-vacuo* between the reaction chamber and the UHV analysis chamber using magnetic transfer arms. The deposition was carried out at 400 mTorr base pressure, using Ar (Arc3 Gases, 99.999% purity) as a carrier gas at a total flow rate of 95 sccm. The dosing times for were 0.1s for TMA, DMAC, and H₂O and 0.4s for TEA. The reactant dose was followed by an argon purge for 15 second, a pump down step for 10 seconds, during which the chamber was evacuated to 10⁻⁵ Torr and a pressurization step for 15 second to bring the chamber back to the operating pressure of 400 mTorr.

The film thickness and optical parameters of the sample were monitored using an *in-situ* multi-wavelength spectroscopic ellipsometer (Film Sense FS-1) attached to the chamber. The ellipsometer was at a 67° ±1° angle and performed measurements at 465 nm, 525 nm, 580 nm, and 635 nm wavelengths using LEDs. This measurement was done after every half-cycle or full cycle and data was collected for 9 seconds for each data point. Due to its high sensitivity to ultrathin film layers, Δ parameter, which characterizes the phase change upon polarized light reflection, is used to characterize surface changes during half-cycles. To acquire optical film thickness values, in-built Cauchy model was used.

The samples' elemental composition was characterized using *in-situ* Auger electron spectroscopy (AES) in the UHV analysis chamber. AES was performed using a coaxial cylindrical mirror analyzer (Perkin Elmer PHI 10-155) with a 100 μ m beam size and a 3 kV electron beam. The spectrometer was operated at a base pressure of 10⁻⁹ Torr, achieved using an ion pump (Digital 500 220 l/s) and a turbo pump (Edwards EXT501).

In-situ Fourier transform infrared spectroscopy (FTIR) measurements on porous silicon substrates were performed to monitor vibrational modes of chemical species at the surface in a homemade reactor described previously⁸² using Thermo Fisher Nicolet 6700 spectrometer and an MCT-A external detector. During the deposition and the measurement, reactor walls and delivery lines were held at 90 °C. Porous silicon substrates were mounted on a sample holder with mounted cartridge heaters to heat the samples to 200 °C. Nitrogen was used as a carrier and purging gas, resulting in an operating pressure of 500 mTorr. The measurements were acquired with a resolution of 6 cm⁻¹ in a range of 650-4000 cm⁻¹ and averaged over 512 scans. Each FTIR spectrum was acquired after five 1 s doses of a reactant, followed by 90 s of nitrogen purge.

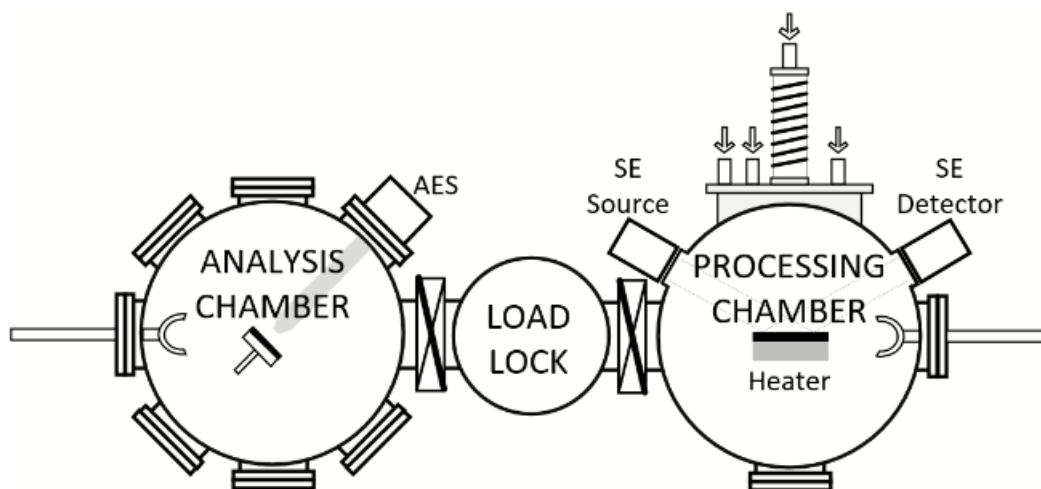


Figure 3.1. Simplified schematic of the chamber system used in this work, including the reaction chamber equipped with *in-situ* spectroscopic ellipsometry and analysis chamber with Auger electron spectroscopy.

3.4 Results and Discussion

3.4.1 Film Thickness Evolution

Based on *in-situ* ellipsometry data, all three Al precursors (TMA, TEA, and DMAC) exhibit similar growth modes on Si-H and Si-OH starting substrates as plotted for 200 °C processing temperature in figure 3.2. The *in-situ* ellipsometry data for the temperature range

150 – 250 °C are shown in figure S3.1. On Si-OH the first ALD cycles show an accelerated growth per cycle (GPC), which slows down to a constant steady-state growth rate, characteristic to ALD. On Si-H however, the GPC starts out slow and then steadily accelerates to achieve the same rate as on Si-OH during steady growth. In the steady-state regime of ALD by TMA/H₂O leads to GPC of 0.13 nm/cycle, TEA/H₂O to 0.11 nm/cycle, and DMAC/H₂O to 0.1 nm/cycle at 200 °C. In the temperature range of 150 – 250 °C the GPC varied in range of 0.11-0.13 nm/cycle for TMA/H₂O, 0.08-0.12 nm/cycle for TEA/H₂O, and 0.08-0.1 nm/cycle for DMAC/H₂O. All precursors exhibited the lowest GPC at 250 °C, while the GPC was highest at 150 °C for TEA and at 200 °C for both TMA and DMAC. The calculated GPC values and their dependence of temperature using TMA and DMAC are in good agreement with previously published results, while the GPC of TEA at 200 °C is slightly higher than previously reported 0.08 nm/cycle.^{29,41,75}

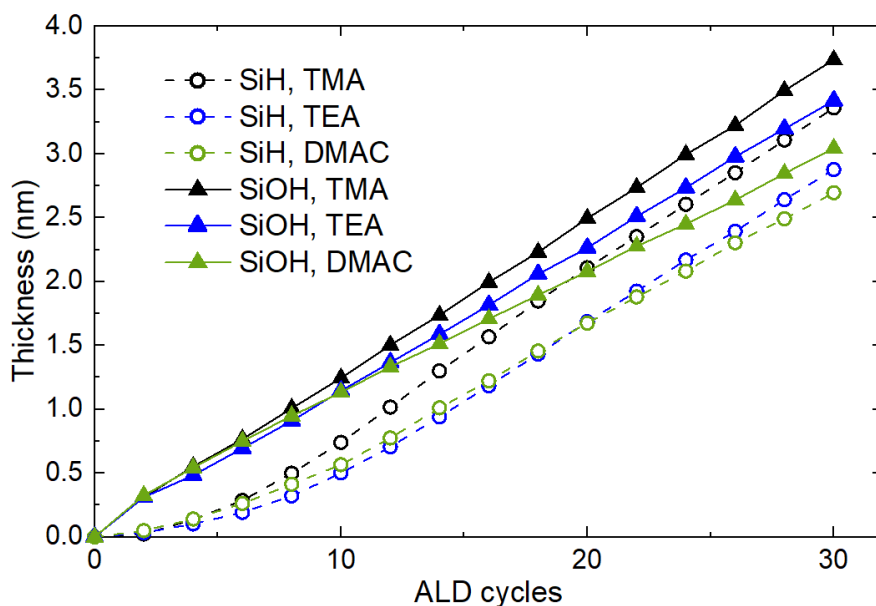


Figure 3.2. The thickness of Al₂O₃ thin film on Si-OH and Si-H surfaces deposited by ALD using TMA/H₂O, TEA/H₂O, and DMAC/H₂O at 200 °C as measured by *in-situ* ellipsometry.

3.4.2 Process Selectivity

To compare the effectiveness of various processes for area-selective deposition purposes a quantitative parameter needs to be defined. Typically, the selectivity fraction parameter S is defined through surface coverage values θ_1 and θ_2 for the desired growth and non-growth surfaces, respectively. In this work we estimate the selectivity fraction S values using thicknesses t_1 and t_2 as they can be more easily obtained through ellipsometry measurements:

$$S(n) = \frac{\theta_1 - \theta_2}{\theta_1 + \theta_2} \approx \frac{t_1 - t_2}{t_1 + t_2} \quad (3.1)$$

When growth proceeds only on the preferred growth surface and not on the preferred non-growth surface S obtains value of 1. When the deposition exhibits no selectivity then the value of S is 0. The preferred growth and non-growth surfaces in this work are Si-OH and Si-H surfaces, respectively. The selectivity fractions as a function of Al₂O₃ film thickness on the Si-OH substrate were calculated for all three processes and are represented in figures 3.3 at 200 °C. The selectivity fractions in temperature range 150 – 250 °C are plotted in figures S3.2 and S3.3 as a function of ALD cycles and as a function of Al₂O₃ thickness on Si-OH, respectively. The values were plotted as a function of film thickness on Si-OH instead of as a function of cycles to factor for the lower growth rate of DMAC vs. TMA and TEA. For all conditions studied, the selectivity fraction starts out at a high value in range of 0.6-0.9 and decays exponentially as more ALD cycles are performed. The high value of S after the first cycle is due to initial accelerated growth on the Si-OH surface and inherent growth delay on the Si-H surface, leading to a high t_1 value and a comparably low t_2 . As more ALD cycles are performed the value of S approaches zero as more nuclei are generated on the Si-H surface, eventually leading to coalescence and to loss of selectivity.

Comparing the selectivity of the ALD processes at temperature range of 150 – 250 °C there is an apparent correlation between the selectivity and the deposition temperature as the selectivity

fraction is lowest for the lower temperature of 150 °C. Moreover, the calculated selectivity fraction at various temperatures is more spread out for the DMAC and TEA compared to TMA, enabling to improve the selectivity by choosing an optimized process temperature. This difference is due to both the change in steady-regime growth rates for TEA and DMAC, and the length of nucleation delay on the Si-H substrate. For area-selective deposition purposes, it is preferable for the S value to remain high for larger film thickness values on Si-OH substrate. As such, at 200 °C TEA seems to be advantageous Al precursor for area selective deposition purposes, while TMA and DMAC exhibit similar selectivity between the two surfaces. However, while DMAC/H₂O exhibited the lowest GPC at 250 °C as determined by *in-situ* ellipsometry, it also shows the longest growth delay on Si-H substrate, leading to highest selectivity fraction values of the conditions measured.

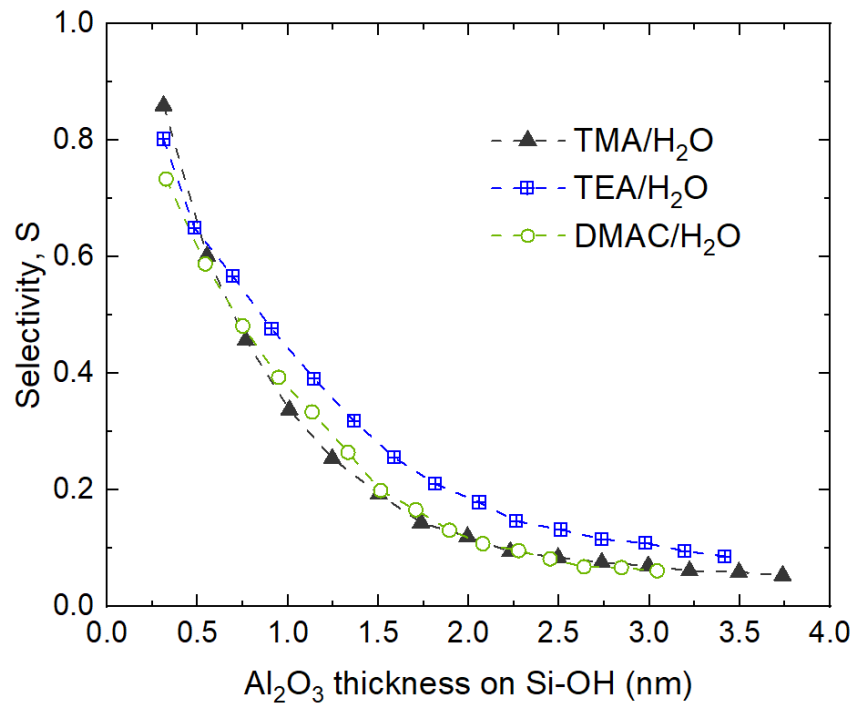


Figure 3.3. Calculated selectivity fraction S as a function of Al₂O₃ film thickness on Si-OH. Data were collected for TMA, TEA, and DMAC ALD processes at 200 °C.

3.4.3. Elemental Analysis by *in-situ* Auger Electron Spectroscopy

In-situ Auger electron spectroscopy (AES) was used to further characterize Al₂O₃ growth on Si-H and Si-OH surfaces at 200 °C as a function of number of ALD cycles. The benefit of using AES for nucleation studies is the high surface sensitivity of the method, enabling the observation of minute changes in the film composition. In addition, as the spectrometer is connected to the chamber system, the measurements can be performed without exposing the sample to atmosphere, preventing contamination. The resulting survey spectra and the Al to Al+Si atomic percentage ratios are shown in figure 3.4 and figure 3.5, respectively. The data were obtained by moving a sample back-and-forth *in-vacuo* between the processing chamber and the ultra-high vacuum analysis chamber for ALD cycles and AES measurements. There is a clear distinction between the Si-OH and Si-H starting substrates. The Si-OH surface shows distinct peaks at 90 eV and 76 eV – belonging to LMM transition of elemental Si and SiO₂, respectively. For the Si-H starting surface there is no detectable SiO₂ signal present, indicating the lack of Si-OH bonds. It is important to note that adventitious carbon and oxygen present on the starting surfaces is due to cleaning steps being performed *ex-situ* prior to loading the sample into the chamber. Likewise, there is a clear shift in the O 1s peak at ~502 eV as it shifts to lower energies compared to the starting substrate as Al₂O₃ is deposited. For quantitative understanding of the measurement results atomic percentages of the elements present in each deposition condition were calculated and are shown table S3.1. As the atomic percentages were calculated using published relative sensitivity factors, larger uncertainties are expected in the values given.⁸³ Nevertheless, the resulting atomic percentages are good indicators of the surface evolution, and the growth trends present. Data indicates a growth delay on the Si-H starting substrate for all Al precursors, with a weak Al peak appearing at the 1st ALD cycle for TMA and at the 2nd cycle for TEA and DMAC. Meanwhile

there is a sharp increase of Al at.% on Si-OH after the very first ALD cycle. Subsequent cycles increase the concentration of Al on the sample for both starting substrates. The Al at.% increases faster on the Si-OH surface compared to the Si-H due to the initial nucleation delay on the latter. Likewise, the growth is faster for ALD using TMA and TEA, compared to DMAC, consistent with the higher GPC determined by ellipsometry. As the film grows thicker and the amount of Si detected reduces, the Al:O stoichiometric ratio approaches 2:3 as expected for Al₂O₃ films. At 25 cycles no Si is detected on the Si-OH substrate for any Al precursors studied. On Si-H the Si signal disappears completely after 25 cycles for TMA and after 50 cycles for TEA and DMAC. There is a weak C signal present throughout the runs, presumed to be from unreacted methyl or ethyl groups, either on the surface, or incorporated into the film. Moreover, it is vital that no chlorine was detected in samples deposited at 200 °C using DMAC at any cycle number, as chlorine residue might have a negative impact on device performance and thus limit the applicability of the precursor.⁸⁴

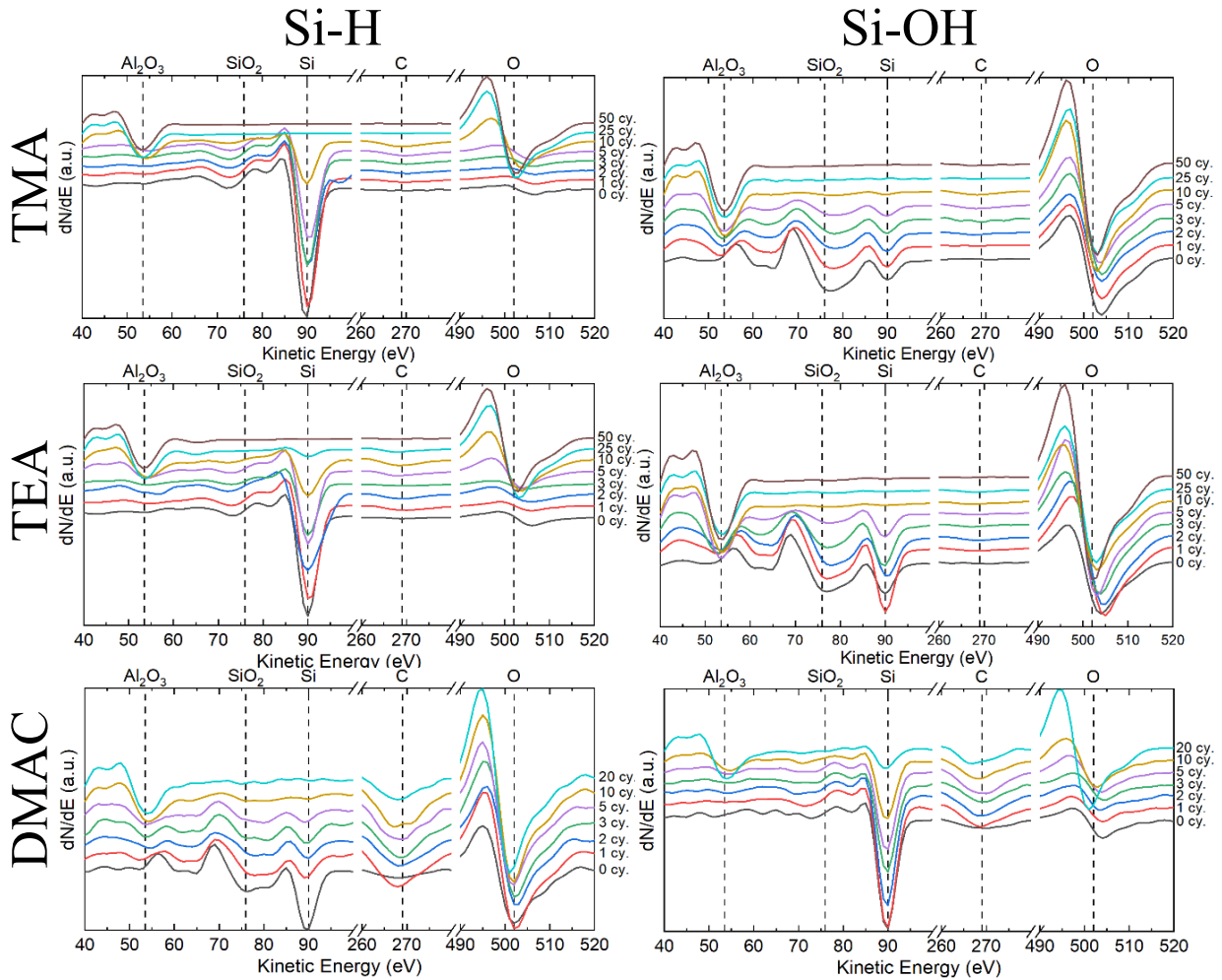


Figure 3.4. Auger electron spectroscopy spectra of Al_2O_3 thin films deposited at $200\text{ }^\circ\text{C}$ on Si-H and Si-OH using TMA (top row), TEA (middle row), or DMAC (bottom row) as Al precursors. The data are presented in derivative mode.

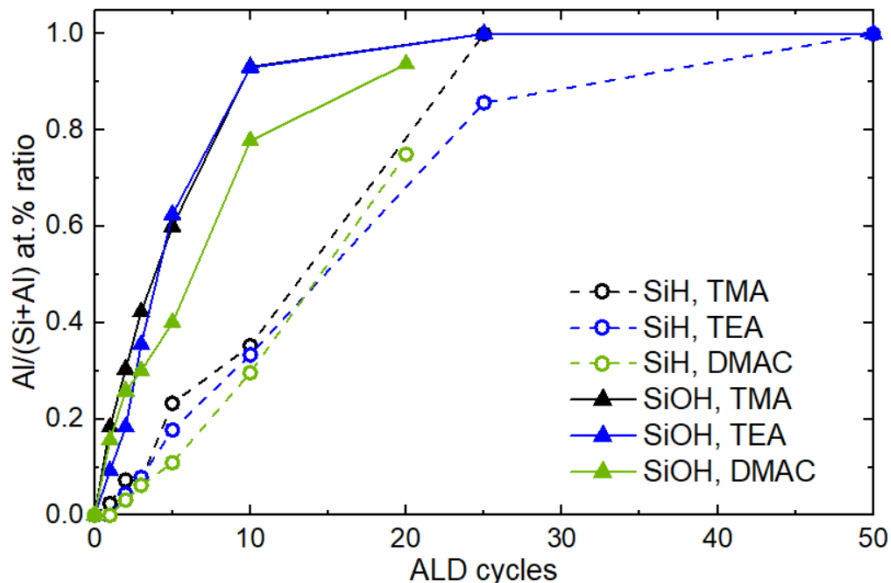


Figure 3.5. Al to Si+Al atomic percentage ratios of Al_2O_3 deposited Si-H and Si-OH starting substrates at 200 °C as measured by *in-situ* Auger electron spectroscopy.

3.4.4 Ellipsometry Trends During Initial Half-cycles

The changes in film properties after each half-cycle were analyzed using *in-situ* ellipsometry for each Al precursor. Despite the complexity of modelling ultrathin films due to their non-conformality and the refractive index being a function of the film thickness, the raw parameters acquired by ellipsometry can be used to extract information about the film growth and nucleation. Specifically, the Δ parameter, describing the phase change of the polarized light upon reflection, is exceedingly sensitive to small changes in ultrathin films. The Δ parameter measured after each half-cycle for ALD at 200 °C on Si-OH, Si-H, and native Si surfaces are shown in figure 3.6, while the data for the process temperature range from 150 °C to 250 °C is shown in figure S3.4. To illustrate the growth behaviors, the data is plotted to show the change in the delta parameter after each dose and averaged over 3 measurements. On the Si-OH and native silicon oxide surfaces the trends show clear Δ decrease after the Al precursor dose and an increase after the H_2O doses. On both surfaces the processes exhibit an increased decrease in the Δ after the first Al precursor exposure compared to the subsequent exposures. This drop is more significant on the

Si-OH compared to the native oxide. On the Si-H substrate, the changes in Δ are much smaller due to the growth inhibition for all three Al precursors. During the first few cycles, the Δ parameter also decreases with H₂O exposure, indicating optical thickness increase due to generation of nuclei. As more cycles are performed, resulting in more growth sites, the changes in Δ grow larger. While it is apparent that the growth does not reach steady regime in 5 cycles, the TMA/H₂O process exhibits largest changes in Δ , resulting from the fastest nucleation and growth.

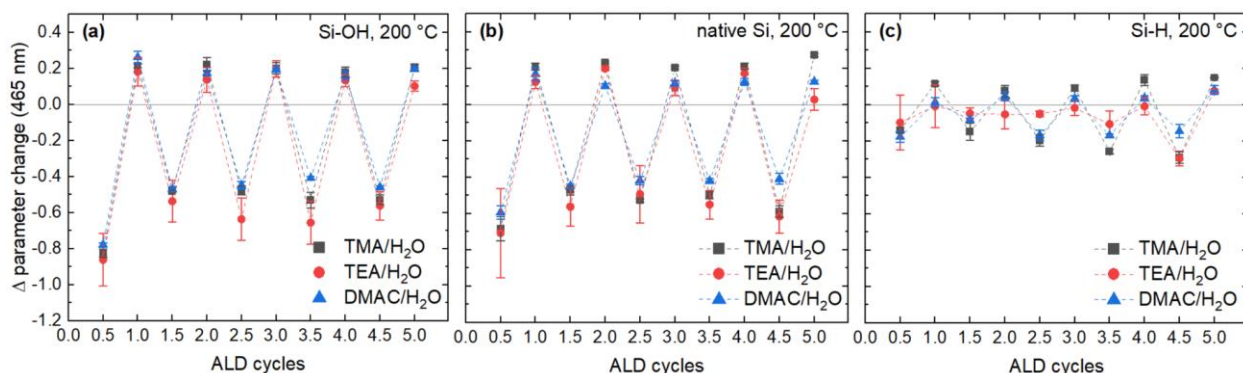


Figure 3.6. Ellipsometric delta parameter changes at 465 nm wavelength during half-cycles of Al₂O₃ ALD using TMA, TEA, or DMAC as Al precursor on (a) Si-OH, (b) native Si oxide, and (c) Si-H surfaces. All data were collected *in-situ* at 200 °C deposition temperature.

3.4.5 *In-situ* Fourier Transform Infrared Spectroscopy Analysis

In-situ Fourier-transform infrared spectroscopy (FTIR) was used to study nucleation and growth of ALD deposited Al₂O₃ films at 200 °C onto hydroxylated and hydrogen-terminated porous silicon surfaces, through reaction between one of the three Al precursors with water as an oxygen source. A FTIR spectrum was obtained after each half-cycle reaction. Since each ALD precursor exposure leaves at most a monolayer on the surface, the silicon wafers were electrochemically etched to form pores in order to enhance absorbance intensity. This allows to monitor the chemical composition changes after each ALD half-cycle.

First, the reaction of TMA and water on Si-OH surface was studied. The difference FTIR spectrum, shown in figure 3.7a, contains a sharp negative peak at 3736 cm⁻¹ after the first dose of

TMA and a broad negative OH absorption peak between 3350-3780 cm^{-1} , indicating removal of initial surface hydroxyl groups through reaction with TMA molecules. The FTIR spectrum also shows the appearance of positive Al-CH₃ peaks at approximately 2960 cm^{-1} and 1212 cm^{-1} , indicating the formation of methyl groups at the surface of the substrate. The positive peak at ~1270 cm^{-1} shows the formation of Si-CH₃ bond, originating from the reaction with siloxane bridges. Difference FTIR spectrum after subsequent dose of water shows a positive peak at 3350-3780 cm^{-1} and negative peaks at 2960 cm^{-1} , 1212 cm^{-1} , and 1270 cm^{-1} which suggest formation of OH group and elimination of CH₃ stretch, CH₃ deformation and Si-CH₃ groups, respectively, consistent with literature.⁸⁵ Integrated peak area values were measured after each cycle for further process quantification as plotted in figures 3.8a and 3.8b. Integrated OH peak area at 3350-3780 cm^{-1} suggests that 98% of hydroxyl groups available at the starting Si-OH surface reacted with TMA molecules which led to high TMA uptake during the first cycle. Integrated area under CH₃ peak at 2880-3010 cm^{-1} shows that only 50% of surface methyl groups reacted with water molecules, resulting in a decreased OH group density at the surface. While the Al₂O₃ film was shown to grow at a constant rate on Si-OH, the absorbance intensity of Al-CH₃ peak starts to decrease after the fourth cycle due to filling of the pores within the silicon that drastically decreases the available surface area.

As the growth initiation of ALD deposited film depends on the chemical nature of the substrate, the experiment was repeated on a porous hydrogen-terminated silicon wafer. The difference FTIR spectrum, shown in figure 3.7b, shows similar CH₃ peaks as on Si-OH surface after the first dose of TMA, however, no negative broad OH peak is observed due to absence of OH groups on the initial surface. The difference FTIR spectrum after the first dose of water shows the Si-CH₃ peak on hydrogen terminated surface remained on the surface as no negative signal is

observed. This Si-CH₃ termination has been previously reported to act as a passivating layer, inhibiting film growth on the surface.⁸⁵ Data also shows slight Al-CH₃ peak shift in 2880-3010 region. Integrated peak area value of the methyl group at 2880-3010 cm⁻¹ is lower on Si-H compared to the Si-OH surface which is indicative of lower Al₂O₃ growth rate on Si-H surface. The trend confirms initial accelerated growth of Al₂O₃ on Si-OH, which reaches steady-growth for the following cycles, while the growth is inhibited on the Si-H surface.

The difference FTIR spectrum for the TEA/H₂O process is plotted in figures 3.7c and 3.7d for Si-OH and Si-H, respectively. The first dose of TEA on porous Si-OH, similar to first dose of TMA, shows that the TEA molecules react with surface hydroxyl group as indicated by a sharp negative peak at 3736 cm⁻¹ and a broad negative OH absorption peak between 3350-3780 cm⁻¹. The FTIR spectrum also shows positive -CH₃, -CH₂, and Si-CH=CH₂ peaks at 2950, 2875, and 1408 cm⁻¹, respectively. The difference FTIR spectrum after 1st dose of water shows the formation of OH group and elimination of surface CH. As shown in figures 3.8c and 3.8d, the integrated area under OH peak at 3350-3780 cm⁻¹ and C-H peaks at 2850-2995 cm⁻¹ for the first four cycles of TEA and water shows similar trend as first four cycles of TMA and water on both Si-OH and Si-H. On Si-OH, 95% of the -OH groups reacted with the TEA, while 50% of the -CH₃ and -CH₂ remained on the substrate after the subsequent water dose. The difference FTIR spectrum for the first dose of TEA on Si-H shows similar C-H peaks as on Si-OH surface. After the subsequent dose of water, the Si-CH=CH₂ peak on hydrogen terminated surface remained unreacted. Data also shows that -CH₃ peak at 2950 cm⁻¹ slightly shifts after a dose of water. Similar to TMA/H₂O, for the TEA/H₂O process the integrated peak area trends confirm initial accelerated growth of Al₂O₃ on Si-OH, which reaches steady-growth in the following cycles, while the growth is delayed on the Si-H surface.

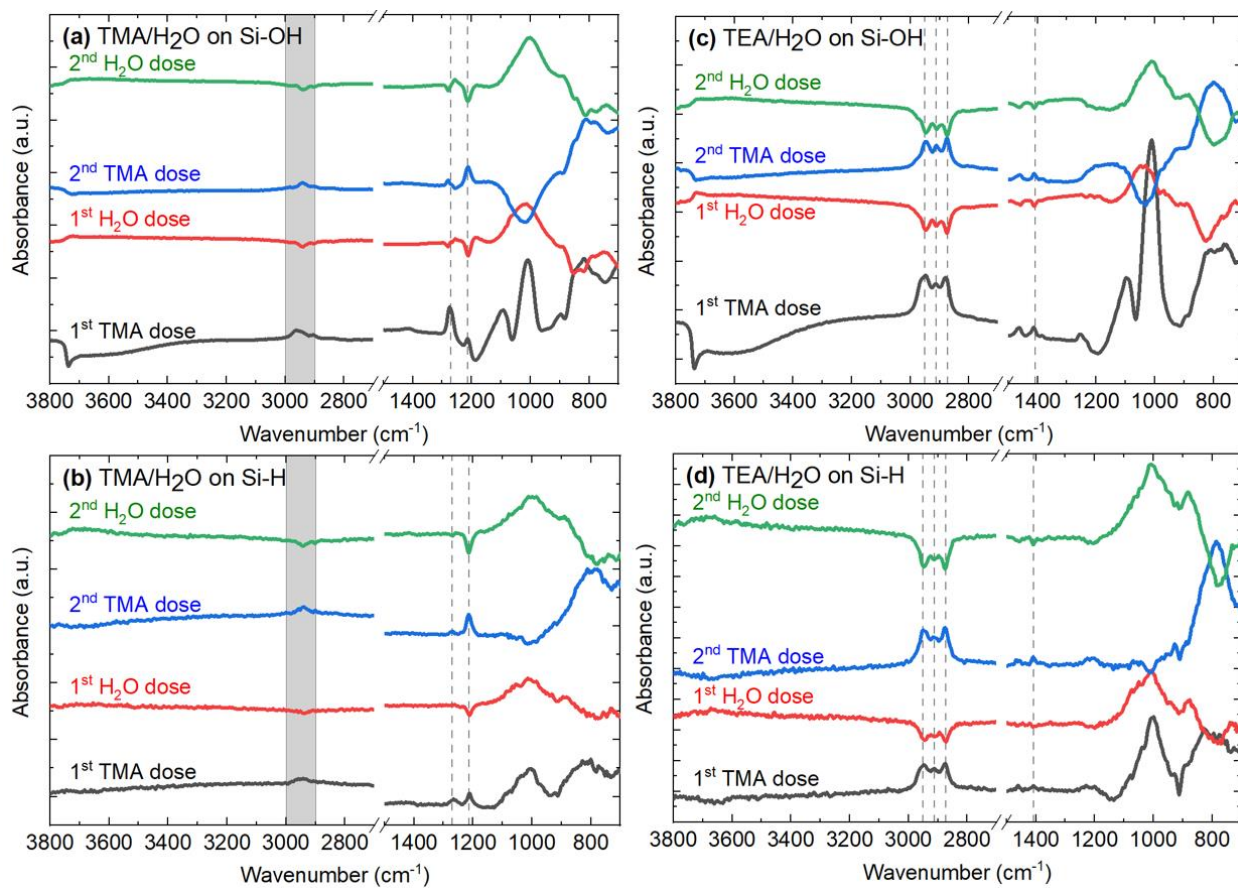


Figure 3.7. Difference FTIR spectra of the half-reactions of the 1st and 2nd ALD cycles of TMA/H₂O (a,b) and TEA/H₂O (c,d) on porous Si-OH and Si-H substrates.

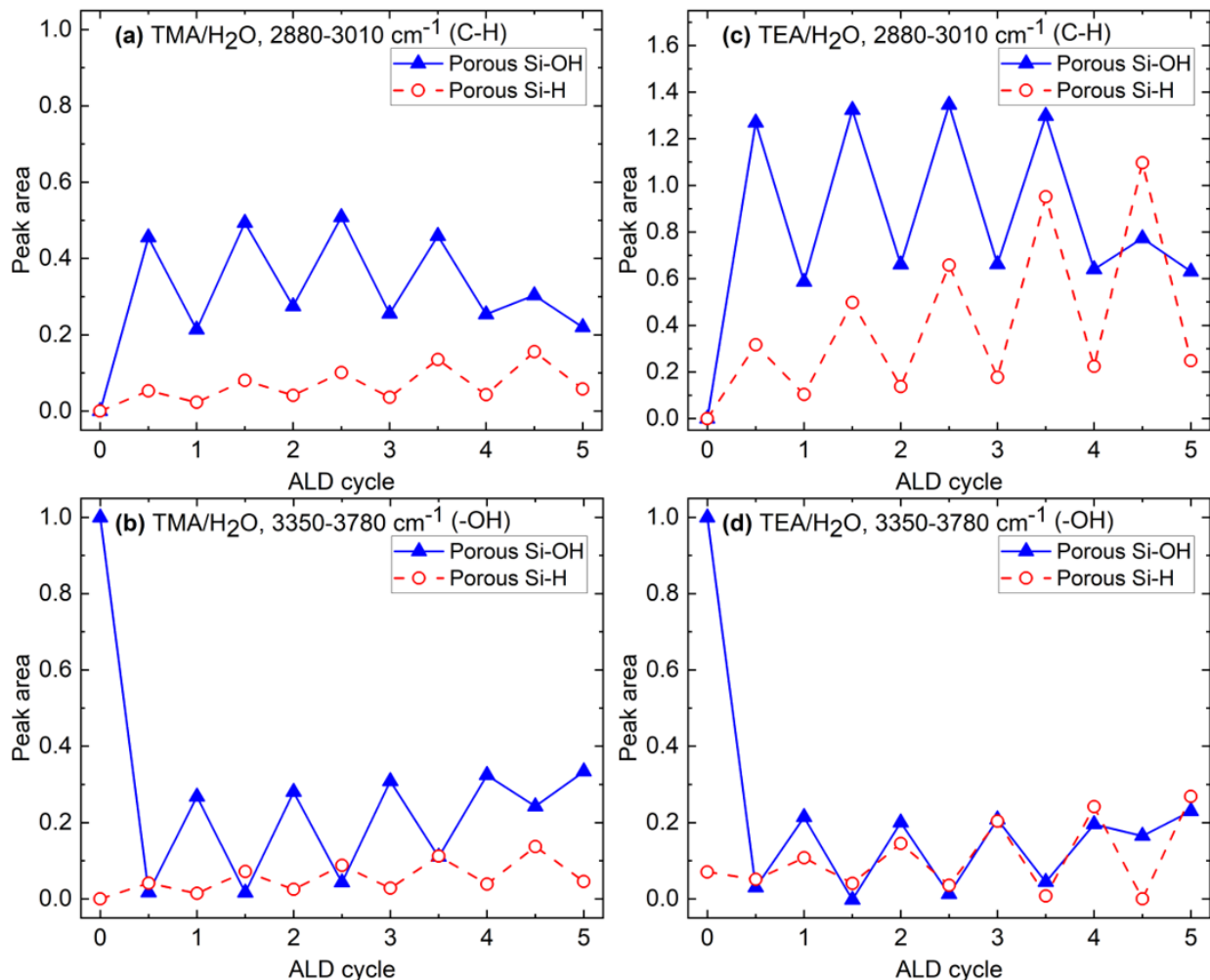


Figure 3.8. Integrated area under -OH peak between 3350-2780 cm^{-1} for (a) TMA/ H_2O and (c) TEA/ H_2O and under C-H peak between 2850-2295 cm^{-1} for (b) TMA/ H_2O and (d) TEA/ H_2O on porous silicon.

3.5 Discussion

A comparison of initial growth behavior of Al_2O_3 films shows that while all three Al precursors studied result in similar general trends on Si-H and Si-OH surfaces, the growth and nucleation rates, and the selectivity values vary due to differences in molecule size and reactivity. The growth rates and selectivity values measured by *in-situ* ellipsometry and Auger electron spectroscopy at 200 °C are in great agreement, indicating the highest selectivity values obtained by TEA precursor. Both measurements show that while the DMAC exhibited the longest

nucleation delay on Si-H, the selectivity was limited by lower GPC on the Si-OH substrate, due to lower reactivity of the precursor. Nevertheless, both TEA and DMAC exhibited improved selectivity compared to more commonly used TMA in the temperature range 150-250 °C.

In-situ ellipsometry and *in-situ* FTIR demonstrate accelerated growth rate during the first Al precursor exposure followed by steady growth on the Si-OH substrate and a growth delay on the Si-H substrate. The accelerated growth rate during the first cycle can be attributed to the increased Al precursor uptake during the first half-cycle as apparent by large decrease in Δ in the ellipsometry data and a larger decrease in the number of C-H bonds compared to the later cycles according to FTIR data. The subsequent slower growth rate is caused by lower number of available reaction sites present due to subsequent water doses incompletely removing the surface ligands at 200 °C, and due to less available -OH bonds on the deposited Al-OH substrate compared to the starting Si-OH surface. Based on the integrated peak areas the -OH group density on the surface is roughly 75% less after a single ALD cycle compared to the starting Si-OH surface for both TMA/H₂O and TEA/H₂O processes. While methyl groups remain on the surface for the TMA/H₂O and ethyl groups for the TEA/H₂O, they exhibit the same reactivity towards H₂O as only 50% of both react. It has been previously shown that increasing processing temperature or using more reactive oxidant, such as O₃ plasma, is more effective at removing -CH₃ ligands present after TMA exposure.⁸⁶ Comparing the change in the Δ parameter after the first Al precursor dose on chemical vs. native Si oxide, it is apparent that the uptake is larger on the former due to the larger concentration of hydroxyl bonds present. The subsequent half-cycles on these surfaces proceed in a steady-regime, with Δ increasing after H₂O exposure, indicating optical thickness decrease as surface ligands are replaced by the -OH and Δ decreasing with the Al precursor doses as they react with the surface, increasing the optical thickness. The changes are smaller for DMAC/H₂O process

compared to TEA and TMA due to the lower precursor reactivity leading to a lower growth rate. Based on this data, the reaction kinetics are limited by the reactivity of the water molecules toward methyl and ethyl groups at the surface resulting in lower concentration of surface hydroxyl groups.

The nucleation period exhibited by all precursors on the Si-H substrate can be explained by the lack of hydroxyl groups on the surface. In lieu of forming -OAlMe₂ groups, TMA has been shown to react with the H-terminated Si to form Si-Me groups.⁸⁵ Likewise, the FTIR results confirm that TEA exposure forms both Si-Me and Si-Et groups on the Si-H surface. These groups passivate the surface in the thermal ALD process, leading to the growth delay on the H-terminated Si surface, visible in the ellipsometry and FTIR data. The subsequent increase in GPC with following cycles is due to deposition of nuclei and the growth of these nuclei. Their growth is initiated by unwanted defects or reactive sites (-OH) on the surface; the presence of background H₂O during the precursor exposure; and dissociative chemisorption of the Al precursor.²⁹ The steady-state growth is reached when the nuclei islands coalesce into a uniform film and the growth proceed similar to that on Si-OH starting surface. The good agreement between the Δ parameter and the integrated FTIR peak areas confirms the effectiveness of studying initial nucleation trends using raw ellipsometric parameters, despite the complexity of modeling ultrathin films or nuclei.

3.6 Conclusion

A detailed *in-situ* studies of initial growth mechanisms of Al₂O₃ ALD using TMA, DMAC, or TEA as Al precursors and H₂O as a co-reactant on Si-OH and Si-H substrates were presented. While all precursors exhibited initial accelerated growth, followed by steady growth on the Si-OH surface and a nucleation delay characteristic to island growth on the Si-H surface, the growth rates, the extent of the growth delay and the reaction mechanisms varied. The GPC was determined as 0.13 nm/cycle for TMA, 0.11 nm/cycle for TEA, and 0.10 nm/cycle for DMAC at 200 °C. The

lower growth rate of the latter is due to larger molecule size and lower reactivity, respectively. Despite the lower growth rates, both TEA and DMAC resulted in better selectivity between Si-OH and Si-H surfaces. *In-situ* AES measurements confirmed the results, indicating the slowest increase of Al:Si at.% ratios using DMAC as the Al-precursor and the fastest for TMA. The mechanisms present during half-cycles were characterized using *in-situ* ellipsometry and *in-situ* FTIR. The higher growth rate during the first cycle on Si-OH was shown to be due to ineffective removal of methyl or ethyl ligands present on the surface by the H₂O exposure. While the first Al precursor dose for both TMA and TEA on Si-OH reacted with 98% of the -OH bonds present, only 50% of the resulting C-H bonds reacted with the subsequent water exposure. The agreement between FTIR data and the measured raw ellipsometric Δ parameter trends confirms the capability to characterize the initial growth trends using ellipsometry, despite the complexity of modelling low thickness films. The trends presented in this work provide insight into the impact of precursor structure on the initial growth trends of alumina thin films and indicate the importance of precursor selection during area-selective deposition utilizing inherent selectivity of the substrates.

3.7 Acknowledgments

This material is based upon the work supported by the National Science Foundation under Grant No. 1704151.

3.8 Supplemental Material

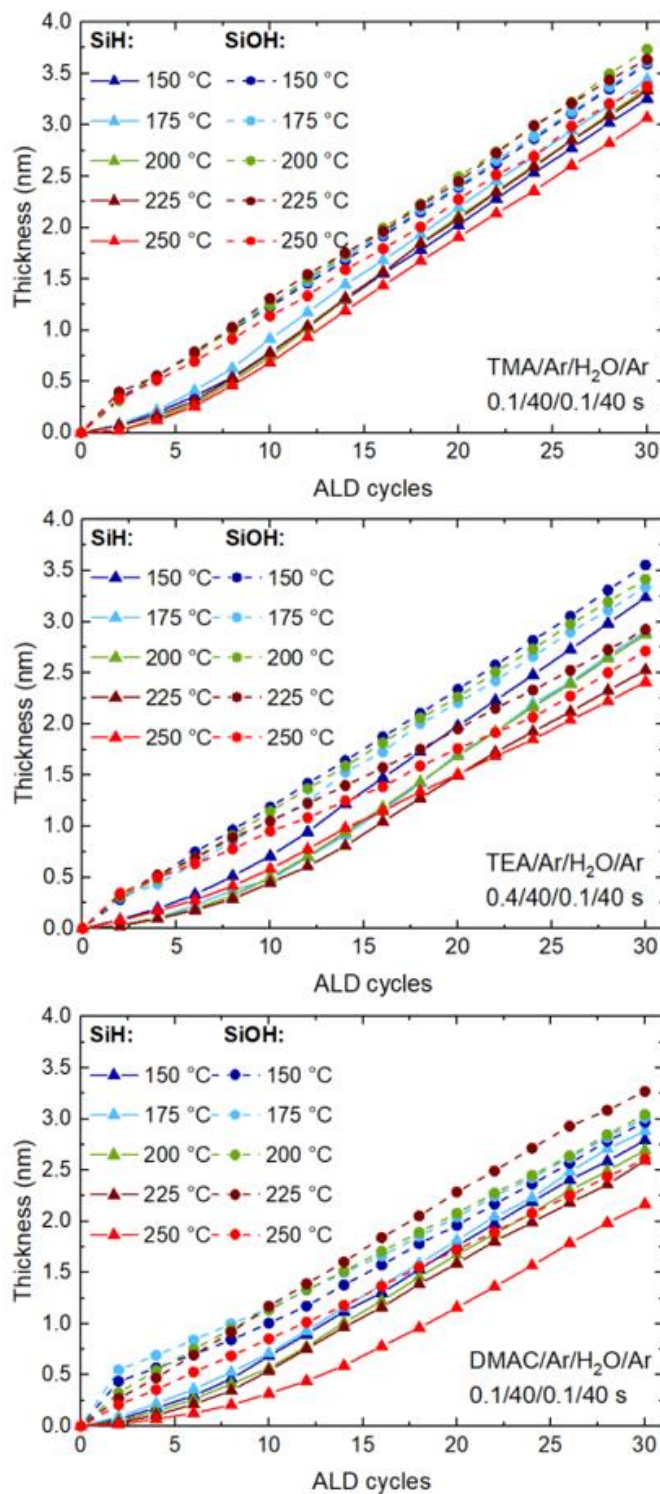


Figure S3.1. The thickness of Al₂O₃ film on Si-OH and Si-H surfaces for ALD by TMA/H₂O, TEA/H₂O, and DMAC/H₂O in temperature range 150-250 °C as measured by *in-situ* ellipsometry.

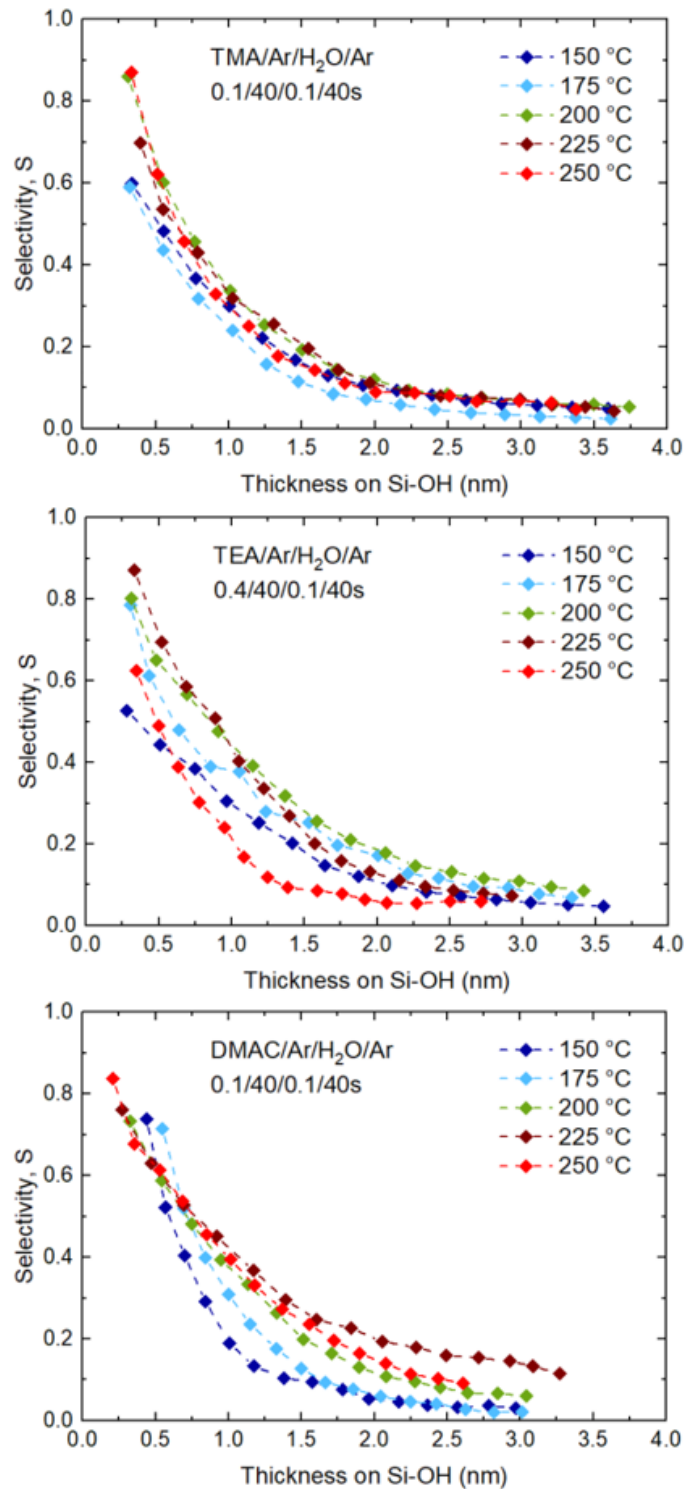


Figure S3.2. Calculated selectivity between Si-OH and Si-H surfaces as a function of Al₂O₃ thickness on Si-OH substrate for ALD by TMA/H₂O, TEA/H₂O, and DMAC/H₂O in temperature range 150-250 °C.

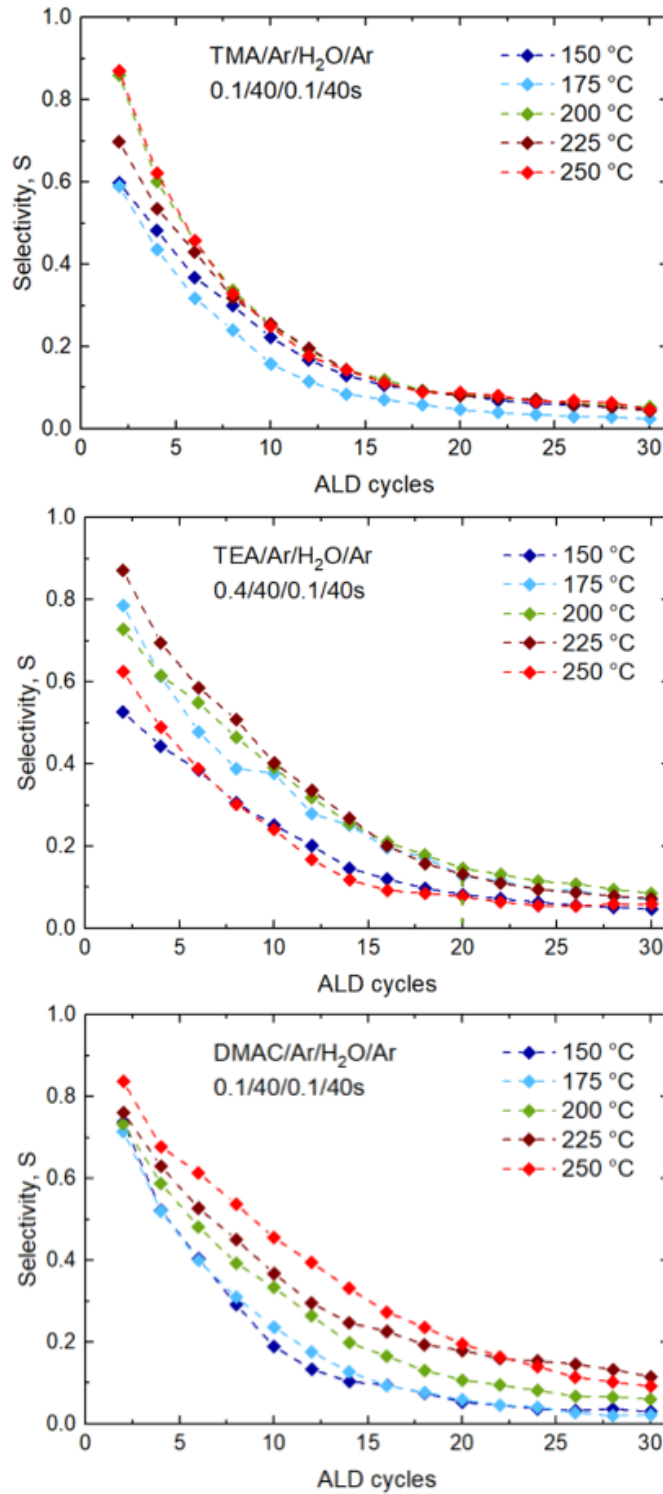


Figure S3.3. Calculated selectivity between Si-OH and Si-H surfaces as a function of Al₂O₃ ALD cycle number for ALD by TMA/H₂O, TEA/H₂O, and DMAC/H₂O in temperature range 150-250 °C.

Table S3.1. Atomic percentages of elements detected from *in-vacuo* Auger electron spectroscopy data as a function of ALD cycles at 200 °C. The measurements were performed on Si-H and Si-OH substrates using TMA, TEA, or DMAC as an Al precursor and H₂O as an oxygen source.

		Number of ALD cycles										Number of ALD cycles							
TMA, Si-H		0	1	2	3	5	10	25	50	TMA, Si- OH		0	1	2	3	5	10	25	50
Al (at.%)		0	0	1	2	6	28	43	42	Al (at.%)		0	11	17	22	30	41	41	42
Si (at.%)		96	94	90	88	80	38	0	0	Si (at.%)		61	49	36	30	20	3	0	0
O (at.%)		4	3	4	5	7	26	57	58	O (at.%)		39	40	40	42	45	51	59	58
C (at.%)		0	3	5	5	7	8	0	0	C (at.%)		0	0	4	6	6	5	0	0
TEA, Si-H		0	1	2	3	5	10	25	50	TEA, Si- OH		0	1	2	3	5	10	25	50
Al (at.%)		0	0	4	7	14	23	41	46	Al (at.%)		0	6	11	22	35	46	45	46
Si (at.%)		91	87	86	82	65	47	7	0	Si (at.%)		73	60	49	40	21	4	0	0
O (at.%)		7	7	7	7	15	23	47	54	O (at.%)		7	7	7	7	15	23	47	54
C (at.%)		2	5	3	3	6	7	6	0	C (at.%)		2	5	3	3	6	7	6	0
DMAC, Si-H		0	1	2	3	5	10	20	DMAC, Si-OH		0	1	2	3	5	10	20		
Al (at.%)		0	0	3	4	6	16	33	Al (at.%)		0	5	8	9	12	21	30		
Si (at.%)		75	69	65	60	49	38	11	Si (at.%)		57	27	23	21	18	6	2		
O (at.%)		13	9	9	11	14	20	39	O (at.%)		33	35	39	36	40	41	48		
C (at.%)		12	3	26	25	30	26	17	C (at.%)		10	33	30	33	30	32	20		

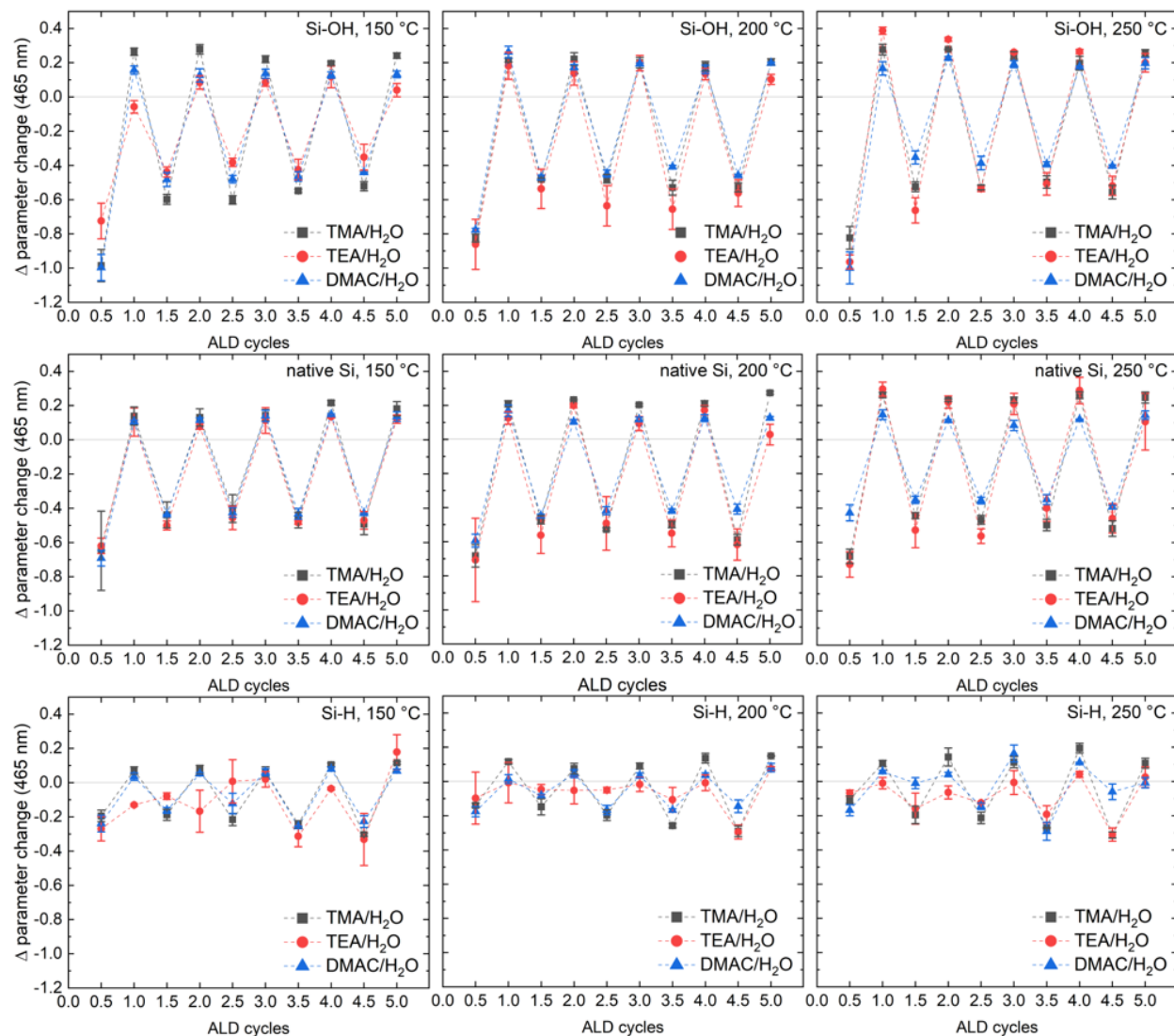


Figure S3.4. Delta parameter change at 465 nm wavelength during half-cycles of Al_2O_3 ALD using TMA/ H_2O , TEA/ H_2O , or DMAC/ H_2O on Si-OH (top row), native Si oxide (middle row), and Si-H (bottom row) surfaces at 150 °C, 200°C, and 250 °C. Δ parameter characterizes the phase change upon polarized light reflection and is correlated with the thin film optical thickness change – in the current regime, the film thickness increases as Δ decreases and vice versa.

3.9 References

1. Knoops, H. C. M., Langereis, E., van de Sanden, M. C. M. & Kessels, W. M. M. Conformality of Plasma-Assisted ALD: Physical Processes and Modeling. *Journal of The Electrochemical Society* **157**, G241 (2010).
2. Ylilammi, M., Ylivaara, O. M. E. & Puurunen, R. L. Modeling growth kinetics of thin films made by atomic layer deposition in lateral high-aspect-ratio structures. *Journal of Applied Physics* **123**, 205301 (2018).
3. Puurunen, R. L. & Gao, F. Influence of ALD temperature on thin film conformality: Investigation with microscopic lateral high-aspect-ratio structures. in *2016 14th International Baltic Conference on Atomic Layer Deposition, BALD 2016 - Proceedings 20–24* (Institute of Electrical and Electronics Engineers Inc., 2017). doi:10.1109/BALD.2016.7886526.
4. Cremers, V., Puurunen, R. L. & Dendooven, J. Conformality in atomic layer deposition: Current status overview of analysis and modelling. *Applied Physics Reviews* vol. 6 21302 (2019).
5. Hackley, J. C., Gougousi, T. & Demaree, J. D. Nucleation of atomic layer deposition films on chemical oxide and H-terminated Si. *J. Appl. Phys* **102**, 34101 (2007).
6. Oh, I.-K. *et al.* Comparative study of the growth characteristics and electrical properties of atomic-layer-deposited HfO₂ films obtained from metal halide and amide precursors †. *J. Mater. Chem. C* **6**, 7367 (2018).
7. Aarik, J. *et al.* Effects of precursors on nucleation in atomic layer deposition of HfO₂. *Applied Surface Science* **230**, 292–300 (2004).

8. McDonnell, S. *et al.* Controlling the atomic layer deposition of titanium dioxide on silicon: Dependence on surface termination. *Journal of Physical Chemistry C* **117**, 20250–20259 (2013).
9. Ande, C. K. *et al.* Role of Surface Termination in Atomic Layer Deposition of Silicon Nitride. *Journal of Physical Chemistry Letters* **6**, 3610–3614 (2015).
10. Longo, R. C. *et al.* Selectivity of metal oxide atomic layer deposition on hydrogen terminated and oxidized Si(001)-(2×1) surface. *J. Vac. Sci. Technol. B* **32**, 3–112 (2014).
11. Puurunen, R. L. Correlation between the growth-per-cycle and the surface hydroxyl group concentration in the atomic layer deposition of aluminum oxide from trimethylaluminum and water. *Applied Surface Science* **245**, 6–10 (2005).
12. Kim, D. H., Baek, S. bin & Kim, Y. C. Energy barriers for trimethylaluminum reaction with varying surface hydroxyl density. *Applied Surface Science* **258**, 225–229 (2011).
13. Baker, J. G., Schneider, J. R., Raiford, J. A., Paula, C. de & Bent, S. F. Nucleation Effects in the Atomic Layer Deposition of Nickel-Aluminum Oxide Thin Films. *Chemistry of Materials* **32**, 1925–1936 (2020).
14. Schilirò, E. *et al.* Aluminum oxide nucleation in the early stages of atomic layer deposition on epitaxial graphene. *Carbon* **169**, 172–181 (2020).
15. de Paula, C., Richey, N. E., Zeng, L. & Bent, S. F. Mechanistic Study of Nucleation Enhancement in Atomic Layer Deposition by Pretreatment with Small Organometallic Molecules. *Chemistry of Materials* **32**, 315–325 (2020).

16. Parsons, G. N. Functional model for analysis of ALD nucleation and quantification of area-selective deposition. *Journal of Vacuum Science & Technology A* **37**, 020911 (2019).
17. Longo, R. C. *et al.* Selectivity of metal oxide atomic layer deposition on hydrogen terminated and oxidized Si(001)-(2×1) surface. *Journal of Vacuum Science & Technology B, Nanotechnology and Microelectronics: Materials, Processing, Measurement, and Phenomena* **32**, 03D112 (2014).
18. Finnie, K. S. *et al.* Influence of Si(1 0 0) surface pretreatment on the morphology of TiO₂ films grown by atomic layer deposition. *Thin Solid Films* **440**, 109–116 (2003).
19. Methaapanon, R. & Bent, S. F. Comparative study of titanium dioxide atomic layer deposition on silicon dioxide and hydrogen-terminated silicon. *Journal of Physical Chemistry C* **114**, 10498–10504 (2010).
20. Green, M. L. *et al.* Nucleation and growth of atomic layer deposited HfO₂ gate dielectric layers on chemical oxide (Si-O-H) and thermal oxide or Si-O-N) underlayers. *Journal of Applied Physics* **92**, 7168 (2002).
21. Hackley, J. C., Gougousi, T. & Demaree, J. D. Nucleation of atomic layer deposition films on chemical oxide and H-terminated Si. *J. Appl. Phys* **102**, 34101 (2007).
22. Hackley, J. C., Demaree, J. D. & Gougousi, T. Growth and interface of films on H-terminated Si from a TDMAH and atomic layer deposition process. *J. Vac. Sci. Technol. A* **26**, 1235 (2008).

23. Alam, M. A. & Green, M. L. Mathematical description of atomic layer deposition and its application to the nucleation and growth of gate dielectric layers. *Journal of Applied Physics* **94**, 3403 (2003).
24. Minjauw, M. M., Rijckaert, H., Driessche, I. van, Detavernier, C. & Dendooven, J. Nucleation Enhancement and Area-Selective Atomic Layer Deposition of Ruthenium Using RuO₄ and H₂ Gas. *Chemistry of Materials* **31**, 1491–1499 (2019).
25. Lemaire, P. C., King, M. & Parsons, G. N. Understanding inherent substrate selectivity during atomic layer deposition: Effect of surface preparation, hydroxyl density, and metal oxide composition on nucleation mechanisms during tungsten ALD. *Journal of Chemical Physics* **146**, 052811 (2017).
26. Kalanyan, B., Lemaire, P. C., Atanasov, S. E., Ritz, M. J. & Parsons, G. N. Using Hydrogen to Expand the Inherent Substrate Selectivity Window during Tungsten Atomic Layer Deposition. *Chemistry of Materials* **28**, 117–126 (2016).
27. Kwon, J., Saly, M., Halls, M. D., Kanjolia, R. K. & Chabal, Y. J. Substrate selectivity of (tBu-Allyl)Co(CO)₃ during thermal atomic layer deposition of cobalt. *Chemistry of Materials* **24**, 1025–1030 (2012).
28. Hubbard, K. J. & Schlom, D. G. Thermodynamic stability of binary oxides in contact with silicon. *Journal of Materials Research* **11**, 2757–2776 (1996).
29. Puurunen, R. L. Surface chemistry of atomic layer deposition: A case study for the trimethylaluminum/water process. *Journal of Applied Physics* vol. 97 121301 (2005).

30. Kim, S. K. & Hwang, C. S. Atomic-layer-deposited thin films with thin layers grown by in situ oxidation. *J. Appl. Phys* **96**, 2323 (2004).
31. Ylivaara, O. M. E. *et al.* Aluminum oxide from trimethylaluminum and water by atomic layer deposition: The temperature dependence of residual stress, elastic modulus, hardness and adhesion. *Thin Solid Films* **552**, 124–135 (2014).
32. Wilk, G. D., Wallace, R. M. & Anthony, J. M. High- κ gate dielectrics: Current status and materials properties considerations. *Journal of Applied Physics* **89**, 5243–5275 (2001).
33. Liu, H. & Ye, P. D. MoS₂ dual-gate MOSFET with atomic-layer-deposited Al₂O₃ as top-gate dielectric. *IEEE Electron Device Letters* **33**, 546–548 (2012).
34. Hoivik, N. D. *et al.* Atomic layer deposited protective coatings for micro-electromechanical systems. in *Sensors and Actuators, A: Physical* vol. 103 100–108 (Elsevier, 2003).
35. Bordihn, S., Mertens, V., Müller, J. W. & Kessels, W. M. M. (Erwin). Deposition temperature dependence of material and Si surface passivation properties of O₃-based atomic layer deposited Al₂O₃-based films and stacks. *Journal of Vacuum Science & Technology A: Vacuum, Surfaces, and Films* **32**, 01A128 (2014).
36. Choi, H. S. *et al.* Improvement of electrical properties of ferroelectric gate oxide structure by using Al₂O₃ thin films as buffer insulator. *Thin Solid Films* **444**, 276–281 (2003).
37. Singh, P., Jha, R. K., Singh, R. K. & Singh, B. R. Preparation and characterization of Al₂O₃ film deposited by RF sputtering and plasma enhanced atomic layer deposition. *Journal of Vacuum Science & Technology B Nanotechnology and Microelectronics Materials Processing Measurement and Phenomena* **36**, 04G101 (2018).

38. Piagge, R. *et al.* Structural and Chemical Investigation of Annealed Al₂O₃ Films for Interpoly Dielectric Application in Flash Memories. doi:10.1149/1.2355710.
39. *United States Patent (19) Suntola et al. 54 METHOD FOR PRODUCING COMPOUND.* (1975).
40. Groner, M. D., Fabreguette, F. H., Elam, J. W. & George, S. M. Low-Temperature Al₂O₃ Atomic Layer Deposition. *Chemistry of Materials* **16**, 639–645 (2004).
41. Li, S. *et al.* Excellent silicon surface passivation using dimethylaluminium chloride as Al source for atomic layer deposited Al₂O₃. *physica status solidi (a)* **212**, 1795–1799 (2015).
42. Bao, Y., Laitinen, M., Sajavaara, T. & Savin, H. Ozone-Based Atomic Layer Deposition of Al₂O₃ from Dimethylaluminum Chloride and Its Impact on Silicon Surface Passivation. *Advanced Electronic Materials* **3**, 1600491 (2017).
43. Bao, Y., Huang, H., Zhu, Z., Lv, J. & Savin, H. Silicon Surface Passivation by Mixed Aluminum Precursors in Al₂O₃ Atomic Layer Deposition. in *Energy Procedia* vol. 92 304–308 (Elsevier Ltd, 2016).
44. Matero, R., Rahtu, A. & Ritala, M. In situ reaction mechanism studies on the atomic layer deposition of Al₂O₃ from (CH₃)₂AlCl and water. *Langmuir* **21**, 3498–3502 (2005).
45. Kukli, K., Ritala, M., Leskelä, M. & Jokinen, J. Atomic layer epitaxy growth of aluminum oxide thin films from a novel precursor and. *Journal of Vacuum Science & Technology A* **15**, 2214 (1997).

46. Katamreddy, R., Inman, R., Jursich, G., Soulet, A. & Takoudis, C. Atomic layer deposition of HfO₂, Al₂O₃, and HfAlO_x using O₃ and metal(diethylamino) precursors. *Journal of Materials Research* **22**, 3455–3464 (2007).
47. Majumder, P., Katamreddy, R. & Takoudis, C. Atomic layer deposited ultrathin HfO₂ and Al₂O₃ films as diffusion barriers in copper interconnects. *Electrochemical and Solid-State Letters* **10**, H291 (2007).
48. Wade, C. R. *et al.* Tris(dialkylamino)aluminums: Syntheses, characterization, volatility comparison and atomic layer deposition of alumina thin films. *Materials Letters* **61**, 5079–5082 (2007).
49. Katamreddy, R., Inman, R., Jursich, G., Soulet, A. & Takoudis, C. ALD and Characterization of Aluminum Oxide Deposited on Si(100) using Tris(diethylamino) Aluminum and Water Vapor. *Journal of The Electrochemical Society* **153**, C701 (2006).
50. Katamreddy, R., Inman, R., Jursich, G., Soulet, A. & Takoudis, C. Controlling interfacial reactions between HfO₂ and Si using ultrathin Al₂O₃ diffusion barrier layer. *Applied Physics Letters* **89**, 262906 (2006).
51. Katamreddy, R. *et al.* Post deposition annealing of aluminum oxide deposited by atomic layer deposition using tris(diethylamino)aluminum and water vapor on Si(100). *Thin Solid Films* **515**, 6931–6937 (2007).
52. Buttera, S. C., Mandia, D. J. & Barry, S. T. Tris(dimethylamido)aluminum(III): An overlooked atomic layer deposition precursor. *Journal of Vacuum Science & Technology A: Vacuum, Surfaces, and Films* **35**, 01B128 (2017).

53. Hiltunen, L. *et al.* Growth and characterization of aluminium oxide thin films deposited from various source materials by atomic layer epitaxy and chemical vapor deposition processes. *Materials Chemistry and Physics* **28**, 379–388 (1991).
54. Tiitta, M. *et al.* Preparation and characterization of phosphorus-doped aluminum oxide thin films. *Materials Research Bulletin* **33**, 1315–1323 (1998).
55. Potts, S. E., Dingemans, G., Lachaud, C. & Kessels, W. M. M. Plasma-enhanced and thermal atomic layer deposition of Al₂O₃ using dimethylaluminum isopropoxide, [Al(CH₃)₂(μ-O i Pr)]₂, as an alternative aluminum precursor. *Journal of Vacuum Science & Technology A: Vacuum, Surfaces, and Films* **30**, 021505 (2012).
56. Koo, J. *et al.* Characteristics of Al₂O₃ thin films deposited using dimethylaluminum isopropoxide and trimethylaluminum precursors by the plasma-enhanced atomic-layer deposition method. *Journal of the Korean Physical Society* **48**, 131–136 (2006).
57. Cho, W. *et al.* Atomic layer deposition of Al₂O₃ thin films using dimethylaluminum isopropoxide and water. *Journal of Vacuum Science & Technology A: Vacuum, Surfaces, and Films* **21**, 1366–1370 (2003).
58. An, K. S., Cho, W., Sung, K., Lee, S. S. & Kim, Y. Preparation of Al₂O₃ Thin Films by Atomic Layer Deposition Using Dimethylaluminum Isopropoxide and Water and Their Reaction Mechanisms. *Bulletin of the Korean Chemical Society* **24**, 1659–1663 (2003).
59. Min, Y. S., Cho, Y. J. & Hwang, C. S. Atomic layer deposition of Al₂O₃ thin films from a 1-methoxy-2-methyl-2-propoxide complex of aluminum and water. *Chemistry of Materials* **17**, 626–631 (2005).

60. Hashemi, F. S. M. *et al.* Aluminum tri-isopropoxide as an alternative precursor for atomic layer deposition of aluminum oxide thin films. *Journal of Vacuum Science & Technology A* **37**, 040901 (2019).
61. Brazeau, A. L. & Barry, S. T. Atomic layer deposition of aluminum oxide thin films from a heteroleptic, amidinate-containing precursor. *Chemistry of Materials* **20**, 7287–7291 (2008).
62. Mai, L. *et al.* Potential Precursor Alternatives to the Pyrophoric Trimethylaluminium for the Atomic Layer Deposition of Aluminium Oxide. *Chemistry – A European Journal* **25**, 7489–7500 (2019).
63. Xia, X., Taylor, A., Zhao, Y., Guldin, S. & Blackman, C. Use of a New Non-Pyrophoric Liquid Aluminum Precursor for Atomic Layer Deposition. *Materials* **12**, 1429 (2019).
64. Cao, L., Mattelaer, F., Sajavaara, T., Dendooven, J. & Detavernier, C. A liquid alkoxide precursor for the atomic layer deposition of aluminum oxide films. *Journal of Vacuum Science & Technology A* **38**, 022417 (2020).
65. Mai, L. *et al.* Unearthing [3-(Dimethylamino)propyl]aluminium(III) Complexes as Novel Atomic Layer Deposition (ALD) Precursors for Al₂O₃: Synthesis, Characterization and ALD Process Development. *Chemistry - A European Journal* **23**, 10768–10772 (2017).
66. Parsons, G. N. & Clark, R. D. Area-Selective Deposition: Fundamentals, Applications, and Future Outlook. *Chemistry of Materials* vol. 32 4920–4953 (2020).
67. Biyikli, N., Haider, A., Deminskyi, P. & Yilmaz, M. Self-aligned nanoscale processing solutions via selective atomic layer deposition of oxide, nitride, and metallic films. in *Low-*

- Dimensional Materials and Devices 2017* (eds. Kobayashi, N. P., Talin, A. A., Davydov, A. v. & Islam, M. S.) vol. 10349 20 (SPIE, 2017).
68. Biercuk, M. J., Monsma, D. J., Marcus, C. M., Backer, J. S. & Gordon, R. G. Low-temperature atomic-layer-deposition lift-off method for microelectronic and nanoelectronic applications. *Applied Physics Letters* **83**, 2405–2407 (2003).
69. Nelson, S. F., Ellinger, C. R. & Levy, D. H. Improving yield and performance in ZnO thin-film transistors made using selective area deposition. *ACS Applied Materials and Interfaces* **7**, 2754–2759 (2015).
70. Ellinger, C. R. & Nelson, S. F. Selective area spatial atomic layer deposition of ZnO, Al₂O₃, and aluminum-doped ZnO using poly(vinyl pyrrolidone). *Chemistry of Materials* **26**, 1514–1522 (2014).
71. Färm, E., Kemell, M., Santala, E., Ritala, M. & Leskelä, M. Selective-Area Atomic Layer Deposition Using Poly(vinyl pyrrolidone) as a Passivation Layer. *Journal of The Electrochemical Society* **157**, K10 (2010).
72. Peng, Q., Tseng, Y. C., Darling, S. B. & Elam, J. W. Nanoscopic patterned materials with tunable dimensions via atomic layer deposition on block copolymers. *Advanced Materials* **22**, 5129–5133 (2010).
73. Gay, G. *et al.* CMOS compatible strategy based on selective atomic layer deposition of a hard mask for transferring block copolymer lithography patterns. *Nanotechnology* **21**, 435301 (2010).

74. Kim, H. G. *et al.* Effects of Al precursors on deposition selectivity of atomic layer deposition of Al₂O₃ using ethanethiol inhibitor. *Chemistry of Materials* **32**, 8921–8929 (2020).
75. Oh, I.-K., Sandoval, T. E., Liu, T.-L., Richey, N. E. & Bent, S. F. Role of Precursor Choice on Area-Selective Atomic Layer Deposition. *Chemistry of Materials* **33**, 3926–3935 (2021).
76. Ghosh, M. K. & Choi, C. H. The initial mechanisms of Al₂O₃ atomic layer deposition on OH/Si(1 0 0)-2 × 1 surface by tri-methylaluminum and water. *Chemical Physics Letters* **426**, 365–369 (2006).
77. Ghosh, M. K. & Choi, C. H. Adsorption reactions of dimethylaluminum isopropoxide and water on the H/Si(100)-2 × 1 surface: Initial reactions for atomic layer deposition of Al₂O₃. *Journal of Physical Chemistry B* **110**, 11277–11283 (2006).
78. Halls, M. D. & Raghavachari, K. Atomic Layer Deposition Growth Reactions of Al₂O₃ on Si(100)-2×1. *Journal of Physical Chemistry B* **108**, 4058–4062 (2004).
79. Halls, M. D. & Raghavachari, K. Atomic layer deposition of Al₂O₃ on H-passivated Si. I. Initial surface reaction pathways with H/Si(100)-2×1. *Journal of Chemical Physics* **118**, 10221–10226 (2003).
80. Widjaja, Y. & Musgrave, C. B. Quantum chemical study of the mechanism of aluminum oxide atomic layer deposition. *Applied Physics Letters* **80**, 3304–3306 (2002).
81. Vandalon, V. & Erwin Kessels, W. M. M. Initial Growth Study of Atomic-Layer Deposition of Al₂O₃ by Vibrational Sum-Frequency Generation. *Langmuir* **35**, 10374–10382 (2019).

82. Gong, B., Peng, Q. & Parsons, G. N. Conformal Organic-inorganic hybrid network polymer thin films by molecular layer deposition using trimethylaluminum and glycidol. *Journal of Physical Chemistry B* **115**, 5930–5938 (2011).
83. Lawrence, D. *Handbook of Auger Electron Spectroscopy*. (Physical Electronics Industries, 1976).
84. Sun, Q. Q. *et al.* Effects of chlorine residue in atomic layer deposition hafnium oxide: A density-functional-theory study. *Applied Physics Letters* **91**, 022901 (2007).
85. Levrau, E. *et al.* In Situ IR Spectroscopic Investigation of Alumina ALD on Porous Silica Films: Thermal versus Plasma-Enhanced ALD. *Journal of Physical Chemistry C* **118**, 29854–29859 (2014).
86. Vandalon, V. & Kessels, W. M. M. What is limiting low-temperature atomic layer deposition of Al₂O₃? A vibrational sum-frequency generation study. *Applied Physics Letters* **108**, 011607 (2016).

CHAPTER 4

Comparison of Chlorinating Co-Reactants for Atomic Layer Etching of Metal Oxides

Using Tungsten Hexafluoride

Holger Saare, Wenyi Xie and Gregory N. Parsons

4.1 Preface

Recent advancements in semiconductor industry have created an exigency for processes that allow to deposit and etch material in conformal matter in three-dimensional devices. While the former is commonly achieved using atomic layer deposition (ALD), the latter can be accomplished by thermal atomic layer etching (ALE), which similarly is a two-step self-limiting method. In this study the effect of co-reactant design is elucidated in ALE of TiO_2 and ZrO_2 using WF_6 as a fluorinating agent and BCl_3 , TiCl_4 , or SOCl_2 as co-reactants. Atomic force microscopy (AFM), *in-situ* ellipsometry, and *in-vacuo* Auger electron spectroscopy (AES) measurements were coupled with thermodynamic modeling to study the ALE processes. All three co-reactants exhibited exposure saturation, characteristic to ALE, and etch rates linearly increasing with temperature. At 170 °C, TiO_2 was etched at 0.24, 0.18, and 0.20 nm/cycle using WF_6 with BCl_3 , TiCl_4 , or SOCl_2 , respectively. ZrO_2 was etched at 325 °C at rates of 0.96, 0.74, and 0.13 nm/cycle correspondingly. The higher temperature needed for ZrO_2 ALE was attributed to lower volatility of resulting ZrCl_4 vs TiCl_4 . In addition, the model predicted a formation of a solid $\text{Zr}(\text{SO}_4)_2$ on the ZrO_2 surface by SOCl_2 , which was not removed by WF_6 at $T \leq 300$ °C. It was shown that using BCl_3 or TiCl_4 resulted in solid B_2O_3 or TiO_2 residue on both metal oxide surfaces, which was removed by subsequent WF_6 exposure. In contrast, using SOCl_2 resulted in a clean TiO_2 surface. In addition, it was demonstrated that both WF_6 and SOCl_2 lead to chemical vapor etching of TiO_2

at $T \geq 200$ °C. This study broadens the understanding of co-etchants role during thermal ALE and expands the range of reactants that can be used for vapor etching of metal oxides.

4.2 Introduction

An etching step is an essential procedure in semiconductor manufacturing to remove unwanted materials from the sample substrate. This is done, for example, to etch trenches, shape via holes, or create patterns. While wet etching methods were historically used for microfabrication, the continuous device miniaturization has limited their use due to their isotropic nature and hard to control etch rates.¹ As such, dry etching technologies are mainly used in advanced processes due to their more precise feature size control and capability to achieve higher aspect ratios.^{1,2} Dry etching technologies include processes that employ physical etching (such as reactive ion etching, sputter etching, or ion milling), or chemical etching (chemical vapor etching, atomic layer etching).

Vapor etching is conventionally used in semiconductor industry to etch the sacrificial layer present in a device. For example, xenon difluoride (XeF_2) or HF vapor combined with water as a catalyst are employed to remove a silicon oxide layer in a silicon MEMS devices.³⁻⁸ In addition to SiO_2 , chemical vapor etching (CVE) of other materials, such as TiO_2 , Al_2O_3 , and Cu have been reported using WF_6 , $\text{HF}/\text{Sn}(\text{acac})_2$, and O_2/hfac , respectively.⁹⁻¹¹ However, chemical vapor etching of many materials is limited due to formation of metal fluorides or other species that are nonvolatile at the reaction temperature. This has enabled the development of atomic layer etching (ALE) process, which is a self-limiting two-step process.¹²⁻¹⁴ A surface modification step is followed by a removal step, where the modified layer is either removed through bombardment by inert ions or by introducing a reactant to volatilize the layer. While the mechanisms of the first

have been studied for more than 30 years, the latter, called thermal atomic layer etching, is gaining traction due to its isotropicity and conformality, required for complex nanopatterns.^{15,16}

Thermal ALE processes have been successfully developed for various materials, including Al_2O_3 ,^{17–20} Si ,^{21,22} SiO_2 ,^{23,24} HfO_2 ,^{25–27} ZnO_2 ,^{28,29} Cu ,^{30–32} W ,^{33,34} TiN ,^{10,35,36} and many more.^{37–46} Several mechanisms have been developed for ALE, including fluorination/ligand-exchange, conversion/etch, oxidation/fluorination, and others.¹⁶ ZrO_2 has been etched using HF as a fluorinating agent and $\text{Sn}(\text{acac})_2$, $\text{AlCl}(\text{CH}_3)_2$, or SiCl_4 to volatilize the fluorinated surface layer through ligand-exchange.¹⁰ Similarly, a TiO_2 ALE process has been developed using alternating doses of WF_6 and BCl_3 .⁹ In this process the WF_6 fluorinates the surface, creating $\text{WO}_x\text{F}_y/\text{TiO}_v\text{F}_z$ layer that is volatile at temperatures above 200 °C, enabling chemical vapor etching (CVE) of the TiO_2 . At lower temperatures ALE can be achieved by BCl_3 exposure, which leads to ligand exchange, producing volatile TiCl_4 and WOCl_4 products and a solid B_2O_3 surface species, which is subsequently etched by WF_6 exposure.

In-situ analysis techniques allow the monitoring of the etching process under the practical conditions, without exposing the sample to atmosphere or interrupting the experiment. *In-situ* spectroscopic ellipsometry can be employed to actively monitor the etch rate or changes in the optical properties of the material being etched. It has been previously utilized to analyze ALE of various materials, including GaN ,⁴⁷ Ga_2O_3 ,⁴⁸ ZnO ,²⁹ Cu ,³⁰ and W .⁴⁹ To confirm the conversion or removal of an element, *in-situ* chemical analysis methods, such as x-ray photoelectron spectroscopy (XPS) or Auger electron spectroscopy (AES) are often used. For example, *in-situ* XPS has been used to study the efficiency of acac vs. hfacH for ALE when combined with chlorine gas⁵⁰ and to study the mechanism of Fe ALE, when etched using Cl_2 and acac.⁵¹ Similarly, *in-situ* AES has been utilized to study the ALE of GaAs when etched using Cl_2 exposure followed by

flash heating⁵² and to investigate both thermal and plasma enhanced ALE of Al₂O₃ and Hf₂O films.⁵³

In this paper the etching characteristics of thionyl chloride (SOCl₂), titanium tetrachloride (TiCl₄), and boron trichloride (BCl₃) when coupled with WF₆ in a fluorination/ligand-exchange atomic layer etching process are compared. The processes are characterized using *in-situ* ellipsometry, *in-vacuo* Auger electron spectroscopy (AES), and atomic force microscopy (AFM). The results indicate that while all three chlorinating precursors lead to ALE of ZrO₂ and TiO₂, the reaction byproducts differ, leading to distinct etch rates and temperature windows. While SOCl₂ has been previously shown to etch TiN,⁵⁴ this is the first ALE process utilizing SOCl₂ as a co-reactant. Although WF₆/BCl₃ combination has been shown to lead to ALE of TiO₂, the drawback of using BCl₃ is that the reaction results in a solid B₂O₃ layer, which has to be removed by subsequent WF₆ exposure.⁹ In contrast, SOCl₂ reaction on TiO₂ results only in volatile species, leaving a clean oxide surface. In addition, we show that at higher temperatures (>190 °C) the exposure of SOCl₂ leads to vapor etching of TiO₂ by converting the metal oxide to volatile TiCl₄ and SO₂ species, while ZrO₂ is not etched due to the low volatility of ZrCl₄. These results improve our understanding of the importance of co-reactant selection during atomic layer etching processes and expand the range of reactants and materials that can be used for vapor etching of metal oxides.

4.3 Experimental Details

4.3.1 Reactor Design

The etching processes were carried out in a home-built warm-walled chamber system as shown in Figure 4.1. The system consists of a processing chamber, equipped with an *in-situ* multi-wavelength ellipsometer, a load lock and an ultrahigh vacuum analysis chamber, equipped with Auger electron spectroscopy (AES). The samples are introduced into the system on a 2-inch

stainless steel puck, which can be transferred between the chambers using linear transfer arms. During processing the sample was heated to a constant temperature using two PID-controlled halogen lamps. Argon (99.999% purity, Arc3 gases) were used as a carrier and purge gas at a flow rate of 95 sccm, as set by mass-flow controllers. The processing chamber was pumped out using a turbo pump (Seiko-Seiki STP-300C) and a backing pump (Alcatel 2021a) with a throttle valve located before the turbo pump used to control the operating pressure, which was set at 400 mTorr.

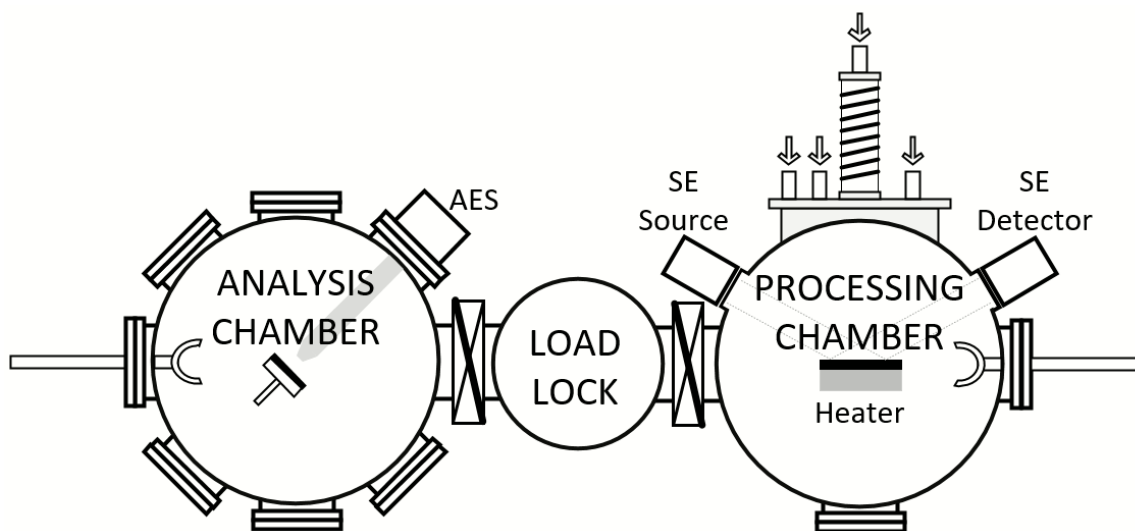


Figure 4.1. Schematic view of warm-walled chamber system. The system consists of a processing chamber, equipped with in-situ spectroscopic ellipsometer (SE) and of an analysis chamber with in-situ Auger electron spectroscopy.

4.3.2 Substrate Preparation and Etching

The TiO₂ substrates used in this study were deposited in the same chamber immediately before the etching process using TiCl₄ (99% purity, Strem Chemicals) and deionized H₂O. The titania was deposited on chemical Si oxide at 170 °C. The zirconia thin films were deposited on alumina thin films using Ultratech Fiji G2 system. The deposition was carried out at 250 °C using TDMA-Zr and DI-H₂O as precursors. All substrates were purged in argon and held at processing

temperature for 30 minutes to allow the conditions to stabilize before etching. Tungsten hexafluoride (99.99% purity, Galaxy Chemical), boron trichloride (99.9% purity, Matheson), thionyl chloride (99% purity, MilliporeSigma), and titanium tetrachloride (99% purity, Strem Chemicals) were used as etchants. The ALE cycles followed a dosing sequence of WF₆/purge/pump/pressurize/x/purge/pump/pressurize with timings of 0.08/15/10/15/x/15/10/15 s, where x stands for BCl₃, TiCl₄, or SOCl₂ with dosing times of 0.08s, 0.1s, or 0.2s, respectively. During the pump step the throttle valve to a turbo pump is opened completely to evacuate the chamber to a base pressure of 10⁻⁵ Torr. The subsequent pressurization step is necessary to bring the system back to the stable operating pressure of 400 mTorr. The vapor etching processes followed the same sequence, but without the WF₆ dosing step.

4.3.3. Process Characterization

The changes in film optical thicknesses during etching processes were monitored using *in-situ* multiwavelength ellipsometer (Film Sense FS-1). The ellipsometer was set at 70° ± 1° incident angle and a data point was obtained after every etching cycle. For greater accuracy, the measurement lasted 10 seconds and output an average of measurement results over that period. The optical film thicknesses were calculated by fitting the obtained raw ψ and Δ values to a Cauchy model.

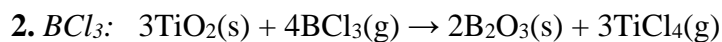
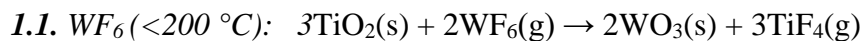
In-vacuo Auger electron spectroscopy (AES) measurements were performed to monitor the elemental composition changes of the metal oxides during etching. The AES system employs a coaxial cylindrical mirror analyzer (Perkin Elmer PHI 10-155) and a 3 kV electron beam. The ultrahigh vacuum analysis chamber was kept at pressure of ~10⁻¹⁰ Torr using an ion pump (Digital 500 220 l/s) and a turbo pump (Edwards EXT501).

The morphology of samples was examined using atomic force microscopy (AFM). The surface roughness data were acquired using Asylum MFP-3D Classic AFM in tapping mode. A silicon probe with cantilever length of 125 μm and force constant of 40 N m^{-1} was used at ambient conditions.

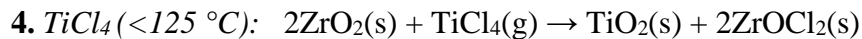
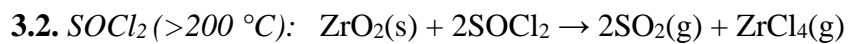
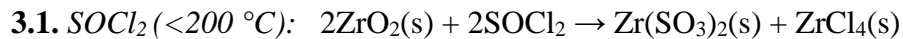
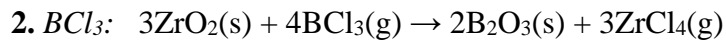
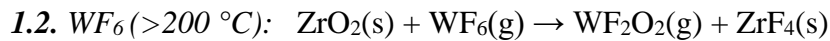
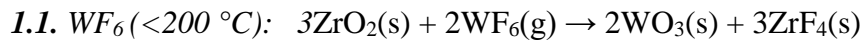
4.4 Results and Discussion

4.4.1. Thermodynamic Modeling of Reactions on TiO_2 and ZrO_2

Thermodynamic modeling⁵⁵ was used to predict the effect of exposure by individual reactants (WF_6 , BCl_3 , SOCl_2 , and TiCl_4) on the chemical composition of TiO_2 and ZrO_2 in the temperature range of 25 to 400 $^\circ\text{C}$. The model outputs the resulting equilibrium composition by minimizing the system's free energy. It is important to note that it is a thermodynamic calculation, it does not include kinetic effects and presumes a closed system. The calculations were done at a pressure of 1.5 Torr with the molecular ratios of TiO_2 to WF_6 , BCl_3 , SOCl_2 , and TiCl_4 being 1:1, 0.75:1, 1:1, and 0.5:1, respectively. Figures 4.2(a,b,c,d) show the expected outcome for WF_6 , BCl_3 , SOCl_2 , and TiCl_4 reacting on TiO_2 . The model predicts that TiO_2 reacts with WF_6 , BCl_3 , and SOCl_2 . Exposing TiO_2 to WF_6 forms a solid TiF_4 and WO_3 layers at temperatures below 200 $^\circ\text{C}$, at higher temperatures, they volatilize as gaseous TiF_4 and WO_2F_2 , enabling chemical vapor etching. While both SOCl_2 and BCl_3 are both predicted to form volatile TiCl_4 , the former results in gaseous SO_2 species, while the latter leaves a solid B_2O_3 layer on the surface, hindering further reactions with BCl_3 . The predicted reactions with individual etchants on TiO_2 surface can be summarized as follows:



Figures 4.2(e,f,g,h) show the expected outcome for WF₆, BCl₃, SOCl₂, and TiCl₄ reacting on ZrO₂. The calculations were done with molecular ratios of ZrO₂ to WF₆, BCl₃, SOCl₂, and TiCl₄ being 1:1, 0.75:1, 1:1, and 0.5:1, respectively. On ZrO₂, the WF₆ reaction proceeds similarly as on TiO₂, fluorinating the zirconia and resulting in solid WO₃ at temperatures below 200 °C and volatile WO₂F₂ at higher temperatures. However, in contrast to TiF₄, the resulting ZrF₄ is predicted to remain solid at all temperatures studied. Similar to TiO₂, both BCl₃ and SOCl₂ chlorinate the zirconia surface. The formed ZrCl₄ is predicted to be volatile at temperatures above 175 °C. The reaction with BCl₃ inhibits further reaction of the surface due to the creation of a B₂O₃ layer, preventing chemical vapor etching by BCl₃, while enabling atomic layer etching of ZrO₂. Exposure of zirconia to SOCl₂ forms a solid Zr(SO₃)₂ layer at temperatures below 225 °C, while only volatile SO₂ and ZrCl₄ are predicted to form at higher temperatures. In lieu of chlorinating the zirconia, exposure to TiCl₄ is expected to convert the ZrO₂ into TiO₂ and ZrOCl₂ at lower temperatures (<125 °C), while no reaction takes place at higher temperatures (>125 °C). The predicted reactions with individual etchants on ZrO₂ surface can be summarized as follows:



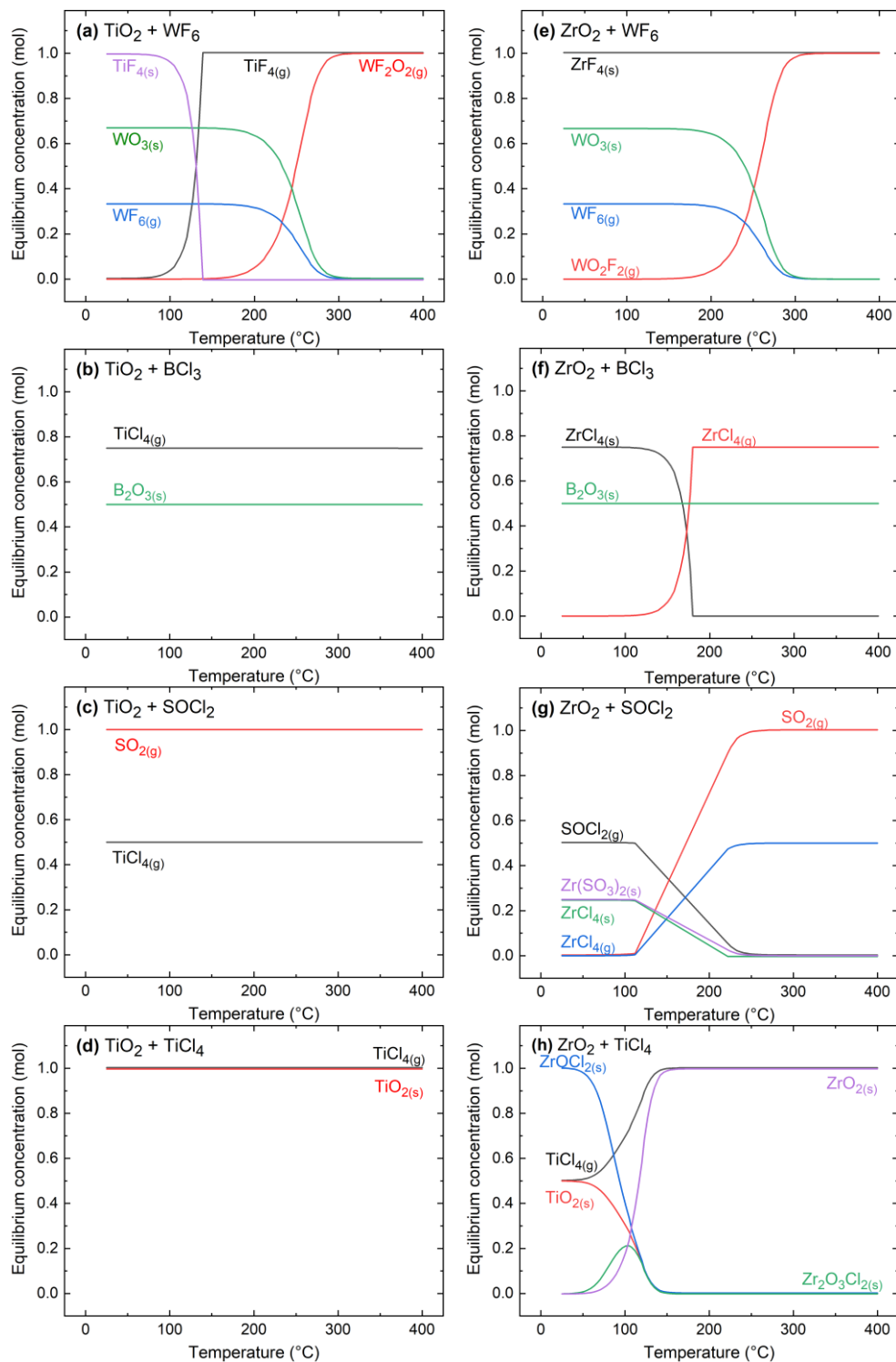


Figure 4.2. Expected equilibrium species determined by thermodynamic modeling in the temperature range from 25 °C to 400 °C for (a/e) 1 mol $\text{TiO}_2/\text{ZrO}_2$ & 1 mol WF_6 , (b/f) 0.75 mol $\text{TiO}_2/\text{ZrO}_2$ & 1 mol BCl_3 , (c/g) 0.5 mol $\text{TiO}_2/\text{ZrO}_2$ & 1 mol SOCl_2 , and (d/h) 1 mol $\text{TiO}_2/\text{ZrO}_2$ & 1 mol TiCl_4 .

4.4.2 *In-situ* Ellipsometry Study of Reactions on TiO₂ and ZrO₂

The effect of exposure of individual reactants (WF₆, BCl₃, SOCl₂, TiCl₄) on the thickness of the titania and zirconia thin films were confirmed by *in-situ* ellipsometry. Before etching, the TiO₂ film was deposited on a silicon wafer by ALD at 170 °C using TiCl₄ and H₂O in the same reactor. The results of all exposures on TiO₂ are plotted in figures 4.3(a,b,c,d). The data shows that TiO₂ is etched by WF₆ exposure at temperatures ≥ 200 °C, confirming previously published results.⁹ At temperatures below 200 °C the optical thickness shows small decrease during initial doses, which stops with subsequent exposures. While the chlorinating reactants BCl₃ and TiCl₄ do not show any apparent thickness changes after the first dose in the temperature range 160–240 °C, the SOCl₂ doses lead to thickness decrease at temperatures above 220 °C. Similar to WF₆, the etch rates using SOCl₂ increase as the temperature increases. The etching of TiO₂ by WF₆ at temperatures above 200 °C confirms the modeling results, as it predicted the formation of solid WO₃ layer at temperatures below 200 °C and volatile WF₂O₂ and TiF₄ species above 200 °C. Likewise, TiO₂ was etched by SOCl₂ at temperatures above 200 °C, predicted by the model to be due to conversion to volatile SO₂ and TiCl₄ species. However, while the thermodynamic modeling predicted the etching to happen throughout the temperature range studied, the etching is kinetically limited at temperatures below 200 °C.

The ZrO₂ films were deposited on alumina thin film at 250 °C using TDMA-Zr and H₂O. The alumina layers were necessary as WF₆ reacts with underlying Si after ZrO₂ has been removed by ALE, resulting in constant W growth at temperatures above 300 °C.⁵⁶ The deposition was carried out in a separate reactor and the sample was transferred before etching. The results of all individual exposures on ZrO₂ are plotted in figures 4.3(e,f,g,h). In contrast to titania, exposing zirconia to WF₆ lead to thickness decrease which stopped after a few initial cycles. Doses of BCl₃,

SOCl_2 , or TiCl_4 do not cause significant changes in the film thickness. The initial decrease of ZrO_2 thickness by WF_6 doses is consistent by model predicting formation of volatile WO_2F_2 species and a solid ZrF_4 , which inhibits further reactions with WF_6 . Despite the model predicting etching of ZrO_2 by SOCl_2 , the reaction is kinetically limited, or a solid $\text{Zr}(\text{SO}_3)_2$ layer is present on the surface in the measured temperature range. As such, vapor etching by SOCl_2 is shown to be realizable for a limited number of metal oxides films.

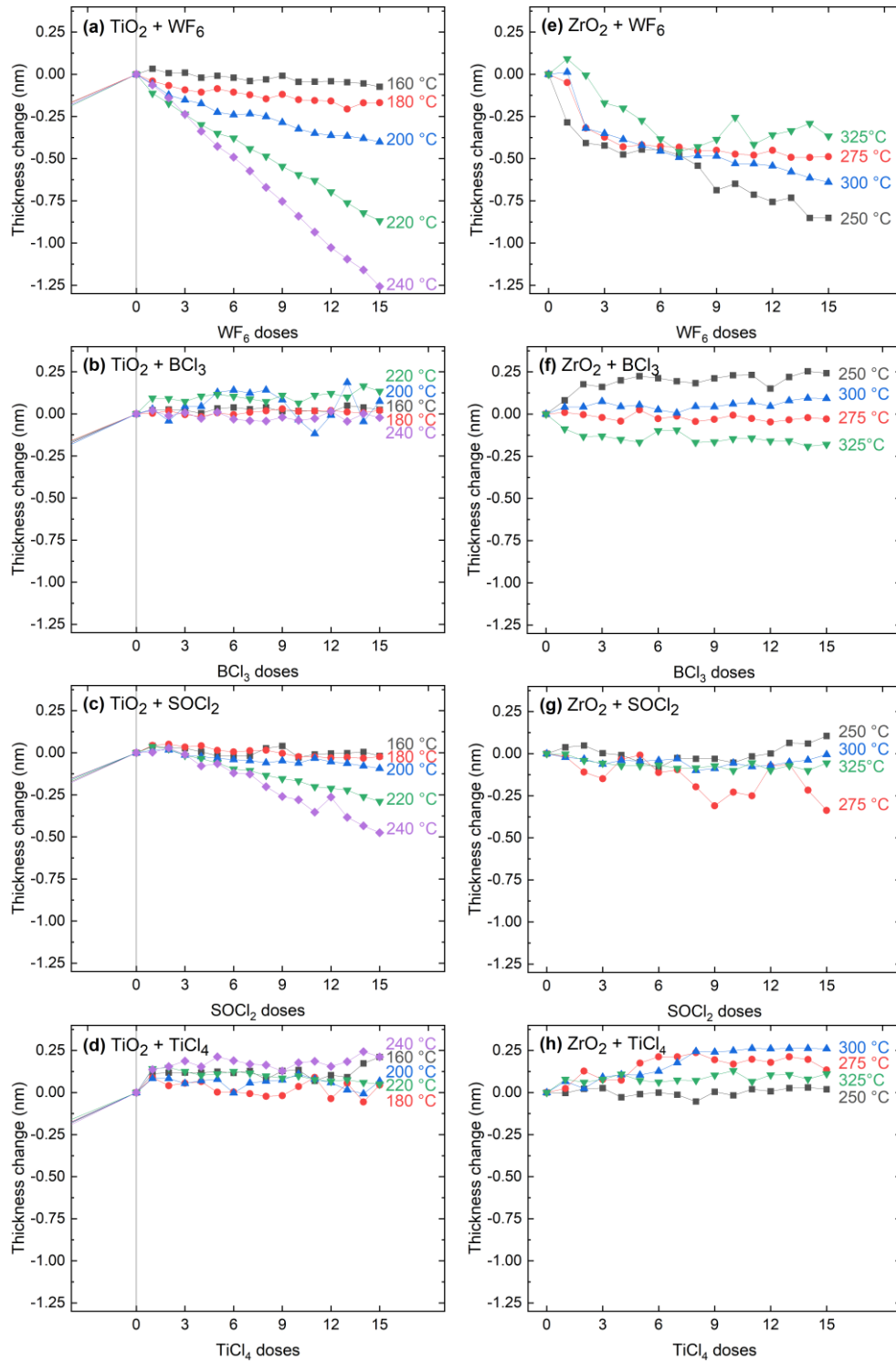
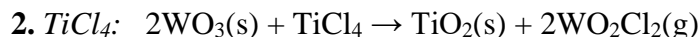
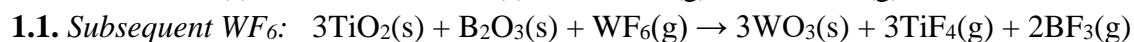


Figure 4.3. Thickness change of TiO_2 and ZrO_2 thin films when exposed to WF_6 (a,e), BCl_3 (b,f), SOCl_2 (c,g), or TiCl_4 (d,h) doses at various temperatures as measured by *in-situ* ellipsometry.

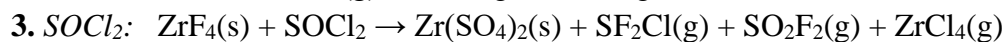
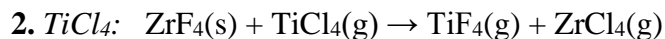
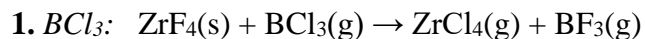
4.4.3 Thermodynamic Modeling of Reactions During ALE

While individually only exposure of WF_6 and SOCl_2 were shown to lead to CVE of TiO_2 at higher temperatures, the formation of solid surface species at lower temperatures can be exploited for a more controlled etch by forming a two-step atomic layer etch process. As WF_6 reacts with the metal oxide film in the first step, a WO_3 layer is formed for TiO_2 and a ZrF_4 layer for ZrO_2 . Thermodynamic modeling was used to predict the species created during the atomic layer etching process. The resulting reaction products as the WO_3 layer, which resulted from TiO_2 exposure to WF_6 , is exposed to the chlorinating reactants, are plotted in figures 4.4(a,b,c). As WO_3 reacts with BCl_3 , volatile WOCl_4 and WO_2Cl_2 species and a solid B_2O_3 layer are created. While the B_2O_3 could be removed with the subsequent WF_6 exposure as shown in figure S4.1, the resulting solid layer could be an undesirable product if incomplete removal of the TiO_2 layer is desired. In contrast, SOCl_2 exposure is predicted to result in volatile SO_2 and WO_2Cl_2 species, effectively removing the layer and leaving a clean surface. According to the model, the WO_3 reaction with TiCl_4 results in a solid TiO_2 and partial chlorination of the layer to WO_2Cl_2 . The predicted ALE chemistry of the WO_3 exposure to chlorinating co-reactants can be summarized as follows:



The reaction products predicted for the chlorination of the ZrF_4 layer, which resulted in ZrO_2 exposure to WF_6 , are plotted in figures 4.4(d,e,f). The BCl_3 pulse is predicted to result in gaseous BF_3 and ZrCl_4 products at temperatures above 200 °C. In contrast, the SOCl_2 exposure generates a solid $\text{Zr}(\text{SO}_4)_2$ in addition to gaseous SF_2Cl , ZrCl_4 , and SO_2F_2 species. As shown in figure S4.1, this layer can be removed by subsequent WF_6 exposure. The TiCl_4 pulse is shown to

not react with the ZrF₄ up to the temperature of ~375 °C, above which volatile ZrCl₄ and TiF₄ are created through ligand exchange. The predicted ALE chemistry of the ZrF₄ exposure to chlorinating co-reactants can be summarized as follows:



The reaction products for the chlorination of the WO₃ and ZrF₄ layers, which resulted from TiO₂ and ZrO₂ exposure to WF₆, respectively, greatly differ according to the modeling output. While a solid B₂O₃ layer is formed by WO₃ exposure to BCl₃, only gaseous byproducts ZrCl₄ and BF₃ are formed by ZrF₄ exposure to BCl₃, resulting in a clean ZrO₂ surface. Likewise, the TiCl₄ exposure is expected to convert the WO₃ to a solid TiO₂, while for ZrF₄ only volatile TiF₄ and ZrCl₄ gases are formed at temperatures above 200 °C. In contrast, SOCl₂ is modeled to convert WO₃ to volatile species, leaving a clean TiO₂ surface, while a solid ZrF₄ is formed on the ZrO₂ surface.

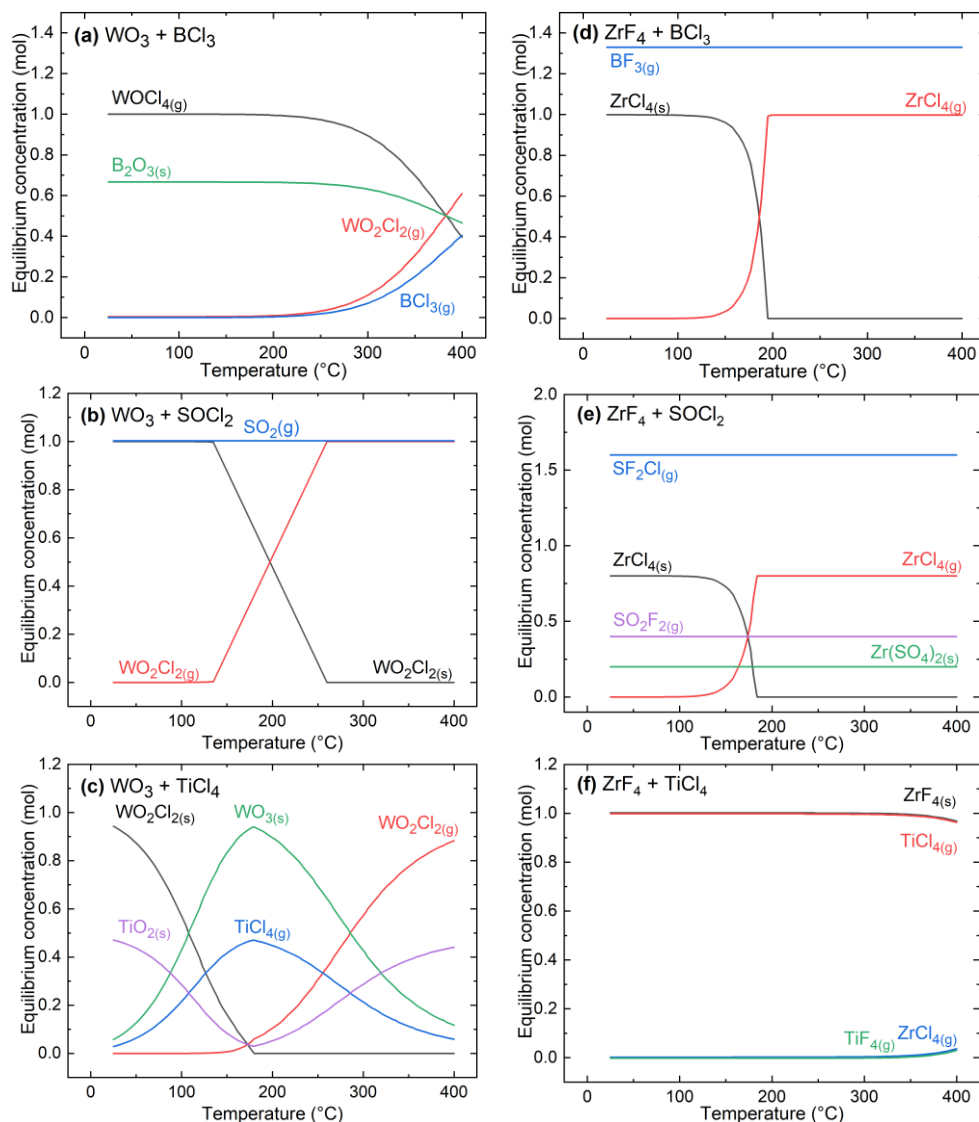


Figure 4.4. Expected equilibrium species determined by thermodynamic modeling in the temperature range from 25 °C to 400 °C for 1 mol WO_3 reacting with (a) 4/3 mol BCl_3 , (b) 1 mol TiCl_4 , (c) 1 mol SOCl_2 , and for 1 mol ZrF_4 reacting with (d) 4/3 mol BCl_3 , (e) 1 mol TiCl_4 , (f) 2.4 mol SOCl_2 .

4.4.4 *In-situ* Ellipsometry Measurements of TiO_2 and ZrO_2 ALE

In-situ ellipsometry was used to obtain the saturation curves for both substrates by determining the etch per cycle (EPC) dependence of the dosing time for each reactant. For this, WF_6 dose times in the ALE cycle were fixed at 0.14 s and the dose times of chlorinating precursors

were varied. Similarly, for the WF_6 saturation, the dose times of $\text{BCl}_3/\text{TiCl}_4/\text{SOCl}_2$ were fixed at 0.14/0.25/0.25 s, while the dose time of WF_6 was varied in independent runs. The results are plotted in figure 4.5, where the EPC is presented as an average etch rate over 10 ALE cycles carried out at 170 °C for TiO_2 and at 325 °C for ZrO_2 . The raw data, based on which the EPC is calculated, is shown in figure S4.2. It is evident that each of the chemistries used reached saturation, confirming the self-limiting nature of the process, characteristic to atomic layer etching. The etch rates of TiO_2 saturated at 0.24, 0.18, and 0.20 nm/cycle for BCl_3 , TiCl_4 , and SOCl_2 , respectively. The saturated etch rates of ZrO_2 are 0.96, 0.74, and 0.13 nm/cycle, respectively. The EPC saturates at 0.08 s dosing times for WF_6 for all processes, while 0.08 s is required for BCl_3 , and 0.2 s for both TiCl_4 and SOCl_2 to reach saturation on both TiO_2 and ZrO_2 .

The obtained saturated dosing times were used in acquiring the etch rate as a function of the sample temperature. *In-situ* ellipsometry measurements were performed in the temperature range of 160-190 °C for the TiO_2 and 250-325 °C for the ZrO_2 as shown in figure 4.6. The etch rate is strongly dependent on the temperature and increases in linear fashion as the temperature is increased for all chemistries. The etch rate of ZrO_2 using $\text{WF}_6/\text{SOCl}_2$ remains close to zero for temperatures ≤ 300 °C, rising to ~ 0.16 nm/cycle at 325 °C. Although the reaction was predicted to occur at all temperatures by the thermodynamic model, the process is kinetically limited. The limiting step is presumed to be the fluorination of the formed $\text{Zr}(\text{SO}_4)_2$ by WF_6 exposure with calculated ΔG values of -16.4, -22.1, and -27.9 kcal at 250, 300, 350 °C, respectively. In contrast, the ZrF_4 ligand exchange by SOCl_2 proceeds at calculated ΔG values of -906.1, -913.2, and -916.8 kcal at the same respective substrate temperatures.

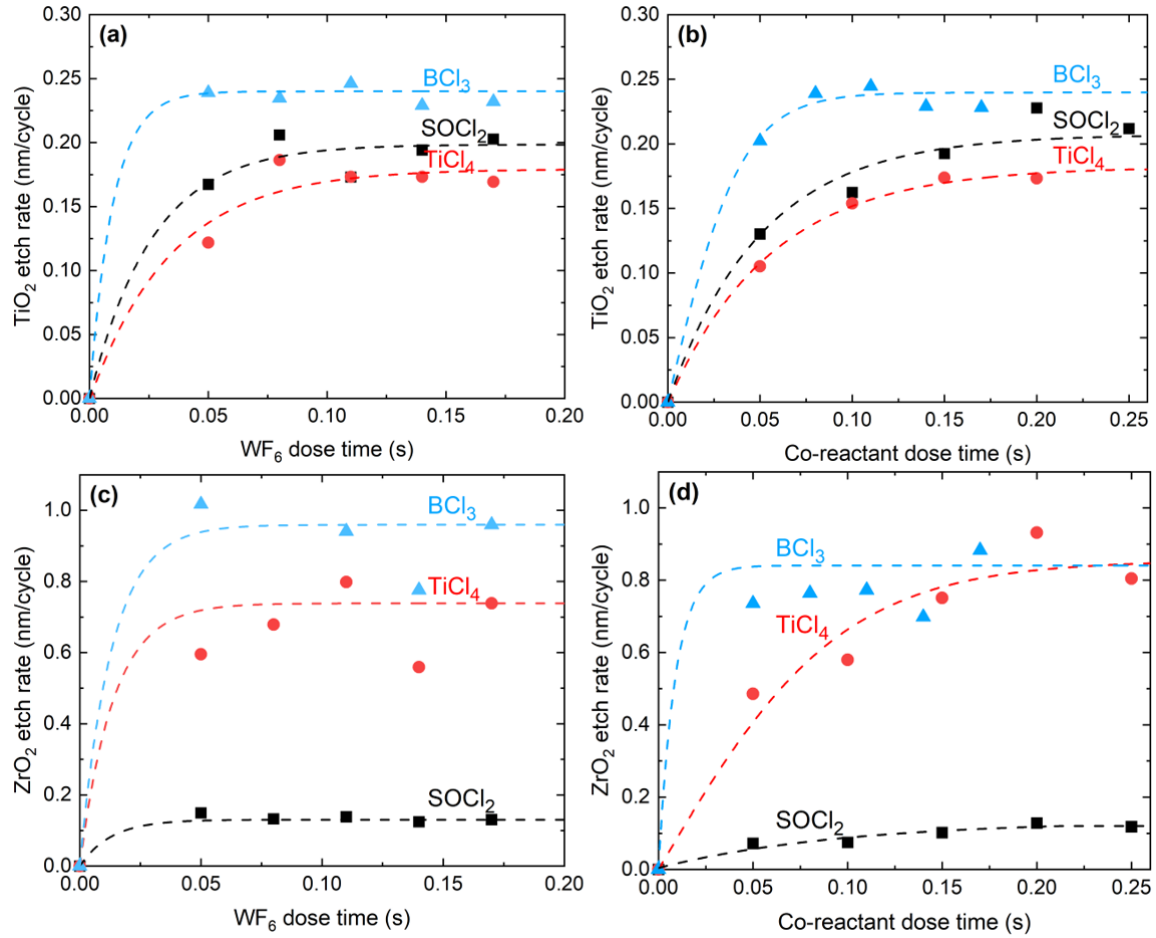


Figure 4.5. Saturation curves of etch rate dependence on WF₆ and co-reactant dose times for TiO₂ (a,b) and for ZrO₂ (c,d). All TiO₂ etching processes were performed at 170 °C and ZrO₂ etching at 325°C. The etch rate per cycle was determined by *in-situ* ellipsometry over 10 ALE cycles.

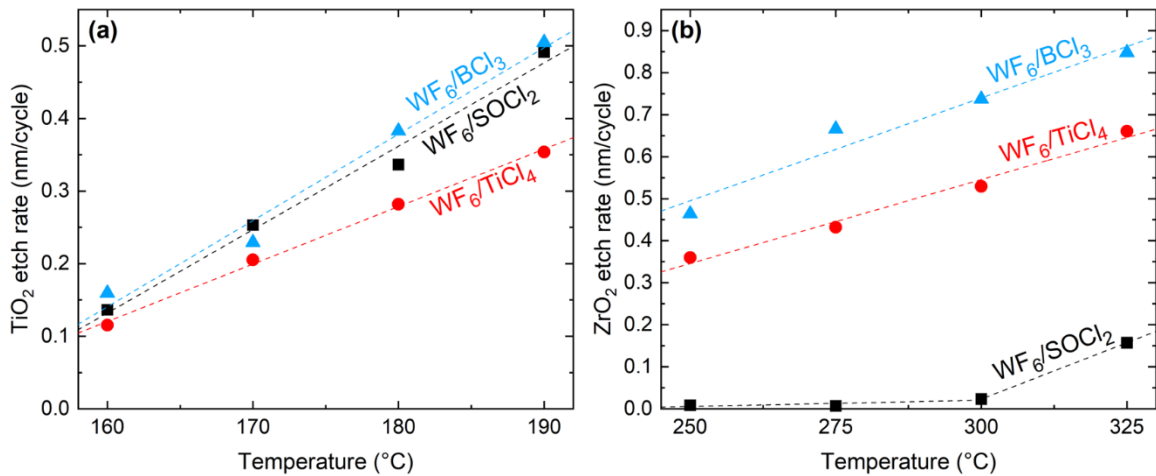


Figure 4.6. Influence of substrate temperature on the etch rates during atomic layer etching of (a) TiO₂ and (b) ZrO₂ thin films.

4.4.5. Elemental Characterization of TiO₂ and ZrO₂ ALE

The atomic layer etching trends were further analyzed by *in-situ* ellipsometry and *in-vacuo* Auger electron spectroscopy. The resulting chemical compositions and optical thicknesses are plotted in figure 4.7 for the titania and figure 4.8 for the zirconia, while the raw AES spectra are shown in figure S4.3. TiO₂ was deposited by 40 ALD cycles on chemical silicon oxide at 170 °C, resulting in a ~2 nm amorphous titania film. The etching was performed at the same temperature by WF₆ and BCl₃, SOCl₂, or TiCl₄ using saturated dosing times determined previously. TiO₂ thicknesses decrease at a nearly constant EPC starting from the first ALE cycle, slightly slowing down when the film thickness reaches close to zero. Ellipsometry measurements indicate complete or near-complete removal of TiO₂ for all etchants. AES measurements were performed before etching and after 5 and 25 ALE cycles. In every case the at.% of Ti decreases and the at.% of Si increases, with no Ti being detected after 25 ALE cycles, confirming etching of the TiO₂ film. While after 5 ALE cycles 7 at.% of boron was detected for WF₆/BCl₃ process and 8 at.% of tungsten for WF₆/SOCl₂ process, these elements were not seen after 25 cycles, indicating a clean etch surface.

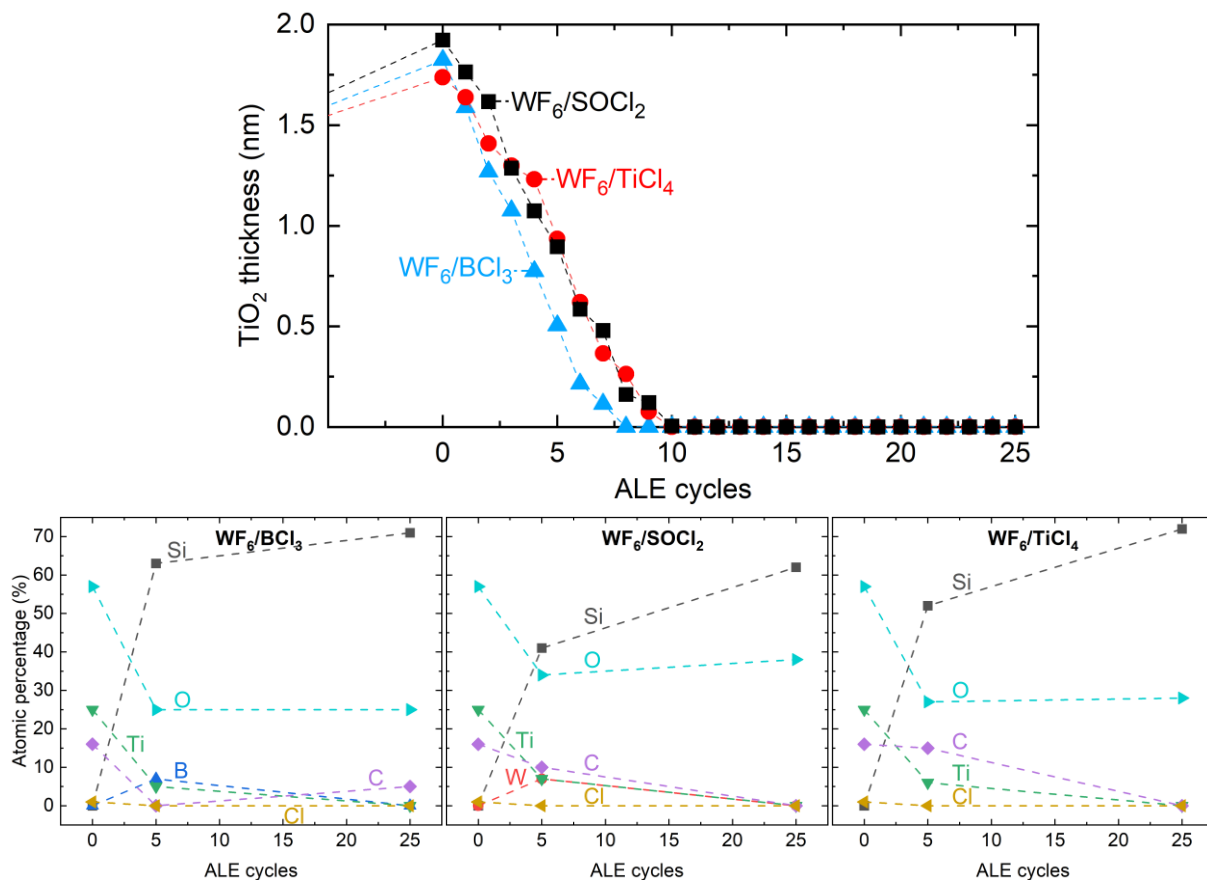


Figure 4.7. *In-situ* ellipsometry (top) and Auger electron spectroscopy (bottom) measurements of TiO₂ thermal ALE using WF₆ and BCl₃, TiCl₄, or SOCl₂ at 170 °C. The ellipsometry data were collected after every ALE cycle, while AES measurements were done before etching and after 5 and 25 ALE cycles.

Approximately 3.5 nm thick zirconia films were deposited on alumina thin films for AES studies. While the thicknesses by WF₆/BCl₃ and WF₆/TiCl₄ processes decreased at a nearly constant rate, the etch rate of WF₆/SOCl₂ was higher at the very first cycle compared to subsequent ALE cycles. AES measurements confirm the etching of ZrO₂ at 325 °C by all processes tried as evident by the decreasing concentration of Zr and appearance of Al. Using BCl₃ as a co-etchant resulted in residue boron of 12 at.% and 3 at.% after 5 and 25 ALE cycles, respectively. In spite of the ellipsometry indicating zero optical thickness of the ZrO₂ film after 25 cycles of WF₆/BCl₃, the AES indicates 2 at.% of Zr remaining on the surface. The ALE using WF₆/TiCl₄ resulted in

1 at.% of Ti present after 5 ALE cycles and none after 25 cycles. Likewise, 3 at.% of ZrO₂ were left over after 25 ALE cycles. As such, more cycles or higher processing temperatures may be needed for complete Zr removal. For WF₆/SOCl₂, 15 at.% of Zr was detected on the surface after 25 cycles due to its lower EPC. Moreover, 2 at.% of S was measured after both 5 and 25 cycles. Despite the thermodynamic modeling predicting the boron in the WF₆/BCl₃ process to be completely volatilized as BF₃ after the BCl₃ exposure, the remaining boron is most likely B₂O₃, which formed through reactions with leftover WO₃ in the film. This is also confirmed by minute W detected in WF₆/TiCl₄ and WF₆/SOCl₂ processes. In the WF₆/SOCl₂ process, the slower etch rate of ZrO₂ after the first ALE cycle can be attributed to the formation of Zr(SO₄)₂, as its removal is kinetically limited compared to the initial ZrO₂ surface. This is also confirmed by the S detected by AES after SOCl₂ exposure. While the ellipsometry indicated complete removal of the ZrO₂ film, in conflict with the Zr at.% measured by the AES, it is important to note that the underlying Al₂O₃ surface increases the complexity of the ellipsometric modeling and leads to larger possible error.

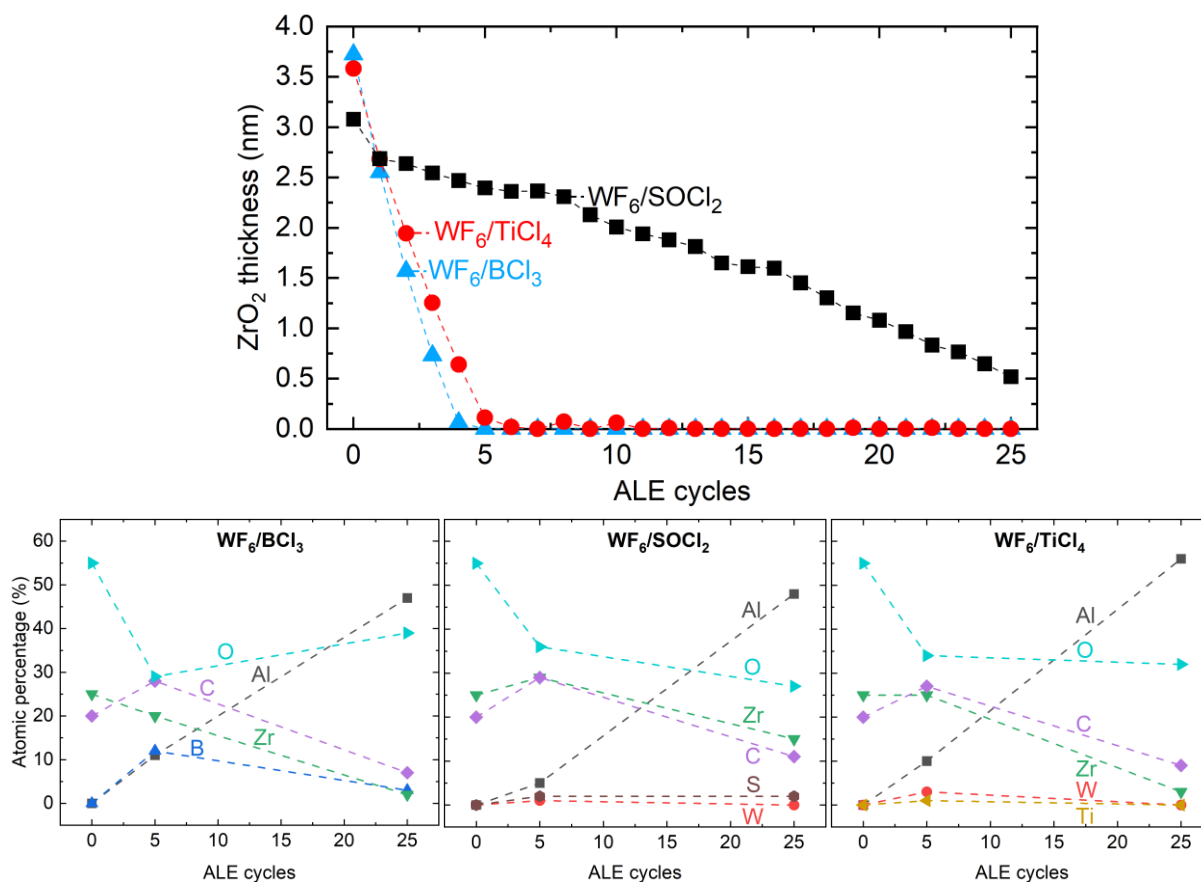


Figure 4.8. *In-situ* ellipsometry (top) and Auger electron spectroscopy (bottom) measurements of TiO₂ thermal ALE using WF₆ and BCl₃, TiCl₄, or SOCl₂ at 170 °C. The ellipsometry data were collected after every ALE cycle, while AES measurements were done before etching and after 5 and 25 ALE cycles.

4.4.6 Surface Morphology of Metal Oxides Etched by ALE

The effect of atomic layer etching on the surface morphology of the samples were determined by atomic force microscopy. The calculated RMS surface roughness of the samples before etching and after 5 and 25 ALE cycles are plotted in figure 4.9, while the surface images are shown in figure S4.3. All the samples resulted in an exceedingly smooth surface with RMS surface roughness below 0.2 nm. Both titania and zirconia indicated surface smoothing by ALE processes. The measured roughness of TiO₂ resulted in slight decrease throughout the etching cycles. Likewise, the initial RMS roughness of ~200 pm for zirconia dropped to ~80 pm after 5

ALE cycles and remained at that value after 25 cycles, indicating uniform etching and no residue in the shape of nuclei on the resulting surface for all processes studied.

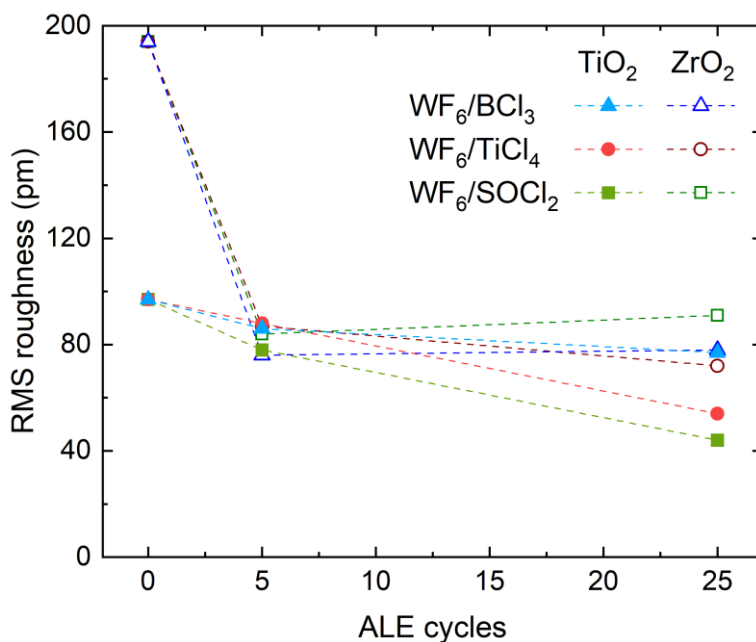


Figure 4.9. RMS surface roughness evolution as a function of ALE cycles as measured by atomic force microscopy. The ALE of TiO₂ films was performed at 170 °C and the ZrO₂ films at 325 °C.

4.5 Conclusion

This work explored the impact of co-reactant structure during thermal atomic layer etching of TiO₂ and ZrO₂ thin films. BCl₃, TiCl₄, and SOCl₂ were studied as co-etchants in a fluorination and ligand-exchange process when coupled with WF₆. In addition to ALE, it was shown that at temperatures above 200 °C, both WF₆ and SOCl₂ led to chemical vapor etching of TiO₂, while none of the reactants individually etched ZrO₂ due to the formation of a solid layer inhibiting further reactions.

The ALE behavior was shown to be strongly dependent on the co-etchant, temperature, and substrate material. The etch rate was characterized using *in-situ* ellipsometry in the temperature range of 160-190 °C for the TiO₂ and 250-325 °C for the ZrO₂. The higher temperature for zirconia was needed due to lower volatility of the formed ZrCl₄ compared to TiCl₄. The EPC

was shown to increase linearly with the temperature for all chemistries, except for ZrO₂ etching using WF₆/SOCl₂, which was limited by the unsuccessful removal of Zr(SO₄)₂ by WF₆ exposure at temperatures ≤300 °C. The etch rates of TiO₂ at 170 °C were measured as 0.24, 0.18, and 0.20 nm/cycles for WF₆ and BCl₃, TiCl₄, or SOCl₂, respectively. Similarly, the respective etch rates of ZrO₂ were 0.96, 0.74, and 0.13 nm/cycle at 325 °C. All of the etchants studied showed saturating EPC as a function of etchant dosing times, characteristic to ALE processes.

The chemical reactions and the resulting compositions were analyzed by thermodynamic modeling and *in-vacuo* Auger electron spectroscopy (AES) measurements. It was shown that during TiO₂ ALE the SOCl₂ exposure leads to volatile species SO₂ and TiCl₄, in contrast to BCl₃ and TiCl₄, which result in solid B₂O₃ and TiO₂ on the surface. However, after complete removal of the TiO₂ film at 170 °C, no B or Ti was detected at the resulting surface, indicating complete removal of the TiO₂ and B₂O₃ films. The ZrO₂ films were deposited on Al₂O₃ layers due to WF₆ reacting with the underlying Si after the complete removal of the zirconia, leading to rapid deposition of W at temperatures above 300 °C. This reaction limits the etching on Si substrate at higher temperatures when complete removal of a metal oxide is desired. In contrast to TiO₂, all co-etchants led to formation of solid species on ZrO₂ after exposure. BCl₃ resulted in B₂O₃, TiCl₄ in TiO₂, and SOCl₂ in Zr(SO₄)₂ at 325 °C as confirmed by AES measurements and thermodynamic simulations. While the resulting layers are removed by subsequent WF₆ exposure, they could be undesirable reaction products when complete removal of the film is not desired. As such, co-reactant selection strongly affects the purity of the final sample depending on the metal oxide being etched. In addition, presence of Zr was detected on the surface after 25 ALE cycles, despite ellipsometry indicating removal of the film. It is currently unclear whether further ALE cycles or higher processing temperature leads to complete removal of zirconia.

Atomic force microscopy measurements were employed to monitor the effect of ALE on the surface roughness of samples. The RMS roughness of TiO_2 and ZrO_2 films decreased as ALE cycles were performed, indicating uniform etching and surface smoothing. The results illustrate the importance of the co-reactant design during thermal atomic layer etching processes depending on the target material to be etched, desired processing temperature range, and the substrate.

4.6 Acknowledgments

This work was performed in part at the Analytical Instrumentation Facility (AIF) at North Carolina State University, which is supported by the State of North Carolina and the National Science Foundation (award number ECCS-1542015). The AIF is a member of the North Carolina Research Triangle Nanotechnology Network (RTNN), a site in the National Nanotechnology Coordinated Infrastructure (NNCI).

4.7 Supplemental Material

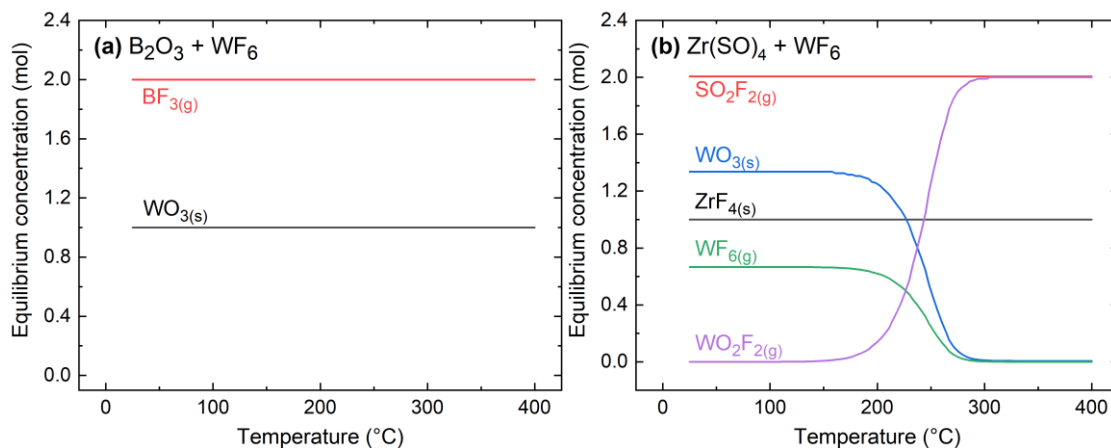


Figure S4.1. Expected equilibrium species determined by thermodynamic modeling in the temperature range from 25 °C to 400 °C for (a) 1 mol B_2O_3 , 1 mol WF_6 , and (b) 1 mol $\text{Zr}(\text{SO}_4)_2$, 2 mol WF_6 .

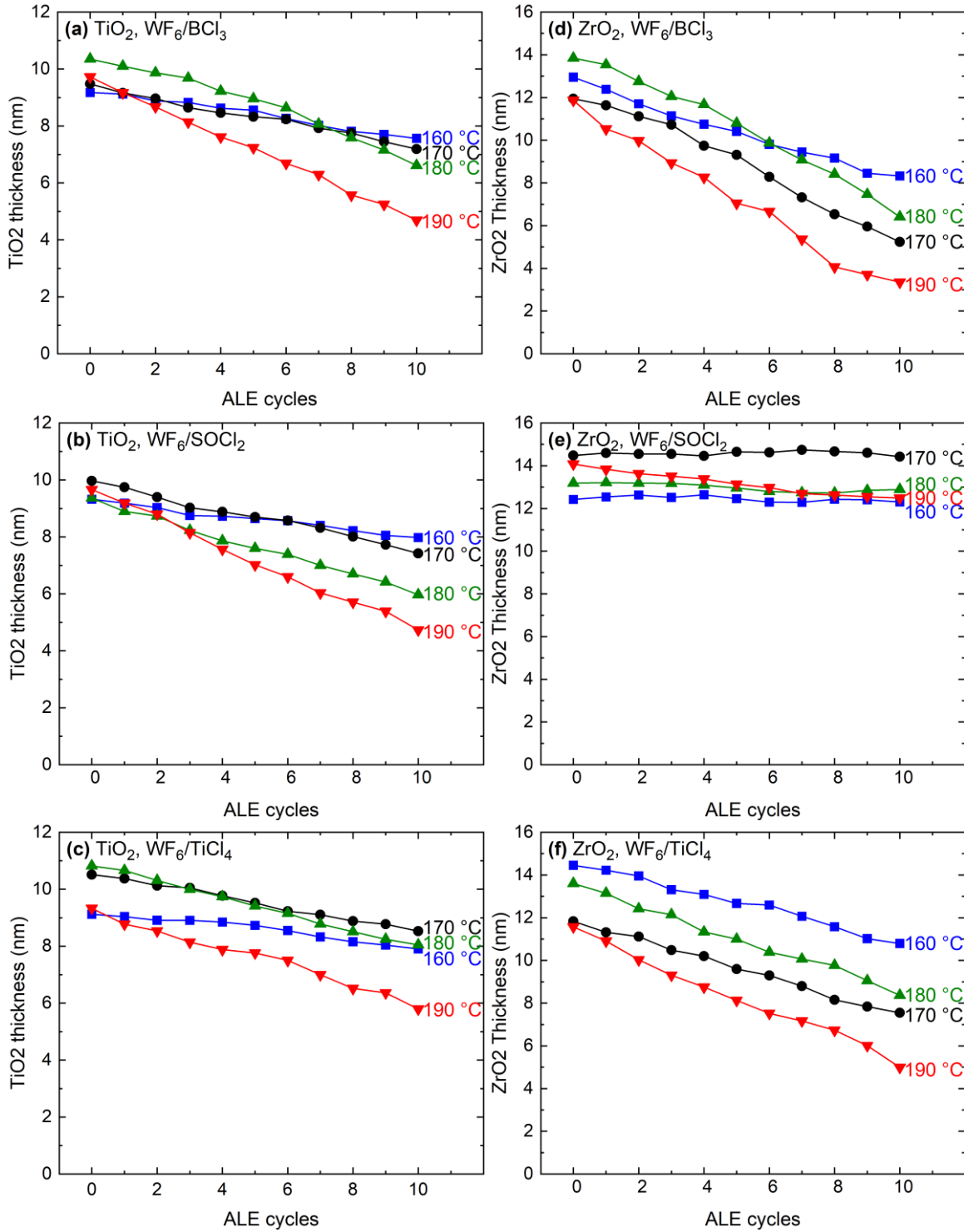


Figure S4.2. Thickness values of TiO₂/ZrO₂ thin films when etched by WF₆ and BCl₃ (a/d), SOCl₂ (b/e), or TiCl₄ (d/f). The TiO₂ was etched at 170 °C and ZrO₂ at 325 °C. Data measured by *in-situ* ellipsometry.

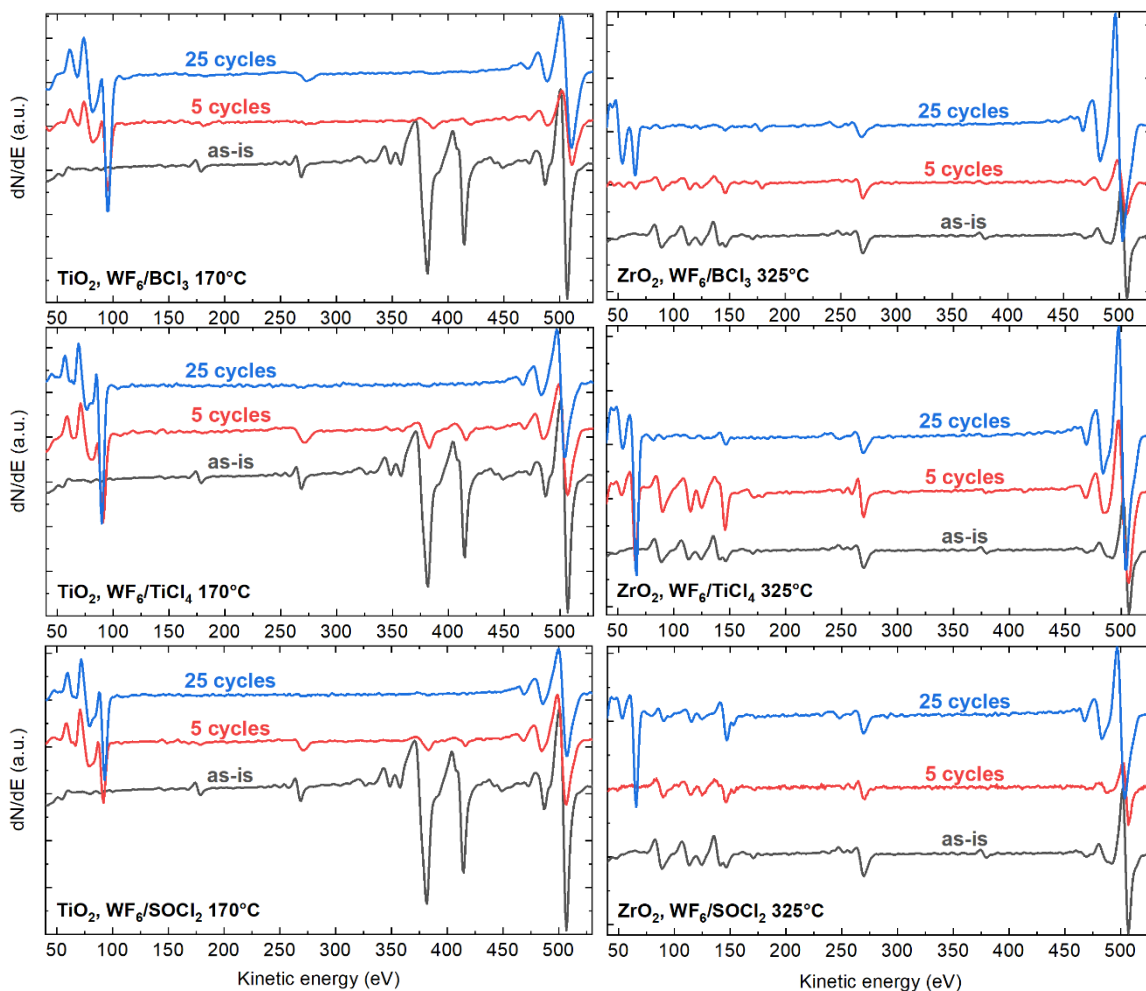


Figure S4.3. Auger electron spectroscopy (AES) spectra of atomic layer etched TiO_2 and ZrO_2 thin films. Spectra are shown before etching, and after 5 and 25 cycles of atomic layer deposition. The TiO_2 films are deposited on chemical Si oxide and etched at 170 °C, while the ZrO_2 are deposited on Al_2O_3 and etched at 325 °C.

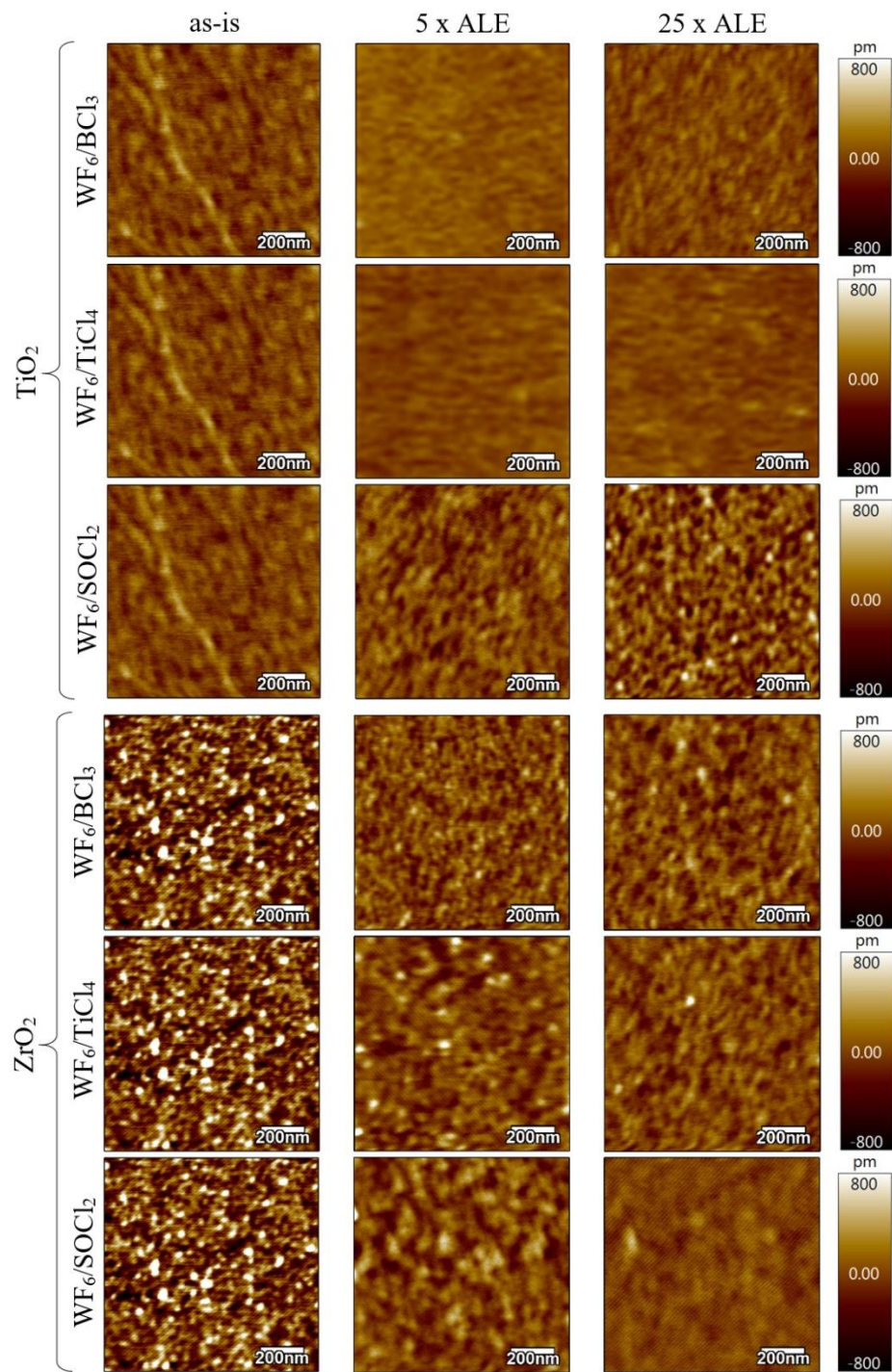


Figure S4.4. Atomic force microscopy images of TiO_2 and ZrO_2 as-deposited, and after 5 and 25 ALE cycles using WF_6 and BCl_3 , TiCl_4 or SOCl_2 .

4.8 References

1. Toofan, M. & Toofan, J. A Brief Review of the Cleaning Process for Electronic Device Fabrication. in *Developments in Surface Contamination and Cleaning* 185–212 (Elsevier, 2015). doi:10.1016/b978-0-323-29961-9.00005-3.
2. Nojiri, K. *Dry Etching Technology for Semiconductors. Dry Etching Technology for Semiconductors* (Springer International Publishing, 2015). doi:10.1007/978-3-319-10295-5.
3. Dagata, J. A. Chemical processes involved in the etching of silicon by xenon difluoride. *Journal of Vacuum Science & Technology B: Microelectronics and Nanometer Structures* **5**, 1495 (1987).
4. Chang, F. I. *et al.* Gas-phase silicon micromachining with xenon difluoride. in *Microelectronic Structures and Microelectromechanical Devices for Optical Processing and Multimedia Applications* (eds. Bailey, W., Motamedi, M. E. & Luo, F.-C.) vol. 2641 117 (SPIE, 1995).
5. Winters, H. F. & Coburn, J. W. The etching of silicon with XeF₂ vapor. *Applied Physics Letters* **34**, 70–73 (1979).
6. Passi, V. *et al.* Anisotropic vapor HF etching of silicon dioxide for Si microstructure release. *Microelectronic Engineering* **95**, 83–89 (2012).
7. Witvrouw, A. *et al.* Comparison between wet HF etching and vapor HF etching for sacrificial oxide removal. in *Micromachining and Microfabrication Process Technology VI* (eds. Karam, J. M. & Yasaitis, J. A.) vol. 4174 130–141 (SPIE, 2000).

8. Lindroos, V., Tilli, M., Lehto, A. & Motooka, T. *Handbook of Silicon Based MEMS Materials and Technologies*. (Elsevier, 2010). doi:10.1016/C2013-0-19270-7.
9. Lemaire, P. C. & Parsons, G. N. Thermal Selective Vapor Etching of TiO₂: Chemical Vapor Etching via WF₆ and Self-Limiting Atomic Layer Etching Using WF₆ and BCl₃. *Chemistry of Materials* **29**, 6653–6665 (2017).
10. Lee, Y., Huffman, C. & George, S. M. Selectivity in Thermal Atomic Layer Etching Using Sequential, Self-Limiting Fluorination and Ligand-Exchange Reactions. *Chemistry of Materials* **28**, 7657–7665 (2016).
11. Steger, R. & Masel, R. Chemical vapor etching of copper using oxygen and 1,1,1,5,5,5-hexafluoro-2,4-pentanedione. *Thin Solid Films* **342**, 221–229 (1999).
12. T. Carver, C. *et al.* Atomic Layer Etching: An Industry Perspective. *ECS Journal of Solid State Science and Technology* **4**, N5005–N5009 (2015).
13. Kanarik, K. J., Tan, S. & Gottscho, R. A. Atomic Layer Etching: Rethinking the Art of Etch. *J. Phys. Chem. Lett* **9**, 37 (2018).
14. Kanarik, K. J. *et al.* Overview of atomic layer etching in the semiconductor industry. *J. Vac. Sci. Technol. A* **33**, 20802 (2015).
15. Fang, C., Cao, Y., Wu, D. & Li, A. Thermal atomic layer etching: Mechanism, materials and prospects. *Progress in Natural Science: Materials International* vol. 28 667–675 (2018).
16. George, S. M. Mechanisms of Thermal Atomic Layer Etching. *Accounts of Chemical Research* **53**, 1151–1160 (2020).

17. Lee, Y. & George, S. M. Atomic layer etching of Al₂O₃ using sequential, self-limiting thermal reactions with Sn(acac)₂ and hydrogen fluoride. *ACS Nano* **9**, 2061–2070 (2015).
18. Lee, Y., Dumont, J. W. & George, S. M. Trimethylaluminum as the Metal Precursor for the Atomic Layer Etching of Al₂O₃ Using Sequential, Self-Limiting Thermal Reactions. *Chemistry of Materials* **28**, 2994–3003 (2016).
19. Fischer, A., Routzahn, A., Lee, Y., Lill, T. & George, S. M. Thermal etching of AlF₃ and thermal atomic layer etching of Al₂O₃. *Journal of Vacuum Science & Technology A* **38**, 022603 (2020).
20. Lee, Y., Dumont, J. W. & George, S. M. Mechanism of thermal Al₂O₃ atomic layer etching using sequential reactions with Sn(acac)₂ and HF. *Chemistry of Materials* **27**, 3648–3657 (2015).
21. Imái, S., Haga, T., Matsuzaki, O., Hattori, T. & Matsumura, M. Atomic layer etching of silicon by thermal desorption method. *Japanese Journal of Applied Physics* **34**, 5049–5053 (1995).
22. Abdulagatov, A. I. & George, S. M. Thermal Atomic Layer Etching of Silicon Using O₂, HF, and Al(CH₃)₃ as the Reactants. *Chemistry of Materials* **30**, 8465–8475 (2018).
23. DuMont, J. W., Marquardt, A. E., Cano, A. M. & George, S. M. Thermal Atomic Layer Etching of SiO₂ by a “Conversion-Etch” Mechanism Using Sequential Reactions of Trimethylaluminum and Hydrogen Fluoride. *ACS Applied Materials and Interfaces* **9**, 10296–10307 (2017).

24. Rahman, R. *et al.* Thermal Atomic Layer Etching of Silica and Alumina Thin Films Using Trimethylaluminum with Hydrogen Fluoride or Fluoroform. *ACS Applied Materials and Interfaces* **10**, 31784–31794 (2018).
25. Murdzek, J. A. & George, S. M. Effect of crystallinity on thermal atomic layer etching of hafnium oxide, zirconium oxide, and hafnium zirconium oxide. *Journal of Vacuum Science & Technology A* **38**, 022608 (2020).
26. Lee, Y. & George, S. M. Thermal atomic layer etching of HfO₂ using HF for fluorination and TiCl₄ for ligand-exchange. *Journal of Vacuum Science & Technology A* **36**, 061504 (2018).
27. Lee, Y., DuMont, J. W. & George, S. M. Atomic Layer Etching of HfO₂ Using Sequential, Self-Limiting Thermal Reactions with Sn(acac)₂ and HF. *ECS Journal of Solid State Science and Technology* **4**, N5013–N5022 (2015).
28. Zywootko, D. R. & George, S. M. Thermal Atomic Layer Etching of ZnO by a “Conversion-Etch” Mechanism Using Sequential Exposures of Hydrogen Fluoride and Trimethylaluminum. *Chemistry of Materials* **29**, 1183–1191 (2017).
29. Mamei, A., Verheijen, M. A., Mackus, A. J. M., Kessels, W. M. M. & Roozeboom, F. Isotropic Atomic Layer Etching of ZnO Using Acetylacetone and O₂ Plasma. *ACS Applied Materials and Interfaces* **10**, 38588–38595 (2018).
30. Mohimi, E. *et al.* Thermal Atomic Layer Etching of Copper by Sequential Steps Involving Oxidation and Exposure to Hexafluoroacetylacetone. *ECS Journal of Solid State Science and Technology* **7**, P491–P495 (2018).

31. Gong, Y., Venkatraman, K. & Akolkar, R. Communication—Electrochemical Atomic Layer Etching of Copper. *Journal of The Electrochemical Society* **165**, D282–D284 (2018).
32. Toyoda, N. & Ogawa, A. Atomic layer etching of Cu film using gas cluster ion beam. *Journal of Physics D: Applied Physics* **50**, 184003 (2017).
33. Xie, W., Lemaire, P. C. & Parsons, G. N. Thermally Driven Self-Limiting Atomic Layer Etching of Metallic Tungsten Using WF_6 and O_2 . *ACS Applied Materials and Interfaces* **10**, 9147–9154 (2018).
34. Johnson, N. R. & George, S. M. WO_3 and W thermal atomic layer etching using “conversion-fluorination” and “oxidation-conversion-fluorination” mechanisms. *ACS Applied Materials and Interfaces* **9**, 34435–34447 (2017).
35. Lee, Y. & George, S. M. Thermal atomic layer etching of titanium nitride using sequential, self-limiting reactions: Oxidation to TiO_2 and fluorination to volatile TiF_4 . *Chemistry of Materials* **29**, 8202–8210 (2017).
36. Marchack, N., Papalia, J. M., Engelmann, S. & Joseph, E. A. Cyclic Cl_2/H_2 quasi-atomic layer etching approach for TiN and TaN patterning using organic masks. *Journal of Vacuum Science & Technology A: Vacuum, Surfaces, and Films* **35**, 05C314 (2017).
37. Konh, M. *et al.* Molecular mechanisms of atomic layer etching of cobalt with sequential exposure to molecular chlorine and diketones. *Journal of Vacuum Science & Technology A* **37**, 021004 (2019).
38. Gertsch, J. C., Cano, A. M., Bright, V. M. & George, S. M. SF_2 as the Fluorination Reactant for Al_2O_3 and VO_2 Thermal Atomic Layer Etching. *Chemistry of Materials* (2019).

39. Lin, X., Chen, M., Janotti, A. & Opila, R. In situ XPS study on atomic layer etching of Fe thin film using Cl₂ and acetylacetone. *Journal of Vacuum Science & Technology A* **36**, 051401 (2018).
40. Chen, K. C., Chu, T. W., Wu, C. R., Lee, S. C. & Lin, S. Y. Atomic layer etchings of transition metal dichalcogenides with post healing procedures: Equivalent selective etching of 2D crystal hetero-structures. *2D Materials* **4**, 034001 (2017).
41. Lee, Y., Johnson, N. R. & George, S. M. Thermal Atomic Layer Etching of Gallium Oxide Using Sequential Exposures of HF and Various Metal Precursors. *Chemistry of Materials* **32**, 5937–5948 (2020).
42. Li, J. *et al.* A Novel Dry Selective Isotropic Atomic Layer Etching of SiGe for Manufacturing Vertical Nanowire Array with Diameter Less than 20 nm. *Materials* **13**, 771 (2020).
43. Aziziyan, M. R., Sharma, H. & Dubowski, J. J. Photo-Atomic Layer Etching of GaAs/AlGaAs Nanoheterostructures. *ACS Applied Materials and Interfaces* **11**, 17968–17978 (2019).
44. Zhu, H. *et al.* Remote Plasma Oxidation and Atomic Layer Etching of MoS₂. *ACS Applied Materials and Interfaces* **8**, 19119–19126 (2016).
45. Chen, K. C., Chu, T. W., Wu, C. R., Lee, S. C. & Lin, S. Y. Atomic layer etchings of transition metal dichalcogenides with post healing procedures: Equivalent selective etching of 2D crystal hetero-structures. *2D Materials* **4**, 034001 (2017).
46. Lu, W. *et al.* In Situ Thermal Atomic Layer Etching for Sub-5 nm InGaAs Multigate MOSFETs. *Nano Letters* **19**, 5159–5166 (2019).

47. Johnson, N. R., Hite, J. K., Mastro, M. A., Eddy, C. R. & George, S. M. Thermal atomic layer etching of crystalline GaN using sequential exposures of XeF₂ and BCl₃. *Applied Physics Letters* **114**, 243103 (2019).
48. Lee, Y., Johnson, N. R. & George, S. M. Thermal Atomic Layer Etching of Gallium Oxide Using Sequential Exposures of HF and Various Metal Precursors. *Chemistry of Materials* **32**, 5937–5948 (2020).
49. Johnson, N. R. & George, S. M. WO₃ and W thermal atomic layer etching using “conversion-fluorination” and “oxidation-conversion-fluorination” mechanisms. *ACS Applied Materials and Interfaces* **9**, 34435–34447 (2017).
50. Konh, M. *et al.* Molecular mechanisms of atomic layer etching of cobalt with sequential exposure to molecular chlorine and diketones. *Journal of Vacuum Science & Technology A* **37**, 021004 (2019).
51. Lin, X., Chen, M., Janotti, A. & Opila, R. In situ XPS study on atomic layer etching of Fe thin film using Cl₂ and acetylacetone. *Journal of Vacuum Science & Technology A* **36**, 051401 (2018).
52. Ludviksson, A., Xu, M. & Martin, R. M. Atomic layer etching chemistry of Cl₂ on GaAs(100). *Surface Science* **277**, 282–300 (1992).
53. Zhou, H., Fu, Y.-C., Mirza, M. M. A. & Li, X. Thermal and Plasma Enhanced Atomic Layer Deposition of Al₂O₃ and HfO₂ Films Investigated by Using in situ Auger Electron Spectroscopy. in *VS 18th International Conference on Atomic Layer Deposition (ALD)*, Incheon, Korea (2018).

54. Sharma, V. *et al.* Thermal gas-phase etching of titanium nitride (TiN) by thionyl chloride (SOCl₂). *Applied Surface Science* **540**, 148309 (2021).
55. HSC Chemistry 7.11. Metso Outotec Finland Oy.
56. Lassner, E. & Schubert, W.-D. *Tungsten: Properties, Chemistry, Technology of the Element, Alloys, and Chemical Compounds*. (Springer, 1999). doi:10.1007/978-1-4615-4907-9.

CHAPTER 5

Effect of Reactant Dosing on Selectivity During Area-Selective Deposition of TiO₂ via Integrated Atomic Layer Deposition and Atomic Layer Etching

Holger Saare, Seung Keun Song, Jung-Sik Kim, and Gregory N. Parsons,

“Effect of reactant dosing on selectivity during area-selective deposition of TiO₂ via integrated atomic layer deposition and atomic layer etching,” *Journal of Applied Physics* 128, 105302, 2020.

5.1 Preface

A key hallmark of atomic layer deposition (ALD) is that it proceeds via self-limiting reactions. For a good ALD process, long reactant exposure times beyond that required for saturation on planar substrates can be useful, for example, to achieve conformal growth on high aspect-ratio nanoscale trenches, while maintaining consistent deposition across large-area surfaces. Area-selective deposition (ASD) is becoming an enabling process for nanoscale pattern modification on advanced nanoelectronics devices. Herein, we demonstrate that during area-selective ALD, achieved by direct coupling of ALD and atomic layer etching (ALE), excess reactant exposure can have a substantially detrimental influence on the extent of selectivity. As an example system, we study ASD of TiO₂ on hydroxylated SiO₂ (Si-OH) vs. hydrogen-terminated (100) Si (Si-H) using TiCl₄/H₂O for ALD and WF₆/BCl₃ for ALE. Using in-situ spectroscopic ellipsometry and ex-situ x-ray photoelectron spectroscopy (XPS), we show that unwanted nucleation can be minimized by limiting the water exposure during the ALD steps. Longer exposures markedly increased the rate of nucleation and growth on the desired non-growth region, thereby degrading selectivity. Specifically, transmission electron microscopy (TEM) analysis demonstrated that near-saturated H₂O doses enabled 32.7 nm thick TiO₂ patterns at selectivity threshold $S > 0.9$ on patterned Si/SiO₂

substrates. The correlation between selectivity and reactant exposure serves to increase fundamental insight into the effects of sub-saturated self-limiting surface reactions on the quality and effectiveness of ASD processes and methods.

5.2 Introduction

Area-selective deposition (ASD) can provide alternative bottom-up options for atomic-scale material placement and nanoscale patterning, thereby complementing top-down lithography in semiconductor manufacturing.¹ Bottom-up ASD can aid in device miniaturization while enabling uniform deposition on complex 3D structures with atomic-scale precision.² Exploiting the observation that adsorption of certain deposition precursors depends strongly on the chemical termination presented on the initial growth surface, noticeable growth can be achieved on a receptive surface while simultaneously limiting growth on adjacent non-receptive regions. As feature sizes shrink to <10 nm, physical alignment and over-lay of multiple features and line-edges become significant challenges. Chemical self-alignment has the potential to bypass the challenges in physical feature alignment, enabling new device designs and manufacturing schemes.³ As such, the field of area-selective deposition is becoming increasingly vital for the continuation of Moore's law and viability of advanced device architectures.

Although in an ideal case no growth should be present on the non-receptive surface, the exposure of ALD precursors can modify surface termination, generating nucleation sites and subsequent undesired film growth.⁴ Area-selective deposition requires eliminating nucleation on the preferred non-growth regions, while maintaining good growth on the preferred growth regions. To combat the problem of unwanted nuclei, a common approach is to passivate the surface by forming patterns of organic molecules or monolayers to block growth on the covered areas.⁵⁻⁸ Another method that does not require organic molecule integration employs intermittent atomic

layer etching (ALE) steps within the ALD cycle, i.e. ALD/ALE “super-cycles”, to periodically remove unwanted nuclei from the non-growth substrate.⁹

Atomic layer deposition of metal oxides on Si-OH vs. Si-H surfaces have been extensively researched related to high- κ dielectric scaling. A work by Puurunen compares behavior of ALD of HfO₂ on varying density of surface hydroxyl groups using three mathematical models: by Alam and Green, by Puurunen and third by Ylilammi.¹⁰⁻¹³ The work shows that while the physical explanations vary, the GPC of ALD using HfCl₄/H₂O is strongly dependent on the -OH concentration on the surface. While 1.0 nm thick chemical SiO₂ exhibits characteristic linear growth, the H-terminated Si surface exhibits a “substrate-inhibited” growth. This trend has been demonstrated experimentally and shown that HfO₂ grown on Si-H are rougher, and have poor electrical properties compared to HfO₂ deposited on Si-OH.¹⁴⁻¹⁷ It has also been shown that during HfO₂ ALD deposition the initially H-terminated surface oxidizes, forming an interstitial layer, which promotes growth.¹⁷⁻²⁰ This substrate-inhibited growth is dependent on temperature and precursors used.^{19,21,22} Similar trends have been demonstrated for other metal oxides such as ZrO₂^{20,21,23-26} and TiO₂^{27,28}.

Previously, our group studied ALD/ALE and reported TiO₂ ASD on SiO₂ with minimal deposition on Si-H surfaces using the same approach used in this work.²⁹ In the ALD/ALE sequence, the ALD cycles were stopped after a small number of nuclei appeared on the Si-H surface, and ALE cycles were introduced to remove the unwanted material. Repeating the ALD/ALE sequence allowed the net film thickness to increase on the desired growth region while minimizing growth on the desired non-growth region. The self-limiting ALE process permits a balance with the ALD, so that etching of the film on the desired growth surface only minutely affects the final deposited thickness.³⁰ A significant advantage of this approach is that both

processing steps are carried out at in a single reactor system at fixed temperature, and require minimal number of steps with no plasma exposure or lift-off necessary.³¹ Compared to more commonly used plasma-enhanced ALE, thermal ALE used in this work enables conformal etching of the material.³² A possible downside is that coupling the deposition and etching sequences increases the total process time. The previous study²⁹ did not examine the effect of reactant exposure on selectivity or perform in-situ measurements, which are the key elements in this study.

In-situ analysis techniques monitor sample properties without interrupting the process or exposing the surface to atmosphere, thereby avoiding sample contamination and simplifying data analysis.^{33–35} Performing sample characterization using in-situ tools is imperative when studying nucleation mechanisms, where minute features on the surface can otherwise become masked or degraded by ambient exposure.^{36,37,38} In addition, critical nuclei can be created in a few cycles, making it difficult to accurately collect data without real-time measurements.³⁹ In-situ ellipsometry has been used to study nucleation of Pt on Al₂O₃,⁴⁰ growth of ultrathin TiN films,⁴¹ nucleation and growth of TiN/Si and TiN/GaN heterostructures,⁴² Cu ASD on Pd vs. SiO₂/SiN,⁴³ and many more processes.^{39,44–49} By probing a material's optical and electro-optical response, film thickness can be measured on different substrates, effectively quantifying the selectivity. Moreover, measuring the film thickness change during the ASD process enables us to understand the mechanism behind selectivity loss and the impact of processing conditions on ASD.

While the effect of reactant exposure time during ALD processing is widely explored and well-understood,^{36,50–55} previous reports of area-selective ALD generally use exposure conditions suitable for the desired deposition, without addressing how exposure and other process variables influence reactions on the non-growth surface. Mackus et al. demonstrated the impact of oxygen exposure on the nucleation of Pt during ALD and showed that longer O₂ dosing time increased the

rate of Pt nucleation on an Al₂O₃ film surface.³⁶ Additionally, the influence of precursor pressure on area-selective deposition of Al₂O₃ on Ti has been previously studied using self-assembled monolayers (SAMs) as blocking layers and was shown that increasing precursor pressure lead to lower selectivity due to increased physisorption on SAMs.⁵⁶

The work presented here explores the effect of ALD reactant dosing times during area-selective ALD of TiO₂ on Si-OH vs. Si-H, which is an isothermal process in the sense that the reaction temperature is held constant throughout the experiment. The ALD/ALE sequence examined was described previously^{29,57} and provides a valuable model to understand ASD and the means to control the extent of selectivity. This work presents a systematic in-situ study addressing the effects of ALD conditions on net ASD selectivity.

5.3 Experimental Details

5.3.1 Reactor Design

The ALD and ALE processes were carried out in a home-built warm-walled reaction chamber equipped with a 4-wavelength ellipsometer (Film Sense FS-1) capable of in-situ measurement of thin film optical properties. A simplified schematic of the reaction chamber is presented in figure 5.1. The sample is introduced to the chamber on a sample chuck, which locks onto a sample stage, heated by PID-controlled cartridge heaters and thermally isolated from the rest of the chamber via ceramic standoffs. The substrate temperature can be controlled between 50°C and 350°C, while the reactor wall is typically 100°C. Compared to isothermal hot-wall reactors, this differentially heated sample holder has the benefit of allowing the sample temperature to be adjusted relatively quickly.

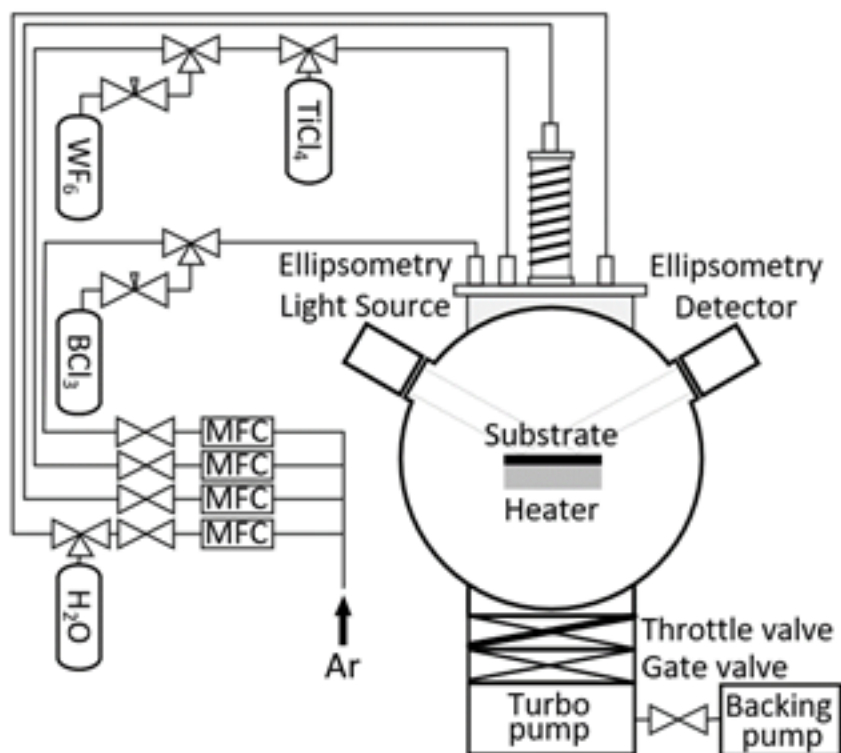


Figure 5.1. Simplified schematic representation of deposition chamber used in this work, including the gas delivery lines setup, pumping system and attached spectroscopic ellipsometer.

The precursors are introduced to the system through four heated stainless-steel gas-delivery lines using argon (99.999% purity, Arc3 Gases) as a carrier and purge gas. Line #1 hosted BCl_3 (99.9% purity, Matheson); line #2 TiCl_4 (99% purity, Strem Chemicals) and WF_6 (99.99% purity, Galaxy Chemical); line #3 deionized H_2O ; line #4 was only used for flowing argon. The argon flow rates were controlled by mass-flow controllers present on each line and the precursors were dosed using pneumatic diaphragm valves (Swagelok, ALD series) controlled by a Python interface using automated process recipes. The gases and byproducts are pumped out of the system using a Seiko-Seiki STP-300C turbo pump backed by an Alcatel 2021a two-stage rotary vane pump with activated aluminum and Sodasorb filters to shield the pump oil from harmful vapors. The pressure was controlled by a throttle valve located before the turbo pump and monitored by a Baratron

capacitance manometer (0-10 Torr range, 0.1 mTorr resolution). During the Ar purge step, the throttle valve position produces a process pressure of 600 mTorr. Dosing leads to a small increase in process pressure due to the precursor partial pressure.

5.3.2 Substrate Preparation

Two types of silicon wafer pieces were used as deposition substrates in this study: (1) boron-doped p-type silicon (100) wafers with 5-10 $\Omega\cdot\text{cm}$ resistivity, blanket-terminated with either a chemical oxide or hydrogen; and (2) Si-H/SiO₂ patterned wafers prepared by photolithographic wet-etching of ~100 nm thick SiO₂, resulting in alternating Si/SiO₂ lines with 6 μm pitch (3 μm lines/spaces). The wet etching process produced a tapered edge on the SiO₂ features. Both the blanket and the patterned wafers were cleaved into approximately 2 x 2 cm squares, submerged for 15 minutes in piranha solution (1:1 mixture of H₂O₂:H₂SO₄) to remove organic residue and to form a hydroxyl-terminated (Si-OH) chemical oxide layer. To form a hydrogen-terminated (Si-H) substrate, the piranha-cleaned wafers were dipped into 5% HF solution for 30 seconds.

Immediately prior to loading samples into the reactor, they were rinsed with deionized water and blown dry with flowing nitrogen. They were then placed onto a sample chuck and secured in place using a physical clamp. The chamber was pumped down to $\sim 10^{-5}$ Torr and the temperature and the pressure were allowed to stabilize for 30 minutes before any processing.

5.3.3 Deposition and Etching Process

Deposition and etching were carried out at 170°C. The TiO₂ ALD sequence included discrete TiCl₄ and deionized water doses with argon as the purge and carrier gas. The dosing times for both precursors were varied from 90 ms to 270 ms. After every dose the chamber was purged with argon for 20 seconds, followed by a 10 second pump down by completely opening the throttle

valve to the turbo pump, evacuating chamber to 10^{-5} Torr. After this pump step, the throttle valve was partially closed and the flow of argon resumed for 15 seconds to bring the system back to the operating pressure of 600 mTorr. This was followed by the subsequent H₂O or TiCl₄ dose step. The timing sequence is designated as TiCl₄/Ar/pump/Ar/H₂O/Ar/pump/Ar = x/20/pump/15/x/20/pump/15 s, where x ranges from 90 to 270 ms.

The atomic layer etching process coupled alternating WF₆ and BCl₃ doses. Based on earlier measurements and thermodynamic calculations,⁵⁷ exposing TiO₂ to WF₆ at T>125°C fluorinates the TiO₂ surface, forming solid WO_xF_y/TiO_yF_z and volatile TiF₄. At T<190°C, subsequent BCl₃ exposure removes the W species and forms solid B₂O₃. The boron oxide is then removed by the next WF₆ dose, thereby achieving self-limiting ALE.⁵⁷ The timing sequence during ALE follows: WF₆/Ar/pump/Ar/BCl₃/Ar/pump/Ar = 0.1/20/pump/15/0.1/20/pump/15 s. Under these conditions, the rate of ALE was measured to be 0.11 nm/cycle under steady-etch conditions.

The ALD/ALE super-cycle sequence used here consists of 30 ALD cycles followed by 5 ALE cycles. The number of ALD/ALE cycles was selected based on successful results published previously.²⁹ This sequence was repeated N times (where N = 10, 20, or 30) and is designated here as (30/5) x N.

5.3.4 Process Characterization

An in-situ four-wavelength spectroscopic ellipsometer (Film Sense FS-1) directly attached to the chamber was used to monitor film thickness during the ALD/ALE sequence. The ellipsometer was positioned at a $65^\circ \pm 1^\circ$ incident angle and ellipsometry parameters Ψ and Δ were acquired at wavelengths 465 nm, 525 nm, 580 nm, and 635 nm. The ellipsometer was isolated from the chamber by two quartz windows and pneumatic gate valves that were opened and closed by electronic actuation in sequence with the process cycle. The gate valves were opened and

ellipsometry data collected only during purge/pump periods, thereby preventing deposition on the windows. For this study, we collected ellipsometric data after every 5 ALD cycles and after every 1 ALE cycle. For the ALD step, data was collected after the water dose, and for ALE, data was collected after the BCl_3 step. Ellipsometry data collection required 9 seconds for full data collection. For blanket substrates, the TiO_2 film thickness was obtained from the ellipsometry data using a Cauchy model in the ellipsometer software which takes into account the temperature-dependence of the optical response.

An example of raw ellipsometry data and the resulting thickness output are shown in Figure 5.2. The values for Ψ , Δ , and thickness are shown for a single super-cycle of TiO_2 ASD on Si-OH surface, consisting of 30 ALD cycles followed by 5 ALE cycles performed at 170°C with 90 ms dosing times for both TiCl_4 and H_2O . While the value of Ψ does not change significantly in this thickness range, there is an evident correlation between the Δ and TiO_2 film thickness values. The Δ parameter characterizes the phase change upon reflection of the polarized light, which is highly sensitive to thickness changes in ultrathin layers.⁵⁸ While analyzing nucleation behavior using spectroscopic ellipsometry data, it is important not to over-interpret the thickness output by the model as it usually presumes a continuous thin film.⁵⁹

To compare selectivity for different materials or process approaches, the selectivity fraction, S , is defined as the difference between the surface coverage on growth surface, θ_1 , and that on the non-growth surface, θ_2 , relative to the total coverage on both surfaces.⁵⁹⁻⁶¹ When the coverage on the non-growth surface is relatively small, a reasonable estimate for S is found using the measured film thicknesses on the growth and non-growth surfaces, t_1 and t_2 , respectively:

$$S = \frac{\theta_1 - \theta_2}{\theta_1 + \theta_2} \approx \frac{d_1 - d_2}{d_1 + d_2} \quad (5.1)$$

When growth proceeds on the desired surface, and no growth appears on the non-growth surface, the process is perfectly selective and $S = 1$. When unwanted growth occurs on the non-growth region, S decreases, reaching 0 when both surfaces become fully covered. By setting a target S , which might be needed for practical ASD applications), one can determine from experimental measurements the threshold thickness that can be achieved on the growth surface before the value of S drops below target and selectivity loss occurs.

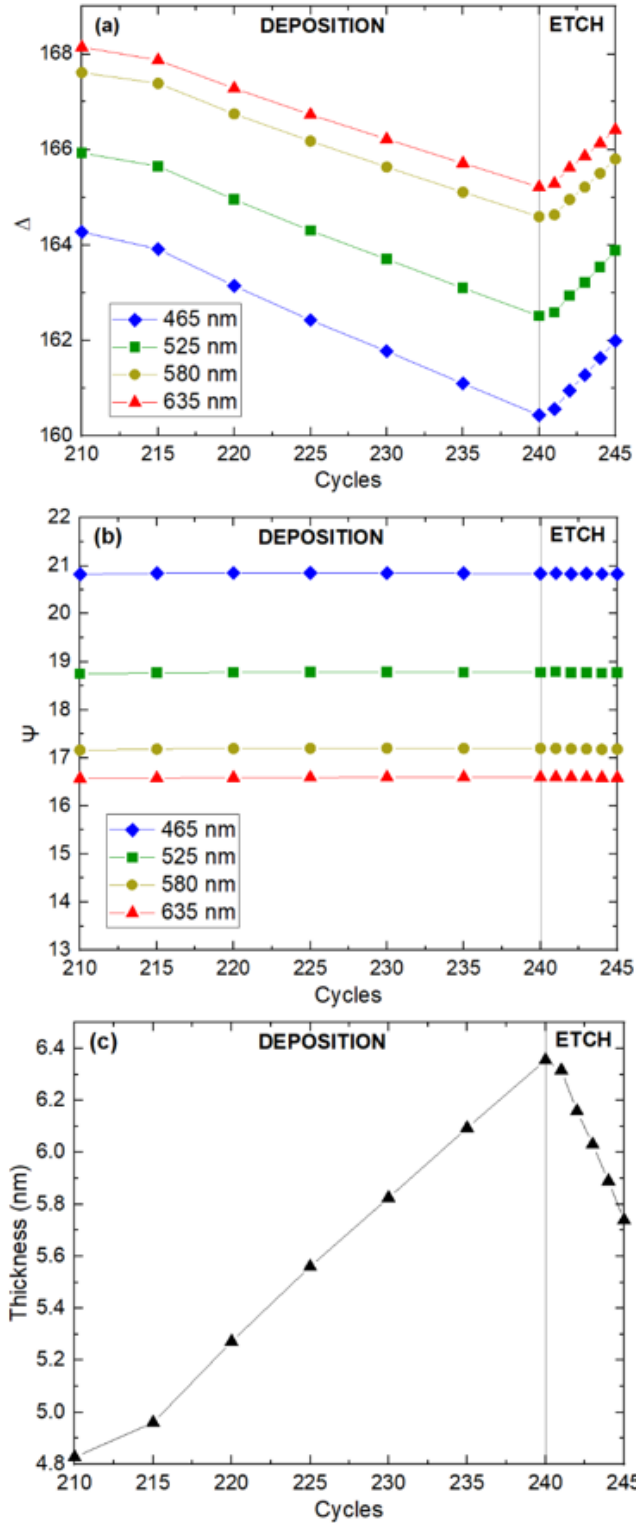


Figure 5.2. In-situ ellipsometry data collected during deposition and etching steps on Si-OH surface. (a) and (b) show the raw delta (Δ) and psi (Ψ) parameters, respectively, which are fitted by a Cauchy model to (c) measure TiO₂ layer thickness.

5.3.5 Material Characterization

The chemical composition of blanket films on Si-OH and Si-H was determined by ex-situ XPS using Kratos Axis Ultra DLD X-ray Photoelectron Spectrometer and the CasaXPS software package. The analysis consisted of survey scans followed by high-resolution scans for the elements Ti, Si, O, Cl, F and C. The energy axes were calibrated using adventitious carbon peak at 285.0 eV. Field emission scanning electron microscopy (FESEM Verios 460L), with a low energy electron detector operating at 10 kV and 0.8 nA was used to obtain the patterned Si/SiO₂ images. Focused ion beam (FIB, FEI Quanta 3D FEG instrument) with a high current Ga liquid metal ion gun was used for a TEM sample preparation. Cross-sectional images were obtained by scanning transmission electron microscopy (STEM, Jeol 2000FX) with energy dispersive spectrometer (EDS) attachment for chemical characterization of the patterned samples.

5.4 Results and Discussion

5.4.1 Effect of Dosing Time on ALD Growth

Figure 5.3 displays saturation curves obtained during steady ALD of TiO₂ at 170°C, where the thickness growth per cycle (GPC) is plotted versus the dosing time of TiCl₄ or H₂O. The curves are obtained by fixing one of the precursor dosing times at 300 ms and varying the other between 0 and 300 ms. The thickness per cycle at each condition was measured after 50 deposition cycles, and the average value plotted vs. dosing time. Note that the shortest time used for open-dosing is 60 ms. This maximum valve switching speed was limited by the computer interface communication rate. Figure 4.3a shows that for a fixed 300 ms H₂O dosing time, changing the TiCl₄ dosing time between 60 and 300 ms had minimal influence on the growth, with good saturation at ~0.05 nm/cycle. Similarly, Figure 3b shows that fixing TiCl₄ dosing time at 300 ms and varying H₂O dosing time results in similar saturation at the same ~0.05 nm/cycle. Saturation

requires ~100 ms of H₂O dosing time, whereas in Figure 3a, saturation is observed for the shortest 60 ms TiCl₄ dosing time.

To study the effect of dosing conditions on nucleation on Si-H surfaces, growth was monitored under different dose conditions. As a first test, the TiCl₄ and H₂O dosing times were set equal to each other at 90 ms, 180 ms, or 270 ms, which can be referred to as “near-saturated”, “saturated”, and “oversaturated” respectively, based on H₂O saturation levels. It is important to note that TiCl₄ dose reached saturation at all dosing times. A total of 150 TiO₂ ALD cycles were performed on freshly prepared Si-H surfaces, and deposition was monitored by in-situ ellipsometry as a function of ALD cycle. For comparison, these three experiments were also repeated on Si-OH substrates. We note from the results shown in Figure 5.3 that all three dosing conditions are close to, or well within the saturated ALD regime. Therefore, the growth on each substrate type is expected to be nearly the same for each dose condition.

The resulting six data sets (Si-OH and Si-H surfaces, 3 dosing conditions each) are shown in Figure 5.4. On the Si-H substrates, all three dosing conditions show similar results, with noticeable growth delay up to ~25 ALD cycles, after which the GPC accelerates to near the steady value of ~0.05 nm/cycle. After 150 cycles, the thickness on all three Si-H surfaces is ~5 nm. The small differences in the growth rates reflect minute run-to-run variations on the surface. Likewise, on Si-OH, the different dose conditions show nearly identical results: 150 ALD cycles yielding ~8 nm of TiO₂ with the lowest dosing time condition yielding the lowest film thickness as expected due to near-saturation condition. Using equation (1), the trend in film nucleation yields a film thickness of ~1.5 nm when selectivity $S=0.9$ for all three conditions. These results indicate that near- and oversaturated H₂O dosing do not substantially affect the initial nucleation delay on the Si-H surface.

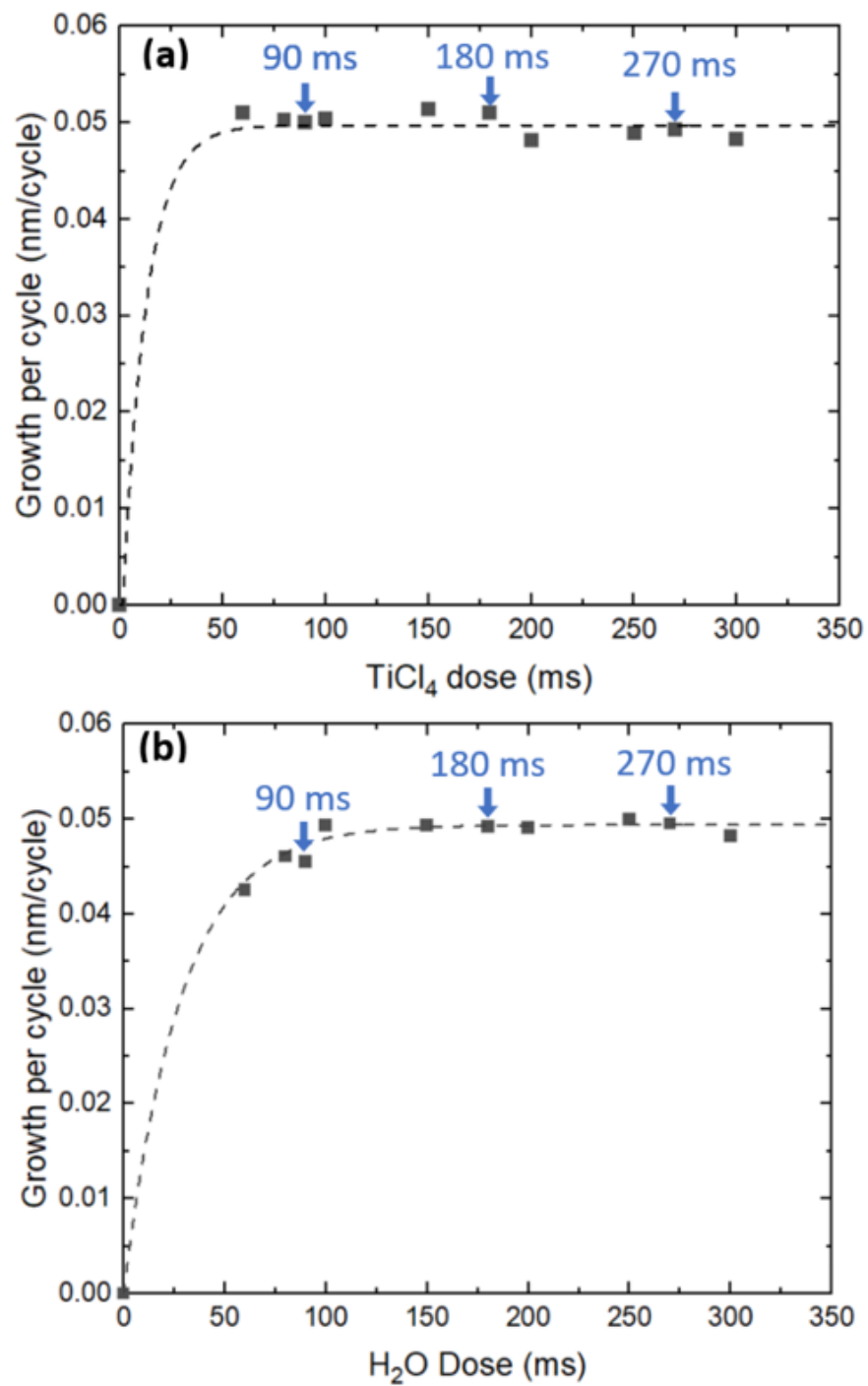


Figure 5.3. Growth per cycle (GPC) of TiO₂ on TiO₂ thin films deposited on Si-OH surface measured by in-situ ellipsometry. One of the precursor dosing times is held constant at 300 ms, while dosing time of (a) TiCl₄ and (b) H₂O is varied.

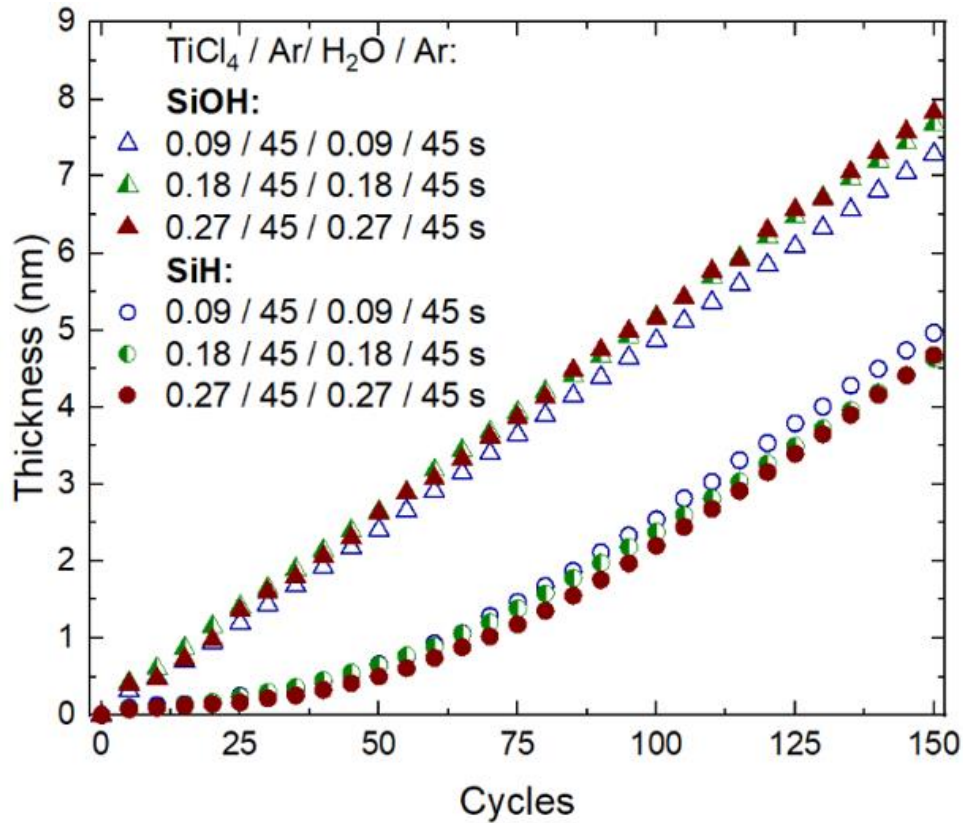


Figure 5.4. The thickness of TiO_2 layer on Si-OH and Si-H surfaces for 90 ms, 180 ms, and 270 ms $\text{TiCl}_4/\text{H}_2\text{O}$ dosing times as measured by in-situ ellipsometry.

5.4.2 Combined ALD/ALE Super-cycles

Next, we worked to understand how different saturated ALD dosing times could influence nucleation on the desired non-growth surface during more extended ASD conditions using ALD/ALE super-cycles. For this test, Si-H substrates were exposed to multiple ALD/ALE super-cycles, where the ALD dosing times per cycle were the same as those used to collect data in Figure 5.4. The ALE cycles followed the conditions described in the experimental section. Figure 5.5 shows the resulting thickness values measured by in-situ ellipsometry, plotted versus number of ALD/ALE super-cycles for all three deposition dose conditions. Note that on the plot, the data collected using 180 ms and 270 ms dosing times are offset on the y-axis by 1 nm and 2 nm,

respectively, to improve data visualization. Comparing results during the first 3-5 super-cycles, the different dosing times show similar trends in film deposition and etching. However, after ~5 super-cycles, for the 270 ms dosing time for both precursors, a significant amount of net deposition is present after ALE. As shown in Figure 5.4, longer $\text{TiCl}_4/\text{H}_2\text{O}$ dose times (without ALE) did not influence the rate of unwanted nucleation on Si-H. However, in Figure 5.5 where ALE cycles are used, longer $\text{TiCl}_4/\text{H}_2\text{O}$ dose times produced more rapid nucleation. This is ascribed to the removal of passivating Si-H bonds by the ALE etchant exposure, which allows more rapid formation Si-O sites that allow TiO_2 growth.²⁹ Interestingly, for all dosing conditions, the ellipsometry data indicates that during each sequence of 5 ALE steps, the amount of film removed per ALE cycle gradually decreases, leaving a thin layer of “un-etched” film on the Si-H substrate. For example, for the case of 90 ms dosing times, ellipsometry indicates that after completing the etching for the 10th or 20th super-cycle, approximately 0.2 nm of TiO_2 remains on the Si-H surface. However, as discussed below, based on results from XPS analysis, the trend in ellipsometry is ascribed to the oxidation of the surface and formation of species not etched by the ALE process, rather than incomplete etching of TiO_2 .

XPS analysis was performed on Si-H samples exposed to various dosing conditions during ALD/ALE to evaluate the film deposition and chemical composition of the surface after the process was completed. The XPS data of the measured Ti 2p signals on samples prepared with various dosing times are displayed in Figure 5.6. All samples (including the starting Si-H) were measured by ex-situ XPS, so differences in adventitious surface carbon and oxygen result from variations in ambient exposure for the different samples tested. However, there is an apparent trend of increasing O at.% as the dosing times and the number of super-cycles increase, which points to the oxidation of the non-growth region, promoting unwanted nucleation. Moreover, the starting

Si-H and all other samples show mild fluorine contamination (>0.2 at.%), which is ascribed to remnant fluorine from the HF-dip surface preparation before deposition. This premise is supported by the observation of clean hydrogen-terminated Si not exposed to ALD displaying F contamination of 3.1 at.%.

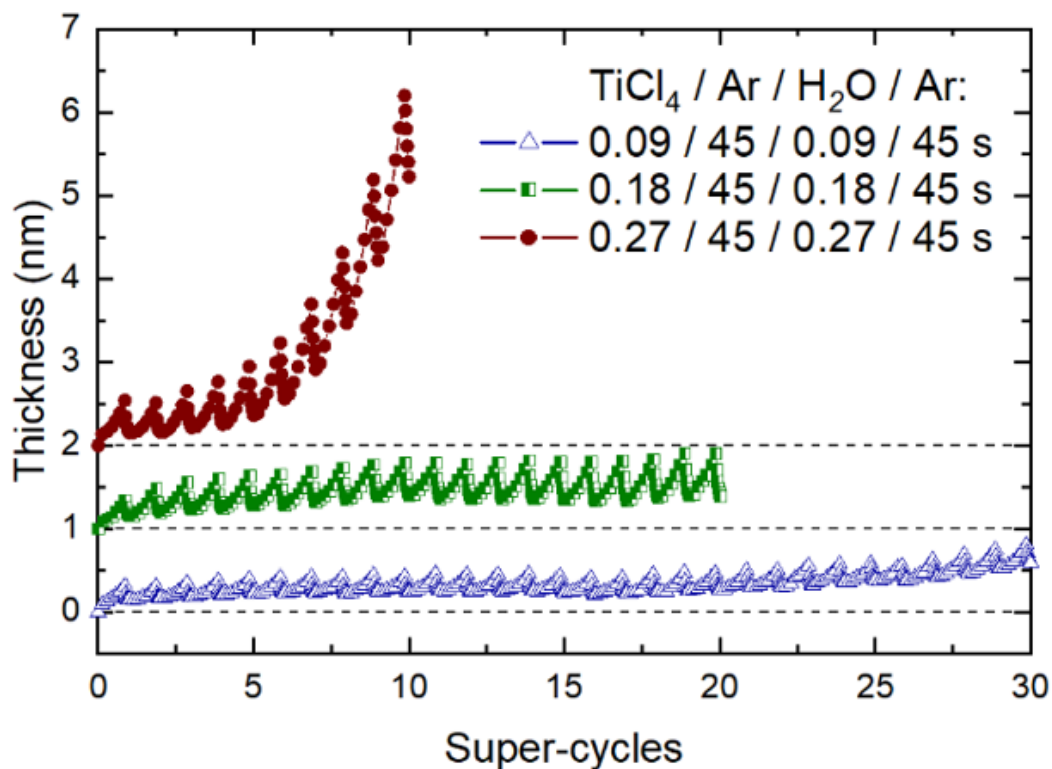


Figure 5.5. The thickness of TiO₂ layer on Si-H as a function of number of super-cycles using TiCl₄/H₂O dosing times of 90, 180, and 270 ms as measured by in-situ ellipsometry. Data is collected after each 5 ALD cycles and after each individual ALE cycle. The data for 180 and 270 ms is offset on the y-axis by 1 nm and 2 nm, respectively, to improve visualization.

After 20 super-cycles using 90 ms TiCl₄ and H₂O dosing times (Figure 5.6a), the XPS Ti 2p spectrum shows no detectable signal. Considering that TiO₂ sensitivity on Si is about 0.3 at.%, the lack of measurable signal indicates that the maximum possible thickness of TiO₂ on that surface is ~0.04 nm, or ~80% of one monolayer,⁶² which is substantially less than suggested by the ellipsometry results in Figure 4.5. Other XPS analysis (shown below) indicates that the WF₆ and

BCl_3 used for ALE modify the surface⁵⁷ and change the surface reflectivity, which the ellipsometry model interprets as thickness increase.

The atomic percentages calculated from the elemental XPS peaks collected on the Si-H surface after ALD/ALE using the different exposure times are summarized in Table 5.1. With XPS data measured after every 10 super-cycles, the 270 ms dosing condition first exhibited the Ti 2p signal at 10 super-cycles (4.5 at.%); the 180 ms at 20 (0.3 at.%); and the 90 ms at 30 (1.2 at.%). This indicates that shorter dosing times help inhibit unwanted nucleation in the combined ALD/ALE process.

The spectra of measured B 1s and W 4d peaks are shown in supplementary material, figure S1. As seen in Figures S1a, b, and c, the exact determination of B 1s signal is complicated due to overlapping Si 2s plasmon loss peak and low concentration of boron. However, the results indicate that only minor amounts of W and B contamination were detected (≤ 0.2 at.%) for higher dosing times.

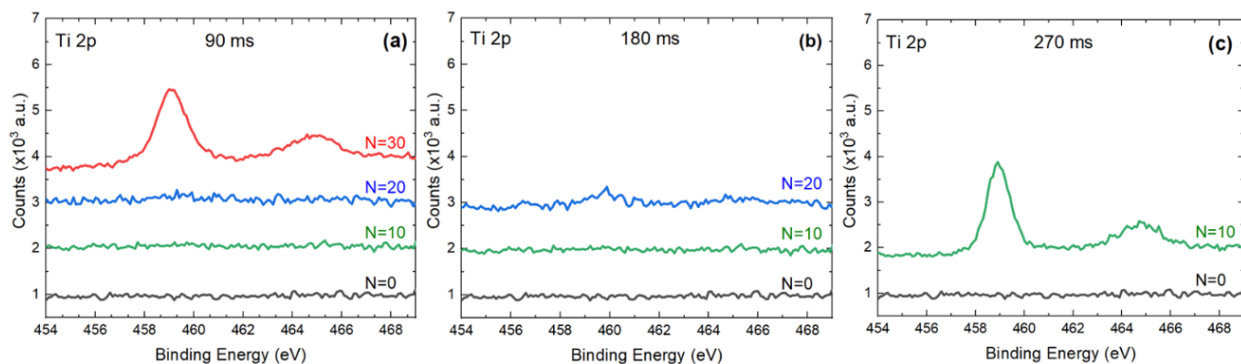


Figure 5.6. XPS data of the Ti 2p signal for deposition carried out using: (a) 90; (b) 180; and (c) 270 ms H_2O and TiCl_4 dosing times for varying number of deposition/etch super-cycles (N) on Si-H.

Table 5.1. Elemental composition of hydrogen-terminated (100) Si wafers exposed to different TiCl₄/H₂O dosing times as measured by X-ray photoelectron spectroscopy (XPS). One super-cycle consists of 30 ALD and 5 ALE cycles.

Dosing time (ms)	Super-cycles	Ti (at.%)	Si (at.%)	O (at.%)	C (at.%)	B (at.%)	W (at.%)	F (at.%)	Cl (at.%)
0	0	0	72.7	9.0	15.2	0	0	3.1	0
90	10	0	72.9	17.2	8.7	0	0	1.2	0
	20	0	70.1	20.7	7.8	0	0	0.5	0.9
	30	1.2	64.1	20.2	10.3	0.1	0	4.1	0
180	10	0	65.4	21.4	12.0	0.1	0.1	0.4	0.7
	20	0.3	58.0	24.9	15.1	0.1	0.2	0.5	0.9
270	10	4.5	43.9	30.1	17.6	0.2	0.2	2.7	0.8

To further distinguish the effect of TiCl₄ and H₂O dose amount on TiO₂ selectivity, the TiCl₄ and H₂O dosing times were varied independently, and Figure 5.7 shows the resulting in-situ ellipsometry data collected during ALD/ALE on Si-H. This experiment consisted of two runs, one using TiCl₄/H₂O dosing times of 270/90 ms and the other using 90/270 ms, respectively. The conditions were otherwise identical to those used for collecting data in Figure 5.5, and data was collected for a total of 15 ALD/ALE super-cycles. The two data sets are clearly distinguishable with the larger H₂O dosing time condition displaying less nucleation delay than the shorter H₂O dosing time condition. Moreover, the shorter H₂O dose condition sample etches to a relatively constant optical thickness of 0.15-0.3 nm after each super-cycle. In comparison, the higher H₂O dosing time condition is unable to etch back to the initial baseline of the optical thickness after the 6th super-cycle, where the thickness after each super-cycle exceeds the previous. At the end of the 15 super-cycles, the 90/270 ms case resulted in a final thickness of ~1.2 nm, while the 270/90 ms TiCl₄/H₂O case had a final thickness of ~0.4 nm. This noticeable difference between two

conditions confirms that H₂O is the major factor in shortening the nucleation delay during ALD/ALE super-cycles on the Si-H surfaces. This effect of H₂O exposure is ascribed to oxidation of the initial hydrogen-terminated surface, promoting growth of mixed Ti/Si oxide. The ALE sequence used here is favorable for etching TiO₂ but not for etching SiO₂.²⁹

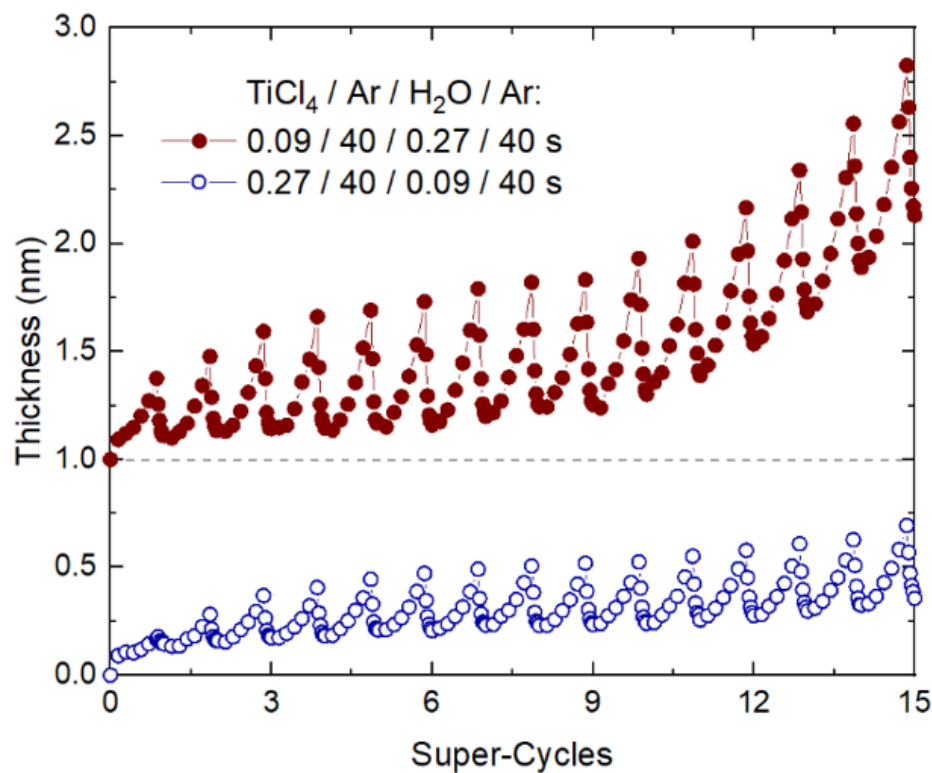


Figure 5.7. The thickness of TiO₂ layer on Si-H for TiCl₄/H₂O 90/270 ms and 270/90 ms dosing times as measured by in-situ ellipsometry. Data is shown for 15 super-cycles, consisting of 30 ALD and 5 ALE cycles each, with data points taken every 5 cycles for ALD and every cycle for ALE. The data for 90/270 ms is offset on the y-axis by 1 nm to improve visualization.

Based on results in Figures 5.6 and 5.7, the conditions using the shortest reactant exposure time are expected to produce the largest selectivity values. Figure 5.8 shows results obtained by in-situ ellipsometry for 90 ms dosing times for 30/5 ALD/ALE condition at 170°C for 30 super-cycles measured during two identical runs, where the ellipsometer was focused on Si-OH and Si-H, respectively. The final thicknesses were ~25.5 nm on the Si-OH surface and ~0.6 nm on the Si-

H surface. Calculating the selectivity defined by equation (1) results in $S \approx 0.95$ for a thickness of 25.5 nm on the preferred growth surface. Extrapolation of the data using a model to quantify and predict nucleation indicates a selectivity of $S > 0.9$ up to 36.9 nm film thickness - a significant improvement from our previously reported result of 15 nm ASD for $S > 0.9$ using fully saturated dosing conditions,^{29,59} and even more notable compared to the ALD-only case, where $S > 0.9$ was limited to only 1.5 nm.

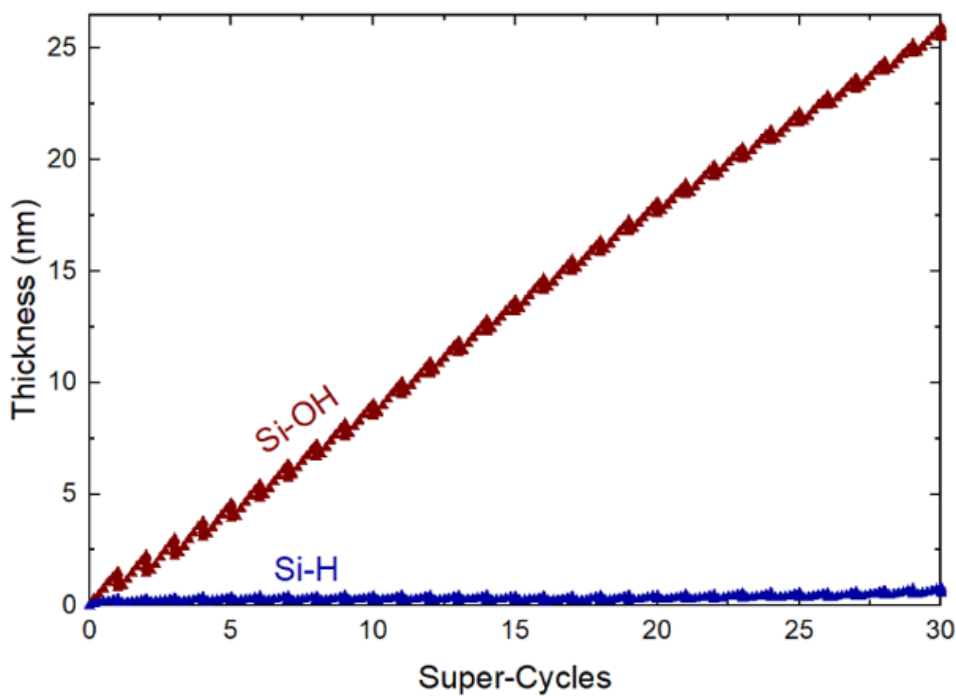


Figure 5.8. TiO₂ film thickness on Si-H and Si-OH surfaces during ALE/ALE super-cycles with 90 ms dosing conditions for TiCl₄/H₂O. The measurement was done by in-situ ellipsometry, with data point taken after every 5 cycles for ALD and every cycle for ALE.

5.4.3 Effect of dosing time on patterned substrates

The effect of reactant dosing duration on the deposition of TiO₂ on Si/SiO₂ patterned substrates was studied using SEM. Figure 5.9 exhibits patterns exposed to 270/270 ms dosing conditions for 10 super-cycles and to 90/90 ms dosing conditions for 30 super-cycles. The first condition set shows a relatively low number of nuclei on both Si and SiO₂ compared to the latter

condition, where noticeable amount of particles are present on both surfaces. These nuclei, not removed by the atomic layer etching, are generated during the process and as such, the higher density of these particles for lower dosing conditions may be ascribed to higher number of super-cycles performed. As such, a cleaning process capable of removing the generated nuclei without damaging the thin film is needed to achieve clean substrates with a thick selective TiO₂ film.

To further study the effect of the reactant doses on promoting deposition on the non-growth surface, cross-sectional STEM images were taken of the Si/SiO₂ patterned substrates exposed to different dosing time conditions, and resulting images are presented in Figure 5.10. The EDS analysis of samples deposited using 90/90 ms dosing times for 30 super-cycles and 270/270 ms dosing times for 10 super-cycles show no visible TiO₂ growth on the Si-H for either sample. However, a thin top layer of the initially hydrogen-terminated surface appears to have oxidized as indicated by a thin green layer visible in TEM-EDS images. As no detectable TiO₂ has deposited on top of this oxidized layer it can be presumed to have oxidized during the preparation of the TEM cross-section. Meanwhile, noticeable TiO₂ growth is present on the SiO₂ surface with measured film thickness of 11.5 nm for the 270/270 ms condition and 32.7 nm for the 90/90 ms condition. Although more detailed higher-resolution images are needed, it appears that the thicker TiO₂ film leads to “mushroom” growth, where the TiO₂ deposits from all directions on SiO₂, including laterally on the Si-H surface near Si/SiO₂ interface.

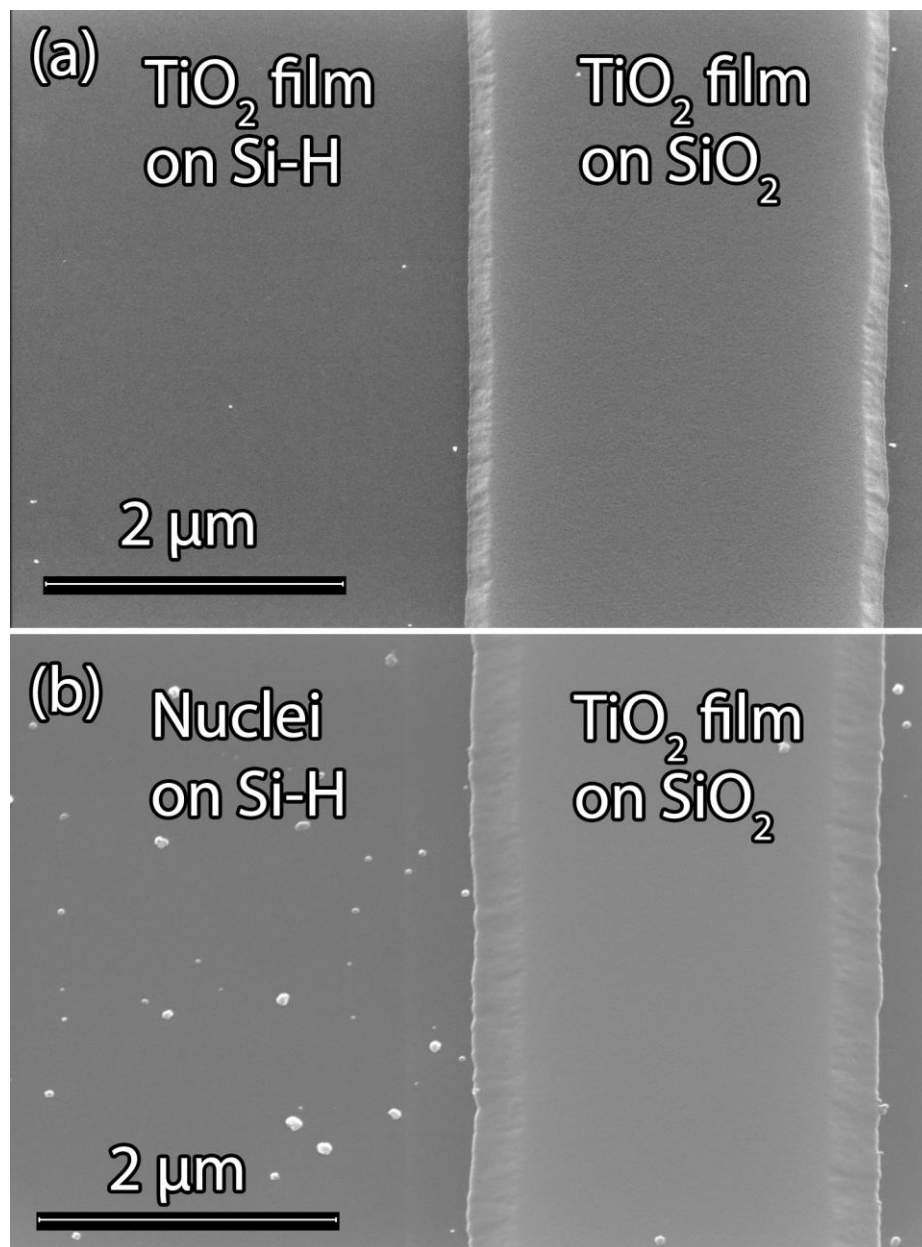


Figure 5.9. SEM images of TiO_2 ALD/ALE on patterned Si/ SiO_2 substrates using (a) 270 ms dosing conditions for 10 super-cycles and (b) 90 ms dosing conditions for 30 super-cycles.

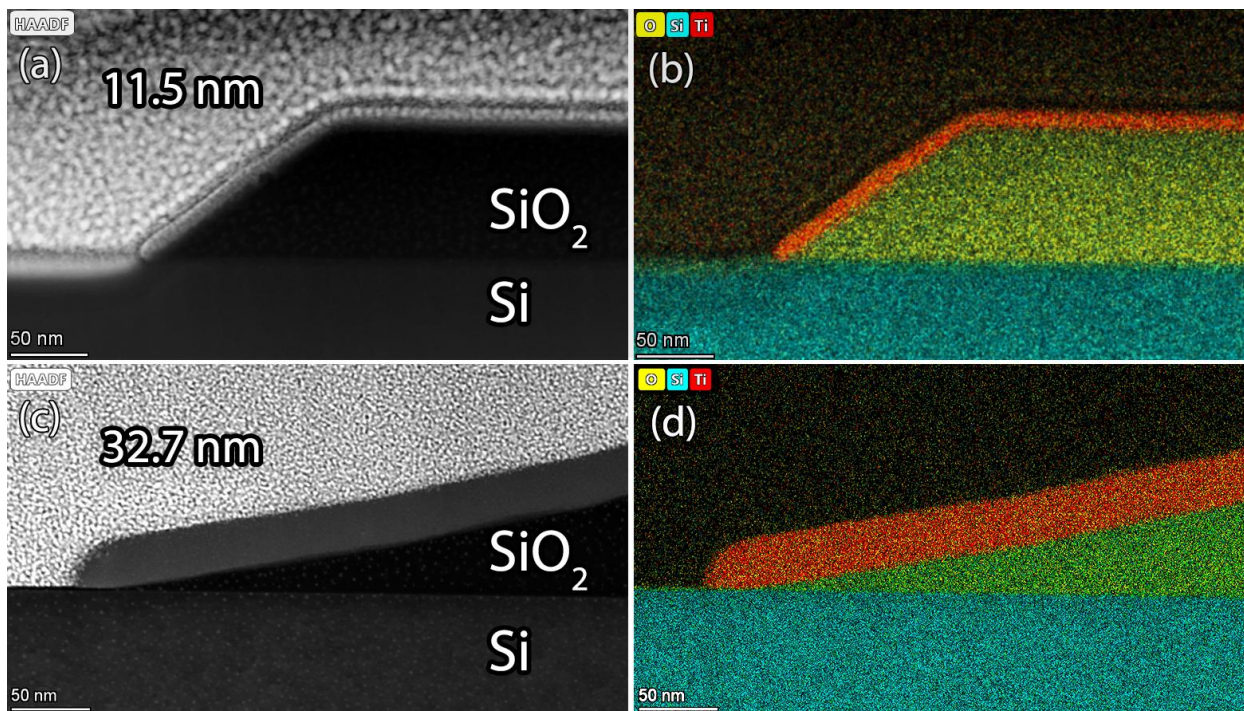


Figure 5.10. (a) Cross-sectional TEM and (b) TEM-EDS mapping of 10 ALD/ALE super-cycles at 270 ms dosing conditions on Si/SiO₂ pattern. (c) Cross-sectional TEM and (d) TEM-EDS mapping of 30 ALD/ALE super-cycles at 90 ms dosing conditions on Si/SiO₂ pattern.

5.5 Conclusion

The effect of reactant exposure on the selectivity of area-selective TiO₂ deposition has been investigated in a combined isothermal ALD/ALE process. In-situ ellipsometry results show that extending the reactant exposure times during ALD maintains nearly the same growth per cycle on both Si-H and Si-OH surfaces. In contrast, overdosing TiCl₄/H₂O during ALD/ALE super-cycles leads to excess thickness increase on the preferred non-growth Si-H surface. Near-saturated H₂O dosing was shown to maintain a selectivity of $S \approx 0.95$ up to TiO₂ film thickness of 25.5 nm on Si-OH surface: a significant improvement from the ALD-only case, which resulted in a film thickness of 1.5 nm at $S \approx 0.9$.

Independently comparing TiCl_4 and H_2O dosing times, the water was found to be the main cause for the selectivity loss, with longer H_2O dosing times exhibiting notably faster nucleation on the Si-H. This loss of selectivity can be attributed to two main factors: 1) overexposure of the reactants leads to increased chance of interactions with the surface, prompting physisorption and generation of potential nucleation sites and 2) water vapor reacts with the exposed surface sites formed during ALE by the removal of Si-H bonds causing the growth of surface oxide species that are not etched by the TiO_2 ALE chemistry.

The mechanisms shown here for ASD using combined ALD/ALE steps indicate that selectivity loss is associated with alternate unfavorable reactions on the non-growth surface during extended ALD reactant exposures. Therefore, this work expands the understanding of effects of reactant exposure during area-selective ALD, where overexposure of one or both of the precursors may have negligible effect during typical ALD, but leads to selectivity loss during area-selective deposition. Although not studied explicitly in this work, adjusting the reactant dose times to improve selectivity could negatively impact the conformality of a desired film coating, for example, in high aspect ratio trenches where relatively long dose times are needed to achieve uniform deposition. As shown here, increasing the exposure beyond near-saturation can have a negative impact on overall deposition selectivity. We believe that achieving conformal deposition while maintaining high selectivity is an important challenge which needs to be addressed in future works. In general, the effect of dosing duration on film nucleation helps to further improve area-selective deposition and the ability to manipulate or minimize unwanted nucleation in future processes.

5.6 Supplemental Material

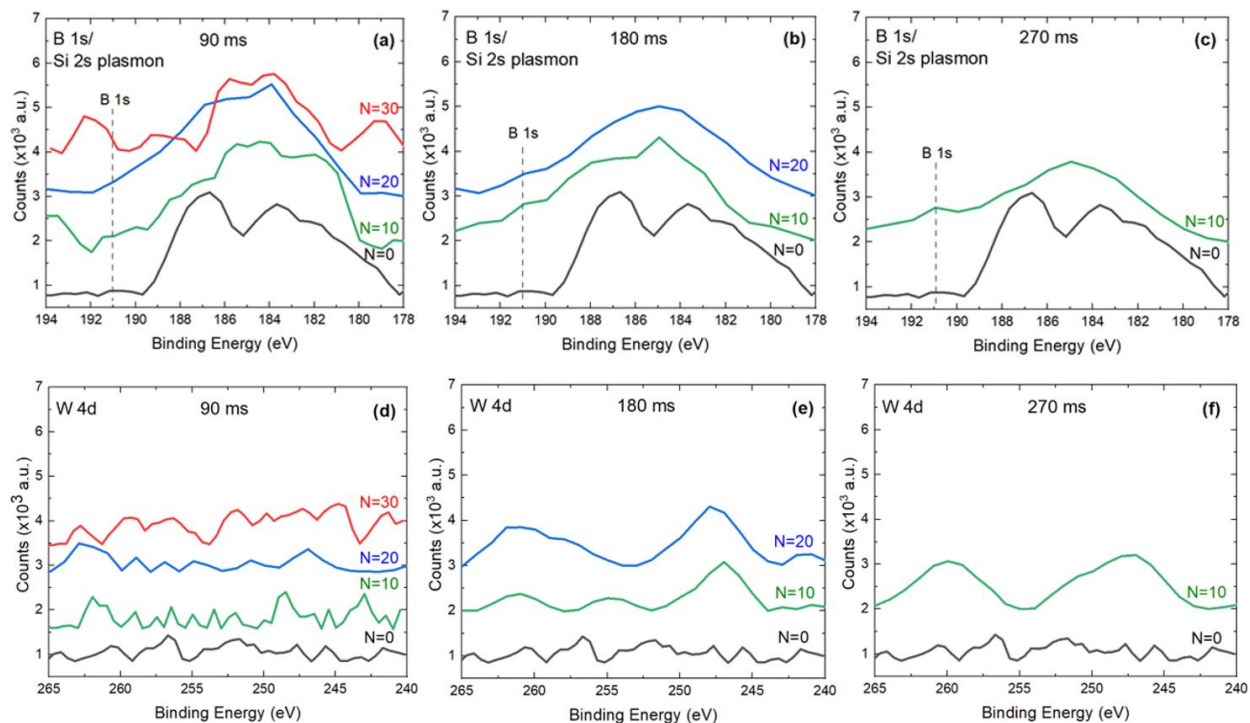


Figure S5.1. XPS spectra of the B 1s/Si 2s plasmon (a,b,c) and W 4d (d,e,f) signal for deposition carried out using: (a,d) 90; (b,e) 180; and (c,f) 270 ms H₂O and TiCl₄ dosing times for varying number of deposition/etch super-cycles (N) on Si-H. One super-cycle consists of 30 ALD and 5 ALE cycles. The B 1s peak is located at 191 eV, overlapped by a Si 2s plasmon loss signal.

5.7 References

1. Biyikli, N., Haider, A., Deminskyi, P. & Yilmaz, M. Self-aligned nanoscale processing solutions via selective atomic layer deposition of oxide, nitride, and metallic films. in *Low-Dimensional Materials and Devices 2017* (eds. Kobayashi, N. P., Talin, A. A., Davydov, A. V. & Islam, M. S.) vol. 10349 20 (SPIE, 2017).
2. Mackus, A. J. M., Merkx, M. J. M. & Kessels, W. M. M. From the Bottom-Up: Toward Area-Selective Atomic Layer Deposition with High Selectivity. *Chemistry of Materials* **31**, 2–12 (2019).
3. Mackus, A. J. M., Bol, A. A. & Kessels, W. M. M. The use of atomic layer deposition in advanced nanopatterning. *Nanoscale* **6**, 10941–10960 (2014).
4. Vallat, R., Gassilloud, R., Eychenne, B. & Vallée, C. Selective deposition of Ta₂O₅ by adding plasma etching super-cycles in plasma enhanced atomic layer deposition steps. *Citation: Journal of Vacuum Science & Technology A* **35**, 1–104 (2017).
5. Minaye Hashemi, F. S., Birchansky, B. R. & Bent, S. F. Selective Deposition of Dielectrics: Limits and Advantages of Alkanethiol Blocking Agents on Metal-Dielectric Patterns. *ACS Applied Materials and Interfaces* **8**, 33264–33272 (2016).
6. Seo, E. K., Lee, J. W., Sung-Suh, H. M. & Sung, M. M. Atomic layer deposition of titanium oxide on self-assembled-monolayer-coated gold. *Chemistry of Materials* **16**, 1878–1883 (2004).
7. Avila, J. R. *et al.* Real-time observation of atomic layer deposition inhibition: Metal oxide growth on self-assembled alkanethiols. *ACS Applied Materials and Interfaces* **6**, 11891–11898 (2014).

8. Chen, R., Kim, H., McIntyre, P. C. & Bent, S. F. Investigation of self-assembled monolayer resists for hafnium dioxide atomic layer deposition. *Chemistry of Materials* **17**, 536–544 (2005).
9. Kanarik, K. J. *et al.* Overview of atomic layer etching in the semiconductor industry. *Journal of Vacuum Science & Technology A: Vacuum, Surfaces, and Films* **33**, 020802 (2015).
10. Puurunen, R. L. Analysis of hydroxyl group controlled atomic layer deposition of hafnium dioxide from hafnium tetrachloride and water. *Journal of Applied Physics* **95**, 4777–4786 (2004).
11. Alam, M. A. & Green, M. L. Mathematical description of atomic layer deposition and its application to the nucleation and growth of HfO₂ gate dielectric layers. *Journal of Applied Physics* **94**, 3403–3413 (2003).
12. Puurunen, R. L. Growth Per Cycle in Atomic Layer Deposition: A Theoretical Model. *Chemical Vapor Deposition* **9**, 249–257 (2003).
13. Ylilammi, M. Monolayer thickness in atomic layer deposition. *Thin Solid Films* **279**, 124–130 (1996).
14. Green, M. L. *et al.* Nucleation and growth of atomic layer deposited HfO₂ gate dielectric layers on chemical oxide (Si–O–H) and thermal oxide (SiO₂ or Si–O–N) underlayers. *Journal of Applied Physics* **92**, 7168–7174 (2002).
15. Green, M. L. *et al.* Nucleation of atomic-layer-deposited HfO₂ films, and evolution of their microstructure, studied by grazing incidence small angle x-ray scattering using synchrotron radiation. *Applied Physics Letters* **88**, 32907 (2006).

16. Gusev, E. P., Cabral, C., Copel, M., D'Emic, C. & Gribelyuk, M. Ultrathin HfO₂ films grown on silicon by atomic layer deposition for advanced gate dielectrics applications. *Microelectronic Engineering* **69**, 145–151 (2003).
17. Damlencourt, J.-F. *et al.* Electrical and physico-chemical characterization of HfO₂/SiO₂ gate oxide stacks prepared by atomic layer deposition. *Solid-State Electronics* **47**, 1613–1616 (2003).
18. Hackley, J. C., Gougousi, T. & Demaree, J. D. Nucleation of HfO₂ atomic layer deposition films on chemical oxide and H-terminated Si. *Journal of Applied Physics* **102**, 34101 (2007).
19. Cho, M. *et al.* Chemical interaction between atomic-layer-deposited HfO₂ thin films and the Si substrate. *Applied Physics Letters* **81**, 334–336 (2002).
20. Gusev, E. P. *et al.* Ultrathin high-K metal oxides on silicon: processing, characterization and integration issues. *Microelectronic Engineering* **59**, 341–349 (2001).
21. Kirsch, P. D. *et al.* Nucleation and growth study of atomic layer deposited HfO₂ gate dielectrics resulting in improved scaling and electron mobility. *Journal of Applied Physics* **99**, 23508 (2006).
22. Aarik, J. *et al.* Effects of precursors on nucleation in atomic layer deposition of HfO₂. *Applied Surface Science* **230**, 292–300 (2004).
23. Copel, M., Gribelyuk, M. & Gusev, E. Structure and stability of ultrathin zirconium oxide layers on Si(001). *Applied Physics Letters* **76**, 436–438 (2000).
24. Ferrari, S., Modreanu, M., Scarel, G. & Fanciulli, M. X-Ray reflectivity and spectroscopic ellipsometry as metrology tools for the characterization of interfacial layers in high-κ materials. *Thin Solid Films* **450**, 124–127 (2004).

25. Puurunen, R. L. *et al.* Island growth in the atomic layer deposition of zirconium oxide and aluminum oxide on hydrogen-terminated silicon: Growth mode modeling and transmission electron microscopy. *Journal of Applied Physics* **96**, 4878–4889 (2004).
26. Kukli, K., Ritala, M., Aarik, J., Uustare, T. & Leskelä, M. Influence of growth temperature on properties of zirconium dioxide films grown by atomic layer deposition. *Journal of Applied Physics* **92**, 1833–1840 (2002).
27. Methaapanon, R. & Bent, S. F. Comparative Study of Titanium Dioxide Atomic Layer Deposition on Silicon Dioxide and Hydrogen-Terminated Silicon. *The Journal of Physical Chemistry C* **114**, 10498–10504 (2010).
28. Mitchell, D. R. G., Attard, D. J. & Triani, G. Transmission electron microscopy studies of atomic layer deposition TiO₂ films grown on silicon. *Thin Solid Films* **441**, 85–95 (2003).
29. Song, S. K., Saare, H. & Parsons, G. N. Integrated Isothermal Atomic Layer Deposition/Atomic Layer Etching Supercycles for Area-Selective Deposition of TiO₂. *Chemistry of Materials* **31**, 4793–4804 (2019).
30. Kanarik, K. J., Tan, S. & Gottscho, R. A. Atomic Layer Etching: Rethinking the Art of Etch. *J. Phys. Chem. Lett* **9**, 4821 (2018).
31. George, S. M. & Lee, Y. Prospects for Thermal Atomic Layer Etching Using Sequential, Self-Limiting Fluorination and Ligand-Exchange Reactions. *ACS Nano* **10**, 4889–4894 (2016).
32. Fang, C., Cao, Y., Wu, D. & Li, A. Thermal atomic layer etching: Mechanism, materials and prospects. *Progress in Natural Science: Materials International* **28**, 667–675 (2018).
33. Langereis, E. *et al.* *In situ* spectroscopic ellipsometry as a versatile tool for studying atomic layer deposition. *Journal of Physics D: Applied Physics* **42**, 073001 (2009).

34. Kief, M. T. In-situ ellipsometry: applications to thin film research, development, and production. in vol. 10294 1029403 (International Society for Optics and Photonics, 1999).
35. Junige, M., Geidel, M., Knaut, M., Albert, M. & Bartha, J. W. Monitoring atomic layer deposition processes in situ and in real-time by spectroscopic ellipsometry. in *2011 Semiconductor Conference Dresden 1–4* (IEEE, 2011). doi:10.1109/SCD.2011.6068739.
36. Mackus, A. J. M., Verheijen, M. A., Leick, N., Bol, A. A. & Kessels, W. M. M. Influence of Oxygen Exposure on the Nucleation of Platinum Atomic Layer Deposition: Consequences for Film Growth, Nanopatterning, and Nanoparticle Synthesis. *Chemistry of Materials* **25**, 1905–1911 (2013).
37. Muneshwar, T. & Cadien, K. Probing initial-stages of ALD growth with dynamic in situ spectroscopic ellipsometry. *Applied Surface Science* **328**, 344–348 (2015).
38. Wind, R. W., Fabreguette, F. H., Sechrist, Z. A. & George, S. M. Nucleation period, surface roughness, and oscillations in mass gain per cycle during W atomic layer deposition on Al₂O₃. *Journal of Applied Physics* **105**, 074309 (2009).
39. Lecordier, L., Herregods, S. & Armini, S. Vapor-deposited octadecanethiol masking layer on copper to enable area selective Hf₃N₄ atomic layer deposition on dielectrics studied by in situ spectroscopic ellipsometry. *Journal of Vacuum Science & Technology A* **36**, 031605 (2018).
40. Baker, L. *et al.* Nucleation and growth of Pt atomic layer deposition on Al₂O₃ substrates using (methylcyclopentadienyl)-trimethyl platinum and O₂ plasma. *Journal of Applied Physics* **109**, 084333 (2011).
41. Langereis, E., Heil, S. B. S., Van De Sanden, M. C. M. & Kessels, W. M. M. In situ spectroscopic ellipsometry study on the growth of ultrathin TiN films by plasma-assisted atomic layer deposition. *Journal of Applied Physics* **100**, 023534 (2006).

42. Patsalas, P. & Logothetidis, S. Interface properties and structural evolution of TiN/Si and TiN/GaN heterostructures. *Journal of Applied Physics* **93**, 989–998 (2003).
43. Jiang, X., Wang, H., Qi, J. & Willis, B. G. In-situ spectroscopic ellipsometry study of copper selective-area atomic layer deposition on palladium. *Citation: Journal of Vacuum Science & Technology A* **32**, 41513 (2014).
44. Junige, M. *et al.* Area-selective atomic layer deposition of Ru on electron-beam-written Pt(C) patterns versus SiO₂ substratum. *Nanotechnology* **28**, 395301 (2017).
45. Raza, M. A., Zandvliet, H. J. W., Poelsema, B. & Kooij, E. S. Selective metallization by seeded growth on patterned gold nanoparticle arrays. *Journal of Applied Physics* **113**, 233510 (2013).
46. Vos, M. F. J. *et al.* Area-Selective Deposition of Ruthenium by Combining Atomic Layer Deposition and Selective Etching. *Chemistry of Materials* **31**, 3878–3882 (2019).
47. Pesce, V. *et al.* Optimization by in situ ellipsometry of ALD and ALE successive steps for the selective Atomic Layer Deposition of Ta₂O₅ on TiN and Si. *AVS 65th International Symposium* (2018).
48. Mameli, A. *et al.* Area-Selective Atomic Layer Deposition of SiO₂ Using Acetylacetone as a Chemoselective Inhibitor in an ABC-Type Cycle. *ACS Nano* **11**, 9303–9311 (2017).
49. Mameli, A. *et al.* Area-Selective Atomic Layer Deposition of ZnO by Area Activation Using Electron Beam-Induced Deposition. *Chemistry of Materials* **31**, 1250–1257 (2019).
50. Niang, K. M., Bai, G. & Robertson, J. Influence of precursor dose and residence time on the growth rate and uniformity of vanadium dioxide thin films by atomic layer deposition. *Journal of Vacuum Science & Technology A* **38**, 42401 (2020).

51. Baji, Z. *et al.* Nucleation and Growth Modes of ALD ZnO. *Crystal Growth & Design* **12**, 5615–5620 (2012).
52. Kuse, R., Kundu, M., Yasuda, T., Miyata, N. & Toriumi, A. Effect of precursor concentration in atomic layer deposition of Al₂O₃. *Journal of Applied Physics* **94**, 6411–6416 (2003).
53. Murray, C. A., Elliott, S. D., Hausmann, D., Henri, J. & LaVoie, A. Effect of Reaction Mechanism on Precursor Exposure Time in Atomic Layer Deposition of Silicon Oxide and Silicon Nitride. *ACS Applied Materials & Interfaces* **6**, 10534–10541 (2014).
54. Kukli, K. *et al.* Effect of selected atomic layer deposition parameters on the structure and dielectric properties of hafnium oxide films. *Journal of Applied Physics* **96**, 5298–5307 (2004).
55. Gordon, R. G., Hausmann, D., Kim, E. & Shepard, J. A Kinetic Model for Step Coverage by Atomic Layer Deposition in Narrow Holes or Trenches. *Chemical Vapor Deposition* **9**, 73–78 (2003).
56. Seo, S. *et al.* Reaction Mechanism of Area-Selective Atomic Layer Deposition for Al₂O₃ Nanopatterns. (2017) doi:10.1021/acsami.7b13365.
57. Lemaire, P. C. & Parsons, G. N. Thermal Selective Vapor Etching of TiO₂ : Chemical Vapor Etching via WF₆ and Self-Limiting Atomic Layer Etching Using WF₆ and BCl₃. *Chemistry of Materials* **29**, 6653–6665 (2017).
58. Garcia-Caurel, E., De Martino, A., Gaston, J. P. & Yan, L. Application of spectroscopic ellipsometry and mueller ellipsometry to optical characterization. *Applied Spectroscopy* vol. 67 1–21 (2013).
59. Parsons, G. N. Functional model for analysis of ALD nucleation and quantification of area-selective deposition. *Journal of Vacuum Science & Technology A* **37**, 020911 (2019).

60. Gladfelter, W. L. Selective Metallization by Chemical Vapor Deposition. *Chemistry of Materials* **5**, 1372–1388 (1993).
61. Parsons, G. N. & Clark, R. D. Area-Selective Deposition: Fundamentals, Applications, and Future Outlook. *Chemistry of Materials* vol. 32 4920–4953 (2020).
62. Shard, A. G. Detection limits in XPS for more than 6000 binary systems using Al and Mg K α X-rays. *Surface and Interface Analysis* **46**, 175–185 (2014).

CHAPTER 6

Atomic Layer Deposition of GeTe-Sb₂Te₃ Phase Change Memories

Holger Saare, Jung-Sik Kim, and Gregory N. Parsons,

6.1 Preface

Phase change memories are chalcogenide-based nonvolatile memories with great potential due to their fast operation, high scalability, and low power consumption. While the phase change memory cells have been primarily deposited by physical vapor deposition, atomic layer deposition of the films would enable production of conformal integrated 3D structures with large capacity and density. In this work ALD of GeTe and Sb₂Te₃ films is studied using trichlorogermane (HGeCl₃), bis(trimethylsilyl)telluride [(Me₃Si)₂Te], and antimony(III)ethoxide [Sb(OEt)₃] as precursors. *In-situ* ellipsometry is used to confirm the deposition on Si-OH, Si-H, W, and TiN surfaces at 70 °C with steady-state growth per cycle of 0.07 nm/cycle and a strong temperature dependence with growth rates dropping to nearly zero at temperatures above 80 °C. Strong run-to-run variations are present in the ellipsometry data for reasons not yet fully understood. X-ray photoelectron spectroscopy (XPS) and X-ray diffractometry (XRD) analysis revealed that the stoichiometry and the crystallinity of the films depends on the substrate and deposited film thickness. It was found that GeTe deposits as crystalline on W substrate, but as amorphous on Si-H, however, both films crystallized after annealing at 170 °C. The ALD processes introduced here contribute to the development of 3D memory devices utilizing phase-change memory materials.

6.2 Introduction

The technological advancement in modern fields such as big data or neuromorphic computing has fostered a greater demand for nonvolatile memory (NVM) technologies.¹⁻³ One of the emerging approaches with great potential are phase change memories (PCM), in which

chalcogenide glass can be converted to crystalline or amorphous phases by heating and cooling steps.⁴ The temperature changes are achieved by running the current through the PCM material using electrodes located at the top and the bottom. Heating the material to the temperature between that of the crystallization and the melting temperature leads to crystallization in nanosecond or even sub-nanosecond regime.⁵ The crystalline-to-amorphous transformation occurs when the cell is melted at higher currents and then rapidly quenched. These phases have significantly different optical and electrical properties, which can be used to represent a binary 0 (amorphous phase, high resistance) and a 1 (crystalline phase, low resistance).⁶ Compared to the other state-of-the-art NVMs, such as flash memory, the PCMs excel in fast operation, high scalability, and low power consumption.⁷⁻⁹

Physical vapor deposition (PVD) has been the main technique for PCM deposition as it allows precise control over the stoichiometry of the material, which has noticeable impact on the electrical properties of the film, and allows deposition of wide variety of compositions.¹⁰⁻¹³ However, unlike atomic layer deposition (ALD), PVD does not result in conformal deposition on 3D structures, which are needed for high density memory cells.^{4,14,15} While various materials have been investigated for PCM applications, most of the research has been focused on Ge-Sb-Te (GST) based cells due to their stability and fast crystallization, with $\text{Ge}_2\text{Sb}_2\text{Te}_5$ (GST225) being commonly studied.¹⁶⁻²² It has been shown that GeTe-rich GST composition leads to higher stability, while Sb_2Te_3 -rich material exhibits a faster operation due to quicker crystallisation.^{23,24} In addition, several dopants have been introduced to alter the properties of the PCM materials. It has been shown that while Sn and Bi increase the switching speed of the memory cells, they lead to inferior thermal stability.^{25,26} In contrast, O, N, C, Si, and Ti increase the thermal stability, but lower the operation speed.^{18,27-33} As such, controlling the composition of the PCM is crucial and

can be altered depending on the application. While several research articles have been published in recent years that have laid the foundation for atomic layer deposited phase PCMs, further research on the process conditions and device properties is needed for the commercialization of the technology.

In this study, thermal ALD of GeTe and Sb₂Te₃ materials are demonstrated using HGeCl₃, (Me₃Si)₂Te, and Sb(OEt)₃ as precursors. The effect of precursor dosing times, process temperature, and different growth substrates were analyzed using *in-situ* ellipsometry. In-depth characterization of the film properties was carried out using ex-situ X-ray spectroscopy (XPS), X-ray diffractometry (XRD), and atomic force microscopy (AFM) to study the chemical composition, surface morphology, and the crystallization of the samples.

6.3 Experimental Details

Atomic layer deposition of GeTe and Sb₂Te₃ films were carried out in a custom warm-wall ALD reactor described previously in more detail.³⁴ Argon (99.999% purity, Arc3 Gases) was used as a purge and carrier gas with a constant flowrate of 95 sccm throughout the process. The operating pressure was regulated by a throttle valve and was kept at 500 mTorr. For deposition, trichlorogermane (HGeCl₃, Gelest) was used as a Ge precursor, bis(trimethylsilyl)telluride (BTMSTe, (Me₃Si)₂Te, Wonik Materials, 98% purity) was used as a Te precursor, and antimony(III)ethoxide (Sb(OEt)₃, Alfa Aesar, 99.9% purity) as a Sb precursor. All precursors were dosed via vapor draw method using pneumatic diaphragm valves (Swagelok, 6LVV-ALD3TC333P-C). While HGeCl₃ was dosed through a metering valve due to the chemical's high vapor pressure, the BTMSTe and Sb(OEt)₃ were heated to 65 °C and 80 °C, respectively, to increase their vapor pressure. The silicon substrates used in this study were boron doped p-type Si (100) with 5-10 Ω-cm resistivity. The hydroxyl-terminated silicon wafers were prepared by

submerging the wafers in piranha solution (1:1 H₂SO₄:H₂O₂) and subsequently rinsing the substrates under deionized water. The hydrogen-terminated silicon substrates were obtained by dipping the wafers into 5% HF solution, rinsed under DI-water and dried under nitrogen flow. Likewise, the W thin films were dipped into 5% HF solution for 60 s and dried under nitrogen before inserting the samples into the chamber to remove the WO₃ layer off the surface. The TiN substrates were cleaned by sonication in acetone for 10 minutes, followed by sonication in isopropyl alcohol for 10 minutes and rinsed under DI-water.

In-situ ellipsometry measurements were performed using Film Sense FS-1 four-wavelength ellipsometer. The ellipsometer obtains raw Ψ and Δ data at 465 nm, 525 nm, 580 nm, and 635 nm wavelengths. The measurements were performed at $65^\circ \pm 1^\circ$ incident angle with measurements performed after every, or every other ALD cycle. The optical film thicknesses were obtained using the Tauc-Lorentz dispersion formula, which is commonly used to describe amorphous semiconductors. The parameters and equations used have been described by Jellison Jr. and Modine.³⁵

The surface roughness of the samples were obtained using Asylum MFP-3d Atomic Force Microscope. The stoichiometry and composition of the film were determined using ex-situ SPECS XPS with PHOIBOS 150 analyzer. XRD measurements were performed using Rigaku SmartLab X-ray Diffractometer to characterize the density and crystallinity of the films.

6.4 Results and Discussion

The growth kinetics of GeTe thin films were investigated *using in-situ* multi-wavelength ellipsometry. The film thicknesses as functions of ALD cycles at 70 °C substrate temperature are shown in Figure 6.1 for various HGeCl₃ and BTMSTe dosing times. To determine BTMSTe precursor saturation, HGeCl₃ was dosed for 0.6 s, followed by a 15 s purge, and a BTMSTe dose

between 0.1 to 1.5 s, followed by a 120 s purge. Similarly, to study HGeCl₃ saturation, HGeCl₃ was dosed between 0.1 to 1.2 s, followed by a 15 s purge, 1.0 s BTMSTe dose, and a 120 s argon purge. The long purge time was necessary to allow the vapor pressure of the BTMSTe precursor to sufficiently regenerate between the cycles. The thickness trends exhibit an accelerated growth rate during the first cycle, followed by a steady-state deposition regime. This indicates that the first cycle operates in substrate-dependent regime, where the precursor absorption is more significant compared to the subsequent GeTe on GeTe steady-state growth. The growth rates of these accelerated initial growths and following steady-state growth are plotted in Figure 6.1 (c) and (d). It is apparent that both HGeCl₃ and BTMSTe saturate at around ~0.2 s dosing times with growth rates of ~0.07 nm/cycle. The growth rate matches well a previously published growth rate of 0.08 nm/cycle at a lower temperature of 60 °C.²⁰ Likewise it is apparent that the growth rate during the first cycle is directly correlated with the steady-state growth rate with higher initial growth leading to higher subsequent deposition rates. In addition to singular doses, the effect of double-dosing the precursors was studied. The growth rate was not affected by dosing 2x0.3 s HGeCl₃ or BTMSTe compared to a single dose.

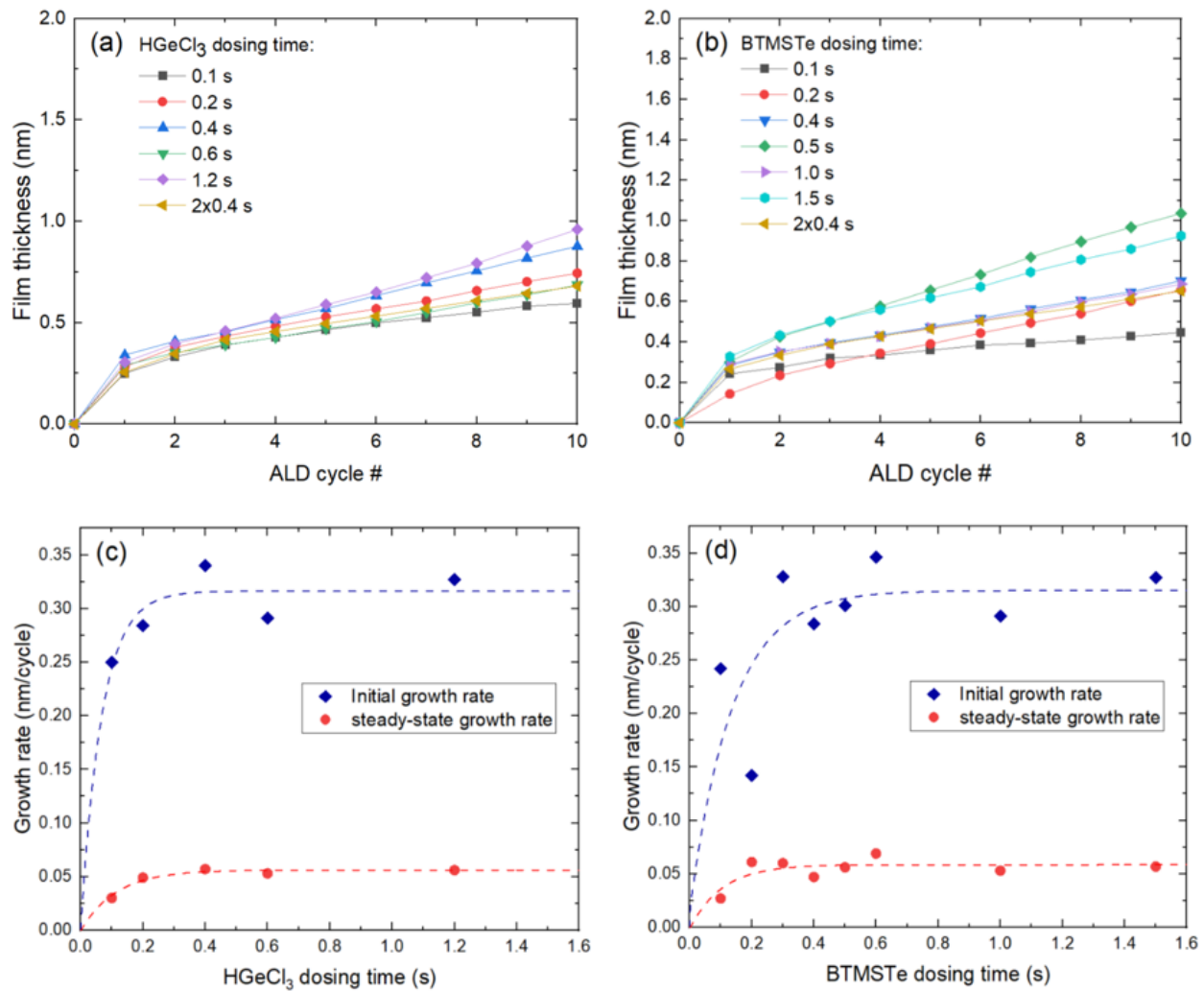


Figure 6.1. Film thickness of GeTe films as a function of the number of ALD cycles at 70 °C for varying (a) HGeCl₃ and (b) BTMSTe dosing times. Resulting first cycle and steady-state growth rates as a function of (c) HGeCl₃ and (d) BTMSTe dosing times.

Figure 6.2a shows the effect of temperature on the growth rate of the GeTe thin films. The experiments were conducted using determined saturated dosing rates of 0.4 s for both HGeCl₃ and BTMSTe at a temperature range of 60-110 °C. The growth trends show strong dependence on the substrate temperature. While initial growth rate decreases steadily with increasing temperature, the steady-state growth rate drops sharply at temperatures above 80 °C. The drop close to a zero growth rate can be explained by the desorption of the more volatile reactants, indicating the

necessity of this process being performed at temperatures below 70 °C. Figure 6.2b displays the effect of precursor purge times on the growth rates of GeTe films. HGeCl_3 or BTMSTe was dosed for 0.4 s, followed by a purge time varied from 0 to 120 seconds, followed by 0.4 s of the other precursor and a 120 s purge. The results suggest a chemical vapor deposition taking place at purge times below 15 s as indicated by increased growth rates. The rates are at maximum when BTMSTe is dosed 5 seconds before the HGeCl_3 , due to lower vapor pressure of BTMSTe and the greater distance from BTMSTe precursor vessel to the reactor compared to HGeCl_3 vessel. When long (120 s) purges are performed after each precursor times the film growth rate drops due to reactant desorption.

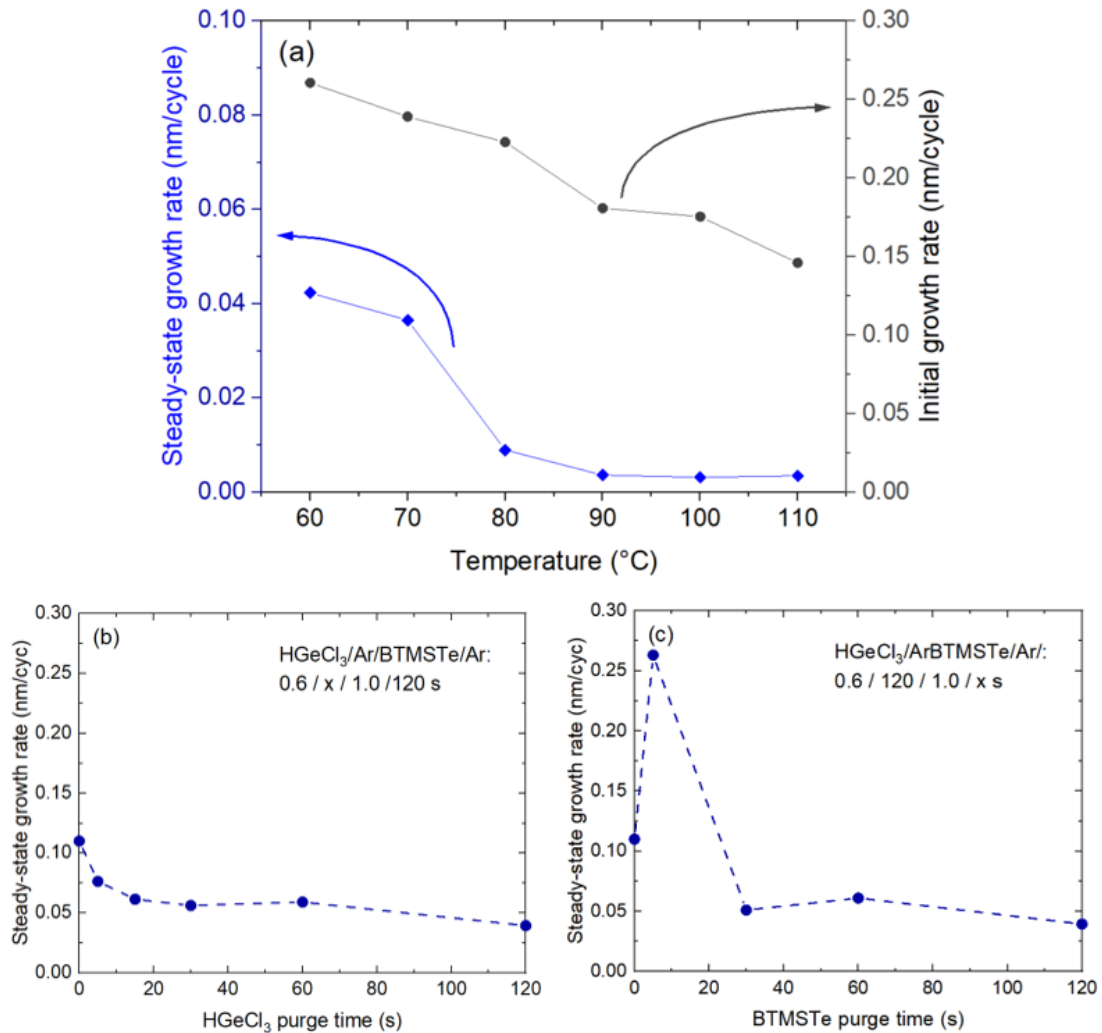


Figure 6.2. Effect of (a) process temperature and (b,c) precursor purge times on the initial and steady-state growth rates of GeTe thin films.

In addition to the Si-OH surface, the GeTe ALD process was analyzed on Si-H, W, and TiN substrates. The determined optimized process conditions of 0.4s HGeCl₃ dose, followed by a 15s Ar purge, a 0.4s BTMSTe dose and 120s Ar purge at 70 °C substrate temperature were used for these studies. The ellipsometric Δ parameter for various number of GeTe ALD cycles performed on the four substrates are shown in figure 6.3. The delta parameter characterizes the phase shift of the polarized light upon reflection off the sample and for ultrathin films the decrease in Δ is directly correlated with the optical thickness increase of the film. It is presented in lieu of

GeTe film thickness obtained from the Tauc-Lorentz model due to the complexity of the samples, which may lead to inaccurate calculated thickness values. In almost all conditions tried, the growth trend is like that demonstrated on Si-OH with initial cycles showing substrate-enhanced growth where the growth rate is higher compared to the subsequent film-dominated regime, where the growth proceeds at a constant rate. However, there is apparent disparity between the measurement results obtained. In addition to small differences in starting Δ parameter values, which can be attributed by minute variations in the initial substrates, there are variations in both the initial growth and steady-state growth regimes. The starkest contrast is visible in the 100 cycle condition on Si-H, where growth exhibits a delay followed by accelerating growth rate. On W and TiN, certain experimental runs result in a longer initial faster growth regime than others before achieving steady-state deposition. It is currently unclear whether these variations are due to artifacts in ellipsometry measurements or disparities in film growth behavior during different runs, requiring further study of the process before it can be successfully applied to depositing phase change memories.

Images acquired by atomic force microscopy after various number of GeTe ALD cycles on W, Si-H, and TiN surfaces are shown in Figure 6.4. Tungsten substrate exhibited large RMS surface roughness of ~ 1.7 nm before ALD was performed and maintained 1.7-1.8 nm roughness throughout 100 ALD cycles, indicating no major changes in the surface morphology. The hydrogen-terminated silicon and TiN substrates exhibit a smooth starting surface with RMS roughness of 60-70 pm. On both substrates the GeTe film exhibits slight roughening after 25-50 deposition cycles, followed by surface becoming smoother again with surface roughness of around 100 pm for both Si-H and TiN starting substrates. This type of roughness evolution has been

attributed to island growth, where the growth GeTe begins as nuclei on the substrate, which eventually coalesce into a uniform film.³⁶

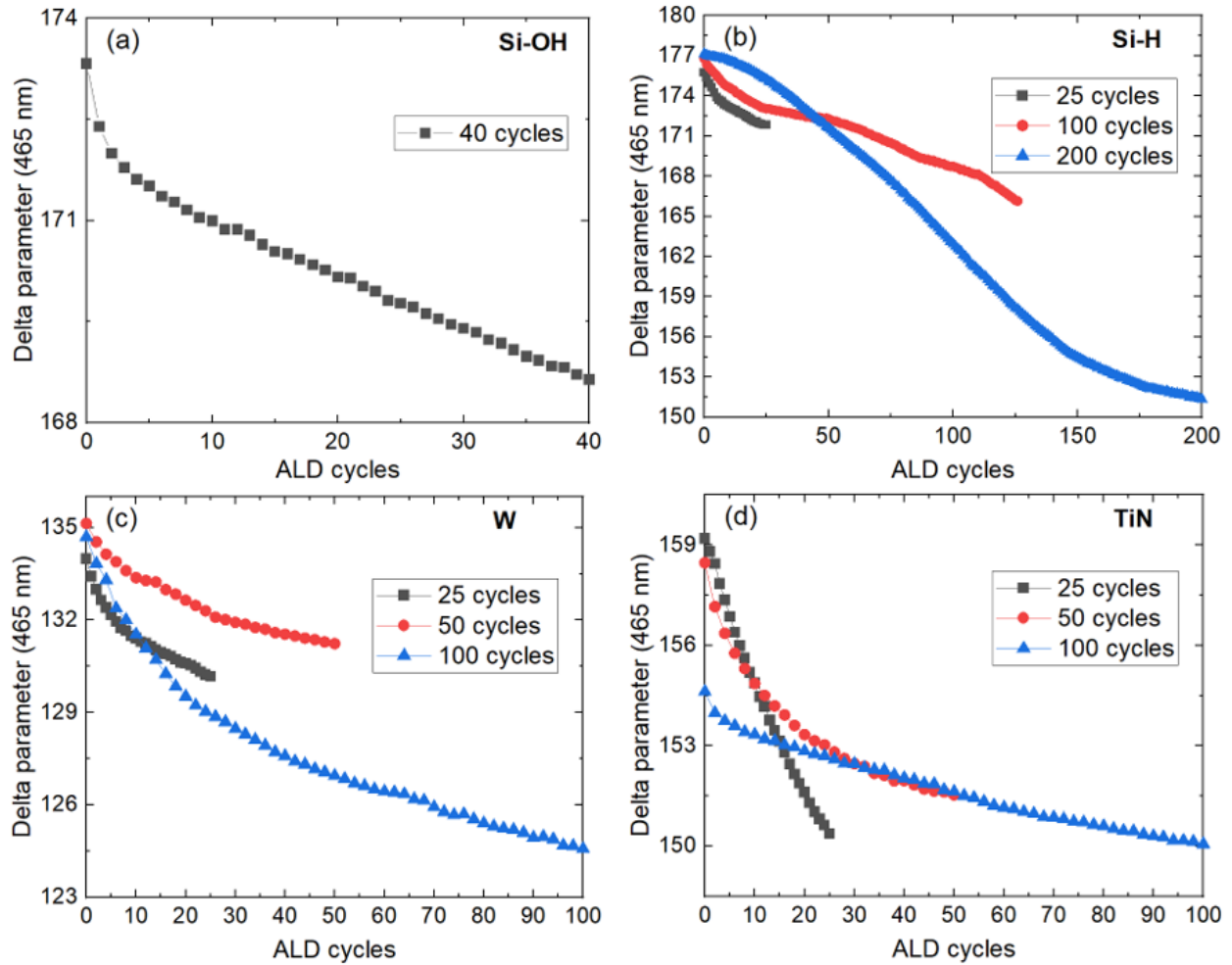


Figure 6.3. Measured ellipsometric delta parameter as a function of GeTe ALD cycles on (a) Si-OH, (b) Si-H, (c) W, and (d) TiN surfaces. Decrease in the delta parameter indicates an increase in the films optical thickness in the current growth regime.

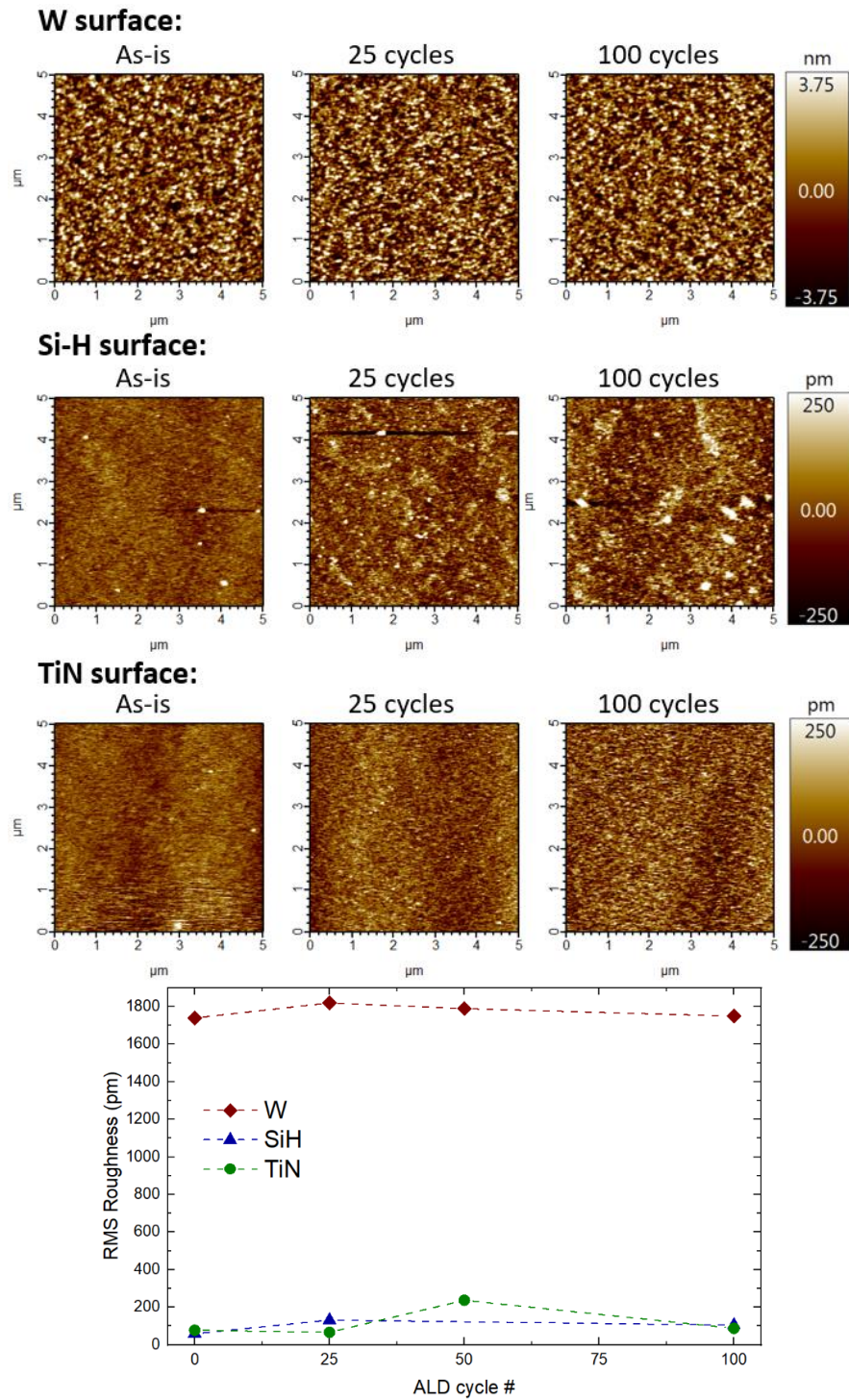


Figure 6.4. Atomic force microscopy images of GeTe ALD on W, Si-H and TiN surfaces for varying number of ALD cycles. The calculated RMS roughness as a function of the cycle number is plotted.

Chemical compositions of atomic layer deposited GeTe on Si-OH, Si-H and W substrates were analyzed by X-ray photoelectron spectroscopy (XPS) as shown in Figure 6.5. On Si-OH the XPS results indicate 1:1 Ge:Te ratio (2.6% of both), which is the target stoichiometry for GeTe. In addition to Ge and Te, O (31.4%), C (14.0%), Si (49.1%), and Cl (0.4%) were detected. On W the film resulted in 2.0% of Ge and 3.2% of Te, resulting in roughly 2:3 GeTe: ratio. In addition, O (39.7%), C (17.7%), F (21.1%) and Si (16.3%) were measured. The fluorine contamination is presumed to be present from HF-treatment done on the substrate prior deposition. Similar to Si-H, on the W substrate the film resulted in roughly 2:3 Ge:Te ratio with 7.1% of Ge and 12.5% Te present. Furthermore, O (58.0%), C(18.6%), and W(3.8%) were detected. The C and O on all samples is presumed to adventitious as measurements were performed *ex-situ*. While further study is needed to understand the cause of 1:1 Ge:Te stoichiometry on Si-OH vs 2:3 Ge:Te on Si-H and W, it can be hypothesized to be due to the number of cycles performed on each sample. As 40 ALD cycles were performed on Si-OH and 100 cycles on Si-H and W, the film stoichiometry might change throughout the process. Alternatively, the change in stoichiometry might be caused by the aging of the precursors, as the film on Si-OH was deposited several months before the films on Si-H and W. As apparent from the spectra, both metallic and oxidated GeTe peaks are present, and it can be presumed that the sample oxidated after being exposed to the atmosphere. The film on the W substrate exhibits the strongest metallic GeTe peak presumably due to a thicker film grown on the sample, preventing complete oxidation of the film.

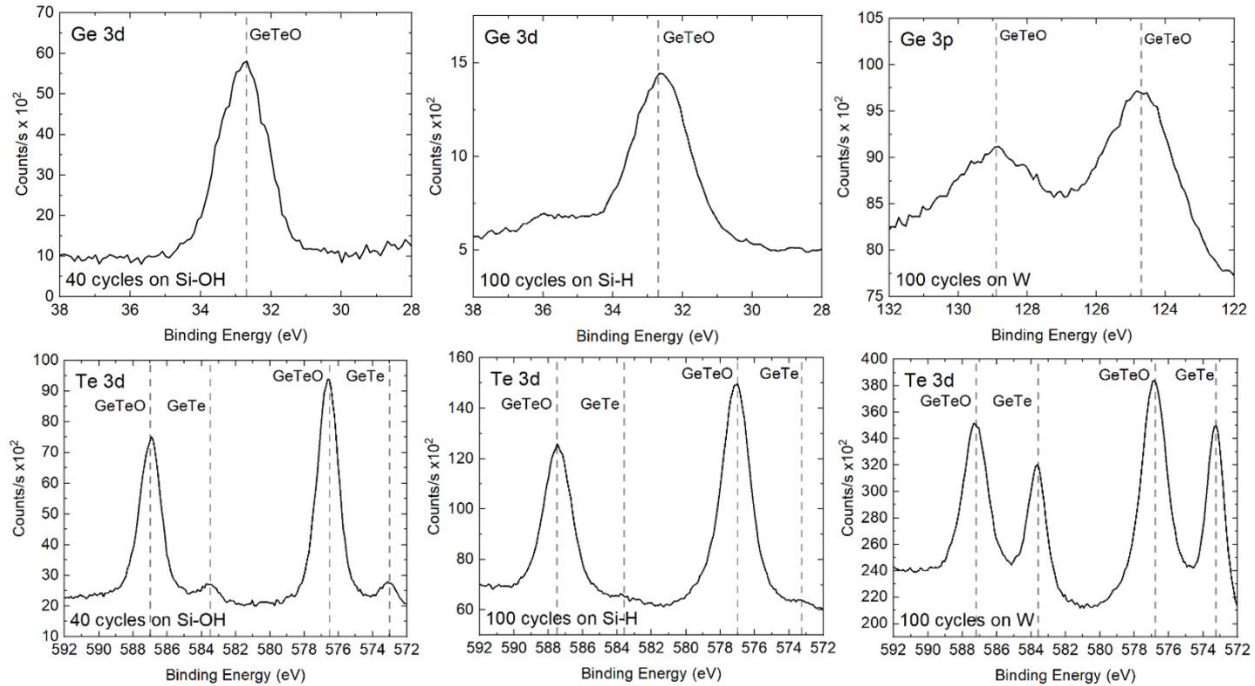


Figure 6.5. XPS spectra of GeTe ALD for 40 cycles on Si-OH (left column), 100 cycles on Si-H (middle column), and 100 cycles on W (right column).

As the operation of the phase change memory material relies on the crystallinity of the material, grazing-incidence X-ray diffraction analysis (GIXRD) was performed on the samples. Spectra of 100 ALD cycles of GeTe deposited on Si-H and W substrates at 70 °C were measured for as-deposited samples and after annealing at 170 °C for 15 minutes under Ar flow. The results are plotted in figure 6.6. While the GeTe film on the Si-H substrate deposits in an amorphous state, after annealing two peaks appear at $2\theta = 51.2^\circ$ and 53.5° , corresponding of GeTe (006) and (042) structures, respectively. The results indicate that amorphous-to-crystalline transition of ALD GeTe happens at 170 °C. In contrast, GeTe deposited on W substrate in a crystalline phase as apparent by the (006) plane peak. It is presumed that the strongly crystalline W substrate acts as a template, enabling deposition of crystalline ALD-GeTe.

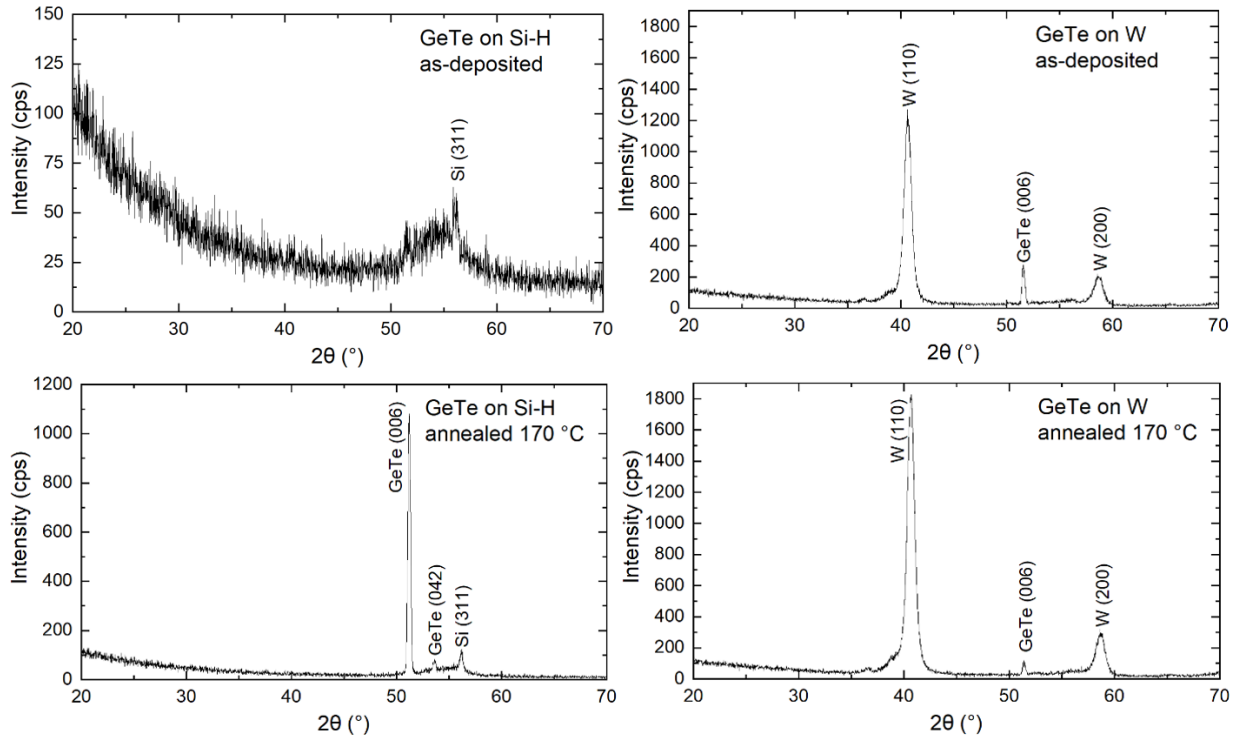


Figure 6.6. Grazing-incidence X-ray diffraction (GIXRD) measurements of GeTe after 100 ALD cycles on Si-H (left column) and W (right column) as-deposited at 70 °C and after annealing at 170 °C for 15 minutes under argon flow.

For successful $\text{Ge}_2\text{Sb}_2\text{Te}_5$ (GST225) deposition it is necessary to combine the GeTe and Sb_2Te_3 ALD processes to achieve the required composition ratios. The growth trends of Sb_2Te_3 deposition on Si-OH, on GeTe and the subsequent GeTe ALD on Sb_2Te_3 at 70 °C are shown in figures 6.7a and 6.7b. Due to the complexity of modeling the thickness of the resulting composite layers, the deposition is characterized by the delta parameter measured at 465 nm wavelength instead. In the current thickness and material regime, a decrease in the Δ indicates an increase in the film optical thickness. On the Si-OH, Sb_2Te_3 ALD results in a growth curve characteristic to island-type growth. The deposition indicates a growth delay, the deposition rate starts slow due to the substrate inhibiting initial growth but accelerates as more nuclei are generated on the surface until constant growth per cycle value is reached. On GeTe substrate Sb_2Te_3 ALD proceeds with a

constant deposition rate. Likewise, GeTe deposits on Sb_2Te_3 with a constant growth rate, without a growth delay or accelerated growth. The steady-state growth of Sb_2Te_3 on GeTe and vice-versa makes the chemistry a viable option to deposit GST225 as it enables more control over the resulting composition of the material.

The XPS spectra of Sb_2Te_3 deposited on Si-OH for 50 ALD cycles at 70 °C is shown in figures 6.7a and 6.7b. The results indicate approximately 1:1 ratio of Sb:Te, with 17.6% Sb and 16.2% Te. In addition, O (36.7%), C (19.0%), and Si (10.5%) were detected. Similar to GeTe results, the final stoichiometry of ALD deposited Sb_2Te_3 may depend on the growth substrate and film thickness. Both metallic and oxidized Sb and Te peaks were detected, the film is presumed to have partially oxidized due to XPS measurement being performed *ex-situ*.

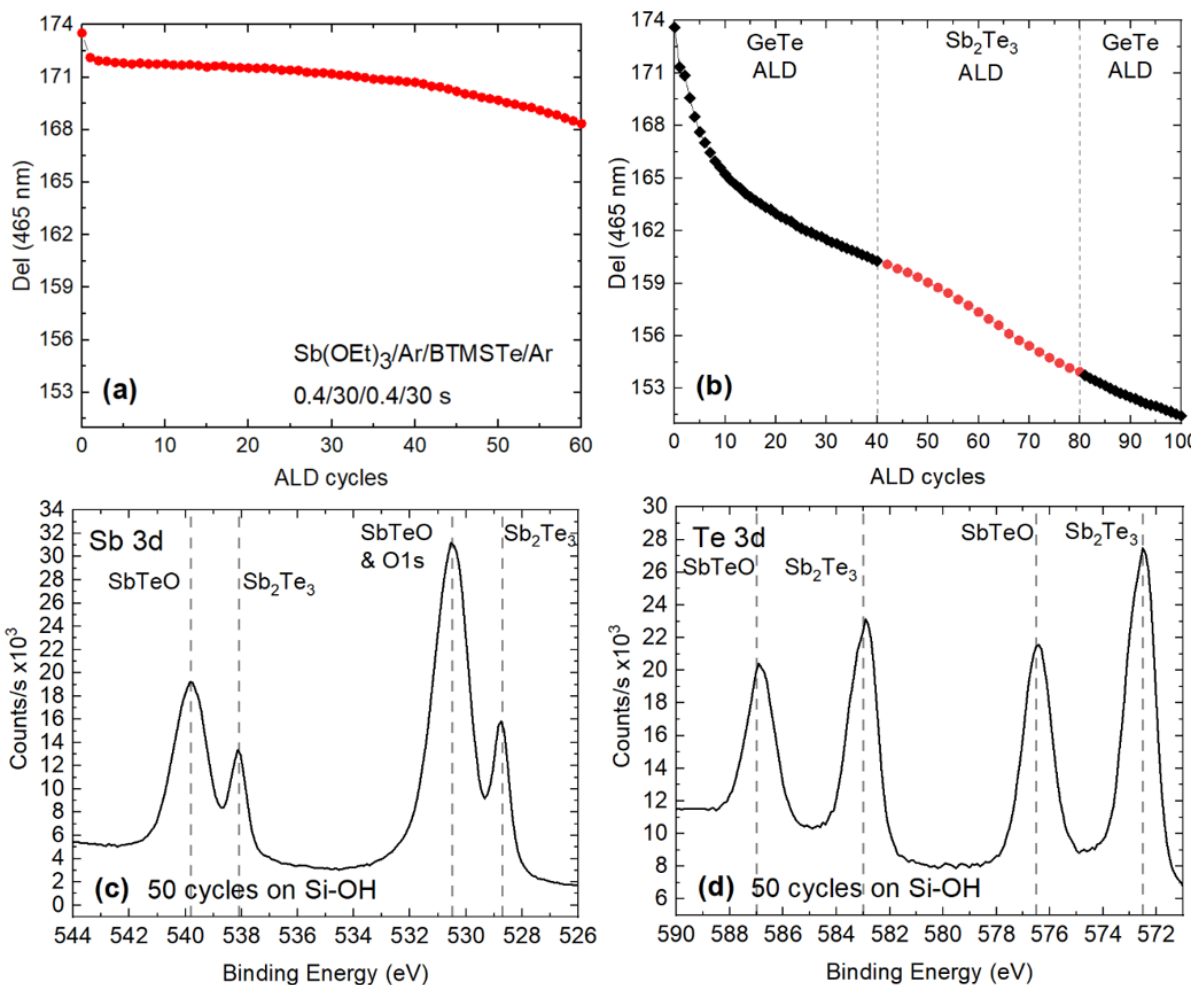


Figure 6.7. Ellipsometric delta parameter at 465 nm wavelength as a function of number of ALD cycles for (a) Sb_2Te_3 ALD on Si-OH and (b) consecutive deposition of GeTe on Si-OH, Sb_2Te_3 on GeTe, and GeTe on Sb_2Te_3 at 70 °C. (c,d) XPS spectra of Sb 3d and Te 3d peaks after 50 cycles.

6.5 Conclusion

Thermal atomic layer deposition of GeTe and Sb_2Te_3 thin films were investigated for their potential application as a phase change memory material. HGeCl_3 and BTMSTe were used as GeTe precursors and $\text{Sb}(\text{OEt})_3$ and BTMSTe as Sb_2Te_3 precursors. On Si-OH substrate, the GeTe deposition resulted in accelerated growth rate during the first cycle followed by steady-regime growth with a growth rate of ~ 0.07 nm/cycle at 70 °C as measured by *in-situ* ellipsometry. The process was found highly sensitive to temperature with GPC dropping close to zero at temperatures

above 80 °C. The GeTe ALD was additionally studied on W, Si-H, and TiN surfaces. On all substrates the growth exhibited initially accelerated growth followed by a steady growth regime, however, significant run-to-run variations were present in the ellipsometry data. The atomic force microscopy revealed film roughening on TiN and Si-H substrates, followed by surface smoothing with subsequent ALD cycles, indicating evolution of nuclei into a uniform film. 1:1 Ge:Te ratio was confirmed on Si-OH by XPS, however, ~2:3 ratio was measured on Si-H and W. The difference might be caused by the initial substrate, GeTe film thickness difference, or due to the aging of the precursors. As crystallinity is a critical characteristic for a PCM cell, XRD measurements were carried out. On Si-H the GeTe film deposited amorphous, but crystallized after annealing at 70 °C. In contrast, the GeTe was crystalline after deposited on W, and remained crystalline after annealing. Basic growth characteristics of ALD Sb₂Te₃ films were studied for potential process integration for GeTe-Sb₂Te₃ material. The Sb₂Te₃ film exhibited a long growth delay on Si-OH substrate, however, deposited instantly on a GeTe film. Likewise, GeTe exhibited instant growth on Sb₂Te₃ layer, confirming the feasibility of the integration of the two ALD processes. This work has demonstrated the viability of ALD deposited phase change memory using HGeCl₃, BTMSTe, and Sb(OEt)₃ at low temperatures and presented challenges for the future research and development of ALD PCM systems.

6.6 Acknowledgments

This work was supported by the Lam Research Corporation Unlock Ideas program. This work was performed in part at the Analytical Instrumentation Facility (AIF) at North Carolina State University, which is supported by the State of North Carolina and the National Science Foundation (award number ECCS-1542015). The AIF is a member of the North Carolina Research

Triangle Nanotechnology Network (RTNN), a site in the National Nanotechnology Coordinated Infrastructure (NNCI).

6.7 References

1. Wong, H. S. P. & Salahuddin, S. Memory leads the way to better computing. *Nature Nanotechnology* vol. 10 191–194 (2015).
2. Burr, G. W. *et al.* Large-scale neural networks implemented with non-volatile memory as the synaptic weight element: Comparative performance analysis (accuracy, speed, and power). in *Technical Digest - International Electron Devices Meeting, IEDM* vols. 2016-February 4.4.1-4.4.4 (Institute of Electrical and Electronics Engineers Inc., 2015).
3. Jeong, D. S. & Hwang, C. S. Nonvolatile Memory Materials for Neuromorphic Intelligent Machines. *Advanced Materials* vol. 30 (2018).
4. Burr, G. W. *et al.* Access devices for 3D crosspoint memory. *Journal of Vacuum Science & Technology B, Nanotechnology and Microelectronics: Materials, Processing, Measurement, and Phenomena* **32**, 040802 (2014).
5. Wuttig, M., Bhaskaran, H. & Taubner, T. Phase-change materials for non-volatile photonic applications. *Nature Photonics* vol. 11 465–476 (2017).
6. Burr, G. W. *et al.* Phase change memory technology. *J. Vac. Sci. Technol. B* **28**, 223 (2010).
7. Fong, S. W., Neumann, C. M. & Wong, H. S. P. Phase-Change Memory - Towards a Storage-Class Memory. *IEEE Transactions on Electron Devices* **64**, 4374–4385 (2017).
8. Pirovano, A. *et al.* Reliability study of phase-change nonvolatile memories. *IEEE Transactions on Device and Materials Reliability* **4**, 422–426 (2004).
9. Wong, H. S. P. *et al.* Phase change memory. in *Proceedings of the IEEE* vol. 98 2201–2227 (Institute of Electrical and Electronics Engineers Inc., 2010).
10. Perniola, L. *et al.* Electrical behavior of phase-change memory cells based on GeTe. *IEEE Electron Device Letters* **31**, 488–490 (2010).

11. Manivannan, A., Myana, S. K., Miriyala, K., Sahu, S. & Ramadurai, R. Low power ovonic threshold switching characteristics of thin GeTe₆ films using conductive atomic force microscopy. *Applied Physics Letters* **105**, 243501 (2014).
12. Sousa, V. & Navarro, G. Material engineering for PCM device optimization. in *Phase Change Memory: Device Physics, Reliability and Applications* 181–222 (Springer International Publishing, 2017). doi:10.1007/978-3-319-69053-7_7.
13. Guo, P., Sevison, G., Agha, I., Sarangan, A. & Burrow, J. Electrical and optical properties of nickel-doped Ge₂Sb₂Te₅ films produced by magnetron co-sputtering. in *Nanoengineering: Fabrication, Properties, Optics, and Devices XV* (eds. Sakdinawat, A. E., Attias, A.-J., Panchapakesan, B. & Dobisz, E. A.) vol. 10730 19 (SPIE, 2018).
14. Laudato, M. *et al.* ALD GeAsSeTe Ovonic Threshold Switch for 3D Stackable Crosspoint Memory. in *2020 IEEE International Memory Workshop, IMW 2020 - Proceedings* (Institute of Electrical and Electronics Engineers Inc., 2020). doi:10.1109/IMW48823.2020.9108152.
15. Narasimhan, V. *et al.* Physical and Electrical Characterization of ALD Chalcogenide Materials for 3D Memory Applications. (2019).
16. Lai, Y. F. *et al.* Stacked chalcogenide layers used as multi-state storage medium for phase change memory. *Applied Physics A: Materials Science and Processing* **84**, 21–25 (2006).
17. Rao, F. *et al.* Multilevel data storage characteristics of phase change memory cell with doublelayer chalcogenide films (Ge₂Sb₂Te₅ and Sb₂Te₃). *Japanese Journal of Applied Physics, Part 2: Letters* **46**, L25 (2007).
18. Liu, B. *et al.* Nitrogen-implanted Ge₂Sb₂Te₅ film used as multilevel storage media for phase change random access memory. *Semiconductor Science and Technology* **19**, L61 (2004).

19. Lyeo, H. K. *et al.* Thermal conductivity of phase-change material Ge₂Sb₂Te₅. *Applied Physics Letters* **89**, 151904 (2006).
20. Adinolfi, V. *et al.* Composition-Controlled Atomic Layer Deposition of Phase-Change Memories and Ovonic Threshold Switches with High Performance. *ACS Nano* **13**, 10440–10447 (2019).
21. Gwon, T. *et al.* Atomic Layer Deposition of GeTe and Ge-Sb-Te Films Using HGeCl₃, Sb(OC₂H₅)₃, and {(CH₃)₃Si}₂Te and Their Reaction Mechanisms. *Chemistry of Materials* **29**, 8065–8072 (2017).
22. Song, S. *et al.* Phase-change properties of GeSbTe thin films deposited by plasma-enhanced atomic layer deposition. *Nanoscale Research Letters* **10**, (2015).
23. Matsunaga, T. *et al.* Structural characteristics of GeTe-rich GeTe-Sb₂Te₃ pseudobinary metastable crystals. *Journal of Applied Physics* **103**, 093511 (2008).
24. Matsunaga, T. & Yamada, N. Structural investigation of GeSb₂Te₄: a high-speed phase-change material. *Physical Review B - Condensed Matter and Materials Physics* **69**, 104111 (2004).
25. Lazarenko, P. I. *et al.* Investigation of transport mechanisms in Bi doped Ge₂Sb₂Te₅ thin films for phase change memory application. in *International Conference on Micro- and Nano-Electronics 2014* (ed. Orlikovsky, A. A.) vol. 9440 944006 (SPIE, 2014).
26. Bai, N. *et al.* Effect of the Sn dopant on the crystallization of amorphous Ge₂Sb₂Te₅ films induced by an excimer laser. *Optics and Laser Technology* **74**, 11–15 (2015).
27. Privitera, S., Rimini, E. & Zonca, R. Amorphous-to-crystal transition of nitrogen- and oxygen-doped Ge₂Sb₂Te₅ films studied by in situ resistance measurements. *Applied Physics Letters* **85**, 3044–3046 (2004).

28. Ryu, S. W. *et al.* Phase transformation behaviors of SiO₂ doped Ge₂Sb₂Te₅ films for application in phase change random access memory. *Applied Physics Letters* **92**, 142110 (2008).
29. Li, T. *et al.* Carbon doping induced Ge local structure change in as-deposited Ge₂Sb₂Te₅ film by EXAFS and Raman spectrum. *AIP Advances* **8**, 025201 (2018).
30. Raoux, S. *et al.* Direct observation of amorphous to crystalline phase transitions in nanoparticle arrays of phase change materials. *Journal of Applied Physics* **102**, 094305 (2007).
31. Navarro, G. *et al.* Innovative PCM+OTS device with high sub-threshold non-linearity for non-switching reading operations and higher endurance performance. in *Digest of Technical Papers - Symposium on VLSI Technology* T94–T95 (Institute of Electrical and Electronics Engineers Inc., 2017). doi:10.23919/VLSIT.2017.7998208.
32. Feng, J. *et al.* Si doping in Ge₂Sb₂Te₅ film to reduce the writing current of phase change memory. *Applied Physics A: Materials Science and Processing* **87**, 57–62 (2007).
33. Wei, S. J. *et al.* Phase change behavior in titanium-doped Ge₂Sb₂Te₅ films. *Applied Physics Letters* **98**, 231910 (2011).
34. Saare, H., Song, S. K., Kim, J.-S. & Parsons, G. N. Effect of reactant dosing on selectivity during area-selective deposition of TiO₂ via integrated atomic layer deposition and atomic layer etching. *Journal of Applied Physics* **128**, (2020).
35. Jellison, G. E. & Modine, F. A. Parameterization of the optical functions of amorphous materials in the interband region. *Applied Physics Letters* **69**, 371–373 (1996).

36. Nilsen, O., Mohn, C. E., Kjekshus, A. & Fjellvåg, H. Analytical model for island growth in atomic layer deposition using geometrical principles. *Journal of Applied Physics* **102**, 024906 (2007).

APPENDIX

Appendix A.1. Integrated Isothermal Atomic Layer Deposition/Atomic Layer Etching Supercycles for Area-Selective Deposition of TiO₂

Seung Keun Song, Holger Saare, and Gregory N. Parsons

Chemistry of Materials **2019**, 31 (13), 4793-4804.

New approaches for area-selective deposition (ASD) are becoming critical for advanced semiconductor patterning. Atomic layer deposition (ALD) and atomic layer etching (ALE), that is, “inverse ALD”, are considered important for ASD, but to date, direct integration of ALD and ALE for ASD has not been reported. This work demonstrates that self-limiting thermally driven ALE, using WF₆ and BCl₃, can be directly coupled with self-limiting thermal ALD, using TiCl₄ and H₂O, in a single isothermal reactor at temperature <200 °C to achieve ASD of TiO₂ thin films on common Si/SiO₂-patterned surfaces without the use of organic nucleation inhibitors. We show that ALD/ALE “supercycles” (where one supercycle comprises, e.g., 30 ALD cycles followed by 5 ALE cycles) can be reliably repeated to yield more than 12 nm of TiO₂ while maintaining a selectivity fraction $S > 0.9$, nearly a 10× improvement over previous reports of inherent TiO₂ ASD. After ALD/ALE (=30/5) 14 supercycles at 170 °C, X-ray photoelectron spectroscopy data show a small Ti 2p signal on Si–H (hydrogen fluoride-cleaned Si), with no Ti 2p signal detected after additional “postetch” ALE cycles. At 150 °C, extended supercycles lead to unwanted particles visible by electron microscopy, which is ascribed to the formation of unreactive mixed silicon/titanium oxide nuclei. The number density of visible particles is consistent with modeled film growth trends. Overall, this work provides new insights into the capabilities for ASD of dielectric materials and a starting point to realize more complex atomic-scale processes using ALD, ALE, and other self-limiting reaction schemes.